Syn-eruptive crystallisation in silicic magmas:

The case of Volcán de Colima, Mexico

Irving R. Munguia Gonzalez

Supervisors: Alison Rust and Katharine Cashman

Co-supervisor: Nick Varley

A dissertation submitted to the University of Bristol in accordance with the requirements for award of the degree of Doctor of Philosophy in the Faculty of Science

School of Earth Sciences

September 29, 2017

Word Count:

52,897

ABSTRACT

Crystallisation occurs as water-saturated magmas ascend during eruptions as a result of a degree of undercooling induced by decompression. Crystal batch textures (crystallinity, morphology, size and number density), zoning patterns and compositions record the kinetics associated with the dynamics of ascent. I evaluate syn-eruptive crystal textures of lavas and pyroclasts that encompass a broad range of eruptive intensities and styles produced at Volcán de Colima, Mexico. Volcán de Colima is an excellent case study given the monotonous bulk compositions of its recent lavas and nearly continuous records of eruptive activity in the last couple of centuries. A sub-Plinian eruption at Colima today, similar to those that occurred in 1818 and 1913, would pose a direct threat to nearly 300,000 people; therefore, developing robust evaluation tools is essential to improve our perceptions of risks associated with its activity. Of the textural parameters measured, crystal aspect ratio and crystal area fraction (crystallinity) are the best correlated with the average discharge rates of the studied suite of steady eruptions. There is a linear relationship between crystallinity and logarithmic discharge rate for products of steady eruptions of Colima that is very similar to trends for other intermediate volcanoes. I applied textural correlations established with well-documented eruptions to estimate eruptive intensities for poorly-observed eruptions of Volcán de Colima such as the 1818 sub-Plinian and the 2005 Vulcanian crises. Syn-eruptive textures in products from the 2005 and 2013 Vulcanian sequences allowed me to study the dynamics of both magma ascent and downwards-fragmentation processes. Finally, I extended the textural analyses to phenocryst-size crystals and found that larger crystals experience significant rim overgrowth during syn-eruptive magma ascent, particularly during low-intensity eruptions. This thesis demonstrates the applicability and efficacy of integrated analysis of late-stage crystal textures as petrological tools to infer and reconstruct syn-eruptive conditions for hazard assessment of volcanic processes.

Author's Declaration

I declare that the work in this dissertation was carried out in accordance with the requirements of the University's Regulations and Code of Practice for Research Degree Programmes. It has not been submitted for any other academic award, unless where individually specified and only included to aid with the interpretation of new results and thus not intended for further examination. Except where indicated by specific reference in the text, the work is the candidate's own work. Work done in collaboration with, or with the assistance of, others, is indicated as such. Any views expressed in the dissertation are those of the author.

……

Irving R. Munguia Gonzalez

September 29, 2017

La Esperanza nunca muere

(Hope never dies)

Acknowledgements

First, I would like to acknowledge Consejo Nacional de Ciencia y Tecnología (CONACYT) Mexico for providing 5 years of funding for the completion of my Ph.D. through the grant No. 465633. Following, I massively thank my supervisors Alison Rust and Kathy Cashman, two admirable volcanologists who patiently shared with me their outstanding knowledge and scientific skills throughout my whole Ph.D. I want to thank Alison and Kathy for always encouraging me to give my best, to forge critical thinking and to keep pushing to find solutions to the unsolved; skills that made me become a better scientist and to face any challenges in life. I also greatly thank my co-supervisor Nick Varley who has been a major support in my professional formation since I commenced back in my bachelor's degree and throughout my whole Ph.D. Nick has been my closest academic mentor and partner in many volcanic adventures that inspired my love for volcanology since the beginning. Likewise, I would like to thank three women who yielded my very life foundations, my mom Adriana, my grandmother Esperanza and my great-grandmother Juanita. Three women who taught me by example that not even the Infinity is a limit and that when one strives to achieve the goals, everything is possible, even when you start from nothing. I dedicate this thesis to them because without them I would have not even been who I am and where I am. On the same line, I am very grateful to my dad, who has always been very supportive on every decision that I take, even if that implies fleeing away ten thousand kilometres away to the other side of the world. I also fondly appreciate and thank my brothers Luis and Lalo as well as my cousins, aunts and uncles for believing in me and contributing with important bits and pieces to who I am.

On the past five years, I had been incredible fortunate to share memorable times with my Uni-family, incredible people who welcomed me to my new home in Bristol since the very beginning. I would like to acknowledge Julie Oppenheimer, my cherished buddy who always

put a smile back on my face, who cheered and ranted with me, and who more importantly, even from the very distance always reminded me to keep believing in myself. I want to thank Vanessa Fairbank, the last of the team who kept me company until the very last stretch, always finding ways to cheer me up and very importantly, for her unique and enormous kindness. I also massively thank Paul Jarvis, a humble, inspiring and exceptional scientist who was always there to share a laugh and to find a conclusive solution to whatever bump was found on the ride. I want to thank my very first friend, Marit van Zalinge, a girl so confident that irradiates power all over the place, yet so kind, that had the patience to be there with me on how to ride the Ph.D. bike. I thank Karen Strehlow for reminding me that I can do it, and that I can keep up even if I look like the threes around Mount St. Helen's after the big blast at the end of my Ph.D. I extend my gratitude to Amy Gilmer, my North American buddy who kept me company on those early-starting days, and to Emma Liu, a very intelligent and strong, yet very humble and kind friend. Thanks to all the ex-G3ers, my first Bristolian family who were part of crazy times, fun times and hard times during four memorable years of my Ph.D.

Because cultural identity would never leave who you are and will be there to provide a comfort zone when you are away, I want to thank my Latino-crew. First, I'm grateful to Alvaro Guevara who immensely supported me uncountable times throughout the ride and kept me positive with that unlimited energy of him. I want to thank Artemio and Caro Cortés, my beloved Colimense Family in Bristol. Two colimenses who crossed in my path to give me the blessing and privilege of having the purest form of "home" that one can wish for when you are physically away. Together with Volcán de Colima, they kept the tropical vibes awake in me. I also thank Claudio Contreras, my Chilean brother, for many passionate discussions about volcanology, how to make Latin-America better, politics, science and life. Although a bit later in my Ph.D. Claudio arrived just in time to my life to help me re-discover that passion for volcanology that put me here in the first place. I am grateful to Omar Gomez and Edith

Rodriguez for being my adventure partners, trekking companions and festival buddies. For showing me that team work is essential in life to succeed. I thank Cristina Araya, Maryory Sarria, Eduardo Becerra and Juan Cobian for expanding the Latin-crew and making it even more fun.

I am grateful to Stuart Kearns and Ben Buse for their patience in the labs and for taking me out of to pit whenever it was required. To Jo Gottsmann and Juliet Biggs for keep pushing me each year with their very useful feedback at each APM. I extend my thanks to everyone else in the School of Earth Science who made the whole experience a lot better. Jon Hanson, Maricel Williams, Tom Sheldrake, Luke Western, Adam McAleer, Maria Chapela, are just to name a few.

I thank Mr. Barry Guckian and the whole Guckian family for their kindness and warmth. Barry Guckian was perhaps one of the most influential persons in the last few years of my Ph.D. and showed me by example that impossible is nothing. I thank Oliver Beard for introducing me to Bristol and sharing many awesome adventures with me during the early days of my life in the U.K. I importantly want to thank all my friends from before the Ph.D. who stayed with me all this time. Pilar Arriola, Jannes Kinscher, Clement Thorey and Marion Talasman for their fantastic hospitality and friendship transported from one continent to the other. Jamie and Hannah Farquharson for sharing fantastic moments of her own lives with me. To Karlita Arriola and Victor Mora for their infinite support, kindness and generosity any time that we get to cross paths. To Isabel Meza for being my partner in travels many times, facing the new life experiences that a typical naïve colimense gets when being put in the U.K. To Victor and Steffi, my very beloved “siblings” that would make me feel that I never left home any time that we met. And finally, I would like to close with a very special mention to Ali Canizalez, my sister, my strength, my support in life and perhaps the person who forced me to believe the most when I was sceptic at the slightest. Thanks to Ali for being the Little Princess

who tamed the Fox and providing me with one of the most honest and purest friendships that anyone could have possibly expect to cross paths with in life.

Table of Contents

List of Figures

List of Tables

Chapter 1

Introduction

1.1. Introduction

During volcanic eruptions, there is a complex, yet continuous feedback between changes in the physicochemical properties experienced by ascending magma and crystallisation, the physical process by which the system aims to attain thermodynamic equilibrium. This connection allows to use petrological and physical characterisation of crystal textures in lavas and pyroclasts to infer the conditions of eruption. One way to correlate crystal textures to the intensive and compositional variables involved in magma ascent and eruption is by comparison with decompression experiments (e.g. *Geschwind and Rutherford, 1995*; *Hammer and Rutherford, 2002*; *Couch et al., 2003*; *Martel and Schmidt, 2003*). Additionally, attributes of syn-ascent crystallisation can be correlated with observed eruption conditions, such as magnitude, eruption rate and eruptive style.

Studies of syn-eruptive crystallisation demonstrate that, when adequately calibrated, crystal textures can be used as petrological tools to reconstruct eruptive scenarios (e.g. *Hammer et al., 1999*, *2000*; *Szramek et al., 2006*; *Wright et al., 2012*; *Preece et al., 2013*, *2016*). Some considerations to bear in mind in studies of syn-eruptive crystallisation are: (1) interpretations are made based on specific physical attributes (e.g. Toramaru et al., 2008); (2) measurements are constrained exclusively on groundmass crystals and exclude phenocrysts (e.g. *Cashman et al., 1992*; *Hammer et al., 1999*; *2000*; *Szramek et al., 2006*), and (3) in individual mineral phases (e.g. *Martel et al., 2000*; *Couch et al., 2003*; (4) studies are focused on single eruptions (e.g. *Hammer et al 1999*; *Preece et al., 2013*, *2016*), or (5) cover relatively short periods of time of eruptive activity (e.g. Mount St. Helens, *Cashman, 1992*; *Cashman and McConnell, 2005*). In this work, I seek to fill some of these gaps using an approach that integrates batch textural parameters and compositional features (e.g. zoning patterns) of plagioclase and mafic microlites and phenocrysts. For my investigation, I use a suite of erupted products that represent a variety of intensities (discharge rates) and eruptive styles within a bicentennial

period of nearly continuous activity at Volcán de Colima, Mexico, which provides an excellent case study because of the relatively constant andesitic bulk composition of its erupted products (~62 wt.% SiO_2) and robust records of historic eruptive activity. Now, is it possible to develop a robust geological tool for the interpretation and reconstruction of syn-eruptive volcanic processes at Volcán de Colima? I hypothesise that a holistic approach towards textural analysis of syn-eruptive crystallisation (physical attributes and chemical zoning), correlated with the physical behaviour of eruptive activity at Volcán de Colima, would provide robust geological tools for the interpretation and reconstruction of syn-eruptive volcanic processes and ultimately the assessment of potential risks associated with them.

I have structured this work into three main chapters using an integrated approach for textural analysis. In Chapter II, I evaluate the intra-eruptive variability of groundmass crystal fraction (φ), number density of crystals (N_A) and their average size ($Sn_{AV.}$) and morphology ($AR_{AV.}$) within a single, well-observed effusive event. This evaluation allows me to assess the effects of syn-emplacement crystallisation and the variations of effusion rates during the eruption on groundmass texture, and ultimately to identify the most adequate sampling sites for textural analysis based on those variations. Then, I expand this evaluation to contrast the textural parameters amongst different eruptive intensities (average volumetric eruption rates, VER) and eruptive styles for well observed steady eruptions of Volcán de Colima in order to assess if there is a correlation between VER and textures at a larger range of effusion rates. I then compare the textural-VER correlations at Colima to similar textural associations at other volcanoes of intermediate composition. Finally, I use the texture-intensity calibrations as tools to estimate VER for a poorly constrained sub-Plinian eruption that occurred in 1818. In Chapter III, I apply the same approach of Chapter II (i.e. VER-textures correlations) to unsteady eruptions, using as case studies two recent Vulcanian eruptions of Volcán de Colima (in 2005 and 2013). Importantly, unsteady Vulcanian eruptions provide a different perspective on

decompression-induced crystallisation, because magma does not ascend continuously but instead stalls at shallow levels prior to rapid decompression. In Chapter IV, I expand the textural analysis of groundmass crystals to larger crystal populations (phenocrysts) and more mineral phases (plagioclase and mafic components). I use crystal zoning patterns to complement the textural analysis of late-stage crystallisation. Examining the entire population of crystals within samples from eruptions of different intensities and styles, as well as textural parameters other than batch attributes, permits more integrated and complete assessments of syn-eruptive crystallisation.

Table 1.1. *Table of symbols and abbreviations used in Chapter I.*

Chapter I - Table of symbols and abbreviations	
Symbol/Acronym	**Definition**
Ab	Albite
An	Anorthite
AR	Crystal aspect ratio
$AR_{AV.}$	Average crystal aspect ratio
C°	Degrees Celsius
km	Kilometres
MPa	Megapascals
N_A	Crystal number density
P	Pressure
P_0	Initial pressure
P_f	Pressure at final conditions
P_{H2O}	Water-vapour pressure
ppm	Parts per million of a given element in a solution
Sn	Crystal size
$Sn_{AV.}$	Average crystal size
T	Temperature
T_0	Initial temperature
T_f	Temperature at final conditions
$T_{Liquidus}$	Liquidus temperature
VER	Average volumetric eruption rates
Vulc.	Vulcanian eruption
wt.%	Percentage of a given element per sample weight
x	Chemical composition of a system
$\Delta P/\Delta t$	Decompression rate
$\Delta P_{H2O}/\Delta t$	Degassing-induced decompression rate
Δt	Duration of a process
ΔT	Degree of undercooling
Δx, Δy or Δz	Relative error of a dimension
φ	Crystal fraction

1.2. Background

Degassing-induced crystallisation exerts an important physical control on eruptive behaviour by imposing substantial changes in magma rheology (*Melnik and Sparks, 1999*). Here I provide a basic overview of topics that are relevant to syn-eruptive crystallisation in magmas and eruption dynamics. I then review previous work on the magmatic system of Volcán de Colima and its eruptive history.

1.2.1. Crystallisation kinetics in magmatic systems

Crystallisation is the transition of a metastable phase into a stable, solid phase under certain environmental conditions (*Teng, 2013*). Multicomponent liquids, such as magmatic melts, crystallise when they are subjected to changes in their intensive bulk properties (P and T). Crystallisation acts to re-equilibrate the system, for example after a drop of temperature (cooling), pressure (decompression), or a combination of both (e.g., crystallisation in a water-saturated magmatic melt, *Geschwind and Rutherford, 1995*; **Fig.1.1A**). From a classical thermodynamic point of view, the response of the system to thermobarometric disequilibrium will depend on its available free-energy (*Gibb, 1974*; *Swanson, 1977*). A system with higher free-energy (P-T above and farther from the liquidus temperature, $T_{Liquidus}$) would be able to accommodate larger changes in T and P without crystallising, whereas for the same changes in intensive parameters, a system with lower entropy would re-equilibrate by forming ordered, solid structures (crystals) (*Swanson, 1977*).

Two kinetic stages that describe the process of crystallisation are nucleation and growth. Nucleation takes place when stable nuclei form from the aggregation of elements in solution in a melt; this stage is followed by growth as the formed nuclei augment with addition of compatible components (*Gibb, 1974*; *Swanson, 1977, Teng, 2013*). Both nucleation and growth rates behave as a bell-function of a degree of undercooling (ΔT) over time ($\Delta T/ \Delta t$) (**Fig.1.1B**; *Hammer and Rutherford, 2002*; *Couch et al., 2003*). ΔT is the difference between the liquidus

temperature and the current temperature of the system ($\Delta T = T_{Liqidus} - T$) and can be a product of cooling of the system ($\Delta T = T_{Liqidus} - T_f$), decompression ($\Delta T = T_{Liqidus} - T_{Pf}$), or to some degree a combination of both processes. During eruption, decompression typically produces larger $\Delta T/\Delta t$ than cooling (*Geschwind and Rutherford, 1995*). For this reason, I focus on the effects of crystallisation from depressurisation due to magma ascent.

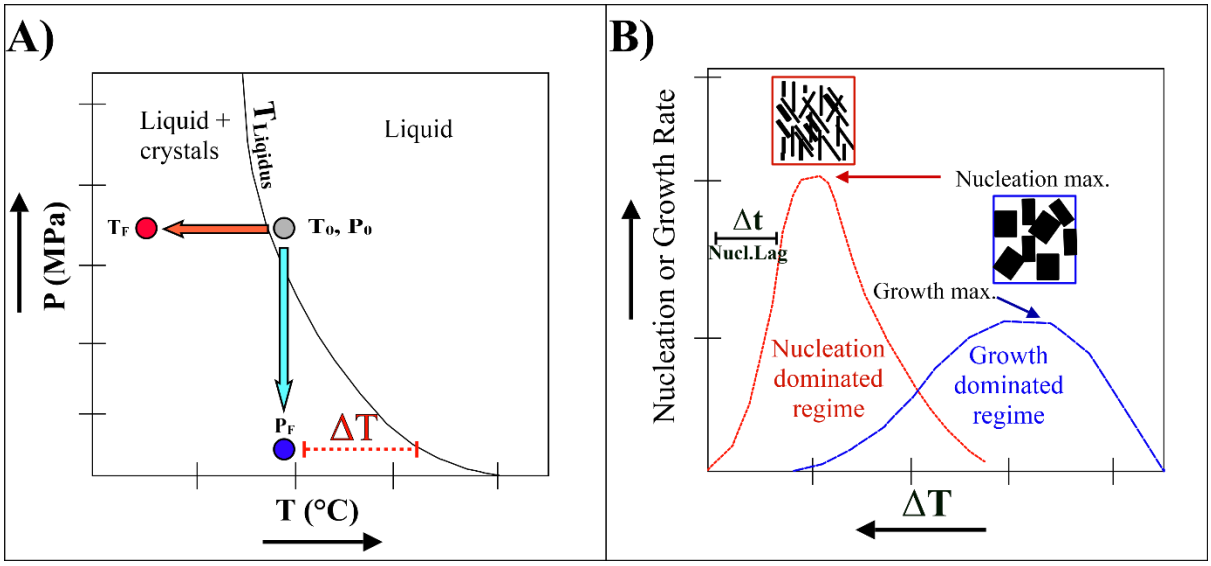

Figure 1.1. *Undercooling schemes.* ***A)*** *Shifts in intensive parameters that generate a degree of undercooling (ΔT) as experienced by a hypothetical batch of water-saturated magma at initial conditions above liquidus (T_0, P_0). Undercooling can be generated by cooling ($\Delta T = T_{Liqidus} - T_f$) or decompression ($\Delta T = T_{Liqidus} - T_{Pf}$), or a combination of both (scheme after Hammer and Rutherford, 2002).* ***B)*** *Crystallisation kinetic processes as functions of a degree of undercooling and time (scheme after Couch et al., 2003). A time lag in crystal nucleation at the beginning of the process; rate maxima, and binary of typical crystal 2-D textures are presented for reference.*

1.2.2. Assessment of degassing-induced crystallisation and its application in natural systems

In nature, ΔT does not remain constant during crystallisation, as crystallisation decreases the chemical potential of the solution (*Arzilli and Carol, 2013*). However, volatile diffusion occurs more efficiently than larger components dissolved in magmatic melts (*Gonnermann and Manga, 2007*), so where crystallisation is controlled primarily by the behaviour of water, water exsolution and degassing would occur faster than crystal formation

and ΔT will remain positive for as long as gas loss prevails. This illustrates the important control of water activity in the melt on magma crystallisation, which in turn can be linked to conditions of magma ascent (decompression).

Crystal textures resulting from syn-eruptive decompression-driven crystallisation integrate the extent of decompression experienced by a magma batch as it ascends from a storage region at depth, through the conduit, and up to the surface. Groundmass crystals (microlites) are the most utilised size-range for ascent-related textural studies since these can be directly associated with the latest stages of crystallisation (*Cashman, 1992*). Some of the textural parameters most commonly studied to interpret crystallisation kinetics of magmatic systems are abundance (φ), number density (N_A), crystal size (Sn) and crystal shape (AR). Of all crystalline phases, the abundance and the anhydrous nature of feldspars make them the most commonly measured mineral for textural analyses of degassing-induced crystallisation (*Shea and Hammer, 2013*).

One approach to inferring magma ascent conditions for natural systems is to determine whether the crystal textures reflect a nucleation-dominated or growth-dominated regime. Nucleation-dominated crystallisation is indicated by numerous (high number density, here reported as number per area, N_A) very small crystals (low size, here reported as √area = Sn; **Fig.1.1B** and **1.2**, *Geschwind and Rutherford, 1995*; *Hammer et al., 1999, 2000*). A nucleation-regime reflects high rates of degassing-induced decompression ($\Delta P_{H2O}/\Delta t$). Rapid crystallisation (nucleation-dominated) also tends to produce highly anisotropic crystal forms (**Fig. 1.1B**), which can be measured using the aspect ratio (AR), where AR = short axis/long axis. Growth-dominated regimes, characterised by fewer but larger crystals for the same overall crystallinity φ, are, conversely, representative of low $\Delta P_{H2O}/\Delta t$ (*Couch et al., 2003*; *Martel and Poussineau, 2007*).

Correlation of eruptive discharge rates and crystal textures in dome-forming, arc stratovolcanoes of intermediate compositions that encase those of Volcán de Colima products (Unzen, *Noguchi et al., 2008*, and Tungurahua, *Wright et al., 2012*) suggest that crystal textures formed syn-eruptively are often preserved without significant post-eruptive changes. This correlation has been applied to inferring the ascent dynamics within the conduit from a combination of textural analyses of crystals found in the erupted products and observations of surface processes such as discharge rates and eruptive styles. However, paths of ascent in most natural systems are likely to be complex; for this reason, it is important to replicate different scenarios of syn-ascent crystallisation under controlled decompression experimental settings to constrain inferences about natural systems.

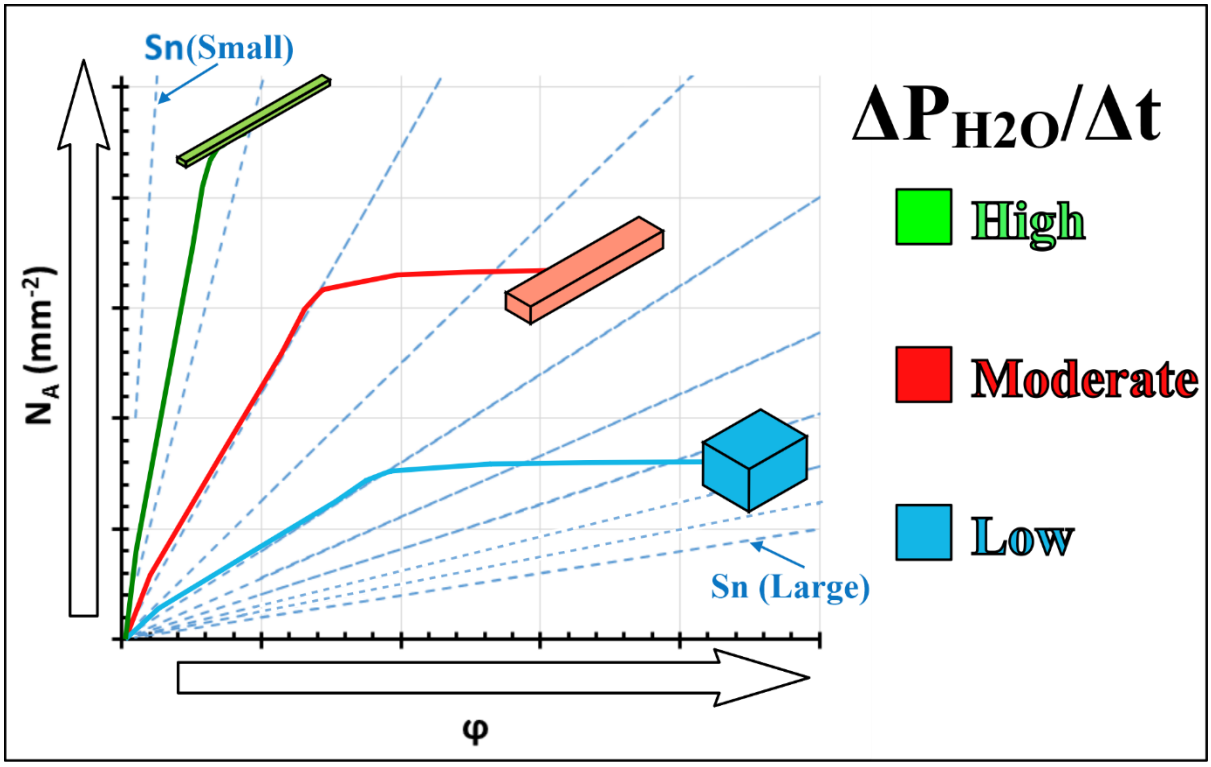

Figure 1.2. *Crystal textural correlations with decompression rates. Textural correlations between crystallinity (φ), number density (N_A), size (Sn) and shape with rates of degassing-induced decompression ($\Delta P_{H2O}/\Delta t$). The dashed blue lines indicate theoretical boundaries of crystal sizes and are constrained from the relation $Sn = \sqrt{(\varphi / N_A)}$. Hypothetical paths depicting textural behaviour during crystallisation a high (green), moderate (red) and low (blue) decompression rates are presented. Example of characteristic crystal shapes associated with the different paths are provided at the end of each of these in the figure, with the more acicular shapes (e.g. green block) associated with the hypothetical high-decompression path and getting progressively more equant at lower decompression rates (e.g. red and blue).*

1.2.3. Decompression-induced experiments – an overview

Controlled decompression experiments are used to assess crystal textures produced under different environments (T, P and x) in relation to the kinetic processes associated with magma degassing. Different degassing-induced decompression paths have been replicated in experiments (**Fig.1.3**). Single-step (**Fig.1.3**) can be used for direct comparisons between the theoretical predictions of the effects of ΔT and $\Delta T/\Delta t$ with crystallisation kinetics (*Hammer, 2008*). However, these experiments are unlikely to replicate the decompression behaviour occurring in natural systems under most conditions, which are more likely to resemble dynamic decompression experiments (e.g. multi-step experiments that consist of decompression followed by dwell, **Fig.1.3**). Importantly, however, crystallisation during dynamic-decompression does not reflect only the effects of changes in ΔT and $\Delta T/\Delta t$, but rather integrates changes in supersaturation from chemical re-equilibration (*Hammer, 2008*; *Shea and Hammer, 2013*). Most importantly, calibration between experimental and natural textures is crucial.

An integrated approach to interpreting late-stage crystal textures of eruptive products, has led to diverse proposed scenarios of magma ascent in volcanic systems. The simplest scenario is that occurring during high magnitude, high intensity, sustained explosive eruptions (e.g., Plinian), where ascent from a magmatic reservoir through the conduit to the surface is sufficiently rapid to allow significant gas exsolution but hinder crystallisation (e.g. Mt. Pinatubo; *Hammer et al., 1999*). This results in low φ, Sn_{AV}., and high N_A, consistent with a nucleation-dominated regime of crystallisation (*Martel and Poussineau, 2007*; **Fig.1.2**). Steady eruptions at relatively low $\Delta P_{H2O}/\Delta t$ (e.g. effusion of lava domes; *Hammer et al., 1999,2000*), in contrast, allow time for crystallisation, thus the groundmass typically has high φ, Sn_{AV}., and low N_A, characteristic of a growth-dominated crystallisation regime. A third scenario allows periods of stagnation during ascent (e.g. intra-explosive, conduit-refill phases; *Geschwind and*

Rutherford, 1995; *Hammer et al., 2000*; *Martel and Poussineau, 2007*). This scenario could be comparable with "multiple-step" decompression experiments, but with the important difference that in natural systems, the ΔP_{H2O} or Δt steps are unlikely to be constant.

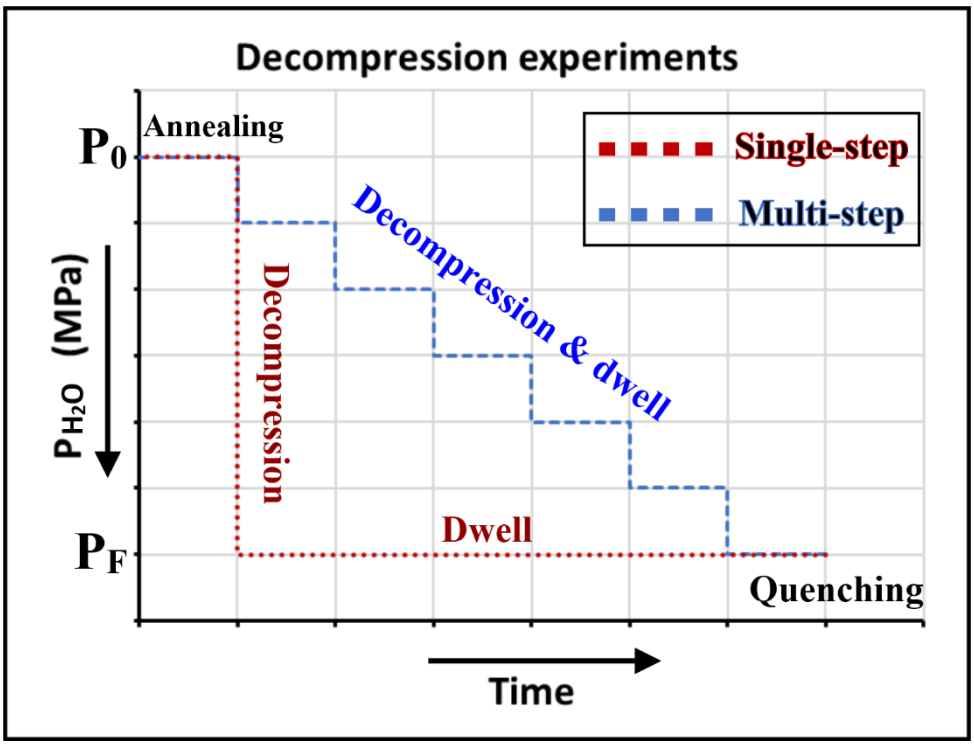

Figure 1.3. *Graphic representation of decompression-induced experiments. Graphic representation of single-step (red) and multi-step (blue) decompression experiments. Experiments are preceded by an annealing time at an initial pressure (P_0), are decompressed at different styles, and are quenched at final pressure (P_F). Figure adapted from Couch et al. (2003).*

1.2.4. Controls of syn-ascent degassing in eruptive style

Melt composition is also important for the kinetics of crystallisation and gas exsolution. Specifically, the higher viscosity of intermediate to rhyolitic melts relative to their mafic counterparts delays volatile diffusion (*Liu and Zhang, 2000*). High melt viscosity also limits the mobility of exsolved volatiles. Under these conditions, loss of the gas phase (outgassing) requires the development of permeability, either by increasing the volume of the gas phase (*Klug and Cashman, 1996*) or by bubble deformation from shearing or bubble collapse (*Gonnermann and Manga, 2003*; *Rust and Cashman, 2004*). The effectiveness of degassing,

through modulation of gas-overpressures, determines whether an eruption occurs in an effusive or explosive fashion (*Woods and Koyaguchi, 1994*), even for magmas of similar gas volume fractions (*Sparks, 2003*).

1.2.4.1. Effusive eruptions

Effusive activity in silicic volcanoes is commonly associated with open-system degassing, as gas can escape vertically due to shearing near the conduit margins or through fractures on the country rock (*Eichelberg, 1995*; *Tuffen et al., 2003*; *Rust et al., 2004*). Examples of effusive activity are lava flows and lava domes. From this perspective, a fundamental question relates to conditions that allow sufficient pre-eruptive degassing to prevent explosive activity.

1.2.4.2. Explosive eruptions

If the ascending magma either never develops or subsequently loses permeability, gas exsolution occurs under closed-system conditions. The resulting overpressure can exceed the viscous limits of the magma, leading to its fragmentation (*Alidibirov, 1994*; *Woods and Koyaguchi, 1994*; *Gonnermann and Manga, 2003*). Common types of explosive silicic eruptions are Plinian, sub-Plinian and Vulcanian eruptions.

The classification of Vulcanian and (sub-)Plinian eruptions is primarily based on the duration of the explosive eruptions, the mass of tephra erupted and the height that the eruptive column reaches in the atmosphere. Based on the classification by *Newhall and Self (1982)*, Vulcanian explosions generate eruption plumes of heights between 1 and 15 km above sea level. This plume height range, and thus the mass eruption rate, overlaps with sub-Plinian eruptions, but Vulcanian eruptions are shorter-duration and thus erupt less tephra. Both Plinian and sub-Plinian eruptions generate relatively steady convective eruption column for hours, but Plinian eruptions distinguished by larger magnitude ($>10^{11}$ kg tephra erupted) and intensity

(columns > 20 km) (*Cioni et al. 2015*). Plinian and sub-Plinian eruptions occur when volatile exsolution decreases magma density, which in turn leads to acceleration of magma that, combined with an increase in bulk viscosity due to degassing, leads to the mechanical failure of magma and ultimately, fragmentation (*Scandone et al., 2007*). Vulcanian explosions, in contrast, do not result from steady magma ascent, but instead depend on localised overpressure accumulation that is often released in pulses. Specifically, gas that is continuously exsolving from depth accumulates in magma below a dense lava plug. When the resulting overpressure exceeds the mechanical strength of the confining load, the sealing cap fragments (*Clarke et al., 2009*). The disruption caused from the sudden decompression causes a downward decompression of the conduit and magma fragmentation caused by brittle rupture from the large strain rate (*Self et al., 1978*; *Alidibirov, 1994*). This fragmentation wave continues to propagate until the tensile strength of magma and the tensile stress forces from decompression balance sufficiently for magma to behave in a ductile manner (*Alidibirov and Dingwell, 1996*). The differences in the dynamics between (sub-)Plinian and Vulcanian eruptions generate associated differences in vesicularity and crystallinity of the eruption products (e.g. *Cashman, 2004*).

1.2.5. Volcán de Colima

Volcán de Colima is the youngest and only active eruptive centre of the Colima Volcanic Complex. This arc stratovolcano is located in the western portion of the Trans-Mexican volcanic belt. Historic and geological records suggest centennial eruptive cycles at Volcán de Colima that include effusive and moderate explosive activity and culminate in major sub-Plinian to Plinian eruptions (*Luhr and Carmichael, 1980*; *1990*). The two most recent sub-Plinian events occurred on the 15 of February 1818 and on the 20 of January 1913 (*Luhr and Carmichael, 1990*; *Robin et al, 1991*; *Luhr et al., 2010*). The bulk chemistry of Volcán de Colima lavas has remained fairly constant within the past two major eruptive cycles (59 to 61.5

wt.% SiO_2), only erupting magmas of slightly more mafic compositions during the sub-Plinian events (*Luhr and Carmichael, 1980, 1990*; *Robin et al., 1991*; *Verma and Luhr, 1993*; *Luhr, 2002*; *Reubi and Blundy, 2008* and *Saucedo et al., 2010*).

The origin of recent Colima lavas (post-1818) has been interpreted to reflect pre-eruptive mixing between a stalled silicic magma in a shallow reservoir and an input of deeper pulses of hydrous basalt from the mantle wedge (*Luhr and Carmichael, 1980*; *Mora et al., 2002*; *Atlas et al., 2006*; *Savov et al., 2008*; *Luhr et al., 2010*) and subsequent long-term crystal differentiation (*Robin et al., 1991*). Alternatively, Colima andesite could form by assimilation and mingling of gabbroic basement with the stalled dacitic melt (*Reubi and Blundy, 2008*; *Reubi et al., 2013*). A clear understanding of the origins of Colima lavas is important to define how variations in chemistry and mineralogy of feeding magmas affect the physical and temporal dynamics of ascent through the conduit and the subsequent emplacement (*Luhr et al., 2010*). For example, it has been recognised that highly explosive eruptions (sub-Plinian or Plinian events) are driven in part by incorporation of magma from deep within the system (e.g. *Luhr and Carmichael, 1980* and *Robin et al., 1991*).

Colima products display mineralogical suites characteristic of andesitic lavas, and comprise phenocrysts and microlites of plagioclase, clino- and orthopyroxene and Fe-Ti oxides as main components. Amphibole is the main water-bearing mineral in Volcán de Colima andesites, however it is not present in great proportions in the most recent historic products (post-1913; 0 -1 vol.%, *Luhr et al., 2002*; *Savov et al., 2008*), but is common in lavas erupted prior to the 1913 sub-Plinian event (2.4-5.3 vol%, *Savov et al., 2008*). For this reason, their rare presence in post-1913 lavas may be residual from the pre-1913 eruptions (*Reubi et al., 2013*). Finally, traces of quartz and olivine are found as rare xenocrysts (*Luhr and Carmichael, 1980*; *Luhr, 2002*; *Mora et al., 2002*; *Reubi and Blundy, 2008*). Phenocryst contents are estimated between 32 – 50 vol.% (*Luhr et al., 2002*; *Mora et al., 2002*; *Reubi and Blundy, 2008*;

Lavallée et al., 2012). All mineral phases except hornblende occur as microlites in groundmass (*Luhr and Carmichael, 1980; Luhr, 2002*).

1.2.5.1. Intensive parameters and water content

Similar compositions between Volcán de Colima andesites and a spessartite (andesite with phenocrysts of hornblende only) from Mascota volcano in the western portion of the Trans-Mexican Volcanic Belt (63.6 and 60.3 ± 0.9 wt.% SiO_2, respectively) permitted the phase relations from experiments on Mascota samples to serve as analogues for Volcán de Colima magmas (**Fig.1.4A**, *Moore and Carmichael, 1998*). *Reubi and Blundy (2008)* pointed out that for Volcán de Colima compositions the Mascota phase diagram would best apply to products associated with magma mixing (e.g. sub-Plinian events) and not so for most of the non-sub-Plinian events (e.g. effusive and Vulcanian eruptions). *Reubi and Blundy (2008)* observed discrepancies between mineral assemblage, compositions and volatile budgets measured in natural samples and projected estimations based on the Mascota phase relations, so they proposed the phase diagram for Mount St. Helens dacites (by *Rutherford et al., 1985*) as a better analogue for the effusive, historic products (**Fig.1.4B**).

Temperatures have been calculated for Volcán de Colima magmas using geothermometry of two-pyroxenes (*Luhr and Carmichael, 1980*; *Luhr, 1992, 2002*; *Savov et al., 2008*), Fe-Ti pairs (*Mora et al., 2002*; *Luhr et al., 2002*; *Reubi and Blundy, 2008*) and Ab-An exchange (*Luhr and Carmichael, 1980*; *Reubi and Blundy, 2008*), and provide the ranges (including uncertainties) indicated in **Figure 1.5**. Crystallisation temperatures of 970 – 985 °C were estimated for the 1913 sub-Plinian eruption (*Luhr, 1992, 2002*). For the intra-cycle events, temperatures of 963 – 1021 °C were constrained for products erupted between 1869 and 1991 (*Luhr, 1992*); 960 - 1031°C for lavas extruded within 1991 and 1998 (*Luhr, 2002*; *Mora et al., 2002*); 901-1015 °C for products erupted between 1998 and 2005 (*Reubi and Blundy, 2008*), and 995 - 1027 °C for 2004 and 2005 lavas (*Savov et al., 2008*). The relative increase in

temperatures over time has been verified by several authors (e.g., *Reubi and Blundy, 2008*; *Savov et al., 2008*).

Volcán de Colima lavas ascend and erupt at water-saturated conditions (*Moore and Carmichael, 1998*). Melt water contents calculated from Ab-An exchange reactions yield 2.5 – 6 wt.% H_2O for products erupted between 1869 and 1991, with the highest values for the 1869 and 1913 products (4.5-6 wt.% H_2O) (*Luhr, 1992*; *Savov et al., 2008*), and lower values for later-erupted magma: 3.4-3.5 wt.% H_2O in 1998-1999 lavas (*Luhr, 2002*), and 1.1- 3.1 wt.% H_2O, for lavas produced in 2004 – 2005 (*Savov et al., 2008*). On the other hand, direct (as opposed to calculated) measurements of volatiles in melt inclusions of samples erupted in 1869 – 1880 yield 0.39 – 3.4 wt.% H_2O (*Atlas et al., 2006*); 1913 samples, as high as 6.2 wt.% (*Reubi and Blundy, 2008*), and 1998-2005 products range at 0.1 - 2.9 wt.% H_2O and 0 – 800 ppm CO_2, providing lower ranges than the Ab-An exchange calculations.

Temperature estimates, mineral compositions and assemblages from products of historic eruptions at Volcán de Colima suggest crystallisation pressures between 60 and 170 MPa (2.3 – 6.6 km depth, based on a crustal rock density of 2.62 g/cm^3) as projected on the Mascota phase diagram with the coloured, dashed-boxes in **Fig.1.4A** (*Luhr, 2002*). Based on St. Helens dacite phase-relations, measured volatile contents and estimated temperatures of the 1998-2005 lavas (0.1 – 2.5 wt.% H_2O at 996 °C), trapping pressures of melt inclusions are estimated at 150 to 10 MPa (**Fig.4B**, *Reubi and Blundy, 2008*).

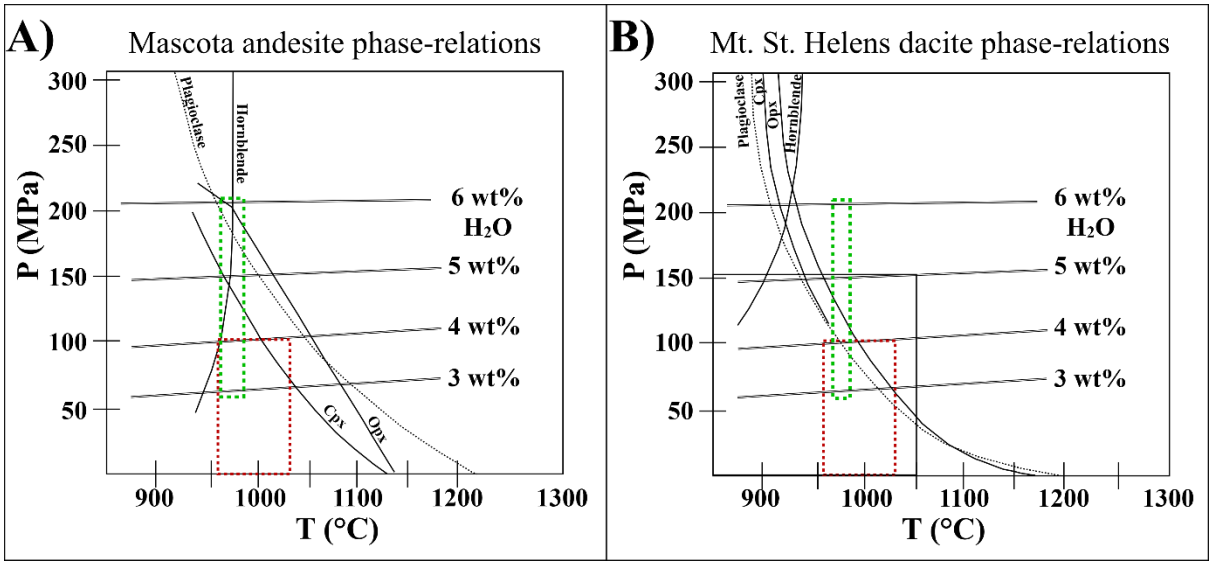

Figure 1.4. *H_2O- saturated phase-relation analogues for Volcán de Colima magma compositions. Phase-relations are:* ***A)*** *for the spessartite andesite of Mascota, Mexico (Moore and Carmichael, 1998), and* ***B)*** *for Mount St. Helens dacites (Rutherford et al., 1985). The near-horizontal solid lines display theoretical boundaries of water content based on pressure and temperature correlations for the given compositions. The curved lines indicate the stability boundaries for the different mineral phases according to the respective labelling. The dashed-boxes indicate ranges of water contents and temperatures estimated using Pyroxene and Fe-Ti- pairs thermometry for Volcán de Colima products (Luhr, 1992, 2002; Reubi and Blundy, 2008). Green box corresponds to 1913 sub-Plinian tephra and red box to lavas erupted between 1869 and 2005.*

1.2.5.2. Volcán de Colima magmatic system

Some analytical studies based on the water content and the chemistry of melt inclusions indicate that magmas experienced continuous crystallisation ~ 6 - 0 km below the summit in Volcán de Colima (*Atlas et al., 2006*; *Reubi et al., 2013*). Petrological and seismic evidence suggest, however, that certain regions within the magmatic plumbing system of Volcán de Colima experience enhanced crystallisation (*Reubi et al., 2013*). Clusters of seismic events tend to be located at three main depths ranges: 1, 3-4 and 7-11 km (including uncertainties) below the summit of Colima (**Fig.1.5**; *Nuñez-Cornú et al., 1994*; *Medina et al., 1996*; *Mora et al., 2002*; *Zobin et al., 2002*; *Reubi and Blundy, 2008*; *Varley et al., 2010b*). The deepest crystallisation cluster (7-11 km) has been associated with the region of magma mixing that produce sub-Plinian eruptions (1818 and 1913; *Moore and Carmichael, 1998*). The second cluster (3-4 km) corresponds to pressures where Colima magmas are thought to attain volatile saturation conditions and thus where crystallisation related to ascent begins (*Reubi et al., 2008*). Lastly, the shallowest cluster (1 km) has been associated with a region where major rheological changes occur in the magma due to extensive volatile-loss (*Varley et al., 2010a; Lavallee et al., 2012*; *Reubi et al., 2013*). Physical evidence (e.g. porosity and porosity distribution, degree of alteration of products, observation of different vents at the crater and seismicity, *Lavallée et al., 2012; Salzer et al., 2014*) and estimates of degassing rates using $^{210}Pb/^{226}Ra$ disequilibria in bulk- and melt inclusion compositions of Volcán de Colima products (*Reubi et al., 2015*) suggest that this shallow region comprises networks of dykes fed by magma batches of short residence with different ascent rates and degassing histories rather than a large magma reservoir (*Reubi et al., 2015*)

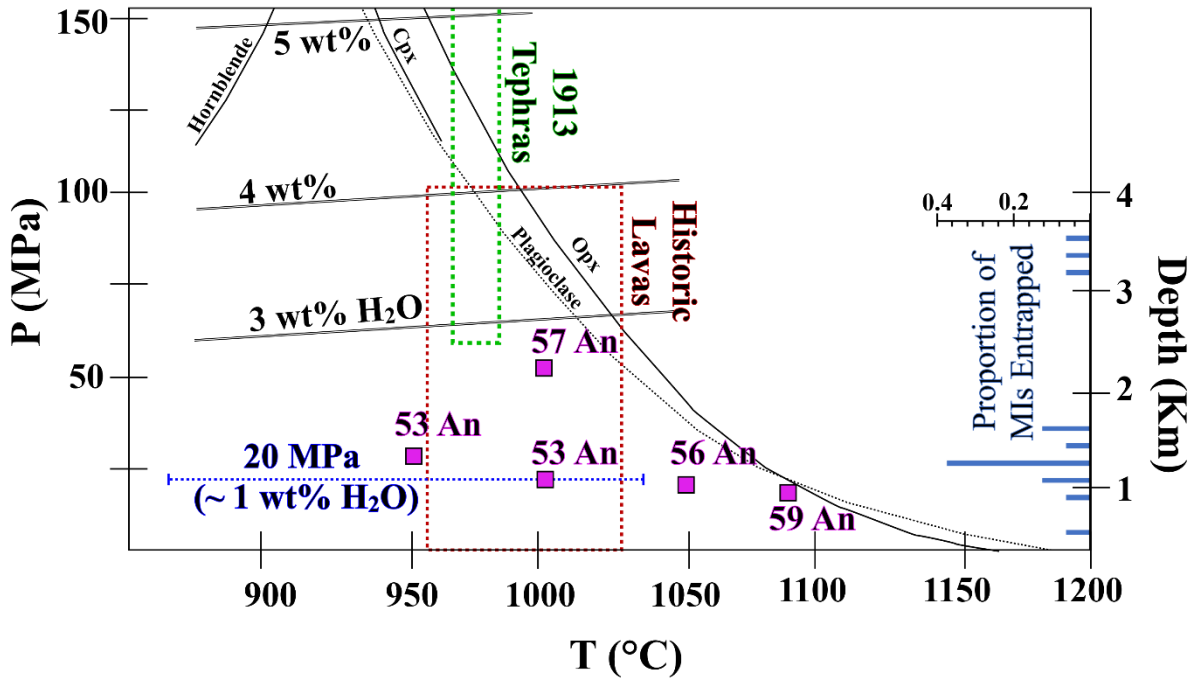

Figure 1.5. *Water-saturated phase-relations analogue for Volcán de Colima magmas based on Mount St. Helens dacitic compositions (Rutherford et al., 1985). The dashed-boxes indicate ranges of water contents and temperatures estimated for historic eruptive products (after Luhr, 1992, 2002; Reubi and Blundy, 2008). Green box corresponds to 1913 sub-Plinian tephra and red box to lavas erupted between 1869 and 2005. Number of melt inclusions trapped at different depths are displayed on the right axis of the diagram (after Reubi et al., 2013). Blue, dashed, horizontal line indicates a rheological threshold region where it has been suggested that Volcán de Colima magmas can experience temporal pre-eruptive stalling (Lavallée et al., 2012; Reubi at al., 2013). Purple-coloured squares indicate the anorthite content of feldspars at the respective P-T conditions.*

Chapter 2

Linking groundmass crystal textures to intensities of eruptions at Volcán de Colima

Author contribution and declaration: For this chapter, I collected, prepared and analysed the rock samples and processed and analysed the textural and DEM data. A. C. Rust and K. V. Cashman provided supervision, advice, and edits during the writing of this chapter. N. R. Varley contributed with the means and knowledge for the collection of samples, the digital images to process the DEM data for Volcán de Colima, and his guidance and advice during the writing of the chapter. H. Dietterich gave support for the processing of the DEM. B. Buse and S. Kearns delivered the guidance and advice pertinent to BSE-imaging and microprobe analysis and processing of chemical data. M. Cassidy kindly contributed the textural dataset of samples derived from the 2013 eruptive stage.

Abstract

It is well established that groundmass crystals can form as water-saturated magma ascends to the Earth's surface during eruptions; the abundance, size and morphology of those crystals are determined by the kinetics of crystallisation, which, in turn, are affected by the degree of undercooling induced during decompression. Analysing microlite textures from eruptive products of both effusive and explosive eruptions provides insight into the paths of magma ascent and the effects of crystallisation on eruption dynamics, and thus is an important tool for volcanic hazard evaluation. I evaluate the groundmass crystal textures (crystallinity, crystal morphology, size and number density) of erupted products from historic dome collapse events, lava flows of different lengths, and explosive eruptions of Volcán de Colima that cover a two hundred-year period of nearly continuous activity. A detailed study of samples collected from different locations on a single lava flow demonstrates that the textures of samples originating from the flow front provide average estimates of crystal textures along the entire flow. This means that inaccessible lava flows can be adequately sampled from secondary deposits such as block-and-ash flows or rock-falls. Moreover, the final lava flow lengths and volumes correlate with average effusion rates, making length an adequate proxy for eruption intensity. Of the textural parameters measured, crystal aspect ratio and crystal area fraction (crystallinity) are most closely correlated with the average discharge rates. An observed linear relationship between crystallinity and log eruption rate is similar to that previously reported for lavas of Merapi volcano (Indonesia) and Vulcanian ash samples from Volcán Tungurahua (Ecuador). This relationship allowed me to use my textural correlations to constrain eruptive intensities for a poorly documented sub-Plinian eruption in 1818 which appears to be similar to the better-observed 1913 eruption.

Keywords: microlites, groundmass textures, plagioclase, intensity, Volcán de Colima

2.1. Introduction

Transitions in eruptive behaviour provide insight into processes within the volcanic conduit, particularly changes in the kinetics of degassing and crystallisation related to changes in magma ascent conditions, and consequent changes in magma rheology and conduit pressures (*Melnik and Sparks, 2002*; *Cashman, 2004*; *Cashman and McConnell, 2005*; *Szramek et al., 2006*; *Martel, 2012*). Quantitative analysis of crystal textures – particularly the groundmass crystallinity (e.g., *Wright et al., 2012*) and the microlite number density (e.g., *Hammer et al., 2000*; *Toramaru, 2006*; *Noguchi et al., 2008*) – can place important constraints on ascent trajectories and rates of magma decompression (e.g., *Cashman, 1992*; *Geschwind and Rutherford, 1995*; *Martel et al., 2000*; *Hammer and Rutherford, 2002*; *Couch et al., 2003*; *Szramek et al., 2006*). Examples include studies that have (1) compared the groundmass crystal textures to the magnitude and style of the eruptions, either via controlled decompression experiments (e.g. *Hammer and Rutherford, 2002*) or through the direct observation of eruptive sequences (e.g. *Hammer et al., 1999, 2000*), and (2) correlated the late-stage crystal fraction of ash particles to estimated magma supply rates (proportional to intensity) as an indirect measure of the rate of magma ascent before or during eruptions (e.g., *Wright et al., 2012*). Other works have linked transitions in eruptive styles to magma supply rate, which controls the time allowed for both crystallisation and degassing (*Cashman and McConnell, 2005*; *Hammer et al 1999, 2000*; *Preece et al., 2013, 2016*). These studies have focused on particular volcanoes, covering either a set of eruptions occurring within a few years (e.g., Mount St. Helens; *Cashman, 1992*; *Cashman and McConnell, 2005*) or transitions in eruptive activity within a single eruptive phase (e.g., Merapi, *Preece et al., 2013*). Here I extend these studies by combining textural analysis with observations of eruptive behaviour that produced samples from a bicentennial period of nearly continuous activity of Volcán de Colima, Mexico. This volcano is an excellent target because it is an open system with frequent eruptive activity; extensive records of historic

eruptive activity have revealed diverse eruptive styles despite an approximately constant bulk magma composition.

The late stage crystallisation kinetics of Volcán de Colima have been studied by *Savov et al. (2008),* who described crystal and vesicle textures of tephra from the 1913 Plinian fall deposits, from one block of the 2004 lava flow and ash samples from a Vulcanian eruption in 2005. They separated the groundmass of the studied products into two groups that they attributed to magma that degassed and crystallised at slow rate within the upper conduit (microlite-rich and glass-poor), and an input of hotter magma from depth (glass-rich and microlite-poor). A quantitative analysis of microlite textures in samples derived from Vulcanian events in 2013 built on this work, and showed that, during Vulcanian eruptions, vesicular (buoyant) magma can ascend through more degassed (denser) magma (*Cassidy et al., 2015*). They further concluded that the specifics of this process might provide a primary control on eruption styles and magnitudes during Vulcanian events at Colima and other volcanoes through direct effects on the chemical differentiation of the magma, viscosity and therefore ascent rates. Importantly, although these studies examined samples from a range of eruptive styles at Volcán de Colima, only the products of Vulcanian eruptions have been analysed in detail (i.e. tephra of eruptions in 2005 and 2013). I extend this work to samples of lava flows, block and ash flows (BAF), and sub-Plinian eruptions to investigate the correlation between the different ascent histories and ascent rates associated with each of these eruptive styles and the textural imprints for their respective erupted products.

I start by quantifying the textural variability of groundmass within a single lava flow, and then among a set of historic lava flows. I compare microlite textures among samples from lava flows with different volumes and emplaced at different rates and place these results in the context of published correlations between lava flow length and effusion rate (e.g., *Walker, 1973*). I then extend my analysis to products from a range of eruption styles at Volcán de

Colima, and to published data from other natural systems with similar bulk compositions. I conclude by constraining magnitude and intensities for a poorly recorded sub-Plinian eruption based on textural calibration. This range of perspectives allows me to distinguish crystallisation textures attained from different parts of the magma ascent and flow emplacement process and provides insight into conditions that promote development of hazardous explosive eruptions and block-and-ash flows.

Table 2.1. *Table of symbols and abbreviations used in Chapter II.*

Chapter II - Table of symbols and abbreviations	
Symbol/Acronym	**Definition**
μm	Micrometres
Ac	Acicular crystal shapes
An	Anorthite
AR	Crystal aspect ratio
$AR_{AV.}$	Average crystal aspect ratio
BAF	Block-and-ash flow
BSE	Back-scatter electron analysis
C	Central
cm	Centimetres
DEM	Digital elevation model
E	East
Eq.	Equant crystal shapes
Fld	Feldspar mineral phases
GM	Groundmass
H_2O Tot. Diff.	Water weight percentage difference of total sample weight before normalisation
ka B. P	Thousands of years before present
km	Kilometres
Kv	Kilovolts
L	Long axis
LF	Lava flow
Log.	Logarithmic value
m	Metres or gradient of a line
m.a.s.l.	Metres above sea level
Maf	Mafic mineral phases (pyroxenes, Fe-Ti oxides, amphiboles and olivine)
mm	Millimetres
N	North
N/A	Measurement does not apply
N_A	Crystal number density
nA	Nanoamperes
PF	Pyroclastic flow
Pn	Sub-Plinian eruptions
R^2	Coefficient of determination
s	Seconds

S	South or Short axis
Sn	Crystal size
$Sn_{AV.}$	Average crystal size
VEI	Volcanic Explosive Index
VER	Average volumetric eruption rates
vol. %	Percentage of a given element per sample volume
W	West
wt.%	Percentage of a given element per sample weight
X	Horizontal axis
Y	Vertical axis
φ	Crystal fraction
ϕ	Grain size: $\phi = \log2(d)$, where d is the grain diameter in mm
$\varphi_{Tot.}$	Crystal fraction of feldspars plus mafic components in groundmass

2.2. Background

2.2.1. Eruptions of Volcán de Colima

The Colima Volcanic Complex is in the western Mexican Volcanic Belt, within the Colima graben and about 100 km from the Middle America Trench (*Luhr and Carmichael, 1981; Luhr et al., 2010*). The youngest, and currently active, centre of the complex is the andesitic stratovolcano Volcán de Colima (~3850 m.a.s.l.), which has historically been the most active volcano in Mexico, and one of the most active in North America (*Luhr and Carmichael, 1980; De la Cruz-Reyna, 1993; Luhr et al., 2010*).

Bulk geochemical analyses from the last ~ 200 years show monotonous compositions, with the exception of major eruptions, which are slightly more mafic (*Luhr and Carmichael, 1980, 1990; Robin et al., 1991*; *Verma and Luhr, 1993*; *Luhr, 2002*; *Reubi and Blundy, 2008*; *Savov et al., 2008*). For that reason, explosive eruptions in 1818 and 1913 have been attributed to mixing between a less evolved andesite (~56 wt. % SiO_2) and a more differentiated andesite (~62 wt. % SiO_2), the latter residing in a shallow reservoir (*Luhr and Carmichael, 1980, 1990*; *Robin et al., 1991*; *Luhr et al., 2010*; *Saucedo et al., 2010*; *Crummy et al., 2014*). Volcán de Colima eruptive products contain phenocrysts and microlites of plagioclase, pyroxene and Fe-Ti oxides. Amphibole is a minor phase (<0.5 vol. %) in post -1913 products and probably residual from the 1913 eruption that contained ~ 4 vol. % amphibole (*Luhr and Carmichael, 1980, 1990*; *Reubi and Blundy, 2008*; *Reubi et al., 2013*). The amphibole content has increased slightly since 2014 (*Capra et al., 2016*). Quartz and olivine are found as rare xenocrysts (*Luhr and Carmichael, 1980; Luhr and Carmichael, 1990*; *Luhr, 2002*; *Mora et al., 2002*; *Reubi and Blundy, 2008*).

To provide context for the textural data, I summarise the eruptive activity at Volcán de Colima since 1818, with emphasis on the eruptions corresponding to my sample set (**Tables 2.2**, **2.3**). The most powerful eruptions are classified as sub-Plinian or Plinian (*Luhr and*

Carmichael, 1990; *Robin et al., 1991*; *Luhr, 2002*; *Luhr et al., 2010*; *Saucedo et al., 2010*). The 1818 eruption has been assigned a VEI of 4 (*Newhall and Self, 1982*) based on reports of darkness during daytime and ash-fall up to 470 km from the volcano, which suggest substantial stratospheric injection of material (*De la Cruz-Reyna, 1993*). Only pyroclastic products (i.e., no lava flows) were generated (*Bretón-Gonzalez et al. 2002*). There are no estimates of the volume of material emitted during the 1818 eruptions because of widespread erosion of both flow and fall deposits (*Macias et al., 2017*).

For 51 years after the 1818 eruption, lava domes formed inside the main crater (*Luhr and Carmichael, 1980*). On the 12th of June 1869, the first lava appeared outside of the volcanic vent (*Bretón-Gonzalez et al. 2002*). The 1869 dome and lava flow are exceptional in that the extrusion occurred through a lateral opening on the northeast side of the volcanic edifice, approximately 100 m below and 1 km from the summit, to form a parasitic dome named Volcancito (**Fig. 2.1**). Part of the extruded lavas flooded the northeast side of a horseshoe-shaped collapse structure which has previously been associated with either a massive blast (~3.6 ka B.P, *Cortes et al., 2010*) or an older (> 23 ka B.P), larger event produced by regional tectonism and edifice instability (*Roverato, 2011*). Another portion of the 1869 lava overflowed the east caldera wall into steeper ground and formed a more elongated lava flow branch to the south-east of its source (*Bretón-Gonzalez et al. 2002*; **Fig. 2.1**). Accounts of the activity of Volcancito suggest that it lasted 65 days (*Arreola, 1915*), however, activity of the parasitic dome itself (e.g. short lava flows, fumaroles and explosions) apparently continued until at least 1878 (*Bretón-Gonzalez et al., 2002*).

The subsequent major eruption occurred in 1913 and is well constrained by historic records and analyses of associated tephra deposits (*Saucedo et al., 2010, 2011*, and references therein). It commenced on 17 January 1913 with BAFs formed from dome collapse. Energetic Vulcanian explosions followed, accompanied by pyroclastic flows and surges (*Saucedo et al.,*

2010). The eruption peaked within 3 days with a sub-Plinian explosion that generated a volcanic plume to a height of ~23 km above the crater and ended with minor pyroclastic flows (PFs) on 24 January (*Saucedo et al., 2010*). After the eruption, the jagged crater had dimensions of ~400-450 m width and 300-350 m depth (*Bretón-González et al., 2002*; *Saucedo et al., 2010*). The total erupted volume was 0.30 km^3 (DRE), of which 0.23 km^3 was tephra fall-out and the remaining portion corresponded to block-and-ash flows (*Saucedo et al., 2011*).

The 1913 sub-Plinian eruption was followed by a hiatus in activity outside of the crater for almost five decades, although intermittent slow extrusion of a lava dome ultimately filled the crater. The most substantial dome growth occurred between 1922 and 1931 and between 1957 and 1959, during which time there were a few explosions (*Bretón-Gonzalez et al., 2002*). By 8 March 1960 the first lavas spilled over the crater wall, but it was not until mid-1961 (*Mooser and Maldonado-Koerdell, 1963*) that a blocky lava flow developed outside of the crater, accompanied by BAFs (*Martin del Pozzo et al., 1987*). The activity continued until late the following year (*Mooser and Maldonado-Koerdell, 1963*) and the lava flow extended ~ 1.2 km from the vent (**Fig. 2.1**). In contrast to later lava flows, it did not develop levees.

Lava flow activity resumed in 1975 on December 11 and 12th (*Thorpe et al., 1977*), initially as small lobes to the north that generated BAFs from lava front collapse. Subsequent, more substantial, flows travelled down the northeast and southeast flanks of the edifice (**Fig. 2.1**). One major lava flow went to the north-east towards Volcancito, then split to form the lava flow lobes labelled 1975 North and 1975 East in **Figure 2.1.** Importantly, however, specifics of activity of the 1975 North branch are missing due to the lack of monitoring at the time and difficult access to the northern side of the volcano. The other major flow (labelled as 1975 East in **Fig. 2.1**) travelled to the southeast. By the 3rd of January 1976, this flow was moving much more slowly than flow branch advancing to the south (1975 South; **Fig.2.1**). The emplacement time is uncertain, although it appears that the 1975 East branch was emplaced

within 60 days (*Bretón-Gonzalez et al. 2002*). Effusive activity to the south continued until the 20th of June (*Thorpe et al., 1977*). The total eruptive volume for the 1975 activity is 0.12 km^3 (*Luhr and Carmichael, 1990*).

The 1998-1999 effusive eruption sequence was well monitored. Lava was first seen on 21 November 1998, accompanied by BAFs. By 1 December, the main flow had divided into 3 branches, following the eastern, central and western parts of El Cordobán ravine respectively (*Saucedo et al., 2002*; **Fig. 2.1**). By the 7 February 1999, the three blocky lava flow branches extended 2.8-3.8km from the crater rim (*Luhr, 2002*). The total lava flow volume is reported as ~0.039 km^3, assuming an average flow thickness of 20m (*Navarro-Ochoa et al., 2002*). A period of slow dome extrusion occurred after the 1998-99 activity, followed by the development of a lava dome on May 2001 that subsequently spilled off the crater into short lava flows in early 2003 (average volume effusion rate < 1 m^3/s; *Varley et al. 2010a*).

In 2004, intense seismic activity accompanied by rock-falls and BAFs was followed on 30 September by lava spilling over the crater rim and descending to the N and WNW of the volcanic edifice (*Macias et al., 2006*; *Zobin et al., 2008*; **Fig. 2.1**). On 6 October, partial collapse of the growing dome produced a remarkable BAF that extended to 6.14 km (*Macias et al., 2006*), which at the time was the longest PF runout since the 1913 events. The maximum lava discharge rate from the vent was also recorded on this day at 7.5 m^3/s; it then decreased until the effusion finished by the end of November or early December (*Zobin et al., 2008*). Until 31 October, the average advance rate of the north flow was 76 m/day (*Macias et al., 2006*). The dimensions reported for the north lava flow are ~2400 m long (*Zobin et al., 2008*) and ~263 m wide (*García-Nava, 2016*); for the WNW flow, ~600 m long and 200 m wide (*Zobin et al., 2008*). The total erupted volume is ~ 8 x $10^6 m^3$.

Explosive activity increased in intensity during February 2005. From February until September, about 30 Vulcanian explosions occurred, reaching a peak in intensity during May

and June of that year. Following the 2005 activity there was a very slow extrusion of lava between 2007-2011 (~0.02 m^3/s, *Hutchison et al., 2013*) which formed a lava dome on the summit of the volcano. The rest of 2011 and 2012 encompassed a period of relative quiescence.

In January 2013, activity resumed after 18 months of quiescence with extremely slow effusion of a summit dome (~0.006 m^3/s, *Thiele et al., 2017*). This was accompanied by four Vulcanian eruptions of moderate intensity, which generated ash columns and ejected ballistics from the 2007-2011 summit dome. They were accompanied by PFs containing material from the old dome as well as new material, and finally were followed by a lava flow. After effusion of the 2013 lava, the eruptive activity decreased, with only minor explosions occurring from November 2013.

Although my study extends only through 2013, I note that eruptive activity at Volcán de Colima has continued and is still on-going. Activity increased from May to July 2014, with two new lava flows developing to the W and SW of the volcano (at ~ 1 -2 m^3/s) and three subsequent flows to the N, SW and S in early July 2015. Particularly intense explosions on 21 November 2014 and 3 January 2015 were accompanied by pyroclastic flows. Finally, major block and ash flows were reported from partial dome collapse on the 10^{th} and 11^{th} of July 2015, generating a total volume of ~0.014 km^3 for the two events (*Reyes-Davila et al., 2016*). Moderately intense explosions have continued to the present (late 2017).

Table 2.2. *Eruption rates and description of events at Volcán de Colima.*

Year of event	* Bulk SiO_2 wt.%	Sampled products	LF Final length (m)	LF area (million m^2)	LF average thickness (m)	LF Estimated volume (million m^3)	Eruption rate (m^3/s)	* Eruption Published times (hours)	* LF Published volume (million m^3)	* Published Eruption rates (m^3/s)	Sources
1818	58.9	Plinian fall-out	N/A	N/A	N/A	N/A	Unknown	Unknown	N/A	Unknown	De la Cruz-Reyna (1993); Luhr and Carmichael (1980), and Saucedo et al. (2010)
1869	60.6	Lava flow	2580 (±5)	2.33 (± 0.014)	18 (±1)	42 (±2.3)	7.47 (± 0.42)	1560	170	30.3	Gonzalez et al. (2002) and Luhr and Carmichael (1990)
1913	57.9	Plinian fall-out	N/A	N/A	N/A	N/A	N/A	4.6	230	13889	Saucedo et al. (2010) and Saucedo et al. (2011)
1961	60.4	Lava flow	1170 (±5)	0.153 (± 0.006)	17 (±1)	2.59 (±0.15)	0.5 (± 0.03)	1440	6	1.16	Luhr and Carmichael (1980); Mooser and Maldonado-Koerdell (1963), and Navarro-Ochoa et al. (2002)
1975	60.8	Lava flow	4500 (±5) (South)	1.23 (±0.023)	14 (±1)	17.5 (±1.23)	3.38 (± 0.24)	1440	61.6	11.9	González et al. (2002); Luhr and Carmichael (1990) and Thorpe et al. (1977)
			890 (±5) (North)	0.147 (±0.005)	10 (±1)	1.44 (±0.15)	0.278 (± 0.03)	1896 688.5	N/A	N/A	
1998	60.1	Lava flow	2226 (±5)	1.56 (± 0.012)	13 (±1)	20.5 (±1.56)	3 (± 0.23)	8424	39	5.71	Luhr and Carmichael (1990) and Navarro-Ochoa at al. (2002)
2004	60	Lava flow	2000 (±5)	0.41 (±0.01)	12 (±1)	4.87 (±0.41)	1.97 (± 0.17)	1896	7.17	2.89	Reubi et al. (2008); Ryan (2010), Savov et al. (2008) and Zobin et al. (2006, 2008)
2013	60	Blocks and ash from BAF	N/A	N/A	N/A	N/A	N/A	N/A	N/A	2.00E-02	Hutchison et al., (2013); Lavallée et al. (2012); Mueller et al. (2013) and Reubi et al. (2013)
2013	Unknown	Lava flow	900 (±5)	0.224 (± 0.005)	5 (±1)	1.12 (±0.22)	N/A	N/A	N/A	2.70E-01	Zobin et al. (2015)

Table Note. "LF" stands for "Lava flow". Data collected or estimated from publications based on the total erupted volume over the total duration of a respective eruption are indicated with an asterix (*) before each column title and the data sources appear at the end of each row. Numbers in parentheses indicate the absolute error based on the DEM resolution used for the measurements and is indicated in the scale indicated in parentheses on the heading of each column. "N/A " indicates that either the respective measurement does not applied or that there is no information available. The values of areas and volumes are expressed as millions of m^2 or m^3 respectively for compactness on the number of characters in the table.

Table 2.3. *Samples collected from eruptive events of Volcán de Colima and the types of analyses applied to them in this study (indicated by 'X').*

Analyses for individual samples					
Event	**Sample**	**Preparation**	**Mineral modes**	**BSE -GM textural analysis**	**Glass chemistry**
1818	S1818	Epoxy mount		X	X
1869	S26	Thin-section		X	X
1913	S1913	Epoxy mount		X	X
1961	S22	Thin-section	X	X	X
1975 N	S28	Thin-section		X	X
1975 S	S30	Thin-section		X	X
1998	S2a	Thin-section		X	
	S3a	Thin-section		X	X
	S1a	Thin-section		X	X
2004	S1	Thin-section	X	X	X
	S5	Thin-section		X	X
	S16	Thin-section	X	X	X
	S04-01	Thin-section		X	
	S04-03	Thin-section		X	
	S04-05	Thin-section		X	
2013	S24	Thin-section		X	
	S23	Thin-section	X	X	X
	S8a	Thin-section		X	
	AshBAF13_3-12	Epoxy mount		X	X

2.3. Methodology

2.3.1 Lava flows and average eruption rates

Previous work has shown that groundmass crystal textures of hydrous mafic-intermediate magmas are strongly affected by the rate of magma ascent within the volcanic conduit. As ascent rate cannot be measured directly, I use the average volumetric eruption rates (VER) as proxy in order to correlate the effects of syn-eruptive crystallisation with a measurement of eruptive intensity.

Where there are reliable estimates of emplacement conditions (e.g., 2004 LF), I calculate average VER using available data for total erupted volume and eruption duration (**Table 2.2**). Where neither volume nor duration are well constrained (e.g., 1818) I cannot estimate VER. Where eruptions included different types of activity (e.g., 2013 BAF and lava flow) I use published VER estimates (*Zobin et al., 2015*). Where there are no published volume data (e.g., the 1975 North lava flow) I calculated volumes using a digital elevation model. I used interpolation of lines in ArcGIS on a DEM for Volcán de Colima to generate terrain profiles. Terrain profiles were constructed, and total flow length measured from the vent (i.e. summit crater) to the front of the emplaced lavas. The paths of the flows (in the cases of bending) were followed for each LF branch individually where diversion occurred. The average slope angles were estimated on both the middle of the lava flows and on the ground adjacent to these, the latter was used as a proxy for the original slope beneath the flows given a fairly uniform terrain (not rugged relief) at the analysed areas. Since the direct incline over which the 2013 LF emplaced is available in a DEM, this was measured as a way to test and compare with the rest ((see **Appendix 2.1** for the consideration of errors and **Appendix 2.3.** for visualisation of the measured profiles).

In addition, volumes of other studied lava flow units were calculated, for comparison with published estimates (**Table 2.2**). Lava flow volumes were calculated from flow areas

outlined with polygons combined with the average thickness determined from a series of transects perpendicular to the lava flow direction (*Deardorff and Cashman, 2012*; **Supplementary material 2.1**). At the same time, I test the correlation between lava flow final length and VER to assess the extent to which this simple parameter, identified by *Walker (1973)* as useful for measuring effusion rates of mafic lava flows, also provides a reliable proxy for effusive eruptions of intermediate composition of Volcán de Colima.

There are no published detailed measurements or observations of the effusive activity at Volcán de Colima prior to the 1990s due to the lack of an established volcano monitoring network. For this reason, combined with unusual conditions of emplacement, the VER and flow lengths of the 1869 and 1961 flows may have the largest uncertainties, however, uncertainties are not reported in the respective publications. For the 1869 LF, I estimate, based on the DEM measurements, that only about a third of the total erupted lava spilled over a deep ravine off the caldera wall; the sample I studied is from this spill-over section (**Fig.2.1**) and the final flow length reported in **Table 2.2** indicates its greatest length. Similarly, the final 1961 LF deposit had to infill a ~100 - 50 m deep crater after the 1913 sub-Plinian eruption before spilling out and flowing down-slope; this created uncertainty (not estimated) in both emplacement time and in the volume of caldera-filling lava (*Luhr and Carmichael, 1980, 1990*; *Bretón-Gonzalez et al., 2002*).

Observations of the 1975 effusive eruption are available for the eastern (not sampled) and southern (sampled) branches but more limited for the northern branch, which I sampled. For this reason, I estimate average effusion rates separately for the southern branch using the known end date of 20 June 1975 and assuming that the northern branch was emplaced over the same 60-day period as the eastern branch. More complete observations on volumes, times and effusion rates are available for the 1998, 2004 and 2013 lava flows. Detailed surveillance of the 2004 LF allowed effusion rate estimates at several points in time (data provided by Nick

Varley). Finally, I assume that the 2013 BAF material is from the 2007-2011 dome extrusion (after reports by *Mueller et al., 2013* and *Zobin et al., 2015*) whose discharge rate was calculated from photographic estimates of the dome volumes before and after individual rock-fall events (*Hutchison et al., 2012*; *Mueller et al., 2013*).

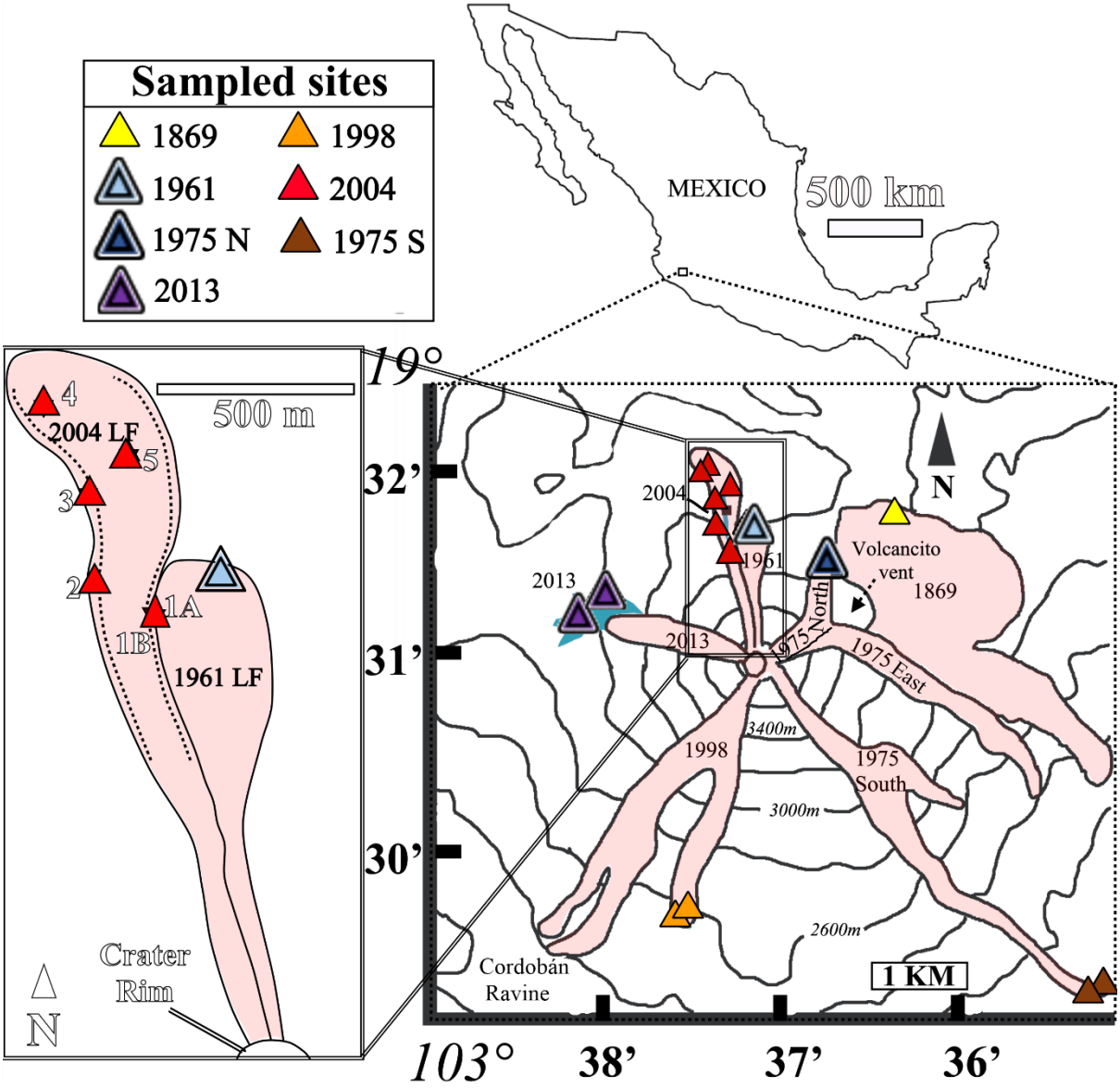

Figure 2.1. *Sampling sites at Volcán de Colima (triangles). Sampled lava flows are shaded in red and the BAF deposits in blue, each labelled with their respective year of eruption. Sub-Plinian air-fall samples were collected at Nevado de Colima to the north of this map. LF samples were collected near the flow fronts except for the 2004 LF where several samples were obtained from different parts of the flow (bottom-left inset; levee-channel margin marked with dashed line).*

2.3.2 Samples, mineral modes and componentry

Samples were collected from the deposits of eight historic eruptions of Volcán de Colima (**Fig.2.1, Table 2.3**). These include pumice from air-fall deposits of the 1818 and 1913 sub-Plinian eruptions (Pn), blocks from the surfaces of the 1869, 1961, 1975 (north [N] and south [S] branches), 1998 and 2004 lava flows (LF), and block-sized clasts and ashy matrix from block-and-ash flows (BAF) associated with the 2013 events. LF samples were collected only near the flow front except for the 2004 LF, which was also sampled along the levees and channel. In general, the blocks sampled from both LF and BAF are dense (vesicularity < 20 vol. %), although a few LF samples are scoriaceous (20 < vesicularity < 40 vol. %); the most vesicular sample (39 vol. %; sample 1B, **Fig. 2.1**) was collected from 2004 LF clinker. Pn samples, in contrast, have vesicularities > 50 vol. %. Polished thin-sections (of LF and dense BAF samples) or epoxy resin mounts (of Pn and ash samples) were produced for optical and back-scattered electron (BSE) microscopy, as well as phase analysis (**Table 2.3**).

Mineral modes were obtained from sets of images covering whole thin-sections from two samples of the 2004 LF, one from the 1961 LF and from clasts from the 2013 BAF (**Table 2.3**). I used a Nikon Eclipse LV1000D-U optical microscope in plain and cross-polarized transmitted light, as well as in reflected light for Fe-Ti oxides. Individual images were taken at a magnification of 50x and stitched together using Nikon Elements BR 4 software. Point-counting on BAF and LF samples was performed using JMicrovision platform covering 400-500 points, which were classified as: feldspars, clinopyroxene, orthopyroxene, Fe-Ti oxides, amphibole, groundmass (glass and microlites) and voids.

The other samples were prepared as thick polished mounts and their component modes were counted from BSE image maps (**Table 2.3**). These samples include tephra from the 1913 Pn and ash from the 2013 BAFs at particle sizes of 2 and 3 ϕ. Composite ash images were constructed using ~ 300 individual BSE images taken at 15 kV at a working distance of 13

mm; magnifications of 300x and 500 x were used for the 2 and 3 ϕ particle sizes, respectively. A map of the 1913 tephra sample was made from 90 individual images taken at 20 kV, 60x magnification, with a working distance of 11 mm. 400 – 1000 points were counted depending on the number required for stability of volume fraction, as determined from a stochastic criterion of an evolution plot on JMicrovision.

Glass compositions of all samples and feldspar compositions of three samples were determined by electron microprobe (**Appendix 2.5**).

2.3.3 Textural analysis

High-resolution (1280 x 960 pixels; 400 second scans) BSE images of the groundmass were collected using a Hitachi S-3500N scanning electron microscope at a beam current of 15kV and a constant magnification of 500x. Brightness and contrast levels were manually adjusted to optimize the grey scale range associated with the range of feldspar compositions.

Ideally the different proportions of groundmass components would be quantified by separating them automatically using grey scale contrast. However, the similarity in the mean atomic number of the glass and the feldspar microlites made it difficult to separate them by simple greyscale thresholding, thus each feldspar crystal was manually delineated using Photoshop®. A binary mask of the feldspar crystals was produced for each area of groundmass analysed, with separate binary images generated for the mafic components (pyroxenes and Fe-Ti oxides) and voids (vesicles and fractures). The area and the long (L) and short (S) axis lengths of a best-fit ellipse were quantified for each crystal from the binary images using Image J (**Fig.2.2**). Microlites were defined as crystals with the square root of area (Sn) < 50 μm. I chose Sn rather than crystal length to classify microlite size because of the large range in crystal shapes (measured as aspect ratio, AR= S/L).

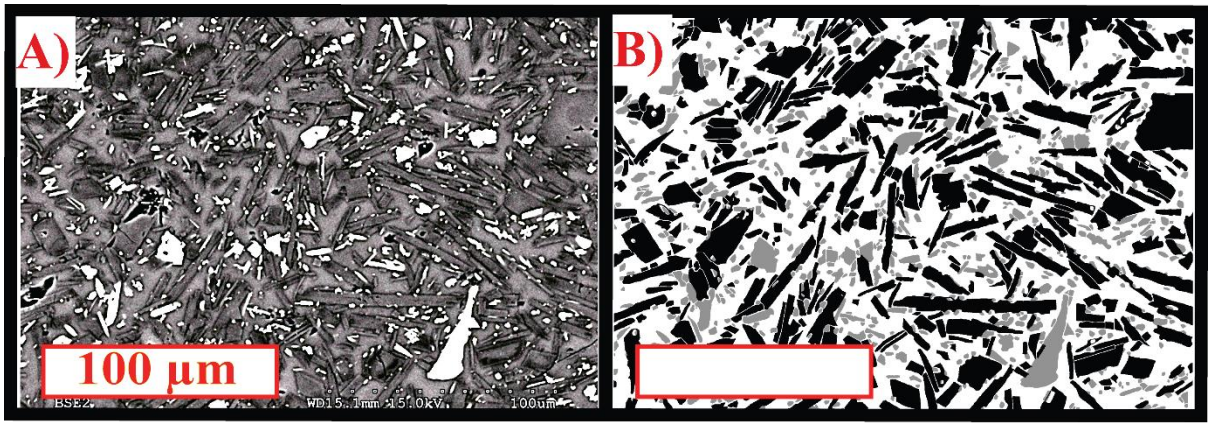

Figure 2.2. *Image preparation process for textural analysis:* ***A)*** *BSE image of the groundmass of sample 1A from the 2004 LF.* ***B)*** *The same image (at the same scale) with individual crystals thresholded and grouped in two different classes: Feldspars (black) and mafic microlites (pyroxenes and Fe-Ti oxides, grey). Both classes are then converted into binary files for the subsequent textural analysis.*

Reference areas of groundmass were determined by subtracting the total phenocryst abundance (feldspars and mafics), vesicles and fractures from each analysed area. The microlite area fraction (φ) was calculated as the total area of microlites (including incomplete crystals that intersect the image boundary) divided by the reference groundmass area. Microlite number density (N_A), in contrast, was calculated by adding half of the number of edge-intersecting particles to the number of crystals not touching edges and dividing by the reference area. Average AR ($AR_{AV.}$) and Sn ($Sn_{AV.}$) values were determined for each sample by averaging data from all complete crystals (i.e. incomplete crystals cut by image edges were not use in AR and Sn estimations). 2-D vales of AR (S/L) were used for consistency with other textural datasets (e.g. *Preece et al., 2013* and *Cassidy et al., 2015*) and for further reasons that are explained in more detail in **Appendix 2.4**.

When more than one BSE image was analysed per sample, I used the cumulative data from all images from one sample to measure both the median and average φ, N_A, Sn and AR and the associated standard deviation (refer to **Table 2.1.** or to the previous paragraph for symbology). Where different samples of the same event were analysed, the results were averaged to obtain the mean textural (and standard deviation) values corresponding to

individual events. As the median and average microlite Sn and AR for each sample are similar (**Supplementary material 2.5**); I use the average value for consistency with other textural studies.

To complement my dataset, I have included feldspar microlite textural data from the 2013 eruption products analysed by *Cassidy et al. (2015)*. The textural parameters that they report are based on analysis of all crystals with Sn<100 μm. I have recalculated φ, N_A, $Sn_{AV.}$ and $AR_{AV.}$ from the dataset provided by these authors to include only crystals with Sn < 50 μm, for direct comparison with my data (refer to **Table 2.1.** for symbology). I also calculated φ for Sn <35 μm to compare with data from *Wright et al. (2012)* on Tungurahua Volcano.

2.4. Results

Various measurements were used to quantify different groundmass textural parameters in samples from LFs, BAFs and tephras from explosive eruptions. First, modal distributions of some textural components in the samples were performed using optical point counting (phenocrysts) combined with BSE (groundmass) image analysis (**Fig.2.3A**) and normalized to a vesicle-free basis (**Fig.2.3B**). The relative proportions of phenocryst + microlites and glass are similar for all the non-sub-Plinian samples; the 1913 sub-Plinian sample, in contrast, has a much lower crystallinity (**Fig.2.3B**). This difference in crystallinity is reflected in the glass composition, which is rhyolitic in all but the sub-Plinian (1818 and 1913) samples, where it is andesitic (**Appendix 2.5.**).

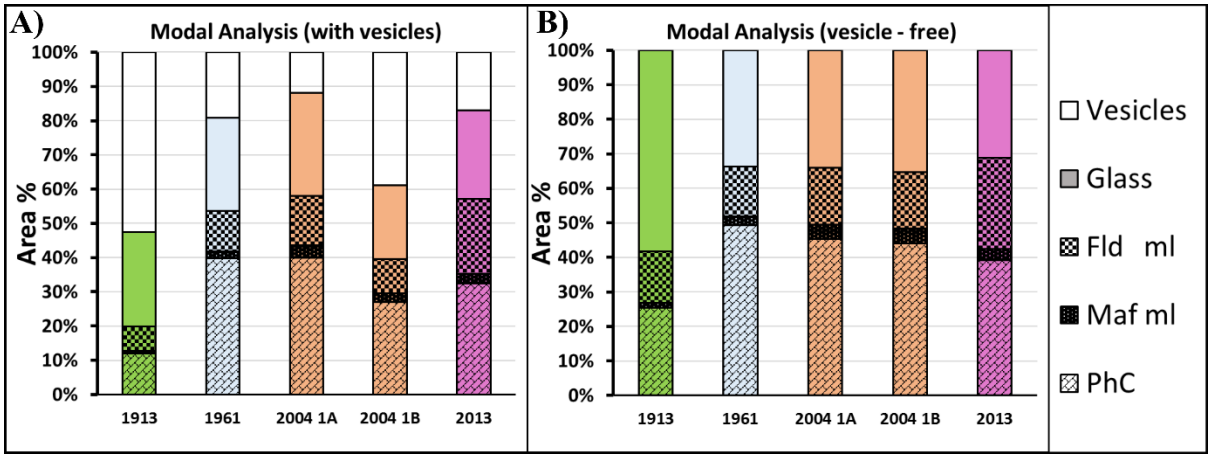

Figure 2.3. *Modal distributions of crystal populations of block samples from BAF deposits (2013), short LF (1961), long LF (2004) and Pn air-fall (1913) products on* ***A)*** *Normalized proportions of all components (including vesicles) and* ***B)*** *Modal proportions on a vesicle-free basis. The eruption year for each sample is indicated at the bottom of each column. Mode values for each component are indicated in* ***Supplementary Table 2.3****. The 2004 samples with dense (1A) and vesiculated (1B) bulk textures are from two different parts of the same block from the 2004 LF.*

Plagioclase microlites vary in size, shape and abundance. One end-member plagioclase texture in the groundmass consists of abundant, small, elongated crystals (**Fig.2.4 A, B**); this end member is found exclusively in the products of the 1818 and 1913 explosive eruptions. At the other end of the spectrum are samples characterized by abundant, relatively large groundmass crystals with equant shapes, and often with rims of contrasting (lower An) composition (**Fig.2.4 D, F**); this end member is found exclusively in samples of the shortest LFs and BAFs. Between these end members are groundmass textures with intermediate crystal sizes and shapes, typically with very thin to no low-An rims (**Fig.2.4 C, E**). These intermediate groundmass characteristics are found in LF samples, as well as some BAF samples.

These textural characteristics are quantified in **Table 2.4** and illustrated in **Figure 2.5** as plots of feldspar microlite number density (N_A) versus crystallinity (φ; **Fig.2.5A**); average crystal size ($Sn_{AV.}$) against average aspect ratio ($AR_{AV.}$; **Fig.2.5B**) and $AR_{AV.}$ versus φ (**Fig.2.5C**). Most obvious are the textural differences between microlites in the sub-Plinian samples (**Fig.2.4 A, B**) and those in the non-sub-Plinian samples (**Fig.2.4 C-F**): the former

have noticeably lower φ and $Sn_{AV.}$). Within the LF suite, samples collected from longer flows tend to have smaller (lower $Sn_{AV.}$) and more acicular (lower $AR_{AV.}$) groundmass crystals, while groundmass crystals in samples collected from shorter LFs and BAF blocks are generally more equant (higher $AR_{AV.}$) and larger (higher $Sn_{AV.}$).

Samples from explosive eruptions are further quantified by component analysis. Components identified in the 1913 Pn sample are mafic and feldspar phenocrysts, groundmass (glass and microlites) and voids. The mafic microlites show little variability in abundance or shape, although sub-Plinian and vesicular Vulcanian ash samples have the lowest mafic microlite crystal fraction and smallest size. There are no clear textural patterns associated with mafic minerals in the rest of the analysed products. The textural parameters determined for the mafic microlite components are reported in **Supplementary Material 2.4**.

Table 2.4. *Feldspar textural parameters in groundmass from erupted products of Volcán de Colima: Crystallinity Crystal fraction (φ), microlite number density (N_A), average microlite size ($Sn_{AV.}$) and average microlite aspect ratio ($AR_{AV.}$). These data are for microlites defined as Sn< 50 µm. When data are averaged from multiple analysed samples, the associated standard deviation is indicated in parenthesis. The results from Cassidy et al. (2015) data are shown with "(Cass)" next to the name of the event. The final two columns of numbers indicate the total (feldspar + mafic) crystallinity for both Sn < 50 µm and Sn < 35 µm.*

Event	φ	N_A (mm^{-2})	$Sn_{AV.}$ (µm)	$AR_{AV.}$ (S/L)	$φ_{Tot}$	$φ_{Tot}$ (Sn < 35 µm)	Analyses
1818	0.13	9682	3.7	0.42	0.14	0.14	1 sample, 1 image
1869	0.29	6810	6.8	0.34	0.35	0.35	1 sample, 1 image
1913	0.15	18271	2.9	0.22	0.16	0.16	1 sample, 1 image
1961	0.29 (0.01)	6500 (332)	6.3 (0.5)	0.51 (0.0)	0.35 (0.02)	0.34 (0.02)	1 sample, 2 images
1975 N	0.39	6617	7.4	0.63	0.43	0.43	1 sample, 1 image
1975 S	0.31	8527	5.6	0.32	0.40	0.35	1 sample, 1 image
1998	0.35 (0.03)	10797 (2260)	5.9 (0.9)	0.38 (0.02)	0.43 (0.03)	0.43 (0.03)	3 samples, 3 images
2004	0.32 (0.04)	8899 (3211)	5.7 (0.7)	0.37 (0.02)	0.39 (0.04)	0.39 (0.04)	5 samples, 10 images
2013 BAF Blocks	0.44 (0.05)	6873 (763)	7.6 (0.8)	0.61 (0.01)	0.49 (0.06)	0.49 (0.06)	3 samples, 3 images
2013 BAF Eq. Ash	0.31 (0.00)	5008 (1159)	7.7 (1)	0.56 (0.04)	0.38 (0.03)	0.36 (0.07)	2 samples, 2 images
2013 BAF Ac. Ash	0.30 (0.01)	4395 (221)	8.5 (0.4)	0.35 (0.04)	0.40 (0.01)	0.40 (0.02)	2 samples, 2 images
2013 LF (Cass)	0.4	6455	7.8	0.52	0.44	0.44	1 sample, 1 image
2013 Ballistic (Cass)	0.33	4160	8.8	0.66	0.45	0.45	1 sample, 1 image
2013 Vulcanian Dense Ash (Cass)	0.38 (0.07)	8316 (2907)	7.0 (1.2)	0.55 (0.06)	0.40 (0.07)	0.40 (0.06)	10 samples, 13 images
2013 Vulcanian Vesicular Ash (Cass)	0.14 (0.02)	7359 (4068)	4.9 (1.2)	0.36 (0.03)	0.25 (0.13)	0.16 (0.11)	5 samples, 5 images

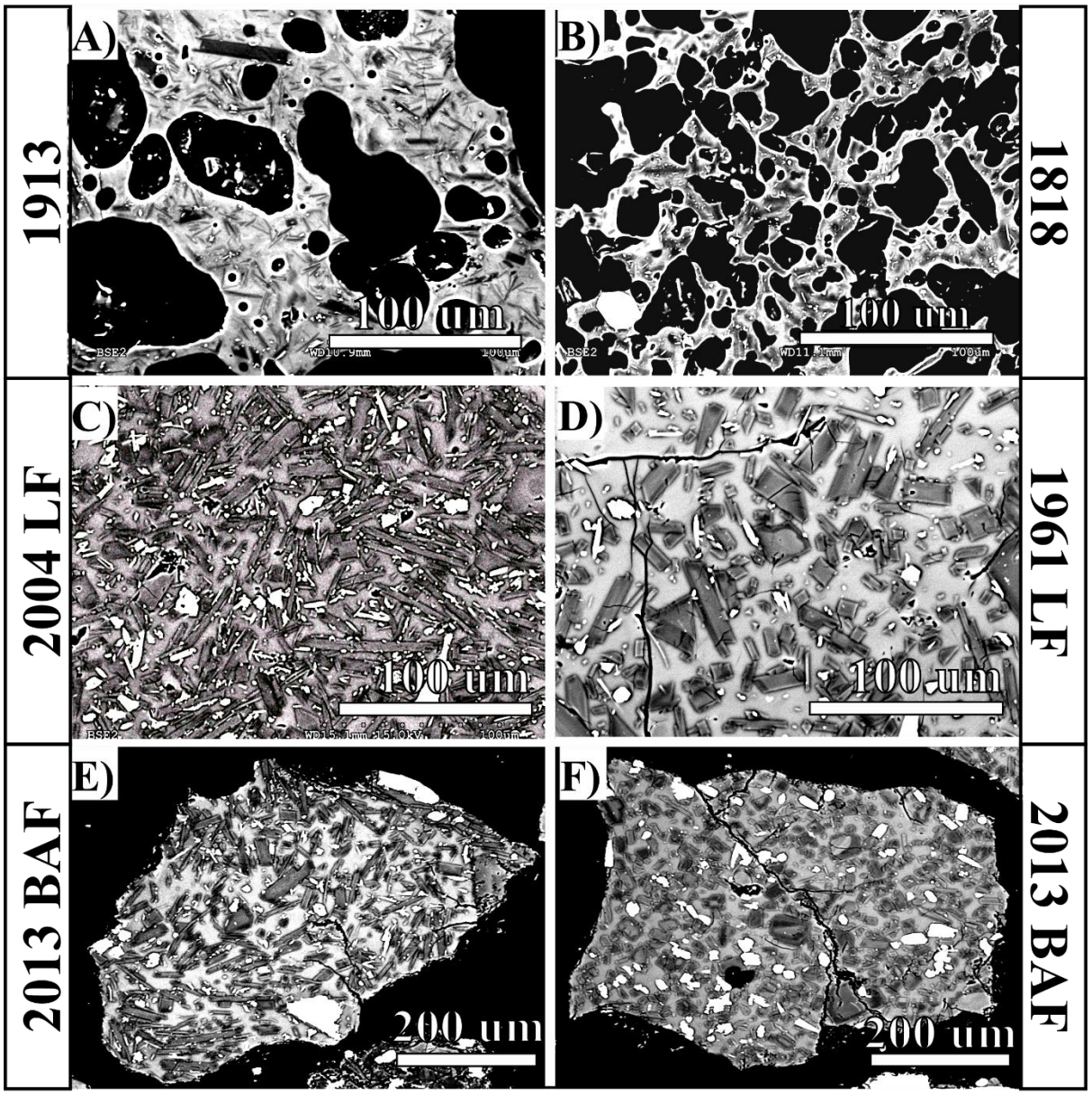

Figure 2.4. *BSE images from a set of erupted lavas and tephra from Volcán de Colima.* ***A, B)*** *Groundmass of Pn tephra from the 1913 and 1818 events, respectively.* ***C)*** *Typical groundmass textures observed in the 2004 LF (Sample 1A).* ***D)*** *Crystalline textures of the groundmass found in the 1961 LF.* ***E, F)*** *2013 BAF ash particles dominated by acicular and equant microlites, respectively.*

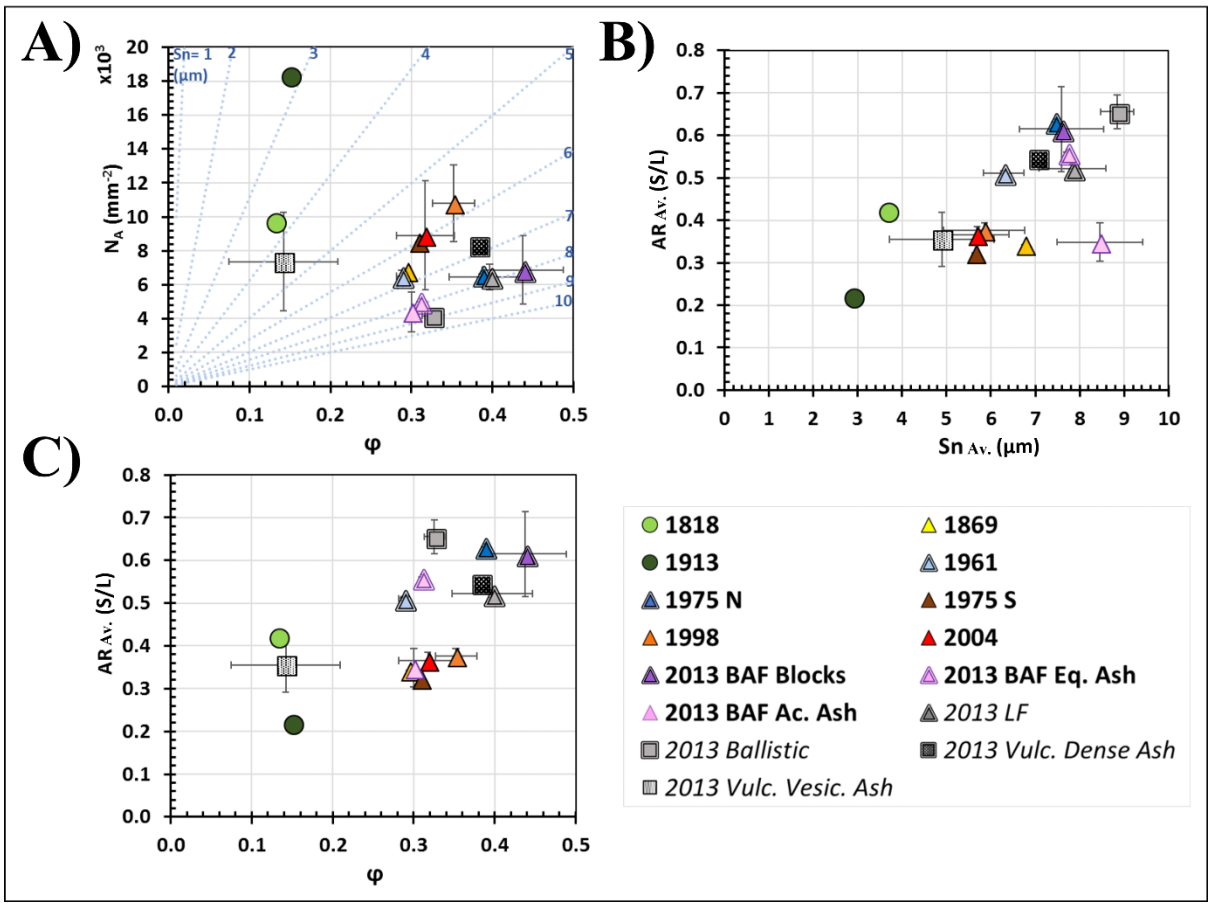

Figure 2.5. *Averaged textural parameters for plagioclase microlites in groundmass of Pn products, LFs and blocks and ash collected from a BAF deposits.* ***A)*** *Number density (N_A) versus crystallinity (φ), with contour lines indicating theoretical boundaries of crystal sizes constrained from the relation Sn= √ (φ/ N_A).* ***B)*** *Average aspect ratio (short/long axis, $AR_{AV.}$) versus average microlite size ($Sn_{AV.}$ = √area of all crystals).* ***C)*** *$AR_{AV.}$ versus φ. The icons with the names in italics represent the samples reported by Cassidy et al. (2015). If multiple samples were analysed, the standard deviation is indicated with error bars; an asterisk in the legend indicates that only one sample was analysed, and therefore error is not indicated. In events where more than one image were analysed and the error bars are not visible, the error is smaller than symbol size. A consequence of the averaging of samples is some discrepancy between the Sn fields in* ***A*** *(defined from the relation $Sn_{AV.}$ = √ (φ/ N_A)) and average Sn of all the same samples in* ***B****. The equivalent plots showing data of individual BSE-images are in* ***Supplementary Material 2.4****.*

2.5. Discussion

Previous work has suggested that some aspects of groundmass crystallinity (e.g. crystal fraction and number density) can be linked to average discharge rates, and, by extension, to transitions in eruption intensities and styles (e.g. *Toramaru et al., 2008* and *Wright et al., 2012*). I use the link between groundmass textures and physical parameters of eruptions as a framework for my analysis. I commence assessing the robustness of my sampling strategy by analysing textural changes within a single, coherent, well observed lava flow (the 2004 LF). I then extend the analysis to a set of events with similar eruptive origin (7 effusive events), and subsequently incorporate the 1913 sub-Plinian event, as well as data from other volcanoes of similar magma composition, to expand the comparison to a range of eruption styles. I finally use the textural calibrations best correlated with average eruptive intensity at Volcán de Colima to assess magma supply rate of the 1818 eruptive sequence from textural analysis of a pumice clast.

In general, sub-Plinian eruptions generate groundmass textures that are distinct from eruptions of lower magnitude and intensities (LFs and BAFs). More specifically, sub-Plinian samples have low crystallinities and a high abundance of small and elongated plagioclase microlites. In contrast, eruptions of lower intensity produce less numerous, larger and more equant microlites. Also, the products from the lowest-intensity eruptions have feldspar crystals with compositionally distinctive albitic rims (e.g., **Fig. 2.4**).

2.5.1 Where within a lava flow are groundmass textures representative of average emplacement conditions?

To understand the relations between lava flow eruption rates and their groundmass textures, it is important to evaluate which portion(s) of the flow preserve textures that represent typical conditions of magma ascent and post-eruptive emplacement of lavas. From a practical perspective, it is particularly important to consider lava flow frontal lobes or toes (hereby

simply referred as "fronts"), as the front, or deposits derived from collapse of the fronts, are sometimes the only feasible sites for sampling lava flows.

I used samples from the 2004 northern lava flow of Volcán de Colima to determine whether the groundmass textures of samples collected at the flow front adequately reflect the average conditions of the eruption, and to evaluate effects of later overprints such as syn- and post-emplacement crystallisation. This flow was chosen because there are extensive observations of its emplacement, it formed a single and simple flow lobe, and samples could be collected along the emplacement path (**Fig.2.1, 2.6A**). Available data shows a peak in effusion rate at 5.16 (± 2.9) m^3/s after ~ 7 days; an early peak in effusion rate is a common feature of effusive eruptions at Volcán de Colima (e.g., *Navarro-Ochoa et al., 2002*), and for lava flows in general (*Walker, 1973*; *Lipman and Banks, 1987*; *Naranjo et al., 1992*). The peak in effusion rate is reflected in the advance rate of the flow front (**Fig.2.6C**), which accelerated during the first few days and then gradually decelerated toward the end of the eruption.

To infer the order of sample emplacement, I used the framework established *by Borgia and Linneman (1983, 1990)* at Arenal volcano, Costa Rica. In this model, the lava in the levees is older than in the adjacent channel. Within the levees, the age is progressively younger further from the vent, whereas within the channel the lava closest to the vent is the youngest (**Fig.2.6B**). I believe this model is adequate for the emplacement of lava flows at Volcán de Colima since it is based on silicic lava flows that do not develop sub-terminal flows or lava tubes. Based on this model, the time of emplacement for each levee sample from the 2004 flow is approximated as the time the lava flow front reached the sampled location (**Fig. 2.6B**, **C**). I quantified textures of six samples from five locations along the flow to evaluate the intra-flow variability, and to assess which samples were most representative of the average eruptive conditions.

Figure 2.6D shows the results of my intra-flow comparison, as well as a comparison of textural parameters for the 2004 flow with those for the complete LF set from Volcán de

Colima analysed in this study (blue horizontal bars, **Fig. 2.6D**). As anticipated, most textural parameters vary with changes in effusion rate during the 2004 eruption (**Fig. 2.6D**), although very close to the range observed among my entire suite of flow front samples. The variations in the measured range of φ, $Sn_{AV.}$ and N_A are equal to approximately the entire range of the respective parameters in the seven lava flows studied. Importantly, however, all textural parameters for the sample collected close to the 2004 flow front (Sample 4; **Fig.2.6B**) are close to the average of all the samples analysed along the flow, especially φ and $AR_{AV.}$ (**Fig.2.5**; **2.6D** and **Table 2.4**). The average aspect ratio, in contrast, is almost invariant among the 2004 samples, with a value that marks an end member of the entire sample suite (**Fig.2.6D**).

The 2004 LF data provide important insights into the evolution of groundmass textures during magma ascent and flow emplacement. First, I suggest that the robustness of the flow front data reflects the timing of eruption: magma at the front was erupted in the middle of the effusive period, after magma in the levees and before magma left in the channel. The strong dependence of lava flow advance on the rheology of magma near the front, and not the rheology of the magma erupting at the vent (e.g., analogue experiments of *Castruccio et al., 2014*), further supports this interpretation. Second, the stability of the $AR_{AV.}$ throughout the flow suggests that AR may record conditions of magma ascent, and that it may be less susceptible than other parameters to syn- and post-emplacement modifications. Taken together, I conclude that flow front samples can be used to estimate both conditions at the vent and conditions of flow emplacement.

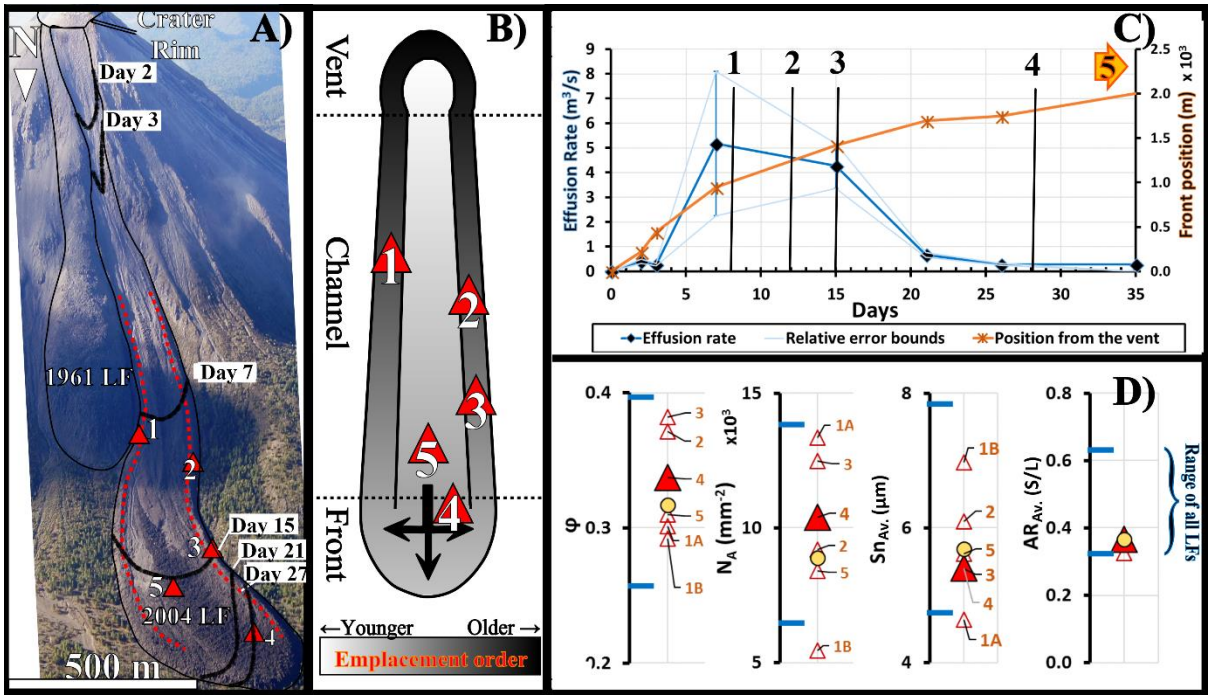

Figure 2.6. *Evolution of the groundmass feldspar textural parameters and eruption rate for the 2004 LF.* ***A)*** *Photograph of the 2004 lava flow with annotations highlighting the channel-levee boudary (red, dashed lines) and the positions of the 2004 LF front with time (thick, black lines). Red triangles indicate sample locations; two samples with different vesicularites were collected at location 1.* ***B)*** *Relative emplacement time of magma in a generic lava flow according to Borgia and Linneman (1990), where darker grey-scale indicates earlier emplacement. The relative positions of the Colima 2004 samples are depicted by triangles.* ***C)*** *Variations in the effusion rate and the flow front distance from the vent through time during the 2004 effusive activity (data provided by Nick Varley). Relative errors for the values of effusion rates are indicated with error bars and delimited with the light-blue lines in the graph (relative error bounds). The elapsed times when the flow front was located at the positions where samples 1 to 4 were collected are indicated by black vertical lines. Sample 5 is in the centre of the channel and so was the last sample of my suite emplaced, as indicated with an orange arrow pointing beyond the time axis.* ***D)*** *Groundmass feldspar textures. Each triangle represents the average groundmass parameters for a single sample. The filled triangle represents the sample collected closest to the LF front (sample 4 in B); the open triangles represent the other samples. Sample numbers are shown in orange (including the two samples collected at location 1, Samples 1A and 1B), except for samples at the $AR_{AV.}$ plot. The yellow dots show the average value of each attribute for all 2004 LF samples. Blue-horizontal lines indicate the range of textural parameters of samples from 7 different LF analysed in this study (**Table 2.4**).*

2.5.2 Testing proxies for lava flow eruption rates

Lava flow length is commonly used as a proxy for volumetric eruption rate (VER), particularly for basaltic lavas (e.g. *Walker, 1973*; *Wadge, 1978*; *Pinkerton and Wilson, 1994*). However, in order to use lava flow length as a VER proxy, the emplacement of the flow has to be limited by its progressive cooling rather than by the erupted volume of lava. Under these conditions, higher VERs cause lava to travel farther before the flow cools sufficiently for the front of the gravity current to resist continued advance; with continued magma effusion, new flow lobes form (that is, the flow field widens rather than lengthens; e.g., Guest et al. 1987). The classic Walker plot of flow length vs. VER, however, has large uncertainties that reflect details of both emplacement and compositional variations.

Here, I test the suitability of flow length as a proxy for eruption rate within the Volcán de Colima system by comparing the final lava flow lengths of well documented historic andesitic lava flows to their average effusion rates. All data are for individual eruptive episodes except for the 1975 lava flow, where I plot, separately, the northern and southern flow lobes. Volcán de Colima andesitic lavas are more viscous than basaltic lava flows, not only because they have a different bulk composition but also because of their high crystallinity. From this perspective, I would expect these lava flows to be shorter and thicker than corresponding basaltic lava flows. At the same time, however, the flows have been emplaced on uniformly steep slopes (**Supplementary Material 2.6**) and along inclined depressions that confine the flows, both of which should increase flow length (e.g., *Dietterich and Cashman, 2014*; *Dietterich et al., 2015*). Indeed, **Figure 2.7A** shows an overall power-law relationship between the final length of Volcán de Colima flows and effusion rate within a 95% confidence value (**Table 2.5**). Also, as anticipated, the Volcán de Colima flows are shorter than basaltic lava flows with equivalent effusion rates (**Fig. 2.8**). However, the power law exponents m (slope in log-log plot) are similar between both lava flow datasets, with Volcán de Colima m being

slightly higher (m= 0.41) than the m = 0.38 value found by *Walker (1973)* and *Malin (1980)* for 40 (mostly basaltic and basaltic andesite) lava flows but resulting in a slope of m= 0.44 when both sets are combined (**Fig. 2.8** and **Table 2.5**).

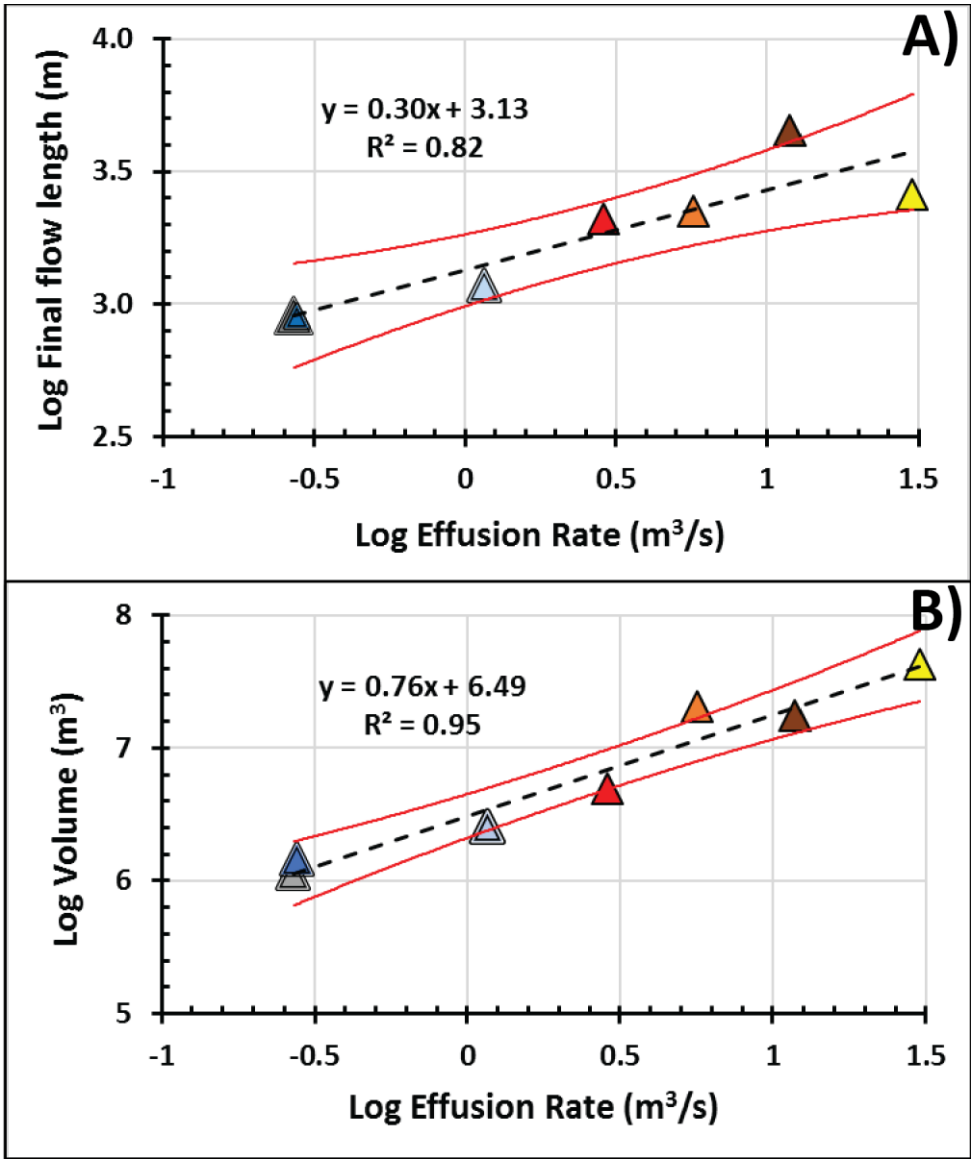

Figure 2.7. *Average effusion rates vs. physical parameters of lava flows at Volcán de Colima.* ***A)*** *Measured final flow lengths against reported average effusion rates (References on* ***Table 2.2****).* ***B)*** *Correlation of my own estimated lava flow volumes to the average effusion rates (****Table 2.2****). The black, dashed-lines are fits to the LF data-set (****Table 2.5****).Confidence intervals of the regression lines (to a 95% probability) are indicated with red lines. Refer to* ***Fig. 2.5.*** *for the legend of the symbols.*

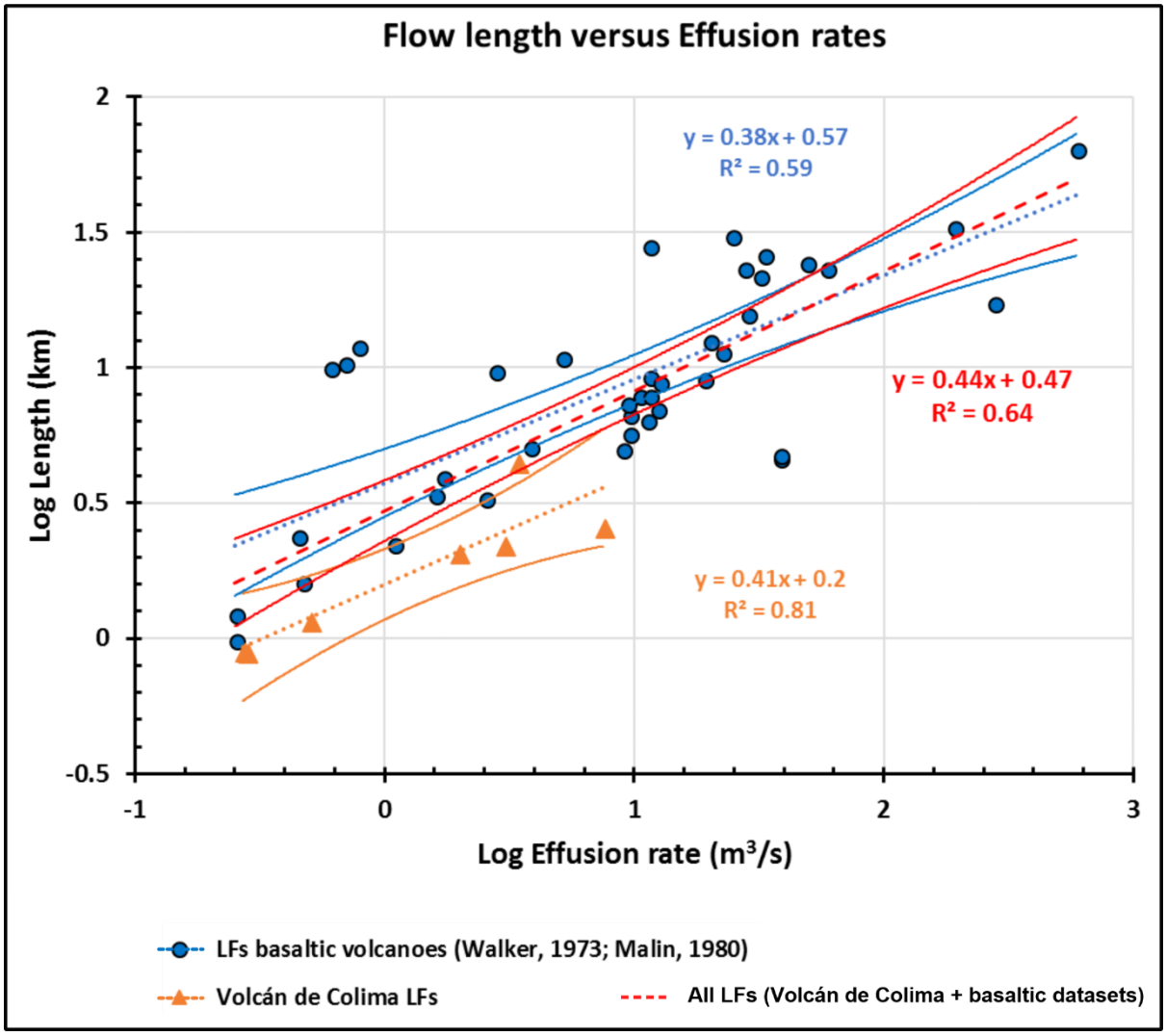

Figure 2.8. *Correlation between final lengths of lava flows and their respective effusion rates for flows at Volcán de Colima and a suite of mostly basaltic lava flows from Mauna Loa, Hawaii and Etna, Italy after Walker (1973) and Malin (1980). Fits to the two data sets individually and to the two datasets combined and the respective confidence intervals (to a 95% probability) are shown with dotted and solid lines respectively. The corresponding equations are displayed coloured-coded accordingly to the fits and are listed in* ***Table 2.5****.*

The fit of the Volcán de Colima data ($R^2 = 0.81$) shows LF length as a sensitive proxy for VER within a 95% confidence value (**Table 2.5**). However, the larger scatter for the mafic LFs dataset ($R^2 = 0.59$) and for both datasets combined ($R^2 = 0.64$) shows that careful consideration should be taken when making assumptions about mafic lavas or for different compositions of lava flows (**Table 2.5**). The scatter in the Volcán de Colima data can be explained, with longer-than-expected flows (e.g., Volcán de Colima 1975S) attributed to

topographic confinement and associated flow lengthening, and shorter-than-expected flows the result of spreading (e.g., Volcán de Colima 1869) during emplacement on unusually flat terrain (e.g., *Dietterich et al., 2015*; **Fig.2.1**) or inherited uncertainties in estimated VER because of protracted crater filling (e.g. 1961).

I also assessed the relation between flow volume and effusion rate. Unlike flow length, lava volume is not affected by topographic confinement, spreading or branching; the power-law relationship between volume and effusion rate shows correspondingly less scatter (R^2= 0.95, **Table 2.5** and **Fig.2.7B**). The good correlation between volume and VER could reflect the open nature of the magmatic system. In open systems, we would expect the observed correlation between volume erupted and VER if the volume of magma erupted is linked directly to the excess pressure driving the eruption.

VERs and corresponding rates of magma ascent and decompression should also be reflected in the kinetics of crystallisation. With my set of Volcán de Colima lava flow front samples, I can test which textural parameters are the best proxies for the average VER conditions (**Fig.2.7B**). **Figure 2.9** shows variations in average crystal size ($Sn_{AV.}$), abundance (N_A) and average shape ($AR_{AV.}$) with changes in the average VER; for the correlation between φ and VER refer to **Figure 2.10**. Of the four parameters analysed as a function of VER (φ included), N_A is the only textural parameter that shows the lowest dependence on VER within the LF suite (**Table 2.5**). This is surprising, as N_A has proved diagnostic of the decompression and ascent kinetics of magma batches in other effusive eruptions (e.g. *Hammer et al., 2000; Noguchi et al., 2008*; *Toramaru et al., 2008*). N_A shows a higher correlation to VER by including the high VER Pn eruption, and it is below a 95% confidence value when the Pn VER is omitted in the correlation (**Table 2.5**). In contrast, φ, $Sn_{AV.}$ and $AR_{AV.}$ show strong negative correlations with VER (**Fig. 2.9A**, **C**, **Fig. 2.10** and **Table 2.5**), with low VER corresponding to the largest φ, $Sn_{AV.}$ and $AR_{AV.}$ As suggested by my intra-flow textural analysis, crystal shape

($AR_{AV.}$) shows the most robust correlation (R^2=0.84) with VER within a 95% confidence value from the set of the four attributes analysed (**Fig. 2.9C**, **Table 2.5**).

The (VER) of effusive eruptions will depend on the pressure gradient driving magma ascent, the rheology of the magma (e.g. φ, porosity and H_2O) and the size of the conduit. My data on Colima lava flows shows that VER, flow length, flow volume and groundmass textures are all related. This correlation may reflect feedback processes between ascent rate and timescales of changes in rheology (and thus resistance to ascent) related to outgassing and crystallisation, as explored by *Melnik and Sparks (1999)*.

Importantly, my data do not show signs of the extensive post-eruptive crystallisation that has been recorded in eruptions of near-liquidus mafic lavas (e.g. Hawaii; *Cashman et al., 1999*). The lack of late-stage crystallisation is similar to observations from eruptions of felsic magmas, where groundmass (microlite) crystallisation is limited as diffusion in highly degassed melts slows, or even halts, as magma volatile contents decrease (*Preece et al., 2013*). An example is provided by dacite lava flows of Uturuncu Volcano, Bolivia, which show much less variation in groundmass φ within individual lava flows than between flows of different lengths (*Muir et al., 2014*). As seen at Colima, this suggests a correlation between effusion rate, crystallinity and flow length. It also supports the interpretation that most groundmass crystallisation occurs during magma ascent, by which point the melt is sufficiently degassed and crystallisation is too slow to have a strong effect on the final φ.

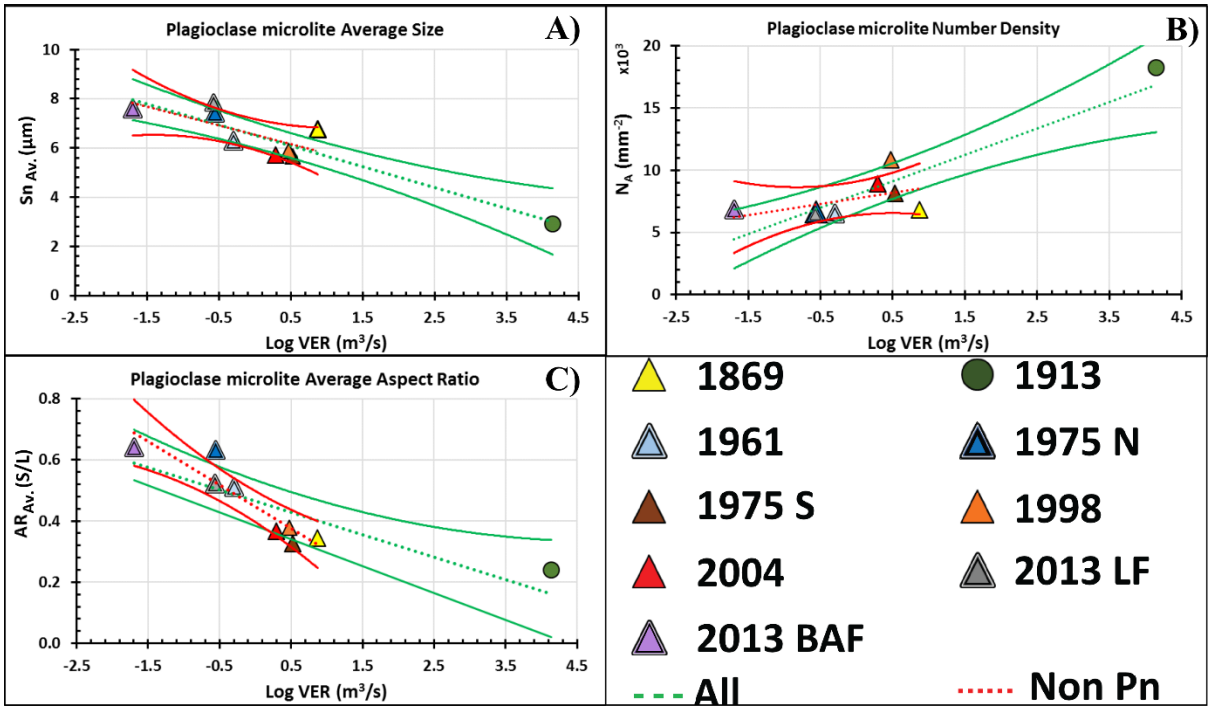

Figure 2.9. *Correlations of groundmass textural parameters with average VER (own estimates of VER in* ***Table 2.2.*** *except for the 2013 events).* ***A)*** *Size,* ***B)*** *Number density, and* ***C)*** *Aspect Ratio of microlite feldspars versus volume eruption rate. The red, dotted-lines display the trend fitting the LF data (triangles) only; the green dashed-lines are the fits to all events shown in the figures, including the 1913 Pn event. Confidence boundaries (to a 95% probability) are displayed colour-coded accordingly to the fits of the datasets. The values to each of the fits are indicated in* ***Table 2.5****.*

Table 2.5. *Straight-line fits for physical and textural parameters. Compilation of straight-line fits for physical features and textural parameters to Eruption Rates. P-values estimated from regression analysis for each of the correlations and the significance of the respective fits (to a 95% probability) are shown in the table. The asterixis (*) next to some of the listed products in the "Data" column indicate that values were obtained from other studies (indicated in the text or **Fig.2.8**. and **2.10**). The final column shows the figures in this work to which each fit is associated. Refer to **Table 2.1** for the meaning of symbols in this table.*

Equations for straight line fits to data in Figures								
Vertical axis parameter	Horizontal axis parameter	Slope	Intercept	R^2	P-Value	Statistically significant when α=0.05	Data	Figure
Final LF length (m)	Log Effusion Rate (m^3/s)	0.3	3.13	0.82	5.3×10^{-3}	YES	All except Pn	2.7-A
Log Volume (m^3)	Log Effusion Rate (m^3/s)	0.76	6.49	0.95	1.88×10^{-4}	YES	All except Pn	2.7-B
Log LF length (km)	Log Effusion Rate (m^3/s)	0.38	0.57	0.59	8.8×10^{-9}	YES	Basaltic LFs *	2.8
Log LF length (km)	Log Effusion Rate (m^3/s)	0.41	0.2	0.81	6.9×10^{-3}	YES	Lava flows	2.8
Log LF length (km)	Log Effusion Rate (m^3/s)	0.44	0.47	0.64	1.43×10^{-11}	YES	All lava flows	2.8
N_A (mm^{-2})	Log Eruption Rate (m^3/s)	881	7736	0.22	2.36×10^{-1}	NO	All except Pn	2.9-A
N_A (mm^{-2})	Log Eruption Rate (m^3/s)	2123	8091	0.81	1.01×10^{-3}	YES	All events	2.9-A
$Sn_{AV.}$ (μm)	Log Eruption Rate (m^3/s)	-0.76	6.54	0.5	4.9×10^{-2}	YES	All except Pn	2.9-B
$Sn_{AV.}$ (μm)	Log Eruption Rate (m^3/s)	-0.85	6.53	0.84	4.9×10^{-4}	YES	All events	2.9-B
$AR_{AV.}$ (S/L)	Log Eruption Rate (m^3/s)	-0.14	0.45	0.84	1.28×10^{-3}	YES	All except Pn	2.9-C
$AR_{AV.}$ (S/L)	Log Eruption Rate (m^3/s)	-0.07	0.47	0.7	4.98×10^{-3}	YES	All events	2.9-C
φ_{Tot}	Log Eruption Rate (m^3/s)	-0.06	0.4	0.88	1.79×10^{-4}	YES	All events	2.10-A
φ_{Tot}	Log Eruption Rate (m^3/s)	-0.04	0.41	0.52	4.32×10^{-2}	YES	All Except Pn	2.10-A
Fld φ	Log Eruption Rate (m^3/s)	-0.05	0.34	0.88	2.57×10^{-4}	YES	All events	2.10-A
Fld φ	Log Eruption Rate (m^3/s)	-0.05	0.34	0.66	1.45×10^{-2}	YES	All Except Pn	2.10-A
Fld φ	Log Eruption Rate (m^3/s)	-0.05	0.35	0.46	9.6×10^{-2}	NO	Merapi domes *	2.10-A
Maf φ	Log Eruption Rate (m^3/s)	-0.01	0.06	0.22	2.05×10^{-1}	NO	All events	2.10-A
$\varphi_{Tot\ (Sn < 35\mu m)}$	Log Eruption Rate (m^3/s)	-0.06	0.4	0.86	3.33×10^{-4}	YES	All events	2.10-B
$\varphi_{Tot\ (Sn < 35\mu m)}$	Log Eruption Rate (m^3/s)	-0.06	0.36	0.83	3.34×10^{-5}	YES	Tungurahua ash *	2.10-B

2.5.3. Groundmass textures of different eruptive styles at Volcán de Colima and other volcanoes

Open-system volcanoes often transition between explosive and effusive activity. These changes in eruptive styles are likely related to variations in conditions of magma ascent within the conduit. To analyse the effects of eruptive styles on groundmass textures, I expand my analysis from lava flow products to tephra derived from the 1913 sub-Plinian eruption, and short-lived, low-volume lava bodies (i.e. portions of domes destroyed during the 2013 Vulcanian activity and rock-falls from 2013 lava flow). The latter are of interest since samples from these shorter lava bodies were not collected in situ due to inaccessibility.

I start with the products of the 2013 activity, where I can compare the componentry of co-deposited blocks and ash. Both types of samples have similar textures (**Fig. 2.5**) that are dominated by high crystallinity particles suggestive of the highly-degassed magma expected to form either within a lava dome or a plug in the shallow conduit. Reports of relatively low gas flux during the 2013 eruptions support this assumption (*Cassidy et al., 2013*). I have shown that flow fronts are representative sampling sites, which allows me to use the textures of BAF blocks from flow front collapse to estimate the average effusion rate during dome/plug emplacement. Additionally, since the terminology "effusion rate" does not apply for all kinds of eruptions included in this section, I use the more general term "volumetric eruption rate" (VER) or simply "average eruption rate", which can be calculated for any eruption style as the total volume of material extruded divided by the duration of the eruptive event.

First, I examine $AR_{AV.}$, which had the strongest correlation with effusion rate and final length for lava flow front samples (**Fig.2.6D**). **Figure 2.9C** shows that the $AR_{AV.}$ trend based on effusive eruptions does not extrapolate linearly to the very high eruption rates associated with Pn eruptions. Although the anomalously low $AR_{AV.}$ of the 1913 tephras could be a stereological problem, it is more likely that the correlation between plagioclase shape and

decompression rate is not linear. In fact, a linear extrapolation of the $AR_{AV.}$ trend for effusive eruptions suggests that an eruption rate of 10^3 should produce microlite-free (infinitely low $AR_{AV.}$) magma (**Fig.2.9C**).

The estimated VER of the 1913 sub-Plinian eruption exceeds this value but erupted samples still have groundmass crystals. One explanation is the compositional difference between the Pn and LF/BAF magmas (including volatile content). Another is that crystal habit changes, for example to hopper or dendritic growth, and therefore that aspect ratio may not adequately measure changes in shapes at high supersaturations (e.g., 2D- 3D problem, *Hammer et al., 2000*) (see **Appendix 2.4** for more details in 2D versus 3D crystal shape data).

The best straight-line fits between groundmass textures and average eruption rate (including the 1913 eruption) are provided by φ and $Sn_{AV.}$ (**Fig. 2.10**; **Fig. 2.9A** and **Table 2.5**), consistent with studies of other mafic-to-intermediate eruptions (*Hammer et al., 2000*; *Preece et al., 2013, 2016*). Advantages of assessing eruption rate from φ are: 1) it is not affected by stereology if crystals are randomly oriented and, 2) it is commonly reported, so that I can directly compare Volcán de Colima data with compilations for other intermediate composition volcanoes such as Merapi (*Hammer et al., 2000*; *Preece et al., 2013, 2016*) and Tungurahua (*Wright et al., 2012*). The comparison is most straightforward for lava dome extrusions at Merapi (1986, 1993, 1994, 2006 and 2010) for which both crystallinity and effusion rate data are available (*Hammer et al., 2000*; *Preece et al., 2013*; *2016*), and the bulk composition is only slightly less silicic than at Colima (~ 56 wt. % SiO_2; *Gertisser et al., 2012* and *Preece et al., 2014*). Groundmass crystallinity data are also available for Tungurahua eruptions with a range of discharge rates (*Wright et al., 2012*), although here eruptions are entirely explosive and magma supply rates are estimated by averaging ash accumulations over two-month periods (different from the total erupted volumes over the total duration of the eruptions as in my study).

The relationship between groundmass plagioclase crystal fractions and eruption rates is similar between the Merapi and Colima datasets, although there is more scatter in the Merapi data and regression analysis suggests that it is not statistically significant (**Fig. 2.10A** and **Table 2.5**). Data for Tungurahua also show a statistically significant inverse correlation between crystallinity and VER (**Table 2.5**), but the fit is shifted to slightly lower φ values with equal slopes with Volcán de Colima data (**Fig. 2.10B**). Tungurahua magma is slightly less silicic (~ 58 wt. % SiO_2; *Hall et al., 1999*; *Samaniego et al., 2011*) than effusive magmas from Volcán de Colima (~ 61 wt. % SiO_2); therefore, the difference in bulk composition unlikely account for the higher φ of the Volcán de Colima magma. Instead I suggest that the offset could reflect differences in methods of measuring eruption rate, the type of sampled material (ash versus blocks, lava) and/or the method used to measure crystallinity. We would expect ash to quench more quickly than blocks from lava domes and flows, thus limiting post-eruption crystallisation. Additionally, ash samples used in the Tungurahua study were texturally heterogeneous, so that the reported crystallinity values are averages of each ash sample.

The variability in Tungurahua ash textures raises a final possibility, which is that eruption style matters. As an example, I use groundmass textures in the products of Vulcanian explosions of Volcán de Colima (*Cassidy et al., 2015*). Like Tungurahua, these samples preserve a wide range of crystallinities with textures that overlap not only my BAF samples, but also those of long lava flows and even the sub-Plinian events (**Fig. 2.5** and **Supplementary Material 2.4**). Such textural variations within products of a single eruption probably reflect a fast downward-propagating fragmentation wave that excavates and ejects material from throughout the conduit during Vulcanian eruptions (*Druitt et al., 2002*; *Clarke et al. 2007*; *Wright et al., 2007*). In this framework, the 2013 dense ash and ballistic textures can be interpreted as magma that stalled within the shallow conduit, whereas the vesicular ash might reflect a volatile-rich, deeper portion of the conduit. These observations underline that one

should be cautios when correlating eruption rates and crystalline textures during unsteady eruptions for different volcanoes.

Of the various Volcán de Colima samples analysed, the groundmass of the 1818 pumice is most similar to that of the 1913 eruption which has an estimated average VER of 1.4 $x10^4$ m^3/s (**Table 2.2** and **Section 2.2.1.**). Compared to the 1913 Pn sample, the feldspar microlites in 1818 Pn have larger $Sn_{AV.}$, lower N_A and slightly higher $AR_{AV.}$ (**Fig. 2.4** and **2.5**, **Table 2.4**, **Supplementary Material 2.4**), which all suggest a slightly lower VER for the 1818 eruption than 1913. However, lower groundmass φ (both total and feldspar alone) for the 1818 sample suggest a higher VER. To make quantitative estimates of VER for 1818, I use $Sn_{AV.}$, feldspar φ and φ_{Tot} (all for Sn < 50 μm), which are the three textural parameters that have good linear correlations with log. VER for the combined dataset of Volcán de Colima effusive and 1913 Pn samples that match the linear correlations based on the effusive correlations alone (i.e. without the 1913 data). Based on the linear fits for the complete dataset (**Table 2.5**, **Fig. 2.9** and **2.10**), the $Sn_{AV.}$= 3.7 μm, feldspar φ = 0.13 and φ_{Tot} = 0.14 values for the 1818 Pn sample correspond to VER of 2.1$x10^3$, 1.6$x10^4$ and 3.9$x10^4$ m^3/s respectively, these values are close to the VER estimate for the 1913 event and allow for the 1818 eruption to be classified as a sub-Plinian eruption as previously suggested by *De la Cruz-Reyna (1993)* from eyewitness records. However, one should consider when making assumptions about the real VER of the 1818 Pn that there is more than an order of magnitude between the three previous estimates constrained using three different textural parameter correlations.

Although the sub-Plinian 1818 and 1913 eruption sequences were relatively steady (c.f. 2013 sequence), both comprised multiple phases of different intensities (*Cioni et al., 2015*; **Section 2.2.1**.), which likely generated variations in textures that are not evident for my study of just one clast from each eruption. A more robust assessment of VER for the 1818 eruption

should include textural analysis of more clasts from both 1913 and 1818 Pn to establish the variations in textures, and the textural parameters of the dominant products.

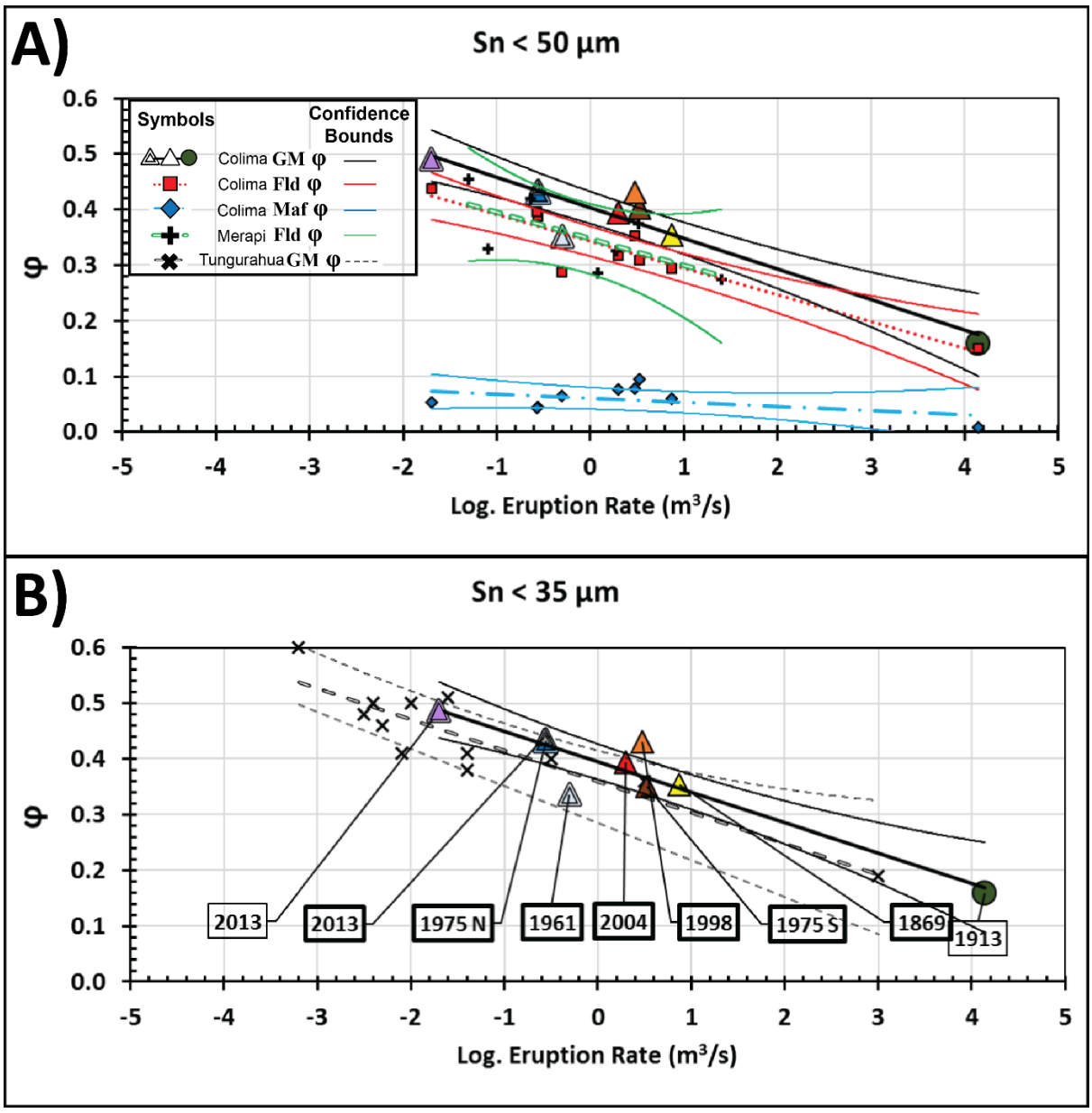

Figure 2.10. *Correlation of average crystal fractions with average VERs (own estimates of VER in* ***Table 2.2.*** *except for the 2013 events).* ***A)*** *Comparison between Volcán de Colima and Merapi crystal fractions and discharge rates (on a log-scale) when Sn < 50 µm. Merapi data from lava domes extruded in 1986, 1993, 1994, 2006 and 2010 (Hammer et al., 2000; Preece et al., 2013, 2016).* ***B)*** *Correlation between total (i.e. feldspar + mafic) groundmass (Sn < 35µm) crystal-fractions and eruption-rates (on a log-scale) for products derived from Colima and Tungurahua volcanoes. Tungurahua data from Vulcanian, Strombolian and Plinian samples collected in 2000-2004 and 2006 (Wright et al., 2012). The boxes indicate the year of eruption for Colima events, with thicker frames for lava flows and slender frames for explosive products. The triangles and circle in this figure correspond to the*

*same eruptions as in **Figures 2.5** and **9** but they mark total microlite content, whereas in other figures these symbols mark results for just the feldspar microlites (which here are indicated by red squares). Refer to **Table 2.5** for values corresponding to the data fits. Confidence boundaries (to a 95% probability) are displayed colour-coded accordingly to the fits of the datasets.*

2.6. Conclusions

Groundmass textural parameters provide excellent petrological tools to reconstruct magma ascent conditions and eruption durations, particularly when combined with other physical proxies such as final lava flow length. To calibrate textural parameters, I analysed samples from (primarily) steady effusive andesite eruptions from Volcán de Colima, which should have simple magma ascent histories. My results not only confirm that when lava flows are simple in form (e.g. do not spread in many branches, *Dietterich et al., 2015*), their final lengths, are good proxies for average effusion rate**,** but also that lava flow fronts are adequate sampling sites for assessing magma ascent conditions from groundmass textures. Importantly, lava flow fronts are commonly the most accessible part of lava flows and are the source of far-travelled block-and-ash flows that also offer good sampling opportunities.

Of the textural parameters that I measured, the aspect ratio ($AR_{AV.}$) of feldspar microlites showed the least variation with location within a lava flow, indicating that it is the least susceptible to modification due to post-eruptive crystallisation or changes in eruption rates during an effusive sequence. Feldspar microlite $AR_{AV.}$ measured in samples collected from the fronts of various Colima andesitic lava flows also showed an exceptional correspondence to the average effusion rate of each event. Good correlations with eruption rate were also found for groundmass (feldspar only and total microlite) crystallinity (φ) and average feldspar size ($Sn_{AV.}$) but not for feldspar number density (N_A). Comparison with data from other andesitic eruptions shows that the slope of the linear φ vs logVER trend is remarkably consistent amongst 8 eruptive events from Volcán de Colima (including from lava domes, lava flows and Plinian deposits), 12 samples from Tungurahua (from Vulcanian, Strombolian and Plinian events; *Wright et al., 2012*), and 7 samples from Merapi (from lava domes; *Preece et al, 2014*). Finally, I applied results from well-constrained eruptions to determine that the average intensity of the 1818 eruptive sequence was similar to the better-observed 1913 sub-Plinian event. Altogether,

my results demonstrate the reliability of well-calibrated textural datasets and how late-stage petrological features can be used as reconstruction tools to constrain dynamics of unknown or poorly observed eruptions. From this, I conclude that groundmass crystallinity and aspect ratio can provide a robust estimate of eruption conditions (magma ascent rate) across a wide range of eruption rates in relatively steady eruptions.

2.7. Appendices and supplementary material

2.7.1. Appendix 2.1: Error estimation for physical parameters of lava flows and volumetric effusion rates

I calculated uncertainties on the effusion rates of the 2004 lava flow (**Fig. 2.6C**) based on physical dimensions of the lava flow measured at various stages during its emplacement. The physical dimensions at the different stages of the 2004 lava flow eruption were obtained through aerial and ground-based imaging with independent uncertainties of 5 metres for width (Δx), 10 meters for length (Δy) and 2 metres for the height (Δz) (*Nick Varley, personal communication*). Based on the uncertainty of each of the lava flow dimensional variables, I estimated the error propagation of the data available for the changes in effusion rate of the 2004 eruption in quadrature (**Equation 1** and **Supplementary Table 2.1**).

$$\text{VER relative error} = \sqrt{((\Delta x/x)^2 + (\Delta y/y)^2 + (\Delta z/z)^2)} \qquad \textbf{(Equation 1)}$$

In **Equation 1**, x = width, y = length and z = height of the lava flow, and assuming that the time variable has a negligible error, the absolute error of the changes in effusion rate (VER) was estimated based only on the relative errors derived from the respective volumes.

Supplementary Table 2.1. *Propagation of error for the 2004 lava flow effusion rates. Effusion rates (VER), the dimensional measurements and the associated independent uncertainties for each of the dimensional variables were directly provided by Nick Varley. The relative and absolute errors for the available VER data were calculated through the addition of the uncertainties of the dimensional variables in quadrature assuming that the time variable uncertainty is negligible.*

Day	VER m^3/s	Dimensional variables (*m*)			Uncertainty of dimensional variables			VER Relative error (**Equation 1**)	VER Absolute error m^3/s
		Width (x)	Length (y)	Height (z)	5/x	10/y	2/z		
2	0.41	86	225	10	0.06	0.04	0.19	0.20	0.08
3	0.27	102	316	11	0.05	0.03	0.19	0.20	0.05
7	5.16	128	955	4	0.04	0.01	0.56	0.57	2.92
15	4.27	169	1388	9	0.03	0.01	0.21	0.21	0.91
21	0.67	208	1554	14	0.02	0.01	0.15	0.15	0.10
26	0.28	208	1609	14	0.02	0.01	0.14	0.14	0.04

Error propagation analysis was also applied to estimate the uncertainties for the area, volume and eruption rate of different lava flows covered in this study (see **Table 2.2**). The independent uncertainties on the dimensional variables for different lava flows of Volcán de Colima from a DEM (**Appendix 2.3**) are 5 metres for width and length, and 1 metre for the height. Similar to the case of the different eruption rates reported for the 2004 lava flow in the previous paragraphs, I assumed a negligible error for the time variable and estimated the absolute errors for eruption rates based on the relative errors obtained from the independent uncertainties of the lava flow physical dimensions.

2.7.2. Appendix 2.2: Regression analysis of the linear correlations for physical and textural parameters with volumetric eruption rates.

In this chapter, I conducted linear regressions between various textural and physical parameters to log VER for different eruptions of Volcán de Colima and other volcanoes (**Fig.2.7**, **2.8**, **2.9** and **2.10**). To test the confidence of the linear relationships I applied a regression analysis. The output components taken to represent the confidence of the regressions were the Coefficient of determination (R^2), the P- value and Confidence intervals. The R^2 values provide an estimate on how strong the correlation of the two variables from a range of 0 to 1, the closer the value is to 1 the better the regression line fits the data. The R^2 values for each of the correlations are displayed in **Table 2.5**. I further tested the hypothesis that the correlations are statistically significant by calculating the P-value. I used a significance level of $\alpha = 0.05$ (95% probability) so that any P-value in my regression must be < 0.05 for the correlation of the different textural variables with log VER to be statistically significant. Finally, I define and display confidence intervals in the different correlation plots to indicate their uncertainty (**Fig.2.7**, **2.8**, **2.9** and **2.10**) at a significance level of $\alpha = 0.05$. The confidence intervals in the plots depict a range of values in which the true best-fit line for each of the correlations (not the data points) lies at a 95% probability confidence. The confidence boundaries are wider when fewer samples are used in the correlations or where at point where the data set clusters less (e.g. at the edges of the linear fits).

2.7.3. Appendix 2.3: Lava flow geometries

I measured individual lava flow lengths in ArcGIS 10 using a digital elevation model (DEM) from *INEGI (2012)* with horizontal and vertical resolutions of 5m and 1m, respectively (**Table 2.2**). In cases where the lava flow branched (e.g. 1998, 1975), each sampled branch was measured individually. Both total lava flow lengths and change in surface elevation were measured using transects from the source-vent to the flow fronts along their centres.

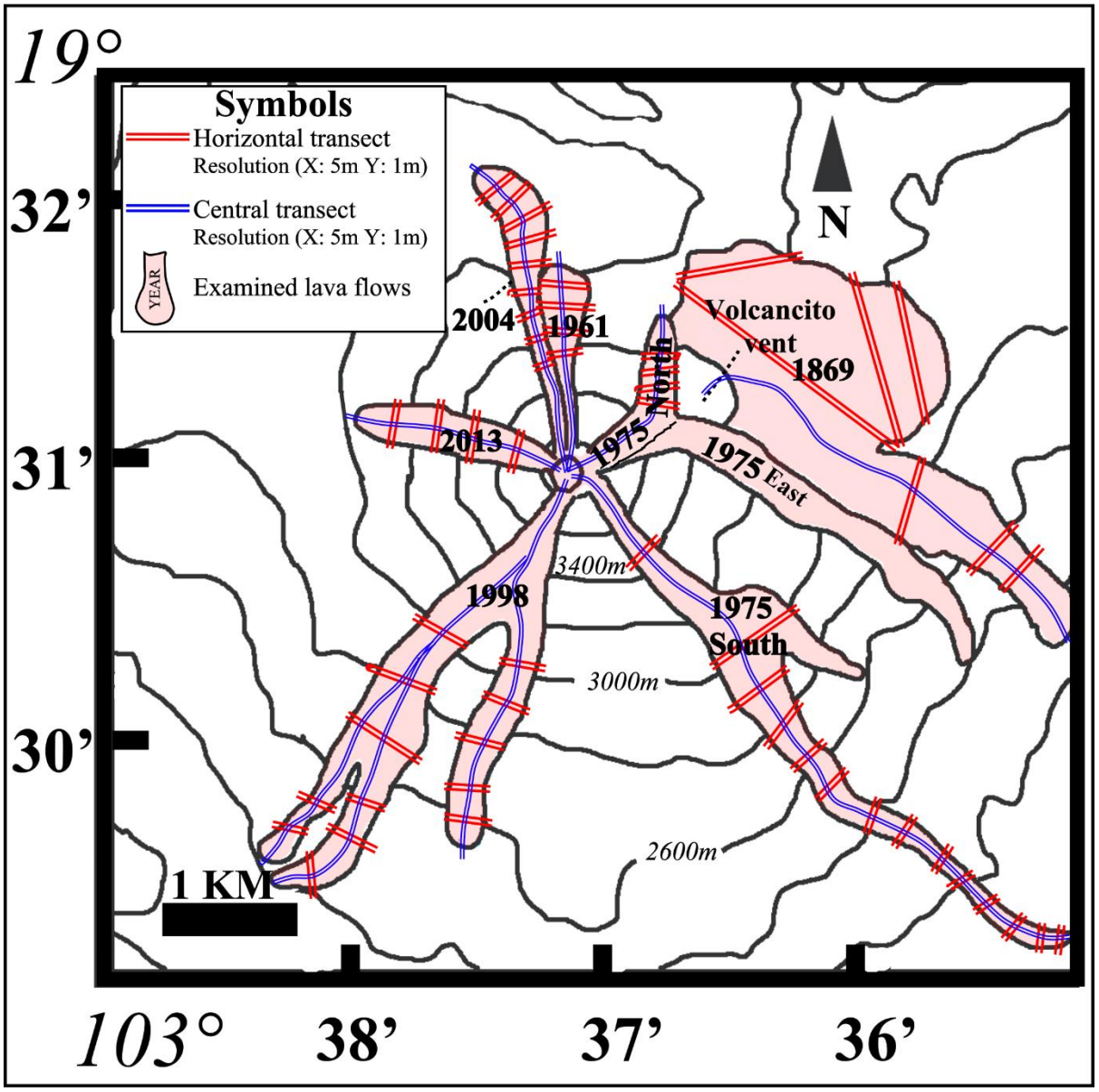

Supplementary Material 2.1. *Map showing lava flows analysed and the transects drawn to assess lava flow lengths, volumes and slopes. The DEM resolution in the horizontal plane is X= 5m per pixel and in the vertical plane it is Y= 1m per pixel as indicated between parentheses in the figure under the transect symbols.*

2.7.4. Appendix 2.4: Justification of the use of a 2D characterisation (AR) in the current textural analysis

Textural batch parameters of crystals (φ, N_A, Sn and AR) are extensively used in textural analysis to attempt to understand the kinetics of crystallisation in magmatic systems (e.g. *Hammer et al., 1999, 2000*; *Hammer and Rutherford, 2002*; *Couch et al., 2003*; *Szramek et al., 2006* and *Preece et al., 2013, 2016*). Most commonly, particularly for shape-related analyses, 2D data directly obtained from digital images of sample cuts (e.g. thin-sections) is converted to 3D, as 2D is said to underestimate the real shapes of the crystals, since (1) crystals of one size could be cut at different axes resulting in a range of apparent sizes, and (2) that larger crystals are more likely to be intersected than smaller ones (*Higgins, 2000*). Software has been developed that estimates 3D shapes of crystals to reduce the stereological effects caused from working with 2D datasets (e.g. CSD-Slice, *Morgan & Jerram, 2006*; and CSDCorrections, *Higgins, 2000*). These 2D- 3D conversion programmes determine 3D best-fit crystal habits by comparison with databases of particle shape distributions, and by applying regression calculations to identify the best R^2 value for the fits of the input database. However, a couple of disadvantages in the approach of these programmes are (1) they assume that all crystals in the analysed sample have a uniform shape when in nature this is unlikely, and (2) they may not adequately resolve crystals of complex shapes (e.g. hoppered & dentritic) since the morphological parameters compared are based on a best-fit ellipse (*Morgan & Jerram, 2006*; *Brugger & Hammer, 2010*).

In fact, I observed these two problems when applying the 2D -3D stereological conversion to my own data through CSD-Slice (**Supplementary Material 2.2.**). The 3D shape output for crystals of my high-intensity eruption sample (green block in **Supplementary Material 2.2.**) suggested after the comparison of my 2D shape measurements (coloured- bars

in the frequency distribution, **Supplementary Material 2.2.**) and the shape dataset of the programme (coloured, dashed-lines in the frequency distribution, **Supplementary Material 2.2.**) was unrealistic according to the shapes observed directly under SEM (**Supplementary Material 2.2.**). *Morgan & Jerram (2006)* suggest inputting a higher minimum number of crystals to analyse when acicular shapes dominate over equant crystal shapes (in this case 250 versus 75 particles respectively). However, for the stereological conversion of the 1913 Pn dataset (the case with most acicular crystals) I analysed 1014 crystals, whilst it was 788 particles in the case of the 2005 BAF dataset (where equant crystals dominated the most) (**Supplementary Material 2.2.**), so the number of particles analysed should not represent a limitation for my analysis. Since I compare crystal batch attributes of samples derived from a wide range of eruptive intensities, including another dataset similar to the 1913 Pn (1818 Pn), for the purpose of the current study I decided to perform the crystal textural analysis on a 2D basis. I believe using 2D data is a valid approach since commonly the 2D long-axis (based on a best-fit ellipse) has been used as a proxy to define crystal size (e.g. *Cashman and Marsh, 1988*; *Marsh, 1988; Higgins, 2006*).

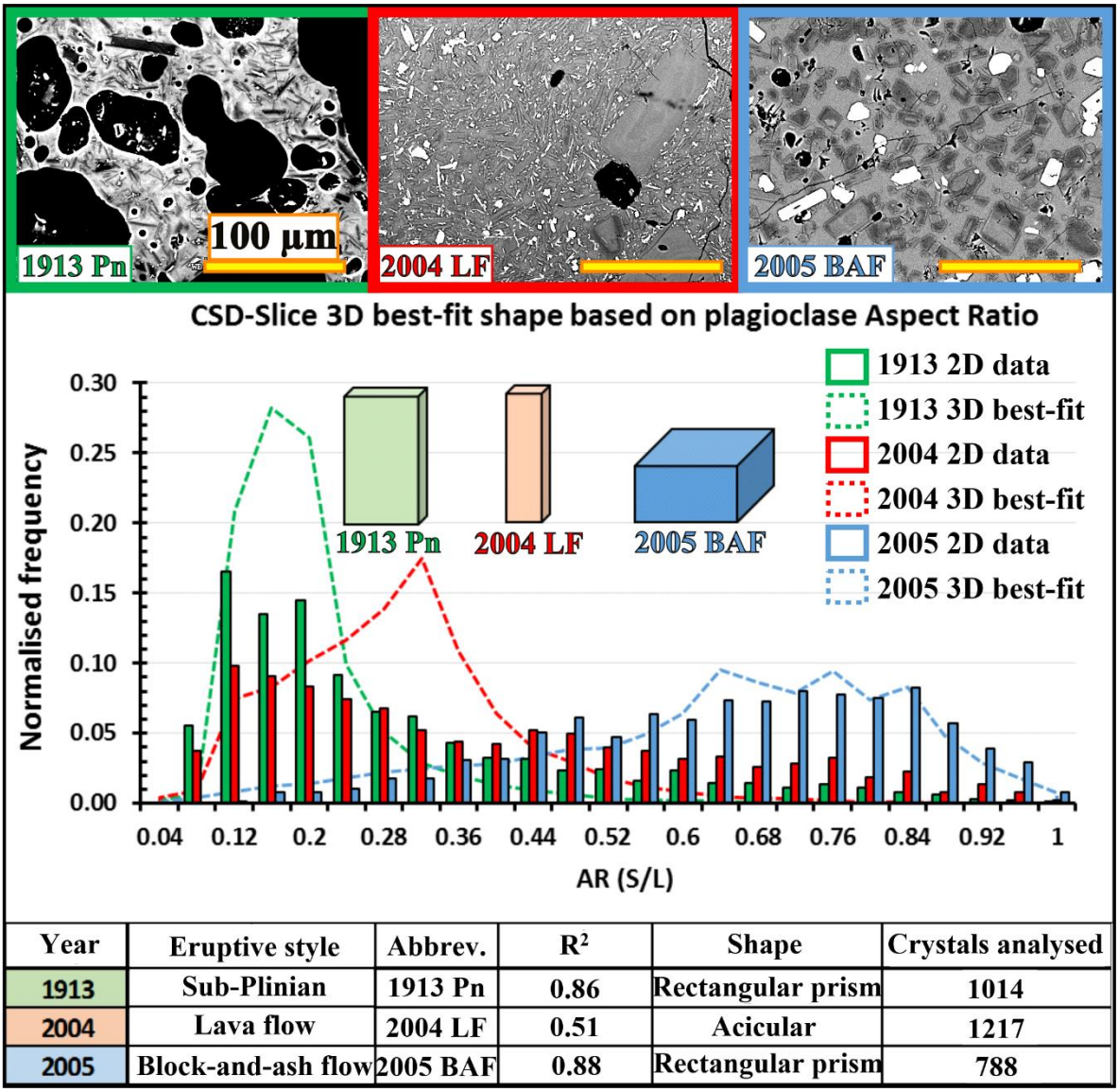

Year	Eruptive style	Abbrev.	R^2	Shape	Crystals analysed
1913	Sub-Plinian	1913 Pn	0.86	Rectangular prism	1014
2004	Lava flow	2004 LF	0.51	Acicular	1217
2005	Block-and-ash flow	2005 BAF	0.88	Rectangular prism	788

Supplementary Material 2.2. *Frequency distribution of 2-D shapes in plagioclase microlites (based in the aspect ratio of short/long axes from a best-fit ellipse) from three different samples of products that represent high- (1913 sub-Plinian), moderate- (2004 lava flow) and low – intensity (2005 block-and-ash flow) events of contrasting eruptive styles of Volcán de Colima. Approximate 3-D crystal shapes are automatically suggested by CSD-slice software (Morgan and Jerram, 2006) based on the best-fit of the comparison between the Volcán de Colima crystal shapes measured in this work and the shape database available in the programme (coloured 3-D- boxes in the figure). Examples of BSE-images of the groundmass textures for the three different eruptions measured are displayed on the upper section of the figure. At the bottom of the figure is a table showing the year of the eruptive events, their eruptive style and the abbreviations used for each of them; R^2 of the databases best-fitting the textural distributions measured; the suggested 3-D shape after the comparison ("Shape" column), and the number of input crystals to perform the textural fits.*

2.7.5. Appendix 2.5: Glass compositions

Glass chemistry was analysed using a Cameca SX100 microprobe with a voltage of 20kV, an intensity of 4nA and a beam diameter of 10 µm (**Supplementary Table 2.2** and **Supplementary Material 2.3**). Na and K were measured first to limit element migration, followed by major oxides and finally minor elements. The weight percentage of each oxide was normalized to 100% of total oxides measured. The volatiles analysed were chlorine and sulphur; H_2O wt. % was calculated by difference from the totals. Glassy embayments of phenocrysts were analysed in the relatively high-crystallinity LF samples, because glass patches sufficiently large to analyse in the groundmass were rare or non-existent.

Supplementary Table 2.2. *Major and minor element and volatile contents in weight percent of glasses from Colima products normalised to 100% anhydrous. The values are averaged from a number of glass spots ("No. of sites" column) within each sample, and the standard deviation is given in parentheses. Water content is calculated from difference from total before normalization. The analyses on LF samples were made on glasses in phenocryst embayments.*

Sample	SiO_2	TiO_2	Al_2O_3	FeO	MnO	MgO	CaO	Na_2O	K_2O	P_2O_5	Cl	SO_2	Cr_2O_3	H_2O Tot.Diff	No. of sites
Detection Limits	0.096	0.059	0.078	0.162	0.156	0.052	0.052	0.14	0.073	0.057	0.039	0.039	0.166	N/A	
1818	63.68 (0.45)	0.71 (0.05)	16.93 (0.55)	4.78 (0.28)	0.09 (0.03)	1.73 (0.12)	4.44 (0.37)	5.30 (0.11)	1.85 (0.17)	0.30 (0.04)	0.13 (0.06)	0.04 (0.04)	0.00 (0.00)	1.2 (0.36)	5
1869	77.66 (0.57)	0.65 (0.03)	11.59 (0.16)	1.41 (0.07)	0.03 (0.02)	0.06 (0.01)	0.34 (0.10)	3.66 (0.66)	4.27 (0.21)	0.07 (0.04)	0.24 (0.03)	0.00 (0.00)	0.02 (0.02)	0.5 (0.59)	6
1913	61.36 (1.02)	0.72 (0.06)	16.22 (0.60)	6.15 (0.53)	0.07 (0.04)	2.75 (0.36)	5.28 (0.27)	5.08 (0.62)	1.83 (0.13)	0.28 (0.06)	0.17 (0.01)	0.06 (0.02)	0.02 (0.02)	2.4 (0.42)	4
1961	76.80 (0.6)	0.62 (0.09)	11.50 (0.38)	1.98 (0.18)	0.06 (0.06)	0.14 (0.09)	0.44 (0.11)	4.51 (0.34)	3.67 (0.14)	0.08 (0.08)	0.13 (0.04)	0.01 (0.01)	0.05 (0.08)	1.7 (0.66)	10
1975 N	77.35 (0.07)	0.51 (0.04)	11.53 (0.07)	1.83 (0.11)	0.04 (0.02)	0.16 (0.05)	0.60 (0.05)	3.75 (0.09)	4.05 (0.17)	0.04 (0.03)	0.09 (0.00)	0.02 (0.03)	0.01 (0.02)	0.6 (0.33)	3
1975 S	75.85 (0.09)	0.67 (0.15)	12.48 (0.37)	2.00 (0.10)	0.07 (0.04)	0.22 (0.07)	0.72 (0.18)	3.76 (0.23)	3.77 (0.09)	0.19 (0.03)	0.23 (0.04)	0.03 (0.02)	0.00 (0.01)	0.6 (0.65)	4
1998	75.73 (0.54)	0.60 (0.12)	12.30 (0.32)	2.02 (0.27)	0.05 (0.04)	0.23 (0.09)	0.71 (0.25)	4.24 (0.24)	3.89 (0.22)	0.07 (0.06)	0.16 (0.03)	0.04 (0.09)	0.01 (0.02)	0.5 (0.81)	14
2004	74.14 (1.01)	0.89 (0.05)	12.60 (0.37)	2.58 (0.61)	0.06 (0.03)	0.26 (0.16)	0.72 (0.37)	4.40 (0.60)	3.99 (0.35)	0.20 (0.13)	0.14 (0.06)	0 (0.00)	0 (0.00)	1.3 (0.73)	7
2013 BAF Blocks	77.42 (0.30)	0.58 (0.02)	11.44 (0.12)	1.61 (0.14)	0.05 (0.03)	0.08 (0.04)	0.25 (0.03)	4.00 (0.08)	4.35 (0.07)	0.04 (0.05)	0.16 (0.01)	0 (0.00)	0 (0.00)	1.4 (0.81)	4
2013 BAF Ash Ac	74.20 (0.52)	0.91 (0.06)	12.51 (0.08)	3.16 (0.04)	0.06 (0.02)	0.30 (0.11)	0.83 (0.04)	3.93 (0.01)	3.79 (0.15)	0.13 (0.00)	0.18 (0.03)	0 (0.00)	0 (0.00)	0.5 (0.03)	2
2013 BAF Ash Eq	77.58 (0.27)	0.59 (0.07)	11.79 (0.48)	1.88 (0.22)	0.03 (0.03)	0.16 (0.05)	0.28 (0.09)	3.06 (0.29)	4.47 (0.30)	0.05 (0.02)	0.11 (0.03)	0.01 (0.01)	0 (0.00)	0.8 (0.61)	12

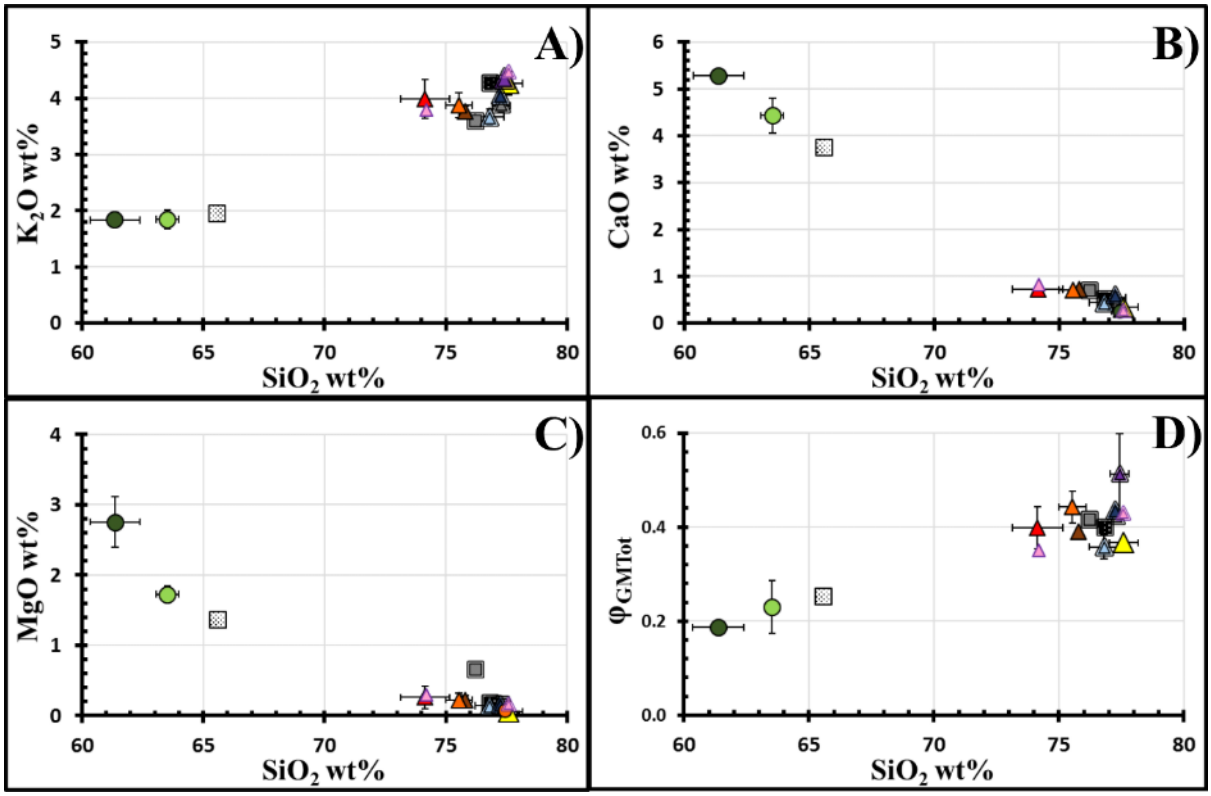

Supplementary Material 2.3. *Glass chemistry.* ***A-C)*** *Chemistry of matrix glass for Volcán de Colima samples, including data from Cassidy et al. (2015).* ***D)*** *Silica versus total groundmass crystallinity. Error bars indicate the standard deviation of all the analysed sites per sample. Refer to* ***Supplementary Material 2.4*** *for symbols.*

2.7.6. Other supplementary tables and figures

Supplementary Table 2.3. *Modal analysis values for physical components of Plinian, lava flow and BAF samples.*

Modal analysis (Area %)					
with vesicles					
Sample	**1913**	**1961**	**2004 A**	**2004 B**	**2013**
Glass	29.7	27.2	30.1	21.6	25.9
GM Feldspars	5.3	11.8	14.5	10.0	21.9
GM Mafics	0.4	2.0	3.7	2.7	2.7
Phenocrysts	12.1	39.8	39.9	26.9	32.5
Vesicles	52.6	19.2	11.9	38.8	17.0
vesicle-free					
Glass	62.6	33.6	34.1	35.3	31.2
GM Feldspars	11.2	14.6	16.4	16.4	26.3
GM Mafics	0.7	2.5	4.2	4.4	3.3
Phenocrysts	25.5	49.3	45.3	44.0	39.2

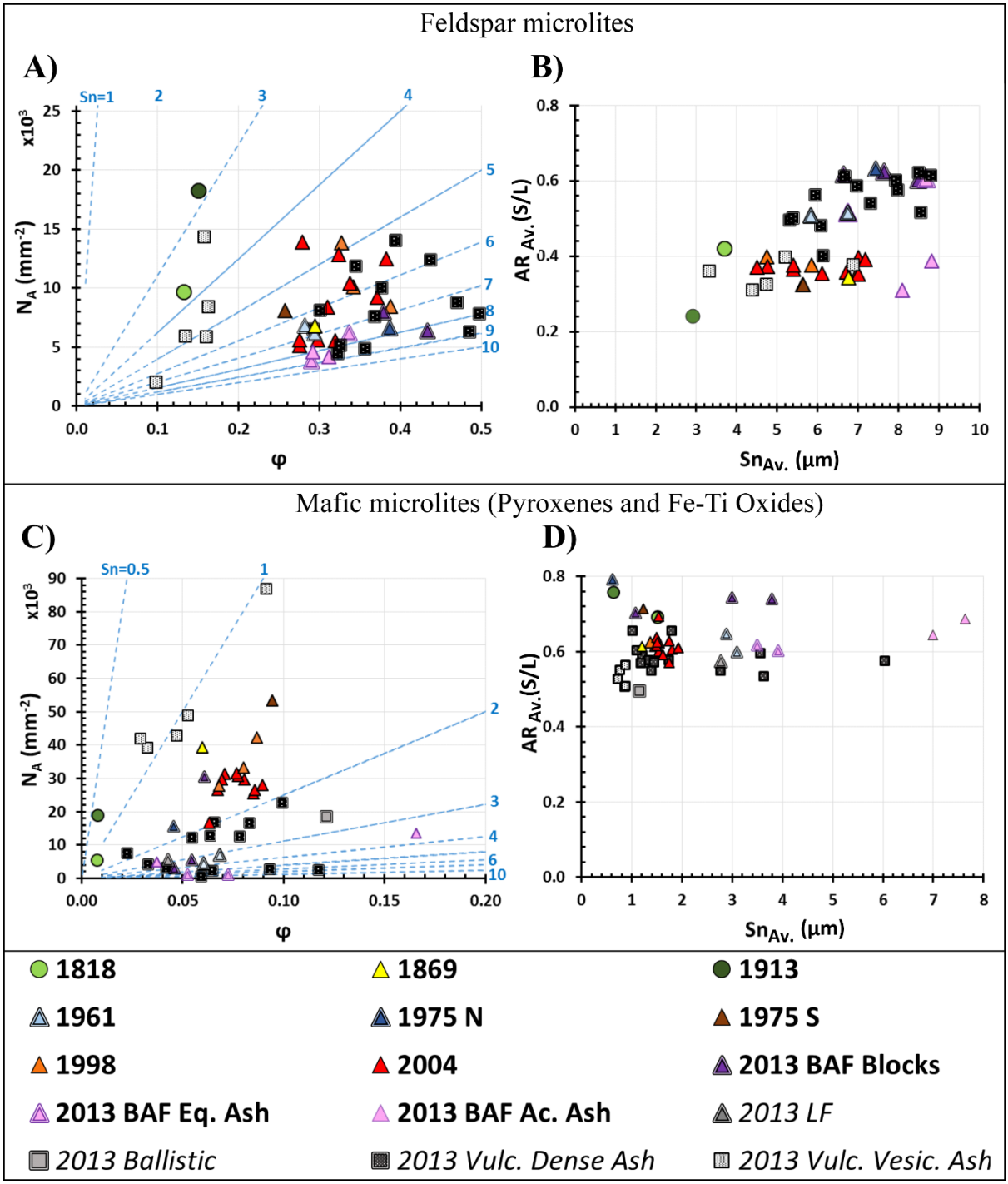

Supplementary Material 2.4. *Groundmass textural parameters (for Sn < 50µm) of every single BSE-image analysed for Volcán de Colima products for* ***A, B)*** *Feldspars and* ***C, D)*** *Mafic components.*

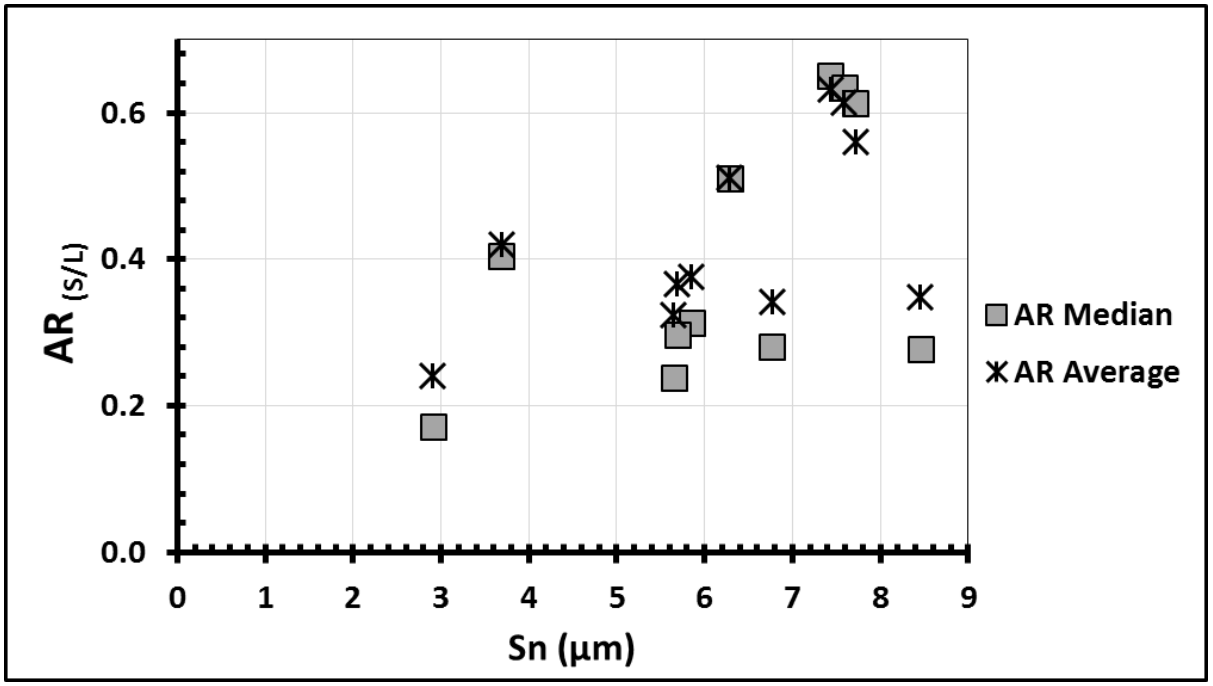

Supplementary Material 2.5. *Variability between the average and median AR values per sample from each eruptive event at Volcán de Colima.*

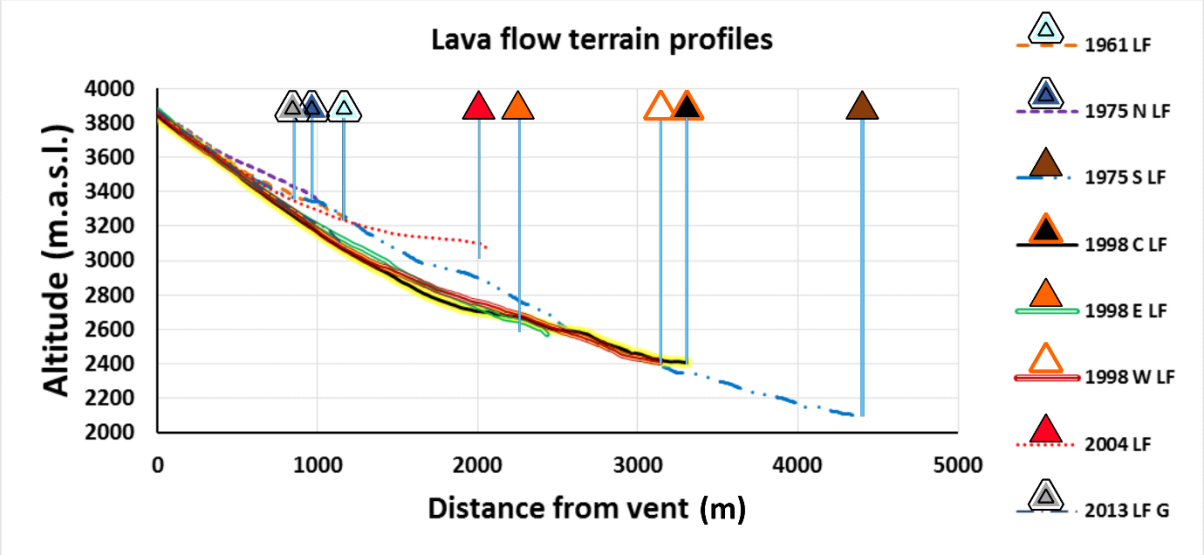

Supplementary Material 2.6. *Terrain profiles indicating the inclination over which historic LFs of Colima travelled and emplaced. Vertical lines and symbols indicate the front of the lava flow deposit. Each profile (distance = 0) commences from the brake in slope at the edge of the crater-vent. Note that this differs from the reference used to measure the total flow length, which was measured from the centre of the vent.*

Chapter 3

Late-stage crystallisation during "Unsteady" eruptions at Volcán de Colima

Author contribution and declaration: In this part of the research, I processed and analysed the textural and chemical data. A. C. Rust and K. V. Cashman provided supervision, advice, and edits during the writing of this chapter. N. R. Varley contributed with advice and his knowledge about the relevant eruptions. B. Buse and S. Kearns delivered the guidance and advice pertinent to BSE-imaging and microprobe analysis and processing of chemical data. M. Cassidy kindly contributed the textural dataset of samples derived from the 2013 eruptive stage.

Abstract

Vulcanian eruptions consist of an interplay between open- and close- eruptive behaviour. I analysed crystal textures of samples originated at different stages of the 2005 and 2013 Vulcanian eruptions at Volcán de Colima to reconstruct the intra-conduit processes involved. The textural analysis shows two separate trends in crystal Size-Shape space for samples, interpreted to relate to crystallisation in diffusion-controlled and interface-controlled regimes. Samples in the two regimes are also distinguished by the presence or lack of sharp, albitic rims on feldspar crystals. Based on samples from steady eruptions, the albitic rims are clear indicators of slow magma ascent. Matrix vesicularity is another textural feature that distinguishes samples from the unsteady eruptions analysed, with the highest vesicularities corresponding to the samples with the lowest crystallinity and crystal aspect ratio, typically associated with fast ascent rates. Correlating crystallinity and crystal shapes with intensities of recorded, steady eruptions allows me to estimate energy values for the products of the 2005 and 2013 eruptions. The textural correlations suggest that block-and-ash flow and dense ash samples in both events analysed crystallised during magma ascent stages of conduit (re)fill, whereas the vesicular Vulcanian ash reflect a stage of higher volatile concentrations compared to the conduit (re)fill stages, similar to the fast-ascent that took place at the sub-Plinian eruptions.

Keywords: Vulcanian eruptions, crystal textures, albitic rims, crystallisation regimes, Volcán de Colima

3.1. Introduction

The development of robust monitoring networks around volcanoes has only occurred within the last few decades, meaning that records of volcanic activity are more scarce and less detailed as we go back in time. Developing tools to reconstruct unrecorded eruptive activity is important to assess and forecast potential scenarios for future volcanic eruptions. Groundmass textures provide petrological records of the dynamics of eruptions, as some of the attributes of crystals are created by the same eruptive conditions that control eruption style and intenisty.

Sub-Plinian and Plinian eruptions are driven by rising bubbly magma through the volcanic conduit which eventually reaches a fragmentation front (*Clarke et al., 2015*). During these high-intenisty eruptions the output of material occurs mainly as a steady flux that can last from a few hours up to several days (*Clarke et al., 2015*), in this manner, similar to the steady flux of lavas during effusive eruptions. On the other hand, Vulcanian and Strombolian eruptions consist of rather short-lived pulses of discharged material alternated with relatively quiet periods where no apparent extrusion of material occurs (*Clarke et al., 2015*; *Taddeucci et al., 2015*). In the latter type of eruptions, the output of material takes place as an unsteady flux compared with the eruptive flux in (sub-) Plinan and effusive eruptions and mass evacuation is not only controlled by the ascent of magma through driven by gas bubbles but is also affected by downward depressurisation of the system (*Clarke et al., 2015*). I hypothesise that the manner in which the dynamics of the eruptive flux is driven (steady versus unsteady way) will ultimately affect the extent and effectiveness of syn-eruptive degassing and crystallisation of magma. Therefore, it is important to consider the evacuation dynamics that act upon steady and unsteady eruptions to more accurately correlate crystal textures and eruptive intenisties in the same way as in Chapter II. In this chapter I group eruptions of Volcán de Colima and other intermediate volcanoes as “steady” (effusive and sub-Plinan events) or

"unsteady" (Vulcanian and Strombolian eruptions) based on the dynamics of the eruptive flux as described in the previous lines.

In Chapter II, I showed that some groundmass textures, particularly crystal shape and crystallinity, correlate with magnitude and intensities of steady eruptions (i.e. effusive and sub-Plinian events) at Volcán de Colima, Mexico (e.g. **Fig. 3.1**). However, the interpretations of textural data are less straightforward when eruptions are unsteady because magma decompression rate varies as the magma ascends. For example, magma may slowly ascend to fill a conduit, stall and re-pressurise before rapid decompression and ejection in a Vulcanian eruption (e.g. *Druitt et al., 2002*).

In a study of a series of unsteady eruptions (Strombolian and Vulcanian) and a relatively steady (sub-Plinian) eruption at Tungurahua Volcano (Ecuador), *Wright et al. (2012)* related groundmass textures to a pre-eruptive Magma Supply Rate (MSR). What they termed as MSR was constrained by averaging the cumulative volumes of tephra over 2-month windows of time, a period much longer than any of the individual eruptions. The textures of products of each eruption varied, but they found that the average groundmass crystallinity (φ) correlated with their estimates of MSR, as calculated from the cumulative volumes of erupted ash (**Fig.4** in *Wright et al., 2012*). The φ – MSR correlation for Tungurahua unsteady eruptions, which is remarkably similar to the φ – VER for steady eruptions of Volcán de Colima (**Fig. 2.10B** in Chapter II), suggests that the supply of magma into the conduit had a dominant control on the degree of groundmass crystallisation. However, *Wright et al. (2012)* did not consider textural parameters other than φ and did not attempt to relate the variability of the groundmass textures generated at each eruptions to the unsteady eruption dynamics. Although in a different way to my VER estimates, the MSR of *Wright et al. (2012)* derives from a division of erupted volume over time, therefore in the subsequent paragraphs I refer to both terms as VER for simplicity and direct comparisons.

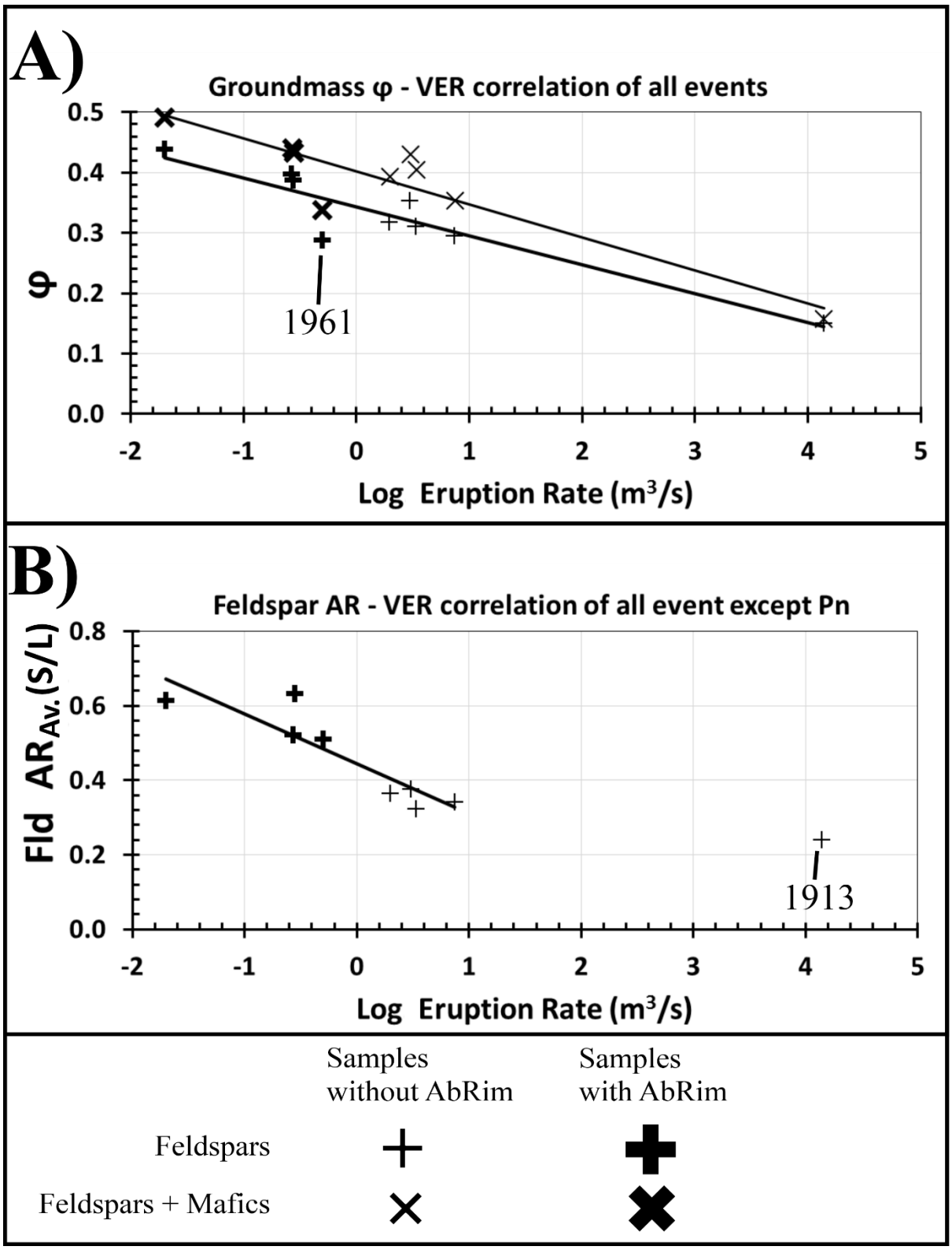

Figure 3.1. *Textural correlations of steady eruptions at Volcán de Colima with average VER.* ***A)*** *Correlation between total crystal-fractions of groundmass (Feldspars + Mafic crystals of Sn < 50µm) and log volume eruption-rates (VER) for Volcán de Colima.* ***B)*** *Correlation between average feldspar shape ($AR_{AV.}$) and log. eruption rates. The trend-lines are fits to the datasets. Thicker symbols indicate the presence of sharp rims of albitic*

composition on feldspars (referred to them as AbRims) in samples from the respective eruptions. For equations of best-fit lines refer to ***Table 2.5*** *in Chapter II. The year of the events that show the least fit to the correlations are indicated in the figure.*

The most common type of non-steady eruptions at Volcán de Colima and other intermediate-composition volcanoes are Vulcanian, high-intensity but short duration events that are commonly associated with lava dome formation. Vulcanian eruption sequences often consist of pulses of different eruptive magnitudes and intensities. Thus, the crystal textures of Vulcanian eruption products will not necessarily reflect continuous crystallisation of magma associated with steady ascent through the conduit but will incorporate the effects of stagnation periods and ejection of material from different depths due to rapid downwards fragmentation. In fact, data from the 2005 Vulcanian crisis of Volcán de Colima were not included with data from steady eruptions in the textures-VER compilation in Chapter II because: 1) the samples of the 2005 crisis are texturally diverse, and the samples collected from the block-and-ash flows (BAFs) could be derived from both effusive and violent explosive stages; and 2) the volumes of erupted material, required to calculate average VER, are poorly constrained. In this chapter, I use the calibrations of textural data from steady eruptions at Volcán de Colima (Chapter II) as a baseline to interpret the textures of individual samples collected from two recent (2005 and 2013) Vulcanian eruption sequences, in order to assess magma ascent conditions during unsteady activity.

Table 3.1. *Table of symbols and abbreviations used in Chapter III.*

Chapter III - Table of symbols and abbreviations	
Symbol/Acronym	**Definition**
Ab	Albite
AbRim	Albitic rim on plagioclases
Ac	Acicular crystal shapes
An	Anorthite
AR	Crystal aspect ratio
$AR_{AV.}$	Average crystal aspect ratio
$AR_{Fld.\ NoPn}$	Aspect ratio of feldspar crystals of all events but the sub-Plinian eruption
Av.	Average value
BAF	Block-and-ash flow
BSE	Back-scatter electron analysis
cf.	Compare to
dL	Change in length of the long axis of a crystal
dS	Change in length of the short axis of a crystal
dt	Duration of a process
Eq.	Equant crystal shapes
Fld	Feldspar mineral phases
Holocryst.	Holocrystalline texture
ind.	Individual
Kv	Kilovolts
L	Long axis
LF	Lava flow
Log.	Logarithmic value
Maf	Mafic mineral phases (pyroxenes, Fe-Ti oxides, amphiboles and olivine)
Max.	Maximum value
mol %	Mole percentage of a given element
MPa	Megapascals
MSR	Magma Supply Rates
N	North
N_A	Crystal number density
nA	Nanoamperes
Or	Orthoclase
PDC	Pyroclastic density current
P_{H2O}	Water-vapour pressure

PhC	Phenocryst-size crystals
Pn	Sub-Plinian eruptions
R^2	Coefficient of determination
S	South or Short axis
Sn	Crystal size
$Sn_{AV.}$	Average crystal size
VER	Average volumetric eruption rates
Vesic.	Vesicular texture
vol. %	Percentage of a given element per sample volume
Vulc.	Vulcanian eruption
wt.%	Percentage of a given element per sample weight
$\Delta P_{H2O}/\Delta t$	Degassing-induced decompression rate
ΔT	Degree of undercooling
φ	Crystal fraction
ϕ	Grain size: $\phi = \log2(d)$, where d is the grain diameter in mm
$\varphi_{Tot.}$	Crystal fraction of feldspars plus mafic components in groundmass

3.2. Background

3.2.1. Vulcanian eruptions

Vulcanian eruptions are explosive events that occur after the removal of a dense magma plug (**Fig. 3.2A**), which allows underlying gas overpressure to be suddenly released in short but often violent bursts. The removal of a shallow capping plug could occur either after the gravitational collapse of a lava dome, or due to excess internal gas pressure accumulated within the conduit. In the latter case, gas exsolved from deeper, volatile-rich magma accumulates underneath a shallow, impervious cap and builds up overpressure (> 10 – 20 MPa, *Martel et al., 2001*; *Melnik and Sparks, 2002*); when the volatile pressurisation exceeds the tensile strength of the overlying degassed magma, the plug fails. The dynamics in the plumbing system precursory to the explosive stages occur relatively rapid (1 – 6 minutes) and due to different reasons, either caused by the gradual failure of the shallow portion of the plumbing system, or as a hydraulic response to sudden pressurisation at depth (*Gottsmann et al., 2011*). In the following paragraphs, I explain the dynamics of Vulcanian eruptions expanding into the stages that precede and proceed explosions (i.e. conduit (re)fill and fragmentation) and characteristic batch textures associated with them.

3.2.1.1. Conduit (re)fill stage

In a study of Vulcanian eruptions at Soufrière Hills Volcano, Montserrat, *Clarke et al. (2007)* used crystalline groundmass textures and bulk densities to estimate pressures of pre-eruptive magma storage. Combining textural information with numerical modelling and results from decompression experiments, they proposed a generic model of magma supply during Vulcanian eruptions (see also *Druitt et al., 2002* and *Wright et al., 2012*). First, magma ascends to (re)fill the conduit (**Fig. 3.2A**), degassing either through the dome or permeable country rock. Volatile exsolution is enhanced at a confining pressure of 3 -11 MPa: the critical zone. Extensive degassing in the critical zone produces high bubble connectivity and a subsequent

burst in crystallisation. Both gas loss and crystallisation eventually lead to bubble collapse and to an increase in the viscosity of the residual melt by up to 8 orders of magnitude (*Voight et al., 1999*), hindering ascent and aiding formation of a dense, impervious magma plug (**Fig.3.2A**). Based on the characteristic high-φ, low N_A and low density of samples associated with the dense plug, *Clarke et al. (2007)* proposed a thickness between 250- 700 m for the plug region.

Below the dense plug, there is a gradual transition towards a low-density, bubbly region resulting from magma that degasses at near-closed-system conditions (i.e. minimal gas escape) (**Fig. 3.2A**). This bubbly region may extend from the base of the dense plug to the maximum depth of the critical zone of degassing; in the *Clarke et al. (2007)* model, magma vesicularity decreases below this level. Closed-system degassing beneath the impervious plug builds the gas overpressure responsible for the explosive behaviour. From this perspective, a conduit stratigraphy from surface to depth between each Vulcanian eruption (pre-explosion conduit) could be divided into a highly degassed, dense cap of magma (at 0 ~ 450 m depth assuming a density of 2500 kg/m^3 for dense rock); an overpressurised, vesicular region (at the base of the dense plug), and a deep, volatile-rich zone (**Fig.3.2A**).

3.2.1.2. Fragmentation stage

The sudden release of overpressure following the removal of the shallow cap leads to the rapid decompression of the magma underneath, generating a downward-propagating fragmentation wave (**Fig.3.2B**). The fragmentation wave can reach velocities up to 50 m/s (*Druitt et al., 2002*), and can propagate until the rheological properties of the magma prevent further brittle failure. At this point, deformation shifts into a viscous regime and magma ascends again as a flow. The maximum fragmentation depth correlates with the eruption intensity and also depends in the diameter of the conduit, reaching just 500 m below the crater surface in some relatively low-intensity explosions, and up to ~2-3 km during high-intensity events (*Druitt et al., 2002; Clarke et al., 2007; Wright et al., 2007*).

Between Vulcanian events, the conduit is refilled with magma, re-forms the dense cap and repressurises (**Fig. 3.2A**). The minimum recurrence time of each Vulcanian cycle will therefore depend on the ascent rate of the infilling magma (*Wright et al., 2007*). Replenishment rates of 0.5- 6 cm/s (10 – 170 m^3/s) have been suggested at intermediate composition volcanoes such as Soufrière Hills, Montserrat (*Druitt et al., 2002*) and Guagua Pichincha, Ecuador (*Wright et al., 2007*).

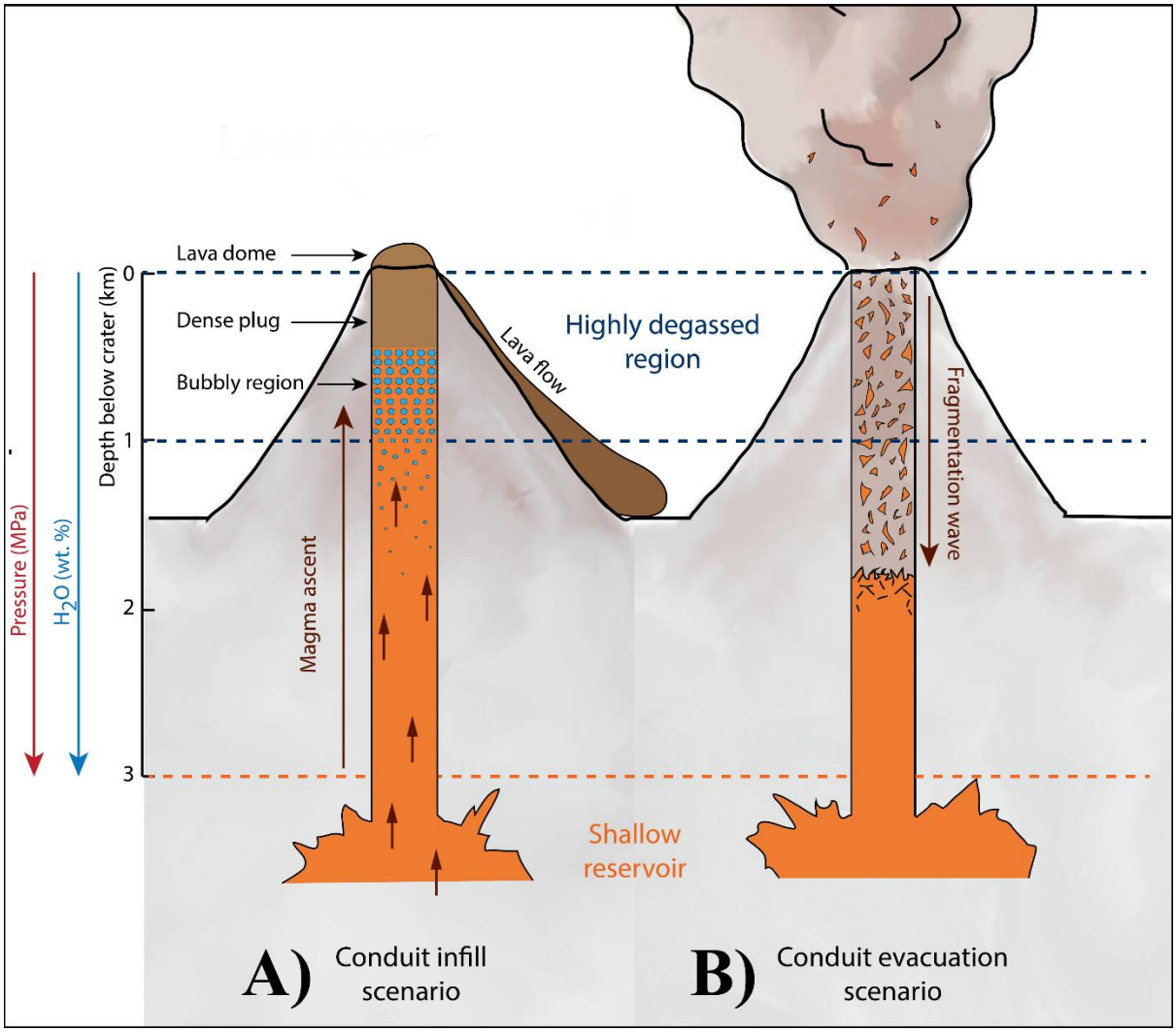

Figure 3.2. *Schematic representation of eruptive stages at Vulcanian eruptions.* ***A)*** *Conduit infill stage where magma ascends from a shallow reservoir and extrudes a lava flow or dome or builds a dense capping magma plug due to extensive degassing.* ***B)*** *Intra-conduit downwards fragmentation caused by dome collapse or the sudden removal and decompression of a dense plug when gas-overpressure exceeds the tensile strength of the capping plug.*

3.2.1.3. Syn-eruptive bubble and crystal textures in Vulcanian eruptions

Decompression-induced crystallisation is driven by the exsolution of H_2O from the melt into bubbles, which, like crystallisation, is a kinetic process affected by decompression rate. If the deepest magma fragmented did not have enough time to devolatilise during the eruption, then the pyroclasts will maintain the bubble and crystal textures associated with the saturation conditions at the pre-eruptive pressure at which they resided. However, with large decompression, the water-rich, deeper magma that is exposed by the evacuation of the shallow

conduit may exsolve its volatiles abruptly and erupt as vesicular, crystal-poor pumice and ash (e.g. *Cashman and McConnell, 2005*) similar to products of (sub-)Plinian eruptions. This is because the volatile diffusion required for vesiculation is faster in melt with higher dissolved water content, and bubble kinetics (nucleation and growth rates) are faster than crystallisation kinetics at these conditions.

The complexity of residence times and rapid, downwards evacuation of the conduit means that the calibration of groundmass textural parameters with long-term magma supply rate for the example of Tungurahua (**Fig 2.10** in Chapter II) should be applied with caution to interpret unsteady eruptions. However, they may provide approximate estimates of the supply rates of magma batches ascending in similar manners as steady-style events at particular stages during unsteady eruptions, such as the intra-explosion replenishing stages that lead to the formation of lava domes or shallow plugs.

3.2.2. Conceptual models for Vulcanian eruptions at Volcán de Colima

Vulcanian activity is the most common eruptive style at Volcán de Colima. As an example, between 2 and 10 Vulcanian explosions of various magnitudes were reported daily during the eruptive period of 2003- 2011 (*Varley et al., 2010a*). In recent years, Vulcanian explosions have intensified and generated pyroclastic density currents (PDCs), with run-out distances approaching those produced during the last sub-Plinian crisis (e.g., 15 km in 1913 versus 10.5 km in 2015). Together, the high frequency and increasing magnitudes of Vulcanian events at Volcán de Colima highlight the importance of understanding the eruption generation mechanisms to produce an adequate assessment of associated risk scenarios. In this manner, two general conceptual models have been proposed for the development of Vulcanian eruptions in Volcán de Colima: one that associates pockets of gas-rich magma with explosive triggers, and another that considers evacuation through brittle failure of magma in the conduit.

3.2.2.1. Gas-rich pockets of magma as trigger for Vulcanian explosions

Cassidy et al. (2015) developed a conceptual model for Vulcanian eruptions of Volcán de Colima, mainly based on groundmass textures of pyroclasts, with some consideration of seismic signals and gas emissions. They classified ash particles from Vulcanian events of 2013 as either "vesicular" or "dense" based on their groundmass vesicularity and attributed differences in groundmass crystal textures (particularly N_A and φ) to different magma ascent paths. They suggested that the dense ash derived from magma that was in contact with the conduit walls and outgassed before eruption, whereas the vesicular ash resulted from pockets of gas-rich magma that rose through the dense magma within the central parts of the conduit, similar to mechanisms proposed for Strombolian-type eruptions elsewhere (e.g. *Blackburn et al., 1976*; *Vergiolle and Brandeis, 1996*; *Vergiolle et al., 1996*).

Others have considered the source mechanisms of long-period seismic signals that precede Vulcanian eruptions of Volcán de Colima. *Zobin et al. (2006)* proposed that rapid exsolution and expansion of gas occurs in the conduit at about 1 km below the surface, and that this gas ascends and acts as the initiation for subsequent explosions at the surface (*Zobin et al., 2006, 2015*). However, *Varley et al. (2010b)* attributed seismic swarms to the brittle fracturing of ascending crystal-rich, highly degassed magma, rather than to the formation of gas slugs.

3.2.2.2. Low- and high- energy conduit fragmentation

Studies of the 2005 Vulcanian crisis identified high-magnitude and low-magnitude explosions with independent mechanisms proposed for their generation. The high-magnitude explosions were attributed to the development of an impervious lava-plug at the top of the volcanic conduit, which allowed exsolved gas to create an overpressurised zone at ~ 100 m below the surface (*Varley et al., 2010a*). Efficient sealing of the vent by capping with the impervious magma was proposed to have occurred within 1-2 hours of the Vulcanian explosions based on measurements of SO_2 flux (*Varley et al., 2010a*), faster than has been

observed at other silicic volcanoes (e.g. 2.5 to 20 hours, *Druitt et al., 2002*). The gas overpressure caused the failure of the dense plug and the violent, high-magnitude explosions. The exposed, underlying magma experienced sudden depressurisation and was highly fragmented, generating ash-rich columns. In contrast, the low energy events had longer-duration with low emissions of gas and solid particles and were either produced relatively quiet or accompanied by weak explosions (*Varley et al., 2010b*). The volatile suite entrapped in products from the low-energy events was mostly associated with a deeper source rather than extensive volatile exsolution of magma in the shallow portion of the conduit (e.g. higher H_2O content, *Reubi et al., 2013*).

3.2.3. Cases of Vulcanian eruptions at Volcán de Colima

In this chapter, I focus on two recent Vulcanian crises (2005 and 2013) for which some observations are available to reconstruct syn-eruptive ascent dynamics and estimate magma supply rates affecting groundmass crystal textures. These two events were similar in style (unsteady, predominantly Vulcanian) but different in overall magnitudes and intensities, with the 2005 crisis lasting longer and generating large pyroclastic flows, and the 2013 comprising a shorter period and generating relatively small Block-and-Ash flows (BAFs). Unlike *Cassidy et al. (2015),* I interpret the crystal textures from the 2005 and 2013 Vulcanian events in the framework of the more common perspective of tapping of magma stored over a vertical (pressure) range in the conduit, rather than pockets of magma ascending through each other. However, I incorporate textural data from *Cassidy et al. (2015)* derived from Vulcanian ash, ballistic and lava flow front blocks in the discussion, which allows me to address a wide range of eruptive styles within a single unsteady eruption. Next, I describe the eruptive sequences for the 2005 and 2013 eruptions in more detail.

3.2.3.1. 2005

A stage of explosive activity commenced early in 2005 following the 2004 effusive activity. On the 17th of February 2005, a Vulcanian explosion was accompanied by a small collapse of the crater rim producing the first reported BAF of the crisis, which was anomalously large for the magnitude of the explosion (*Varley et al., 2010a*).

The 2005 sequence included approximately 30 Vulcanian explosions over 9 months (February to September), with the largest explosions (VEI= 2-3) occurring on 15, 30 of May, and 5 June. Intermittent dome growth (of 2 – 4 x 10^5 m^3) was observed between some explosions; these temporary domes had a lifespan of 1-2 days before they were destroyed by subsequent explosions (*Varley et al., 2010a*). A maximum eruption rate of 1.2 – 4.6 m^3/s was inferred for the peak of the eruptive crisis based on the observed extrusion rate of the domes. A total erupted volume of $2.86x10^6$ m^3 was estimated for the whole 2005 crisis, however, this only represents a minimum as it was estimated from basal avalanche deposits and excluded data from some ravines; an additional $0.36x10^6$ m^3 were calculated from pyroclastic surge deposits, with no ash-fall volumes quantified (*Vargas-Gutierrez, 2009*).

3.2.3.2. 2013

Before the explosive stage in 2013, a lava dome slowly grew between 2007 and 2011 with average effusion rate of 0.03 m^3/s (*Mueller et al., 2013*). Within the two weeks preceding the explosive stage, clear deformation was observed at the summit of the volcano and precursory seismic signals were detected, but there was no significant emission of gas (*Zobin et al., 2015*), consistent with a dense plug in the shallow conduit. The Vulcanian phase commenced on the 6th of January 2013; the release of the accumulated excess of pressure accounts for the subsequent mechanical failure of the 2007-2011 dome. There were frequent explosions between the onset and the end of March (with up to 30 events per day), however, after the initial explosion, the most significant Vulcanian bursts took place on the 11th, 13th

and 29th of January 2013, sometimes accompanied by BAFs (*Zobin et al., 2015*). Of the larger events, the final one was the most energetic at 1.5 x10^{11} Joules compared to 2.3 – 7.2 x 10^{10} Joules for the other three explosions (*Zobin et al., 2015*). A lava dome commenced to infill the partially destroyed older lava dome at an average rate of 0.27 m^3/s after the 11th of January explosion (reaching an estimated volume of 1.3 x 10^6 m^3; *Zobin et al., 2015*), spilling over the west flank of the volcano by the beginning of March as a lava flow (*Zobin et al., 2015*).

3.3. Methodology

3.3.1. Sample suite

Block-size clasts and ash were randomly sampled from pyroclastic deposits associated with the 2005 and 2013 eruptive sequences. 5 block samples were collected from deposits of the 2005 eruption and 3 blocks from 2013 (**Table 3.2**), as well as ash from each respective BAF deposit. All block samples are dense (5 vol. % < vesicularity < 18 vol.%, **Figure 3.8**). The ash samples were mechanically sieved and separated by size. The size-groups 2 and 3 ϕ from each Vulcanian event were selected for further analysis since there were few particles at larger sizes and smaller fractions were too small to perform textural analysis.

Either polished thin-sections or mounts in epoxy resin of the samples were produced for subsequent modal, textural and chemical analyses of the groundmass crystals. Groundmass crystal textures of feldspars (Sn < 50 μm) were measured and quantified for the block-size clasts and ash samples from the 2005 and 2013 eruptions using the methodology detailed in Chapter II (**Section 2.3.3**). Due to resolution limitations, the analysis does not include crystal sizes Sn < 2 μm. Excluding crystals < 2 μm in textural analysis of Chapter II was inconsequential because the samples used there, lacked micron-sized crystals; however, sample 24, a holocrystalline block from a 2013 BAF (**Fig. 3.4C**), contains abundant crystals that are too small to resolve (i.e. < 2 μm) and so φ and N_A are underestimated for this sample. Modes of different groundmass texture types were determined for the ash fraction of the BAFs (**Fig. 3.5**), and textures quantified in four grains. To extend the 2013 dataset I include textural data from Vulcanian tephra ("dense" and "vesicular" ash of 30-240 μm size) and lava samples (ballistic and lava blocks) derived from the explosive and effusive phases of the 2013 sequence (from *Cassidy et al., 2015*). *Cassidy et al. (2015)* reported groundmass texture data based on Sn < 100 μm. I re-calculated the textural parameters for their samples using their raw data and

only crystals in the range $2 < Sn < 50$ μm to facilitate comparison with my data from other samples.

To put analyses of 2005 and 2013 samples into context, I compare them to several samples from the best-constrained lava flow and sub-Plinian eruptions of Volcán de Colima. These include 6 lava blocky lava flow samples collected along the levees and the central channel of the 2004 lava flow (2004 LF), and a pumice clast from the 1913 sub-Plinian (1913 Pn) air-fall deposit, collected about 9km north of the vent (**Table 3.2**). A more detailed analysis of these samples can be found in Chapter II.

Table 3.2. *Groundmass textural parameters of Volcán de Colima eruptive samples based on individual crystal sizes (Sn < 50 µm). The asterixis (*) next to some of the listed products in the "Sample Name" column indicate that values were obtained from more than one image and the associated standard deviation is indicated in parenthesis.*

Event	Sample Name	Fld φ	N_A (mm^{-2})	$Sn_{AV.}$ (µm)	$AR_{AV.}$ (S/L)	GM φ_{Tot}
1818	S1818	0.13	9682	3.69	0.42	0.14
1869	S26	0.29	6810	6.77	0.34	0.35
1913	S1913	0.15	18271	2.91	0.22	0.16
1961	S22*	0.29 (0.01)	6500 (332)	6.29 (0.46)	0.51 (< 0.01)	0.34 (0.03)
1975 N	S28	0.39	6617	7.43	0.63	0.43
1975 S	S30	0.31	8527	5.65	0.32	0.4
1998	S2a	0.39	8442	6.98	0.35	0.47
	S3a	0.33	13845	4.74	0.4	0.41
	S1a	0.34	10104	5.84	0.38	0.41
2004	S1*	0.3 (0.02)	13346 (543)	4.64 (0.13)	0.37 (< 0.01)	0.38 (0.03)
	S5	0.31	8413	5.62	0.32	0.4
	S16*	0.29 (0.02)	5456 (203)	6.97 (0.17)	0.37 (0.02)	0.37 (0.03)
	S04-01	0.34	10388	5.4	0.37	0.4
	S04-03	0.38	12480	5.39	0.38	0.45
	S04-05	0.37	9192	6.1	0.35	0.45
2005	S9	0.46	11607	6.17	0.53	0.52
	S2*	0.34 (0.02)	6574 (719)	6.95 (0.25)	0.64 (0.03)	0.45 (0.05)
	S3	0.33	8105	6.1	0.39	0.38
	S4	0.35	18364	4.34	0.42	0.42
	S10	0.42	8209	6.91	0.59	0.48
2013	S24	0.5	6306	8.49	0.6	0.56
	S23	0.43	6361	7.65	0.62	0.49
	S8a	0.38	7951	6.64	0.62	0.43
	Ac-AshBAF13_1-13	0.33	4184	8.82	0.39	0.38
	Ac-AshBAF13_0-12	0.3	4605	8.09	0.31	0.37
	Eq-AshBAF13_1-11	0.29	3850	8.68	0.6	0.46
	Eq-AshBAF13_3-12	0.29	6167	6.74	0.52	0.36

3.3.2. Textural classification

I classified samples from the 2005 and 2013 crises into four main groups based on the dominant groundmass feldspar textures observed in BSE-images (see Chapter II for acquisition details), focussing on crystal shape ($AR_{AV.}$), the presence/absence of sharp albitic rims (from this point I simply refer to these albitic rims as "AbRims"), and crystallinity (**Table 3.3**). Most samples were classified as either "Acicular" or "Equant". In both Acicular and Equant textural categories, number density (N_A) and average size ($Sn_{AV.}$), and therefore φ, vary substantially relative to AR_{AV}. Other samples are classified as "Bimodal" or "Holocrystalline" (**Fig. 3.3B** and **Fig. 3.4C**).

Table 3.3. *Textural classification of Block-and-ash flow samples from the 2005 and 2013 eruptions at Volcán de Colima. Four main groups (with some subclasses) are defined based on crystal shapes, albitic rims and matrix crystallinity. Visual examples are found in the figures indicated in the last column of the table.*

Textural group	Subclasses	Matrix description	Feldspar shape ($AR_{AV.}$)	Sharp, albitic rims	Figure
Acicular	None	Microlites in glassy matrix	Most crystals of all sizes are acicular ($AR_{AV.} \leq 0.4$)	None	3.3A, 3.4D
Equant	None	Microlites in glassy matrix	Most crystals of all sizes are equant ($AR_{AV.} \geq 0.5$)	Most crystals	3.3C, 3.4A, C
Bimodal	Same $AR_{AV.}$	2 different size groups of microlites: 1) large, less abundant 2) small, more abundant	Most crystals of all sizes are equant	Most crystals	3.3B
	Different $AR_{AV.}$		Larger crystals are equant, smaller crystals are acicular	Large crystals do have, small crystals lack	
Holocrystalline	Single feldspar population	Almost no discernible glass. Most abundant crystals are < 10 um	2 types: 1) most crystals of all sizes are equant 2) most crystals of all sizes are acicular	Acicular crystals lack, equant crystals do have	3.4C, Supp. Material 3.2
	Bimodal	Almost no discernible glass. 2 different size groups of microlites	Same as the two subclasses of bimodal class	Same as the two subclasses of bimodal class	
	Silica polymorph minerals	Almost no discernible glass.	Large, equant feldspars with sharp albitic rims with silica polymorph minerals	Large, equant crystals do have	

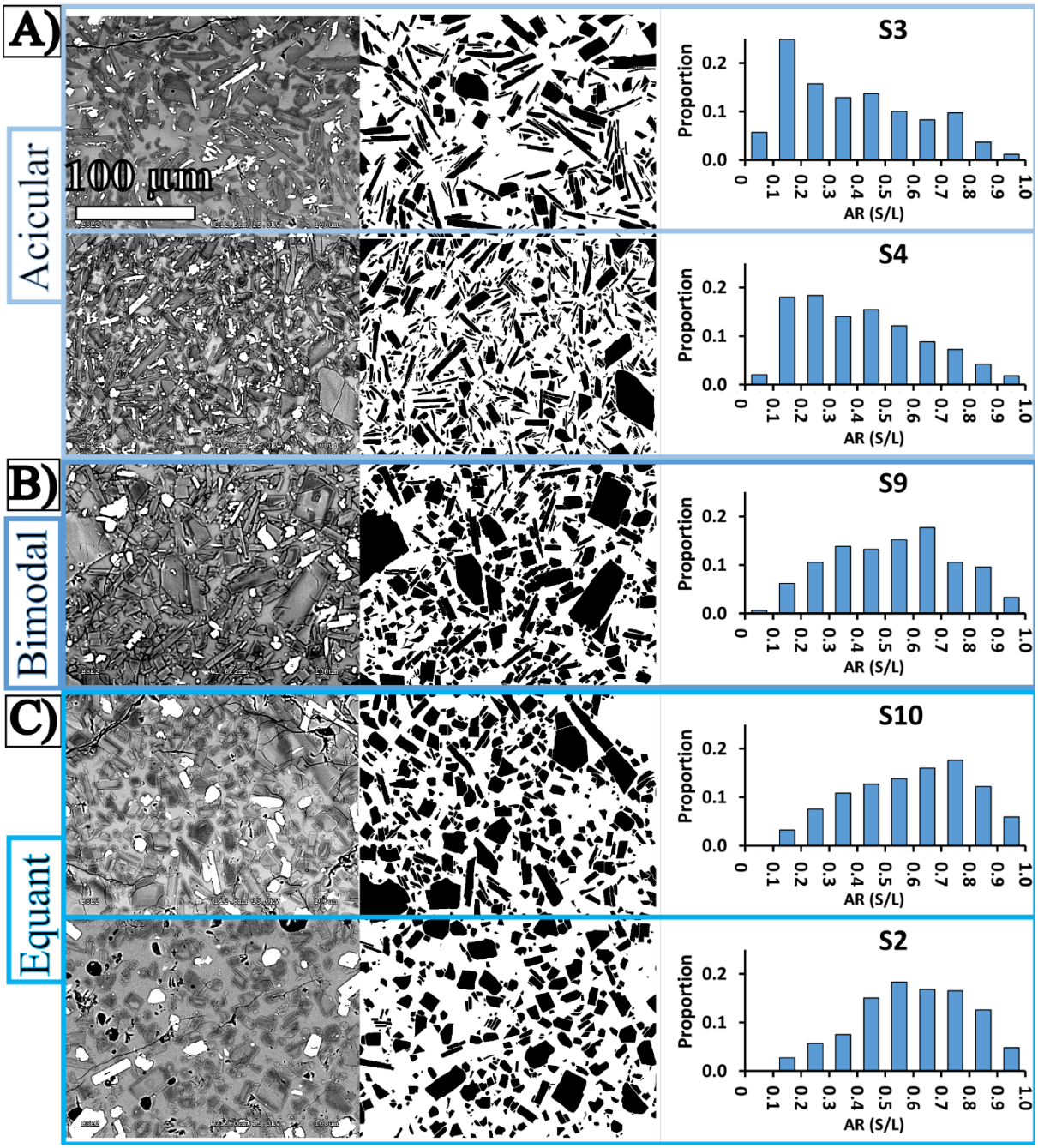

Figure 3.3. *BSE images and feldspar binary masks of block samples collected from the 2005 BAF deposits of Volcán de Colima. Modes of microlite shapes (AR) (5 < Sn < 50µm) are displayed on the left of each sample frame. The samples shown are texturally grouped as* ***A)*** *Acicular,* ***B)*** *Bimodal (two distinctive crystal populations), and* ***C)*** *Equant. The white bars on the top image corresponds to 100µm and all the BSE- and binary images included in the figure have the same scale.*

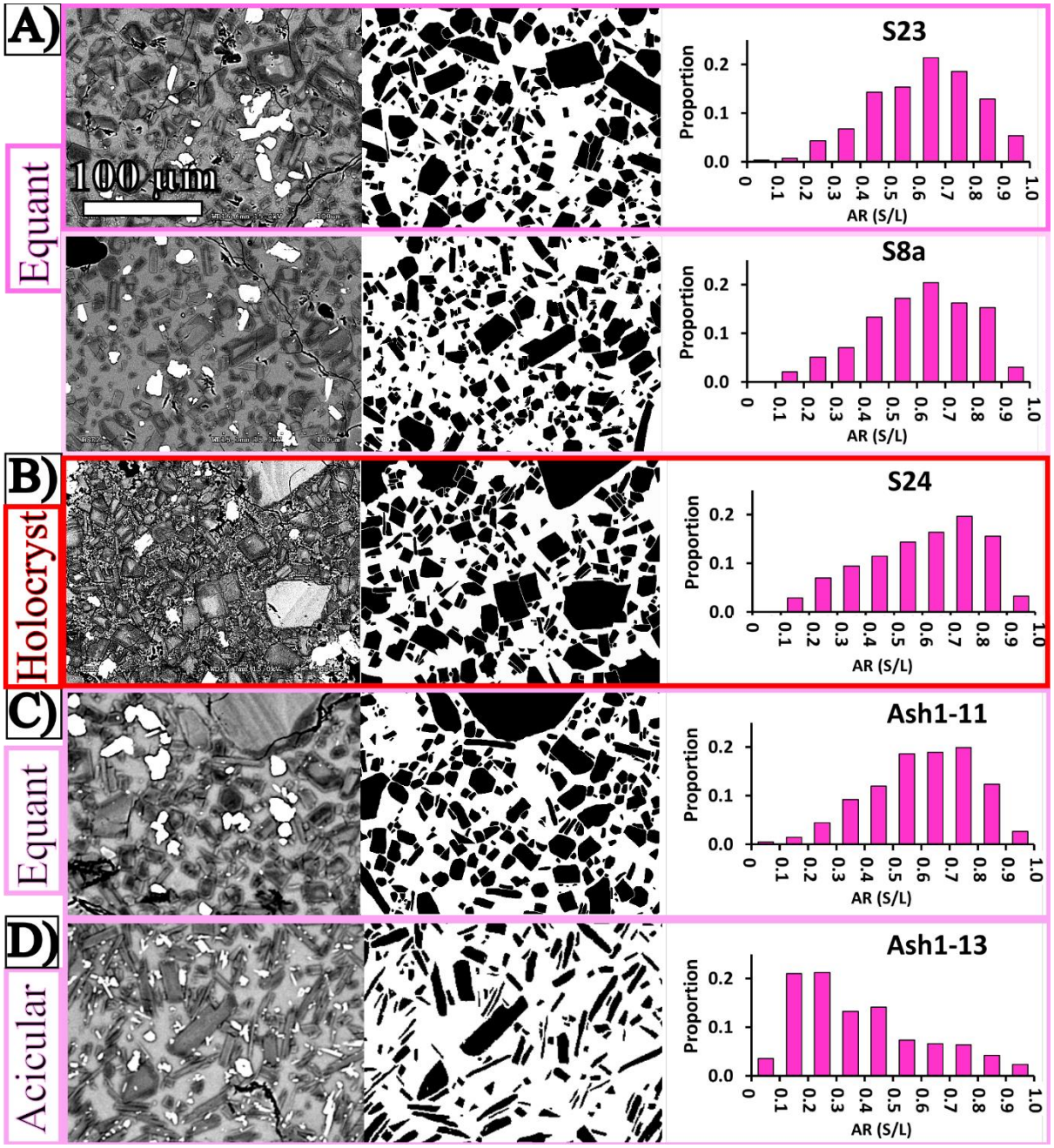

Figure 3.4. *BSE images and feldspar binary masks of block and ash samples collected from the 2013 BAF deposits of Volcán de Colima. Modes of crystal shapes (AR) (5 < Sn < 50µm) are displayed on the left of each sample frame. The samples shown are texturally grouped as* ***A)*** *Equant (block samples),* ***B)*** *Holocrystalline (block sample),* ***C)*** *Equant (ash sample), and* ***D)*** *Acicular (ash sample). The white bars on the top image scales for 100µm and applies to all the BSE- and binary images included in the figure.*

3.3.3. Ash componentry

Composite images from the 2005 and 2013 BAFs were built for ash particles at sizes of 2 and 3 ϕ using ~ 300 individual BSE images taken at 15 kV, at a working distance of 13 mm and magnifications of 300x and 500x. Subsequent point counting was performed for each sample to estimate the proportion of the different textural components. Between 400 and 1000 points were counted using the JMicrovision platform. For point counting, I assigned the same classes based on the same textural classifications as for the block components: Acicular, Equant, Bimodal and Holocrystalline (**Fig. 3.5C** and **Table 3.3**), with only the addition of Phenocryst shards that exclusively applies to ash. Since my purpose is to analyse the crystal groundmass textures, I also calculated the proportion of the textural components on a phenocryst-free basis (i.e., particles composed of only crystal shards were subtracted).

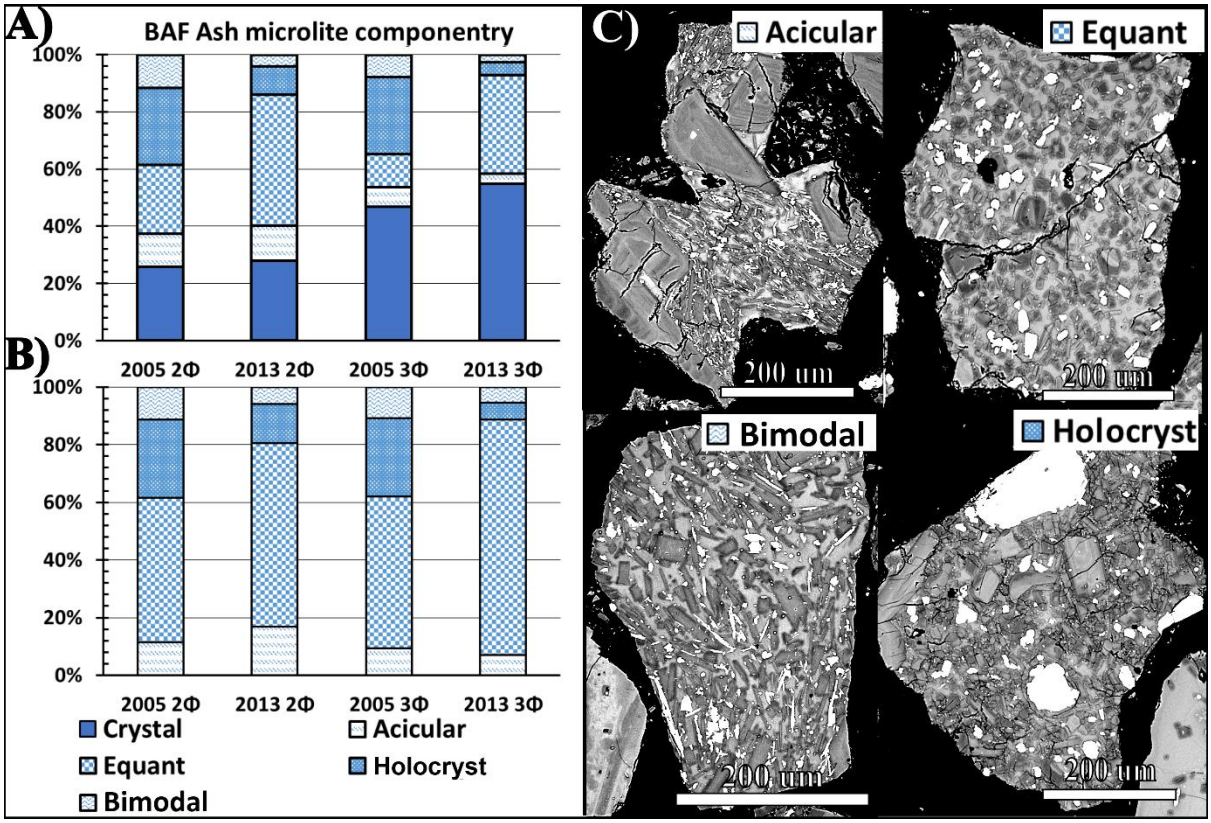

Figure 3.5. *Textural modes of BAF individual ash particles from the 2005 and 2013 events at two different sizes (2 and 3 ϕ) including (**A**) and excluding (**B**) particles composed entirely of a fragment of a broken phenocrysts. **C)** BSE images of individual ash particles are shown with the symbol assigned to each texture as an example.*

3.3.4 Feldspar chemistry

For chemical analysis of groundmass plagioclase crystals, I targeted four samples from three different eruption types associated with textural end-members in the suite of Volcán de Colima eruptive products analysed in this chapter and Chapter II. One is sample 1913 Pn, pumice from the 1913 sub-Plinian tephra fall deposit, containing very small, acicular crystals ($Sn_{AV.}$ = 2.9 µm, and $AR_{AV.}$ = 0.22) that show no compositionally distinct rims (**Table 3.2** in this chapter and **Fig. 2.4A** in Chapter II). The second is sample S1 from the 2004 lava flow, which is characteristic of long LFs (> 2km), has larger and slightly less elongated microlites than 1913Pn ($Sn_{AV.}$ = 4.6 µm, and $AR_{AV.}$ = 0.37, for crystals in Sample S1), without clearly compositionally distinct rims (**Table 3.2** in this chapter and **Fig. 2.4C** in Chapter II). Finally, samples S2 and S9 from the 2005 eruption were chosen to represent short (low VER; Chapter

II) LFs (< 1.2km) and lava domes. In contrast to the 1913 Pn (high VER) sample, crystals are large and equant in shape ($Sn_{AV.}$ = 6.2 µm, and $AR_{AV.}$ = 0.64, for crystals in sample S2), and there is an obvious contrast between rims (darker in BSE-images) and cores (lighter in BSE-images) (**Table 3.2** and **Fig. 3.3C**).

Feldspar compositions were analysed using an Electron Microbeam JEOL JXA8530F Hyperprobe. To achieve the best possible spatial resolution an accelerating voltage of 20kV was used, an intensity of 10 nA and a beam size of 1 µm. Na and K were analysed first, followed by major and then minor elements.

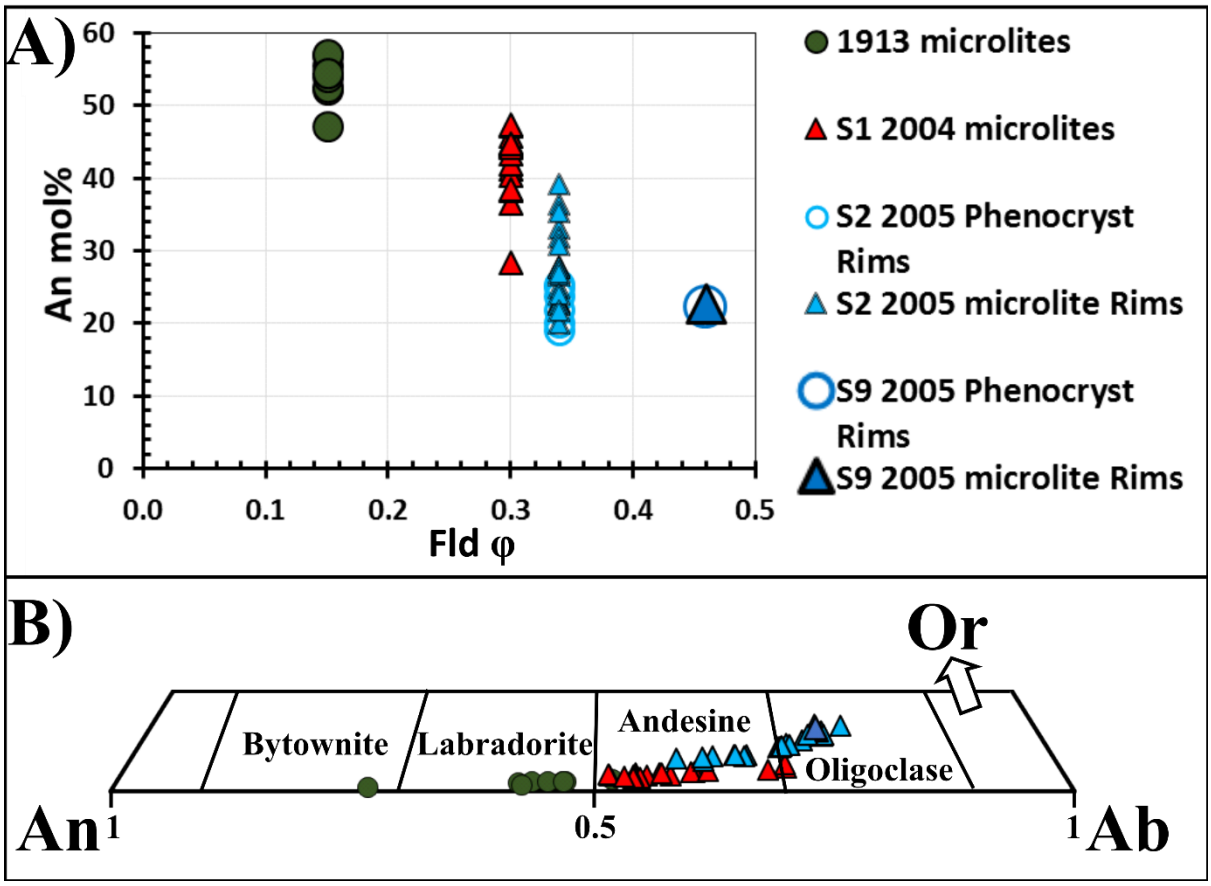

Figure 3.6. *Range of feldspar compositions in Pn (1913), LF (2004) and BAF (2005) samples.* ***A)*** *Anorthite content of individual microlites and phencoryst rims within individual samples of different eruptive styles in correlation with their respective feldspar φ.* ***B)*** *Microlite compositions projected on an An-Ab-Or ternary plot.*

3.3.5. Dimensional measurements of isolated crystal compositions

To assess the extent to which the development of an AbRim affected the final shapes of crystals, I isolated cores of all crystals within one BSE-image of sample S2 from the 2005 BAF subtracting the area of the AbRim to the area of the whole crystal for each crystal and then applied a Greyscale-An mol. % calibration for feldspar sizes $5 < Sn < 50$ µm.

3.4. Results

3.4.1. Groundmass textures in 2005 and 2013 BAF products

The groundmass crystal textures analysed in all of the products collected from the 2005 and 2013 unsteady eruptions fall within four different groups: Acicular, Equant, Bimodal, or Holocrystalline (refer to **Section 3.3.** Methodology and **Table 3.3** for details). From my sample suite, the ash-size populations of both eruptive events include the four textural groups previously listed (**Fig. 3.5**); the block-size group does not include all texture types (**Fig. 3.3** and **3.4**), but the number of samples analysed is too small to assess the textural modes of blocks.

The five analysed block-sized samples from the 2005 BAF have groundmass crystallinities (φ) of $0.33 \leq \varphi \leq 0.46$, which is at the high end of the range of φ for the whole suite of eruptive products of Volcán de Colima (**Table 3.2** in this chapter and **Table 2.4** in Chapter II). However, the individual samples are texturally diverse with substantial variation in N_A (6574 to 18364 mm^{-2}), $Sn_{AV.}$ (4.3 – 7 μm) and $AR_{AV.}$ (0.39 -0.64) (**Table 3.2, Fig. 3.3**; cf. **Table 2.4** in Chapter II). No quantitative textural analysis was performed for the BAF ash-fraction of the 2005 event. Sharp, more albitic rims on the equant feldspars of the 2005 samples are evident as dark rims in BSE-images (**Fig. 3.3B-C**).

Three blocks and four ash grains were analysed from the 2013 BAF; they cover a similar range in crystallinity and average aspect ratio as the 2005 sample set: $0.29 \leq \varphi \leq 0.5$ and $0.31 \leq AR_{AV.} \leq 0.62$ (**Table 3.2**). However, the number densities are generally lower and the average crystal size larger ($3850 \leq N_A \leq 7951$ mm^{-2}, 6.6 μm $\leq Sn_{AV.} \leq$ 8.8 μm) than the 2005 suite. Notably, the 2013 sample set includes the holocrystalline sample S24 (**Fig. 3.4C**), which if microlites of Sn < 2 μm were included, would have considerably higher φ and N_A, and lower $Sn_{AV.}$ (**Table 3.2** and **Fig. 3.7**). The feldspar crystals in most, but not all, of the 2013 samples have albitic rims with sharp boundaries (**Fig. 3.4**).

There are also both similarities and differences in the ash componentry of the 2005 and 2013 BAFs (**Fig. 3.5**). There is an increase in the abundance of crystal (phenocryst) shards with decreasing grain size (from 2ϕ to 3ϕ) in both 2005 and 2013 BAF ash (**Fig. 3.5A**). On a crystal-shard-free basis (**Fig. 3.5B**), ash particles from both BAFs are dominated by feldspar microlites of equant shapes (64 – 87 % PhC-shard-free basis). However, particles with acicular microlites represent the second most abundant class in the 2013 ash (7.5 – 17 %), whereas in the 2005 ash, the Acicular textures are at about the same proportion as the Bimodal (13-16 % and 15 – 16 % respectively). On the other hand, the holocrystalline textured particles are 37 % of the 2005 ash (in both 2ϕ and 3ϕ size fractions), making it the second most abundant class in 2005 ash, and by far more abundant than in the 2013 ash sample (6.4 – 14 %). In summary, there is considerable overlap in the 2005 and 2013 BAF sample sets, but the 2005 groundmass tends to have smaller, and more numerous crystals, and the ash fraction has a larger proportion of holocrystalline particles and a lower proportion of acicular-textured ash particles than the 2013 material (**Table 3.2**, **Fig. 3.3** and **Fig. 3.4**).

3.4.2. Groundmass textures in 2013 Vulcanian products

Considering the entire set of textural data available for the 2013 sequence, including my new BAF blocks and ash data, and the Vulcanian tephra (both dense and vesicular ash) and block lava sample data from *Cassidy et al. (2015)*, I observe a general similarity amongst the textures of all products, with the striking exception of the vesicular Vulcanian ash.

The groundmass of the vesicular Vulcanian ash samples is distinctive, not only in its relatively high bubble content but also the consistently low crystallinity ($0.1 \leq \varphi \leq 0.16$; for Sn < 50μm) (**Table 3.2, Fig. 3.7A** and **Fig. 3.8**). Other 2013 samples, including dense Vulcanian ash, have substantially higher crystallinities ($0.29 \leq \varphi \leq 0.5$) (**Table 3.2, Fig. 3.7A** and **Fig. 3.8**). Notably, the vesicular Vulcanian ash particles have similar or even lower crystallinities than the 1913 Plinian tephra (**Table 3.2, Fig. 3.7A**). Despite the difference in φ, the vesicular

and dense Vulcanian ash particles have similar ranges in N_A (5 - 15 x10^3 mm^{-2}); all other 2013 samples (BAF ash, BAF blocks, LF, ballistic) fall within a narrower N_A range of 4 - 8x10^3 mm^{-2} (**Table 3.2, Fig. 3.7A**). The microlites in the vesicular Vulcanian ash also have relatively low and consistent $AR_{AV.}$ ($0.3 \leq AR_{AV.} \leq 0.4$) compared to the dense ash which extend from $AR_{AV.}$ = 0.4 (the upper limit of the vesicular ash) to $AR_{AV.} > 0.6$ (**Table 3.2** and **Fig. 3.7B**). Some ash from the BAF has acicular crystals with the same $AR_{AV.}$ as the vesicular Vulcanian ash but all other samples are within the range of the dense Vulcanian ash (**Table 3.2** and **Fig. 3.7B**).

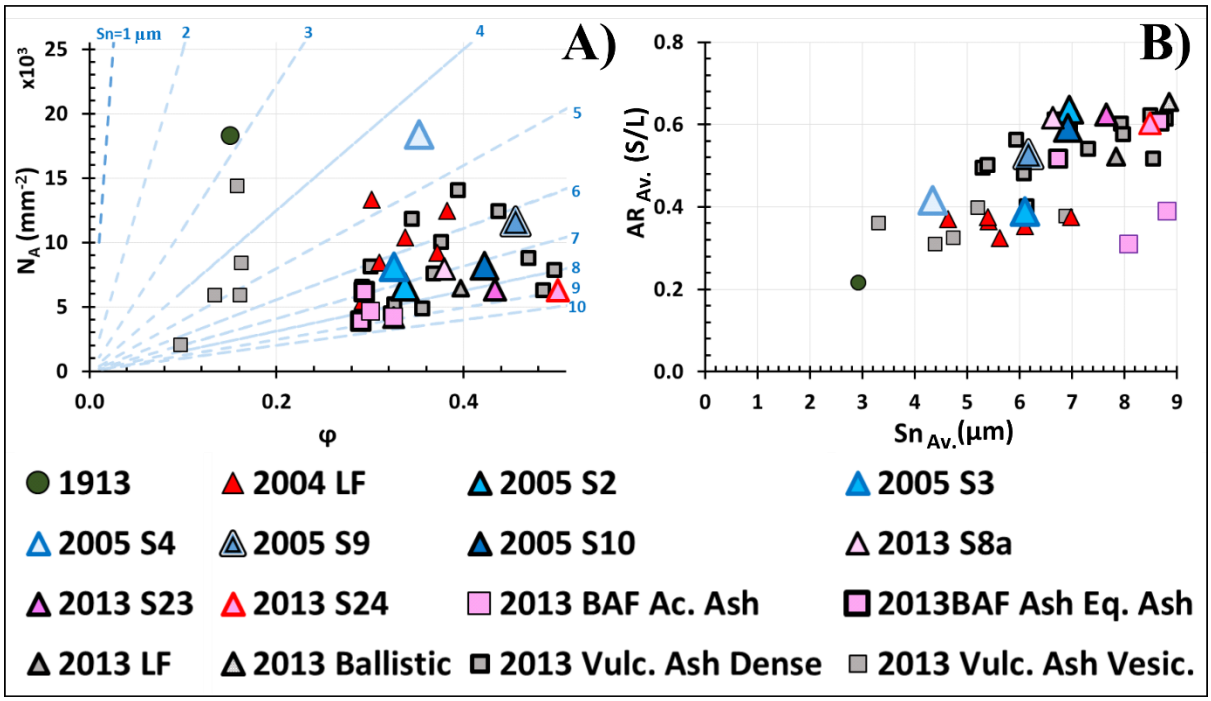

Figure 3.7. *Groundmass textural parameters of individual samples of Volcán de Colima eruptive products (for Sn < 50µm).* ***A)*** *Number density (N_A) versus crystallinity (φ), with contour lines indicating theoretical boundaries of crystal sizes constrained from the relation Sn= √ (φ/ N_A).* ***B)*** *Average aspect ratio (short/long axis, $AR_{AV.}$) versus average crystal size ($Sn_{AV.}$ = √crystal area). Grey-filled icons represent samples from the 2013 crisis as reported by Cassidy et al. (2015).*

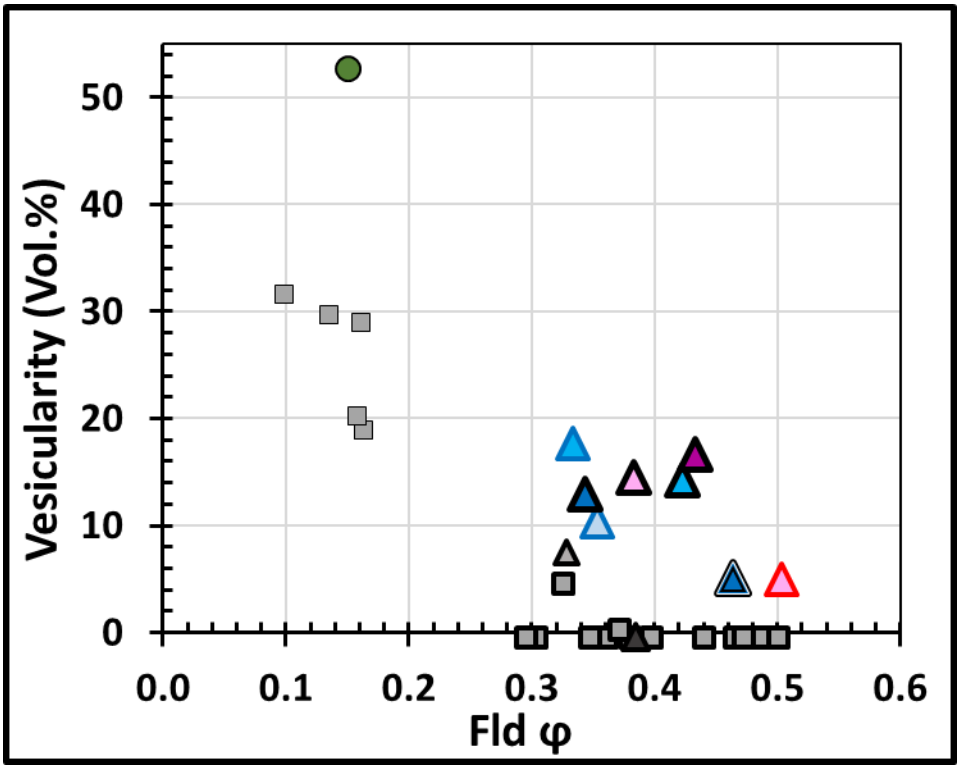

Figure 3.8. *Sample vesicularity versus groundmass feldspar crystal fraction for samples derived from the 2005 and 2013 Vulcanian eruptive sequences at Volcán de Colima. See **Fig. 3.7** for symbols.*

3.4.3. Textural trends

Two main trends can be observed between $Sn_{AV.}$ and $AR_{AV.}$ in the whole sample set of Volcán de Colima analysed in this chapter: 1) a positive correlation between $Sn_{AV.}$ and $AR_{AV.}$ (increasing $AR_{AV.}$ with increasing $Sn_{AV.}$, **Fig. 3.7B**), with some of the 2013 products at the high end of this trend (LF, BAF equant ash, BAF holocrystalline block and dense Vulcanian ash), and 2) an increase in crystal size maintaining a constant $AR_{AV.}$, where the acicular BAF ash (2013 BAF Ac. Ash) is at the large $Sn_{AV.}$ end-member (**Fig. 3.7B**). The 2013 vesicular Vulcanian ash data also fit the second (~ constant $AR_{AV.}$) trend, and surprisingly fall mostly within the same $AR_{AV.}$ range as the 2004 LF and the 2005 acicular block samples (**Fig. 3.7B**). Importantly, the feldspars in samples forming the first trend (increasing $AR_{AV.}$ with increasing $Sn_{AV.}$) have sharp, albitic rims, whereas the crystals in the constant $AR_{AV.}$ trend lack the distinct rims (**Fig. 3.7B**).

3.4.4. Plagioclase compositions

Feldspar compositions were measured in samples that originated from events of different intensities and eruptive styles (**Fig. 3.6)**. Here, I compare the composition of the darker rims of S2 and S9 from the 2005 BAF with other representative microlites of products derived from different eruptive intensities and styles such as 1913 Pn and 2004 LF. In general, the plagioclase microlites in the 1913 Pn pumice are the most An-rich, followed by the 2004 lava flow and then the 2005 samples (**Fig. 3.6**). On average, the anorthite (An mol%) content of the microlites and phenocryst rims is inversely correlated with groundmass feldspar crystallinity (**Fig. 3.6A**). There is an overlap between the An compositions of microlites from the lava flow and some microlite and phenocryst rims from 2005 (sample S2), although the S2 plagioclases extend to more evolved compositions (**Fig. 3.6A-B.**). Some of the microlites from the 2004 lava flow are zoned with less evolved rim compositions. Because these microlites are rare in my samples, they are not representative in this study and are not shown in **Fig. 3.6**.

The distinctive rims on the microlites and phenocrysts in some 2005 samples (shown in **Fig. 3.4** and **3.5**) have the most evolved compositions (AbRim).

3.5. Discussion

In Chapter II, we observed a negative correlation between average Volumetric Eruption Rates (VER) and some groundmass textural parameters such as feldspar average shape ($AR_{AV.}$) and total groundmass crystallinity (φ_{Tot}) for steady eruptive events at Volcán de Colima (**Fig. 5** in this chapter and **Fig. 2.10** in Chapter II). However, some of the events included within the correlations between VER and the groundmass textures also show important scatter, suggesting that other factors, in addition to ascent rate, could have an important effect on late-stage crystallisation.

Total (feldspar + mafics) groundmass crystallinity showed a good correlation with average VER for a suite of steady eruptions of Volcán de Colima except for the 1961 event (**Fig. 3.1A** and **Table 2.5** in Chapter II). Two possible reasons for the misfit of the 1961 eruption are: 1) there were scarce observations on the development of the eruptions, that inherited uncertainty to the VER estimates, and 2) groundmass φ could have been affected by a slightly higher proportion of phenocrysts relative to other effusive events (**Fig.2.3** in Chapter II). Some studies have suggested that crystallization may occur around pre-ascent crystals as it is energetically more efficient delaying groundmass crystallization up to shallower levels in the conduit at an extent relative to the undercooling generated by the decompression rate (*Martel, 2012*, *Riker et al., 2015*). Textural proof of the latter process could be the presence of albitic rims around phenocrysts and microlites of this sample.

In Chapter II, I showed that crystal $AR_{AV.}$ displays a good fit to the average VER for effusive products but the trend does not extrapolate to high-intensity, explosive products (e.g. 1913 Pn, **Fig. 3.1B**); this is likely due to changes in crystal habits related to very high undercoolings that cannot be accurately quantified by using a best-fit ellipse measurement of AR (see **Appendix 2.4** in Chapter II for reference). For instance, some hopper and dentritic shapes were found for groundmass crystals in the 1818 and 1913 Pn samples analysed in

Chapter II (**Fig. 2.4 A-B**). The consistency of crystal $AR_{AV.}$ within effusive eruptions (e.g. the 2004 LF dataset in **Fig.2.6D** in Chapter II) indicates that it is mainly defined during magma ascent and that there is minimal post-eruptive alteration of AR. In general, crystal shape correlates with VER for effusive events such as lava flows and lava domes, remaining relatively constant within individual effusive sequences despite shifts in effusion rates during the eruptions (**Fig. 2.6** and **Fig. 2.9C** in Chapter II). Indeed, the 1961 eruption data are consistent with the $AR_{AV.}$ -VER trend based on other steady eruptions (**Fig. 3.1B**), despite having anomalously low φ (**Fig. 3.1A**); moreover, the presence of albitic rims in the 1961 sample is consistent with the lower VER inferred from $AR_{AV.}$ than inferred from φ.

Limitations in the correlation of groundmass φ or $AR_{AV.}$ and eruption intensity should be expected in Vulcanian eruptions given the diverse histories and ascent paths that magma can experience during ascent.

3.5.1. Growth patterns and textures associated with ascent paths

In Chapter II, I showed that $AR_{AV.}$ marks a clear division between the high-and intermediate-intensity eruptions and the low-intensity events. In this chapter, I also noted that an obvious difference between low- and high- intensity eruptions is the presence or lack of sharply contrasting rims of albitic composition in feldspars (AbRims), respectively (**Fig. 3.1**). In fact, when we compare crystal $AR_{AV.}$ and the presence of AbRims for all of my Volcán de Colima sample-set, we observe two different trends relative to crystal $Sn_{AV.}$ (**Fig. 3.9**.). Feldspar crystals with AbRims form a trend with $AR_{AV.}$ that increases with increasing Sn_{AV}, whereas crystals without development of obvious AbRims have relatively constant $AR_{AV.}$ with increasing $Sn_{AV.}$ (**Fig. 3.9**).

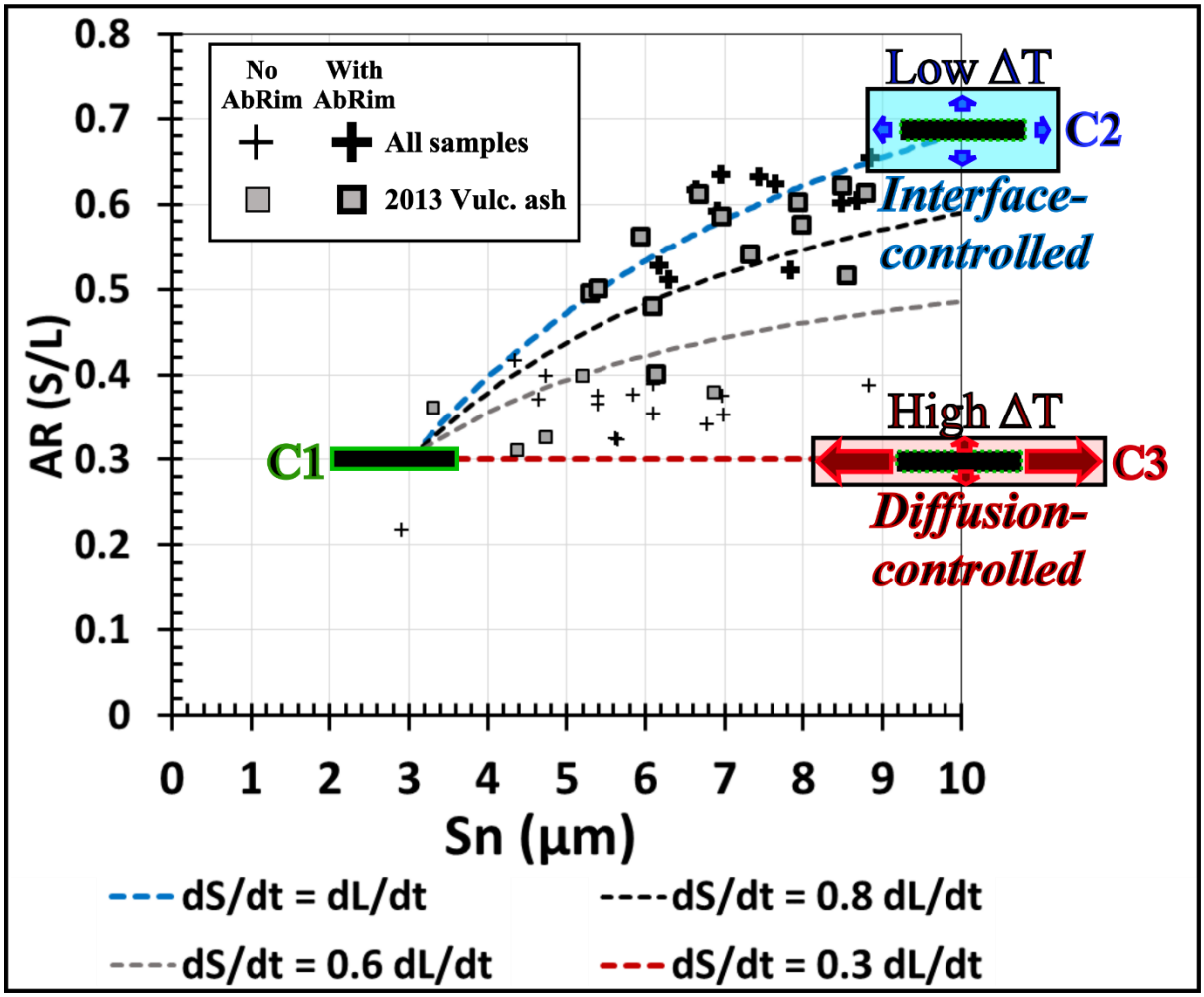

Figure 3.9. *Interface- and diffusion-controlled growth regimes (after Hammer, 2008) depicted with examples of hypothetical crystals. Each hypothetical crystal is located at an edge of modelled trends corresponding to different growth regimes. The hypothetical growth regimes are based in the change of the shorter crystal lattice (dS) over time (dt) relative to the change of the longer lattice (dL) in time. The hypothetical crystals are: initial crystal (C1, Sn= 3µm, AR=0.3), end member at dS/dt= dL/dt (C2, Sn= 10µm, AR=0.7), or end member at dS/dt= 0.3 dL/dt (C3, Sn= 10µm, AR=0.3). In the depiction, the trends followed by the two end-members represent an Interface-controlled regime (blue path with blue end-member sketched crystal) and a diffusion-controlled regime (red path with red end-member sketched crystal). The arrows inside the sketched crystals show the dominant growth of the crystal lattices. The average feldspar shapes ($AR_{AV.}$) and sizes ($Sn_{AV.}$) of Volcán de Colima samples are displayed as references based on **Figure 3.7B**, with thicker outlined symbols indicating that the feldspars in the corresponding samples have AbRims. The 2013 dense and vesicular Vulcanian ash samples appear with different symbols as only one BSE-image was where directly observed for each group so the presence of AbRims was not verified for all of them. Refer to **Table 3.1** for acronyms and abbreviations.*

Hammer (2008) described two crystal growth regimes that particularly affect crystal shape. The first regime is *interface-controlled* growth, during which slow attachment of compatible elements to the growing crystal phase are distributed throughout the surface of the crystal by the surrounding melt phase. The distribution of atoms around the surface of the growing crystal produces relatively equant crystals (i.e. AR close to 1, e.g. crystal C2 in **Fig. 3.9**). This growth regime is prevalent at lower degrees of undercooling (low ascent rates), which for the case of my samples can be associated with effusive events of low VER such as the 1961, 1975 N and 2013 LFs (**Fig.2.5** in Chapter II, **Fig. 3.1B** in this chapter).

In the second regime, *diffusion-controlled* growth, the attachment of compatible elements to the crystal is much faster than their mobility within the melt (*Hammer, 2008*). In this regime, the melt adjacent to the growing crystal gets depleted in compatible elements and saturates in incompatible elements; therefore, as corners or edges develop in the crystal, these sites will surpass the melt saturated in incompatible elements before the rest of the crystal and reach fresher melt, which promotes more unidirectional crystallisation (*Hammer, 2008*). This regime will produce crystals with elongated or complex shapes (low AR, e.g. crystal C3 in **Fig. 3.9**). This growth-regime dominates at larger degrees of undercooling over interface-controlled growth and is therefore characteristic of higher decompression/ascent rates such as the 2004, 1998, 1975S and 1989 LFs from my Volcán de Colima sample suite (**Fig.2.5** in Chapter II).

In **Figure 3.9** I illustrate hypothetical evolutions of crystals in magma batches of steady and unsteady eruptions based on crystal growth regimes and the textural trends of my sample set. The growth regimes presented in **Figure 3.9** are based in the change of the shorter crystal axis (S) over time (t) relative to the change of the longer lattice (L) in time. We start with a crystal C1 of Sn= 3μm and AR = 0.4, which corresponds to a 5.5 μm long axis (L= √(Area/AR)) and 1.6 μm short axis (S= L*AR). I then model the growth of the crystal for different ratios of

growth rates for the two axes (dS/dt ÷ dL/dt = dS/dL). For end-member interface-controlled growth, dS/dL =1; for progressively lower dS/dL values, growth is more diffusion-controlled.

Superimposing my Volcán de Colima dataset on these hypothetical AR vs Sn growth paths shows a striking association of crystals in the interface-controlled growth trend with the development of AbRims (**Fig. 3.9**). The association of AbRim with an interface-controlled growth (as well as higher φ values) suggests that these magma batches experienced more time crystallising at lower degrees of undercooling (i.e. low ascent rates) compared to samples along the more diffusion-controlled trend.

The hypothesis that AbRims are more important in interface growth regimes can be tested by measuring the relative areas of different plagioclase compositions in sample S2, a 2005 BAF block. **Figure 3.10B** shows that AbRims are ubiquitous on groundmass plagioclase, and that AbRims grow at a rate proportional to the core size, with larger (thicker) rims developing around larger crystal cores. This indicates that their final size is defined by the available crystal surface on which they crystallise rather than differences in kinetics of crystallisation. I applied further textural analysis to assess the shape ($AR_{AV.}$) versus size ($Sn_{AV.}$) of isolated groundmass crystal cores and the respective equivalents as whole crystals (i.e. adding the effects of the AbRim) in size (Sn) ranges of 5 μm (**Fig. 3.10C**). This comparison suggests relatively constant $AR_{AV.}$ between cores and entire groundmass crystals, with average differential slopes of 0.002 ($\sigma = 0.001$) for all the size ranges (**Fig. 3.10C**). The consistency of $AR_{AV.}$ suggests that: 1) all the crystals analysed grew at the same rate attaining similar AR, or 2) the overgrowth of albitic rims finally dictated crystal shape. Since AbRims grow proportional to an available surface area for crystallisation (**Fig. 3.10B)**, I prefer the interpretation of a relatively constant growth-rate of groundmass crystals from early (i.e. cores) to final (i.e. AbRims) stages of crystallisation.

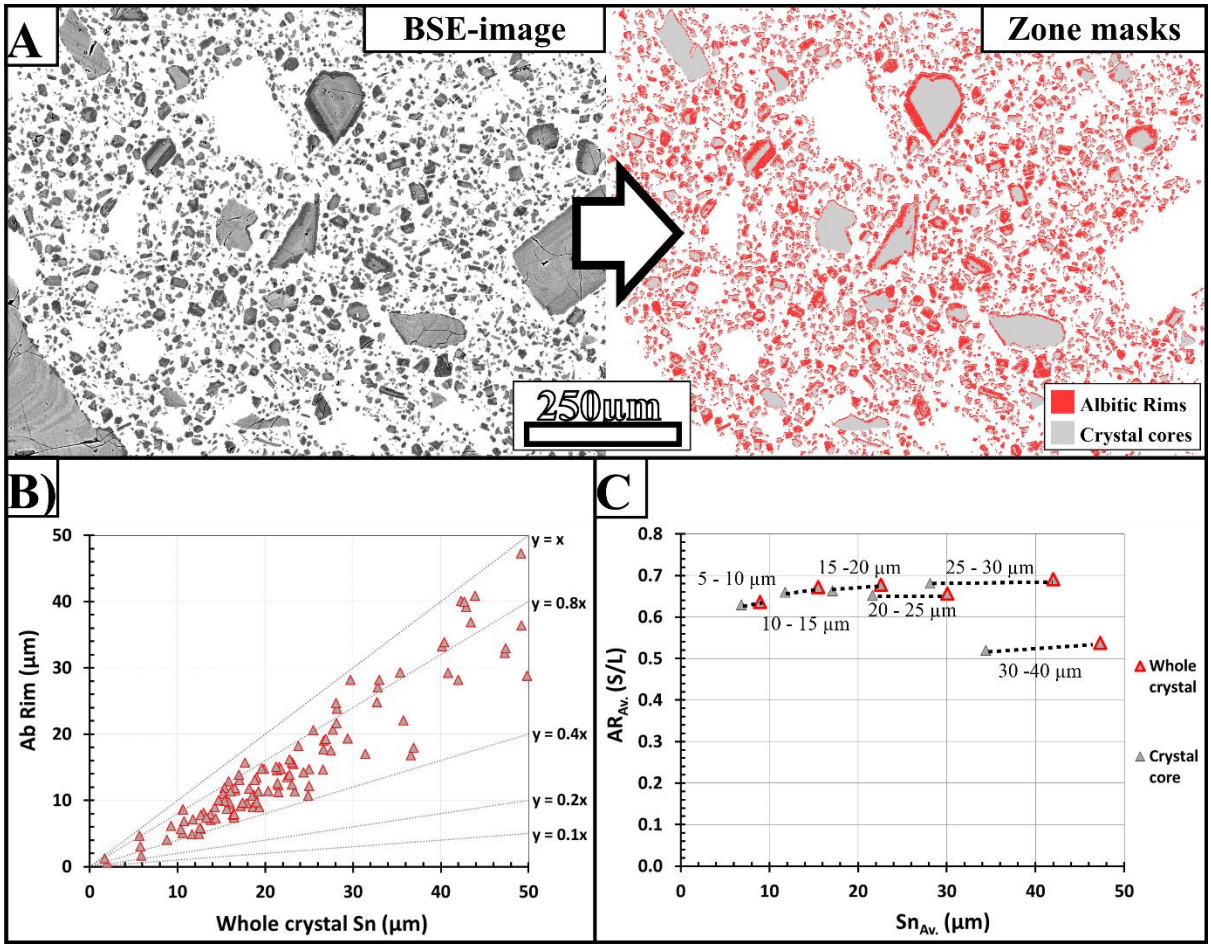

Figure 3.10. *Textural proportions of albitic rims in groundmass.* ***A)*** *Textural discrimination of individual crystal areas from BSE-images of a 2005 BAF block of Volcán de Colima.* ***B)*** *Proportion of AbRim and whole crystal sizes (Sn = √Area) of individual crystals. The grey, dashed-lines show different ratios of AbRim/ whole crystal. Most AbRims in the crystals analysed have a uniform thickness, meaning that they represent a perpendicular cut along one of the main growing axes.* ***C)*** *Shape distribution of crystals with and without the AbRim for a range of feldspar sizes based on the core Sn (size ranges indicated above the dotted lines). The dotted lines link cores and whole crystal data points that are associated and have slopes ranging between 0.0004 and 0.0033.*

Patterns of groundmass crystal growth provide insight into conditions of magma ascent. In silicic systems such as Volcán de Colima, the viscosity of magma increases dramatically with degassing. If magma is ascending slowly, it will have more time to devolatilise, and the resultant increase in melt viscosity and extensive crystallization could significantly decelerate or halt ascent particularly at shallow-isobaric conditions. Crystals developing in the shallow parts of the conduit will therefore grow under water-poor conditions, where diffusion of the

crystallizing components in the melt will be slower. At the same time, however, crystallisation will continue for as long as there is the chemical potential for it to proceed. The result of continuous crystallization at these conditions will be not only crystals with more equant shapes (high $AR_{AV.}$) growing in an interface-controlled regime, but also the development of a compositional contrast at the latest stages of crystallisation, to maintain chemical equilibrium with the surrounding melt. In the case of feldspars, the diffusion of Ca-Al becomes less efficient as the melt gets more viscous with lower H_2O wt.%, and instead it is replaced by smaller, compatible crystallising component that are more mobile at these highly devolatilised conditions: Na-Si (*Martel, 2012*). Also, protracted crystallisation changes the melt composition, making it richer in alkali components (**Supplementary material 2.3**, Chapter II). As a result, continuous crystallization at shallow depths and slow degrees of undercooling could generate the sharp, albitic rims around more An-rich cores in feldspars.

3.5.2. Textural correlations for different eruptive stages during the 2013 crisis

Recalling the general structure of a volcanic conduit between Vulcanian eruptions (e.g. *Clarke et al., 2007*), I place at the shallowest level, a dense, highly degassed, capping plug of magma. Below the dense plug, there is a gas-rich (vesicular) region where overpressure builds. Deeper in the conduit, the magma becomes richer in dissolved volatiles, with fewer gas bubbles. The physical conditions of each of these regions can be correlated with the associated crystal textures.

The dense cap of magma is formed from very slow ascent and substantial degassing in the shallowest portion of the magmatic column (*Cashman and Blundy, 2000* and *Melnik and Sparks, 2002*). The groundmass crystal features expected to develop in this region are: high φ, $Sn_{AV.}$ and $AR_{AV.}$, and low N_A. These textures are observed in the blocks and equant-textured ash collected from BAF deposits, as well as in the ballistic blocks and dense Vulcanian ash from the 2013 crisis (**Table 3.2, Fig. 3.4A, D** and **Fig. 3.7**). All these products also show highly

evolved matrix glass compositions and the presence of AbRims (**Supplementary material 2.1** in Chapter II and **Fig. 3.6.**). They likely represent parts of a shallow magma plug crystallising within an interface-controlled regime (e.g. **Fig. 3.9**).

In 2013, two different stages of very low effusion rates can be identified. The first one corresponds to the 2007-2011 lava dome (0.03 m^3/s, *Mueller et al., 2013*), which sat on the summit of Volcán de Colima until it was partially destroyed by the beginning of the Vulcanian stage in January 2013 (*Zobin et al., 2015*). The second stage is associated with the slow effusion of a lava dome that infilled the remnants of the former lava dome after individual Vulcanian explosions (*Zobin et al., 2015*). The 2007-2011 magma therefore had a much longer residence at shallow conditions than in the 2013 case; for this reason, I expect the products of the long-lived 2007-11 dome to be higher in φ, $Sn_{AV.}$ and $AR_{AV.}$ relative to those of the 2013 dome. A way to discern between both slow-ascent events using crystalline textures is useful given that the BAF deposits from which the samples were collected likely incorporated components of both domes.

Based on textures, samples S23 and S8a and some of the dense Vulcanian ash samples are likely associated with the 2007-2011 dome (high φ, $Sn_{AV.}$, $AR_{AV.}$; low N_A and surrounding AbRims) (**Table 3.2**, **Fig. 3.4D** and **Fig. 3.7**). Although S24 also shows characteristics of very slow ascent (**Table 3.2, Fig. 3.4C**, **Fig. 3.7** and **Supplementary material 3.3**), its holocrystalline nature indicates a more prolonged shallow storage than S23 and S8a, making it difficult to correlate with the primary crystallization processes in other samples from the 2013 crisis. Holocrystalline textures are also present in the BAF ash fraction (**Fig. 3.5**), which were likely incorporated from remnants of older domes or parts of the conduit walls that devitrified (continued crystallising) at very shallow conditions (~400m) for an extended period (*Cashman et al., 2008*; *Schipper et al., 2015*). Since samples S23 and S8a can be linked with the slow

effusion of the 2007-11 dome, I associated their average textural parameters with the average VER of this dome in Chapter II (called "2013 BAF" on **Fig.2.5**, **2.9** and **2.10** in Chapter II).

Samples associated with the shorter-lived 2013 dome could be the equant BAF ash and some of the dense Vulcanian ash samples (**Table 3.2.**, **Fig. 3.4A** and **Fig. 3.7**). Although similar to the 2007-11 products in feldspar $Sn_{AV.}$, $AR_{AV.}$ and in the presence of AbRims, these samples fall within the lower φ range for all samples analysed, excluding the Pn and vesicular Vulcanian ash samples (**Table 3.2**, **Fig. 3.4A** and **Fig. 3.7**). In particluar, the BAF ash component was dominated by equant ash particles (**Fig. 3.5**) meaning that the main BAF source likely derived from a dense, shallow plug.

It is hard to associate any of my samples to the postulated foamy region underneath the dense cap (e.g. **Fig. 3.2A**), since theoretically, groundmass in these samples should be high in N_A, and higher in vesicularity than the samples from the dense plug (*Clarke et al., 2007*). The previous textural associations could describe some of the Vulcanian ash samples, particularly those with high vesicularity and high N_A (**Fig. 3.7**, **Fig. 3.8** and **Supplementary material 3.1**).

The final textural associations in the 2013 sample-set relate to magma from the deep-conduit region. During the 2013 crisis, four Vulcanian eruptions were observed, with the final and most energetic one on the 29th of January (*Zobin et al., 2015*). The different magnitudes of these explosions suggest that magma was ejected from a range of conduit depths. I do not have data (e.g. matrix glass volatile contents) to infer specific depths for each sample; instead I qualitatively assess relative depths from textural ranges. The crystalline textures observed in samples directly derived from Vulcanian explosions (i.e. Vulcanian ash samples from *Cassidy et al., 2015*), mainly segregate by φ and $AR_{AV.}$ (**Fig. 3.7**). As previously discussed, the dense Vulcanian ash likely derived from the shallower portion of the conduit rather than from deeper. On the other hand, as mentioned above, the vesicular Vulcanian ash most likely corresponds to fragmented and ejected material from depth (e.g. **Fig. 3.2B**), since very low φ and low $AR_{AV.}$

suggest high ascent or replenishment rates (e.g. *Druitt et al., 2002*). The variation in N_A and $Sn_{AV.}$ within the vesicular ash samples would then be related to the degree of undercooling, that is the extent of time available for crystallisation before the melt quenched ($\Delta T/\Delta t$). A shorter time available for volatile degassing from the melt would also be reflected in magma quenching with a lot of bubbles (vesicular). Therefore, lower φ, N_A, $Sn_{AV.}$ and high vesicularity suggest that the sample was fragmented deeper in the conduit and was erupted and quenched fast enough to minimise crystallisation.

I also propose that acicular ash samples from the BAF are from relatively deep in the conduit (**Table 3.2**, **Fig. 3.4B** and **Fig. 3.7**). The BAF acicular ash and the vesicular ash from the Vulcanian events share a common $AR_{AV.}$ but differ in other parameters: BAF acicular ash has lower N_A (4184-4605 mm^{-2}) and larger $Sn_{AV.}$ (8.1 - 8.8 μm) than the textural ranges of vesicular ash (N_A, 2060 – 14393 mm^{-2} and $Sn_{AV.}$, 4 – 6.4 μm) (**Table 3.2**, **Fig. 3.7**). The textural distinctions between the BAF acicular ash and the vesicular Vulcanian ash indicate that although their source was the deep-conduit region, the BAF samples were probably represent fast replenishment of the conduit between Vulcanian explosions (e.g. **Fig. 3.2A**), rather than rapid syn-eruptive decompression and fragmentation (e.g. **Fig. 3.2B**).

After the explosive stage, a transition to effusive activity initiated the end of the 2013 Vulcanian sequence. The 2013 flow filled the crater and spilled over the west flank of the volcano (*Zobin et al., 2015*). Given the steady nature of this final event its groundmass textures can be directly associated with an average effusion rate of 0.27 m^3/s, as presented in Chapter II.

3.5.3. Estimates of eruptive dynamics from textures for the 2005 events.

In this final discussion, I associate groundmass textures in the 2005 BAF samples with different eruptive mechanisms based on the stratigraphic structure of a pre-eruptive Vulcanian conduit model in a similar way as it was developed for the 2013 event. I then use crystal textures associated with steady ascent to estimate VER values using textural fits in the same way as for eruptions in Chapter II.

Block samples S3 and S4 (**Fig. 3.3**) have textural features that suggest fast ascent, such as low φ and $AR_{AV.}$ (**Table 3.2** and **Fig. 3.7**). However, they differ in N_A and $Sn_{AV.}$: S4 shows N_A, $Sn_{AV.}$ and $AR_{AV.}$ closer to the 1913 Pn (i.e. very high eruption rate) sample, although φ is substantially higher and the vesicularity substantially lower than in the Pn Sample (**Table 3.2**, **Fig. 3.3A**, **3.7, 3.8** and **Supplementary Material 3.1**). The low φ, low $AR_{AV.}$ and lack of AbRims of S3 and S4 (**Fig. 3.7** and **3.8**) suggest crystallization due to rapid replenishment of the conduit (*Martel, 2012*) and diffusion-controlled growth. Since continuous replenishment stages followed by the effusion of short-lived domes were reported between explosions in 2005 (*Varley et al., 2010a*), these samples most likely crystallized from the deep-conduit region and ascended during a stage of rapid replenishment. The higher N_A and lower $Sn_{AV.}$ in S4 relative to S3 suggest that this sample likely ascended at a faster rate. Finally, φ of this group is not as low as in samples of the 2013 Vulcanian vesicular ash, and so are not considered to be a portion of deep-conduit material fragmented that quenched at depth during sudden decompression (**Table 3.2**, **Fig. 3.7**). I did not analyse Vulcanian ash from 2005 and therefore I can only compare 2005 products with the Vulcanian ash data from 2013.

Sample S9 has the highest φ of my 2005 sample suite and follows in N_A just below S4. However, two crystal populations of differing $Sn_{AV.}$ and $AR_{AV.}$ can be distinguished (**Fig. 3.3B** and **Supplementary material 3.3**), and therefore the two populations cannot be used to define a meaningful average for the whole crystal population. The AR and Sn microlite modes (**Fig.**

3.3B and **Supplementary material 3.3**) show two pulses of crystal growth in sample S9, one that can be associated with lower ascents (large, equant crystals) and a much faster one at volatile-rich melt conditions (smaller, acicular and more abundant crystals). Irregular overgrowths around some of the larger crystals are also consistent with a fast second growth pulse (**Fig. 3.3B**).

A final group includes S2 and S10, which clearly stand out from the rest of the samples in having the largest $Sn_{AV.}$ and $AR_{AV.}$, but with φ and N_A falling within the range of the rest of the samples. These textures and the obvious presence of AbRims suggest slow ascent and shallow residence times that favoured interface-controlled growth; these samples thus likely correspond to a long-lived pre-explosive stage that built the first plug that was destroyed at the onset of the Vulcanian crisis.

These interpretations regarding the origins of my 2005 block samples indicate that, in contrast to the 2013 sample set, all the 2005 samples that I analysed likely crystallised during ascent rather than being transported from depth during the Vulcanian explosion. Whereas the acicular group likely crystallised during fast intra-explosive conduit replenishing stages with little to no dwelling times (S3 and S4, **Fig. 3.3A**), S2 and S10 experienced slow ascent likely followed by a stationary stage at shallow conditions (**Fig. 3.3C**), probably before the onset of the 2005 crisis. The history of S9 is more complex, likely involving different steps of ascent and stagnation in the conduit where it developed a bimodal crystal population (**Fig. 3.3B** and **Supplementary material 3.3**), therefore making it impossible to correlate it with a unique ascent rate. None of my 2005 block samples are holocrystalline, indicating that these did not remain static for long enough to devitrify, although the sample set is too small to be representative. Finally, the dominant groundmass crystal texture in the BAF ash fraction is the equant shapes as in 2013 (**Fig. 3.5**), indicating that the main input source for PDCs was from shallow, dense regions of magma.

2005 shows more diversity in groundmass textures than 2013, not just in a higher relative particle content of holocrystalline and bimodal-size crystal populations, but also in more abundant, acicular textures (**Fig. 3.5**). This textural diversity could reflect a more prolonged period of eruptions and a broader range in magnitude and intensity of the individual explosive and effusive stages that comprised the 2005 crisis relative to 2013.

I can estimate individual VERs for the block samples associated with magma ascent (as opposed to downward-fragmentation) except for S9 (given its bimodal nature) fitting their crystal textures within the texture-VER correlations for Volcán de Colima products performed in Chapter II (**Fig. 3.11**). I estimated average VER (proportional to magma supply rates) based on the linear regression of φ_{Tot} for all events (including Pn) and $AR_{AV.}$ for all events (excluding Pn), given their good fits in the textural regressions to VER for Volcán de Colima samples (R^2 in **Table 2.5** of Chapter II and **Fig. 3.1A**).

Table 3.4. *Estimates of average VER (in a log scale) for different stages of Volcán de Colima eruptions using textural calibrations from reported VER values. Measured groundmass textural values from BSE-image analysis are displayed for individual samples from the 2005 BAF, 2004 lava flow (**Table 3.2**) and the 2013 Vulcanian ash (Cassidy et al., 2015), and averaged for estimations based on textural sample groups (**Fig. 3.3** for the 2005 grouping). Standard deviations are indicated in parenthesis for the different 2005 and 2013 textural groups. The equations used to perform the estimates correspond to the linear correlations of quantified groundmass textures and the calculations of physical parameters (**Table 2.5** in Chapter II).*

Event Year	Sample	φ_{Tot}	$AR_{AV.\ NoPn}$ (S/L)	VER φ_{Tot} ind.	VER φ_{Tot} group	VER $AR_{AV.}$ ind.	VER $AR_{AV.}$ group
2005	S2	0.45	0.64	-0.91	-1.20 (± 0.41)	-1.34	-1.19 (± 0.21)
	S10	0.48	0.59	-1.49		-1.04	
	S3	0.38	0.39	0.31	-0.07 (± 0.54)	0.42	0.32 (± 0.14)
	S4	0.42	0.42	-0.45		0.22	
	S9	0.52	0.53	-2.25	N/A	-0.58	N/A
2004	S1	0.38	0.37	0.36	N/A	0.55	N/A
	S5	0.40	0.32	0.03		0.88	
	S16	0.37	0.37	0.47		0.52	
	S04-01	0.40	0.37	-0.05		0.59	
	S04-03	0.45	0.38	-0.96		0.51	
	S04-05	0.45	0.35	-0.90		0.67	
2013	Dense Vulc. Ash	0.39	0.52	0.19	-0.82 (± 1.19)	-0.48	-0.70 (± 0.47)
		0.36	0.48	0.61		-0.22	
		0.44	0.62	-0.65		-1.24	
		0.48	0.40	-1.25		0.35	
		0.56	0.61	-2.72		-1.18	
		0.43	0.59	-0.54		-0.98	
		0.35	0.61	0.82		-1.16	
		0.42	0.60	-0.31		-1.09	
		0.42	0.50	-0.26		-0.33	
		0.54	0.58	-2.32		-0.91	
		0.40	0.50	0.02		-0.37	
		0.50	0.56	-1.71		-0.80	
		0.55	0.54	-2.54		-0.66	
	Vesicular Vulc. Ash	0.19	0.40	3.46	3.46 (± 0.76)	0.37	0.68 (± 0.26)
		0.13	0.38	4.57		0.51	
		0.25	0.31	2.44		1.00	
		0.20	0.36	3.26		0.63	
		0.19	0.33	3.57		0.89	

For the samples placed within the pre-crisis stage (S2 and S10), I estimate average VERs of 0.03 – 0.12 m^3/s ($10^{-1.5}$ – $10^{-0.9}$) based on φ_{Tot} and 0.05 – 0.09 m^3/s based on $AR_{AV.}$ ($10^{-1.3}$ – $10^{-1.0}$) (**Fig. 3.12** and **Table 3.4**). This VER range places them near the slower end of the VER spectrum of Volcán de Colima eruptions analysed in Chapter II (**Fig. 3.12**), which comprise lava domes or short lava flows (final length < 1170m) and, like S2 and S10, have AbRims (**Fig. 3.11**).

The VER estimates for samples S3 and S4 are between 0.35 and 2.06 m^3/s ($10^{-0.5}$ – $10^{0.3}$) using φ_{Tot} and 1.66 to 2.62 m^3/s ($10^{0.2}$ – $10^{0.4}$) using $AR_{AV.}$ (**Fig. 3.1** and **Table 3.4**). The $AR_{AV.}$-derived eruptive intensities for the 2005 acicular block samples (1.2. – 4.6 or $10^{0.08}$ – $10^{0.66}$) fall within the range reported for domes observed extruding in the crater between the explosive stages of the crisis (*Varley et al., 2010b*), supporting my suggested textural interpretation that these samples correspond to a fast replenishment stage (**Fig. 3.12**). This final observation indicates again that when ascent rates are not very high, and crystals develop more complex shapes, $AR_{AV.}$ has the best correlation with average VER amongst the textural parameters that I analysed for steady magma ascents.

The robustness of the textural parameters used to estimate average ascent/eruption rates is verified using individual samples of the 2004 LF and the 2013 Vulcanian ash samples. **Figure 3.12** shows the average reported VER and the maximum effusion rate for the 2004 effusive sequence. VER values for the individual 2004 samples, from fits to φ_{Tot}, place most samples at lower eruptive rates than the average, some even within the low ranges where we would expect the development of AbRims (which I do not see in the samples). VER estimates from $AR_{AV.}$, on the other hand, are closer the reported average VER value, and are below the maximum effusion rate reported for the 2004 sequence and correctly outside the AbRim VER range. The VER from $AR_{AV.}$ therefore, match the reported physical parameters of the eruption with the observed crystal textures better than VER from φ_{Tot}.

VER estimates from fits to $AR_{AV.}$ place the dense Vulcanian ash samples at the lower VER range, dominantly within the AbRim growth zone and therefore matching the observed AbRims (**Fig. 3.11**, **3.12**). The estimates for dense Vulcanian ash seem realistic when put into textural context with the whole eruptive suite using textural fits to AR_{AV}. The same cannot be said for vesicular ash, as this is in the same range as the 2004 LF samples. In reality, there is a significant difference in φ between the vesicular Vulcanian ash and the 2004 LF samples, with the φ of the ash samples closer to the 1913 Pn (**Fig. 3.7A, Fig. 3.8**). The φ of the vesicular ash samples suggests that they crystallised at high enough ascent rates that $AR_{AV.}$ is no longer the most reliable parameter to use for VER constraints (as for the case of Pn eruptions; Chapter II). This explains the larger VER determined using the fit to φ_{Tot}, which suggests VERs that are similar to Plinian eruptions (**Fig. 3.12**). In contrast, using φ_{Tot} places VER estimates for the dense ash samples are intermediate values and out of the AbRim zone (**Fig. 3.12**). Although I cannot confirm the presence/lack of AbRims for some of the Vulcanian ash samples (given the limited number of images in *Cassidy et al., 2015*), I can correlate their $AR_{AV.}$ following the trends observed in **Figures 3.7** and **3.9** and therefore suggest that the VER estimates using $AR_{AV.}$ are realistic (**Fig. 3.12**).

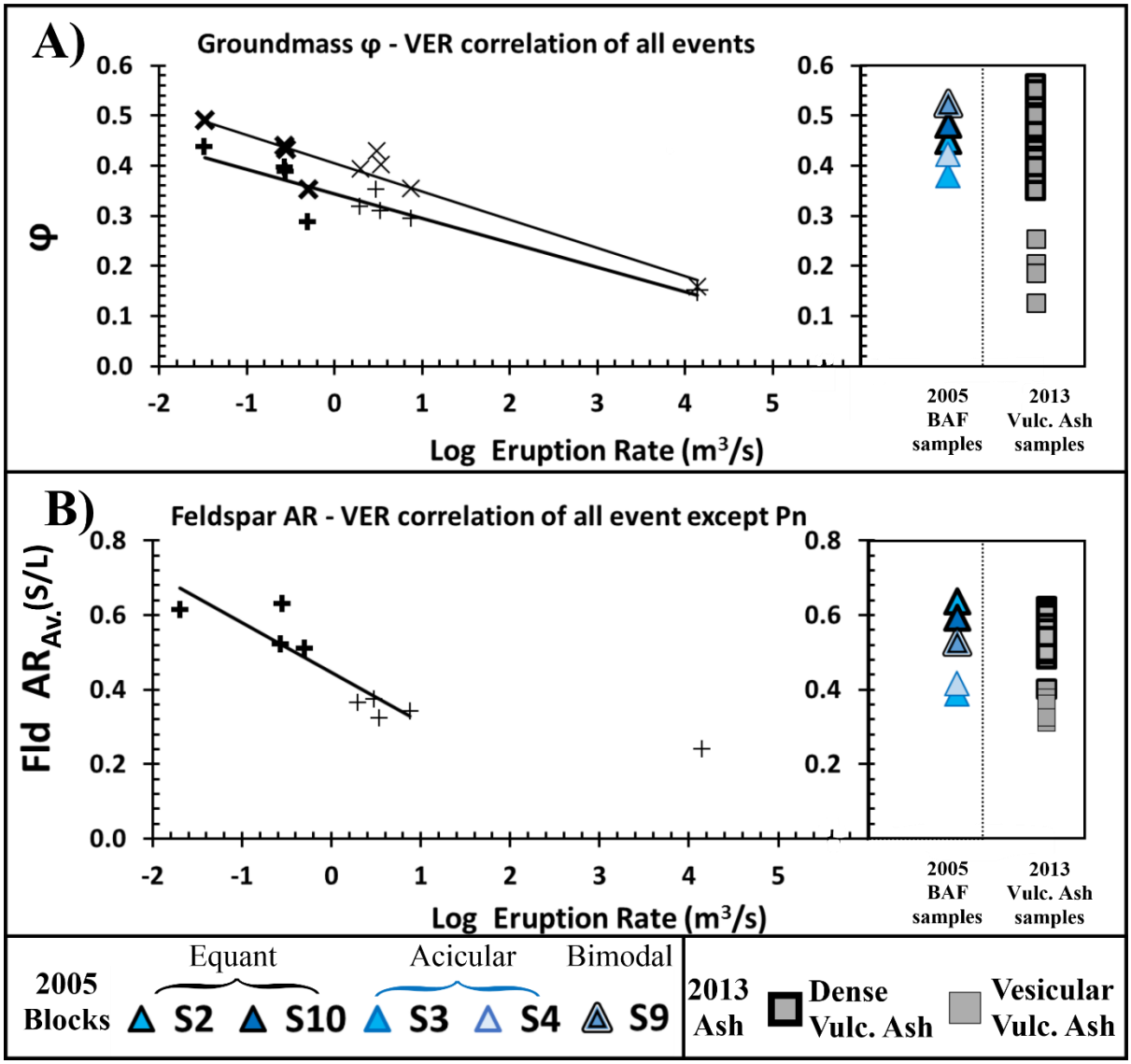

Figure 3.11. *Textural distribution of samples from the 2005 BAF and the 2013 Vulcanian explosions (only shown along the vertical axis – corresponding to the textural parameters - on the right side of both frames). The 2005 and 2013 textural ranges are contrasted to* ***A)*** *Total (feldspar + mafic) and feldspar φ -log. VER correlations for all events, and* ***B)*** *Feldspar $AR_{AV.}$ - log. VER correlation for all but the Pn event of Volcán de Colima. Refer to* ***Figure 3.1*** *for acronyms and abbreviations of the correlated events.*

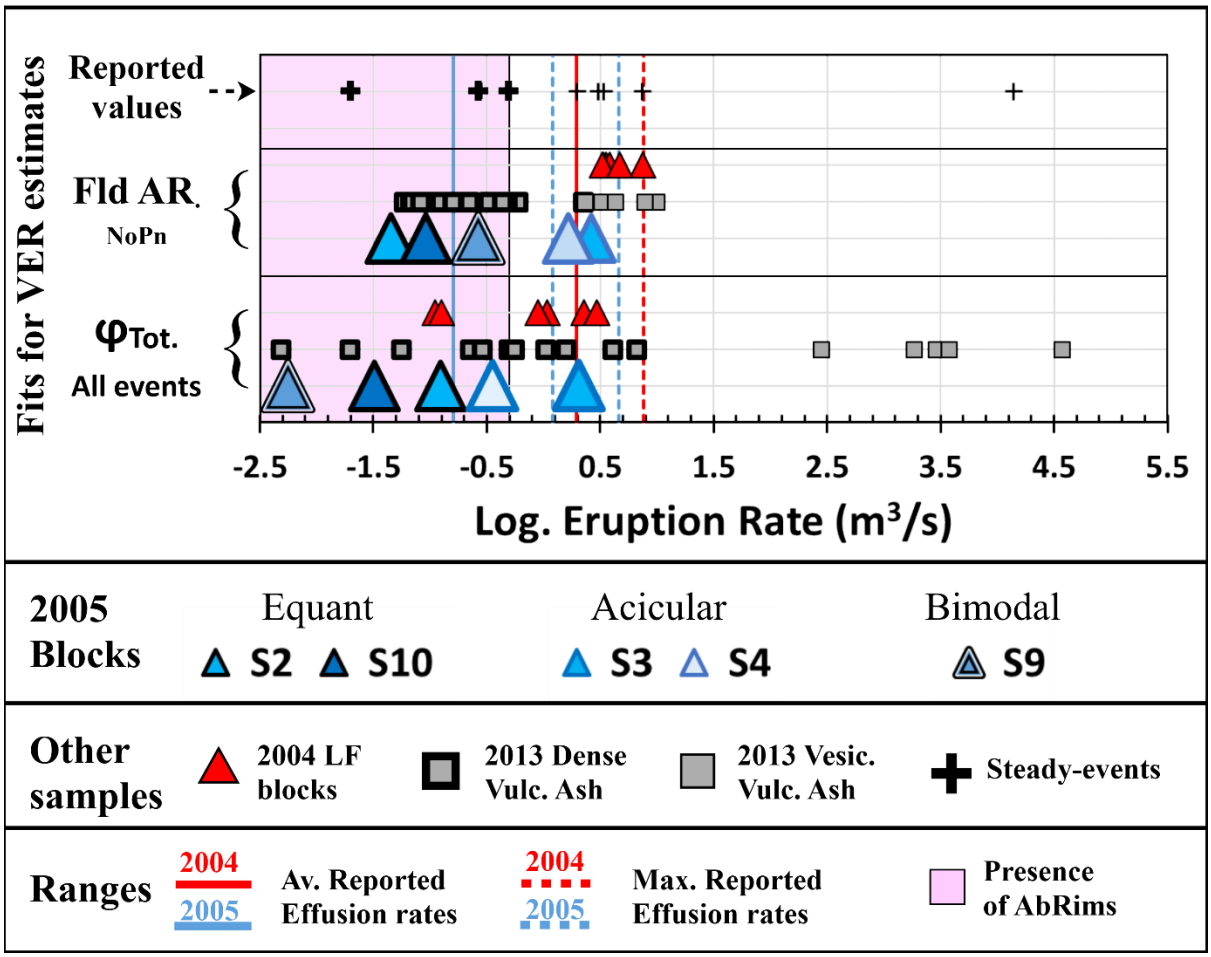

Figure 3.12. *Projections of eruptive intensities for 2005 BAF, 2004 LF and 2013 Vulcanian ash samples based on crystal groundmass textures (for Sn < 50µm). In the figure, only the VER estimates are projected (along the horizontal axis) without any projections for textural values (no values along the vertical axis), therefore the labels on the left side are just to indicate what VER values are projected based on textural estimates indicated in* **Table 3.4***. The VER estimates projected in the figure were made from the fits of correlation equations to the logarithm of reported VER of individual events for 1) Total φ (fld + maf) of all events (label φ Tot.$_{All}$ events), and 2) AR$_{AV.}$ of all events but the sub-Plinian eruption (AR$_{AV.}$ NoPn). The 2005 block samples are displayed grouped by their dominant textural feature (i.e. equant, vesicular and bimodal). Average reported VER values (based on deposit volumes and eruption durations) for a suite of Volcán de Colima Steady events (studied in Chapter II) are included for reference at the top of the figure. Ranges of eruption rates reported for fast-growing domes between Vulcanian eruptions in 2005 (Varley et al., 2010a), average effusion rate in 2005 (Reubi et al., 2013), average VER for the 2004 effusive event and maximum VER reported during 2004 are indicated with vertical, coloured lines. The range of VER within which AbRims are observed is highlighted in pink.*

3.6. Conclusions

Some eruptions are mainly controlled by buoyant magma that rises driven by gas bubbles, eventually, this magma can either extrude gently out of the volcanic conduit as lava flows or domes, or reach a fragmentation front in the shallow conduit. When bubble-driven magma ascent is the main dynamic process controlling the mass output in an eruption, the eruption tends to occur in a sustained, quasi-steady fashion from a few hours to a few days (*Clarke et al., 2015*). Other process that can affect the output of mass in an eruption is a very rapid depressurisation of the conduit that leads to fast propagating downward fragmentation, excavation and ejection of mass that is driven by an abrupt pressure contrast between the suddenly exposed material in the conduit and the external atmospheric pressure (e.g. **Fig. 3.2B** ; *Clarke et al., 2015*). When downward fragmentation of magma in the conduit is the process behind the extrusive mass output the depletion of the system generally occurs much faster than what it takes for the conduit to replenish and the flux can no longer sustain and becomes unsteady (e.g., Vulcanian eruptions). It is important to discriminate between the conduit dynamics behind the extrusion of material during eruptions to perform more accurate interpretations of syn-eruptive processes using a textural-based analysis and its correlation to physical eruptive behaviours. In this chapter, I grouped eruptions of Volcán de Colima as "steady" (i.e. effusive and Sub-Plinian eruptions) and "unsteady" (i.e. Vulcanian) to interpret crystal textures on a more adequately basis for their respective syn-eruptive dynamics.

In Chapter II, I observed that samples derived from Vulcanian eruptions did not fit the texture-VER correlations presented for steady eruptions. This suggested that it was necessary to approach differently the unsteady conditions of Vulcanian eruptions. Therefore, in this chapter I evaluated and identified the eruptive mechanisms behind different stages of unsteady-(Vulcanian) eruptions at Volcán de Colima through batch textural parameters and other groundmass textural attributes in eruptive products. Average aspect ratio ($AR_{AV.}$), contrasted

with the presence or absence of albitic rims (AbRims) on feldspar crystals, revealed striking differences between the products of low-intensity and high-intensity eruptions (**Fig. 3.1**). Moreover, this AbRim- $AR_{AV.}$ association was used to discriminate samples that crystallised under an interface-controlled regime from those that crystallized under a diffusion-controlled regime (**Fig. 3.9**).

The batch crystal attributes and the compositional textures (i.e. AbRim) were used to identify and differentiate between two different dynamic processes taking place in the volcanic during Vulcanian eruptions. The first process corresponds to a stage of conduit (re)fill, which is controlled by conditions of bubble-driven magma ascent (**Fig. 3.2A**). For this reason, the crystal textures that result during this stage ultimately reflect the integrated conditions of decompression-induced crystallisation, just as it is the case at what I classified as steady-style eruptions. The second stage is the component that differentiates the Vulcanian eruption from the steady eruptions, when a fragmentation wave travels downwards through the conduit and ejects magma residing at different depths (**Fig. 3.2B**). The crystal textures of the latter eruptive stage reflect supersaturation conditions relative to the depths at which they were residing. The degree of supersaturation and the timescale available between the sudden exposure to atmospheric pressure at fragmentation and quenching affect the resulting textures. My data show that they impose the equivalent large $\Delta P_{H2O}/\Delta t$ observed in (sub)Plinian eruptions (**Fig. 3.11** and **Fig. 3.12**).

I estimated a VER value for eruptive products of the 2005 and 2013 Vulcanian sequences at Volcán de Colima fitting the textural parameters in the texture-VER regressions that I derived in Chapter II (**Table 3.4.**). The estimated VER for the different erupted products of the Vulcanian eruptions analysed suggest that: 1) the VER values derived from my linear regression of $AR_{AV.}$ - VER show good agreement with estimated VER values reported by *Varley et al. (2010a)* on the effusion of lava domes during the 2005 Vulcanian crisis (**Fig. 3.12**).

2) The presence or absence of AbRims in the groundmass feldspars in the 2005 and 2013 Vulcanian products analysed also matches adequately the VER range estimated for the different samples using my linear regression of $AR_{AV.}$ – VER. This is, the textural-VER regressions of samples with feldspars with AbRims yield VER values that correspond with the VER ranges where rims are observed in slow steady eruptions (**Fig. 3.11** and **3.12**). However, the VER values obtained using an $AR_{AV.}$ – VER regression for products associated with an intra-conduit fragmentation stage (e.g. vesicular Vulcanian ash), are much lower than can possibly be realistic (e.g. *Alidibirov and Dingwell, 1996*; *Clarke et al., 2015*); this is confirmed by the low φ (**Fig. 3.12**) and the high groundmass vesicularity of these samples (**Fig. 3.8** and **Supplementary material 3.1**). In the case of the VER regression estimates for the vesicular Vulcanian ash products, when I derive VER using the GM φ_{Tot} – VER regression, yield values correspond more realistically to high and very high intensities (~ $10^{2.5}$ – $10^{4.5}$ m^3/s, **Fig. 3.11**) than $AR_{AV.}$, near the range for sub-Plinian eruptions (**Fig. 3.11**), and in agreement with estimates experimentally and numerically constrained (*Clarke et al., 2015*).

In detail, the case-studies approached in this chapter confirm that $AR_{AV.}$ – VER regressions can be used to constrain VER of low to intermediate intensity processes (conduit refill), while φ_{Tot} works best for processes associated with high to very high decompression rates during Vulcanian explosions. However, there are also technical limitations to consider when constraining VER from $AR_{AV.}$ and φ_{Tot} measurements, including: (1) Complex crystal shapes (e.g. hopper, dentritic) developed at high $\Delta P_{H2O}/\Delta t$ can affect 2D $AR_{AV.}$ interpretations, and (2) syn-eruptive crystallisation of phenocrysts at low-intensity eruptions could reduce groundmass φ_{Tot} (Chapter IV).

In summary, my results suggest that late-stage crystal textures can be used to reconstruct eruptive conditions of poorly-observed events. This approach is most effective when different batch attributes are integrated (e.g. AR and φ), and when other textural factors

are considered; these include the presence/lack of AbRims (**Fig. 3.1**, **3.11** and **3.12**), matrix vesicularity (**Fig. 3.8** and **Supplementary material 3.1**) and potential overgrowth (φ of overgrowth) on phenocrysts (Chapter IV). Integrated textural assessments are particularly useful for interpreting different stages in unsteady eruptive sequences, where magma decompression paths are not smooth and cannot be easily inferred from other deposit characteristics.

3.7. Supplementary material

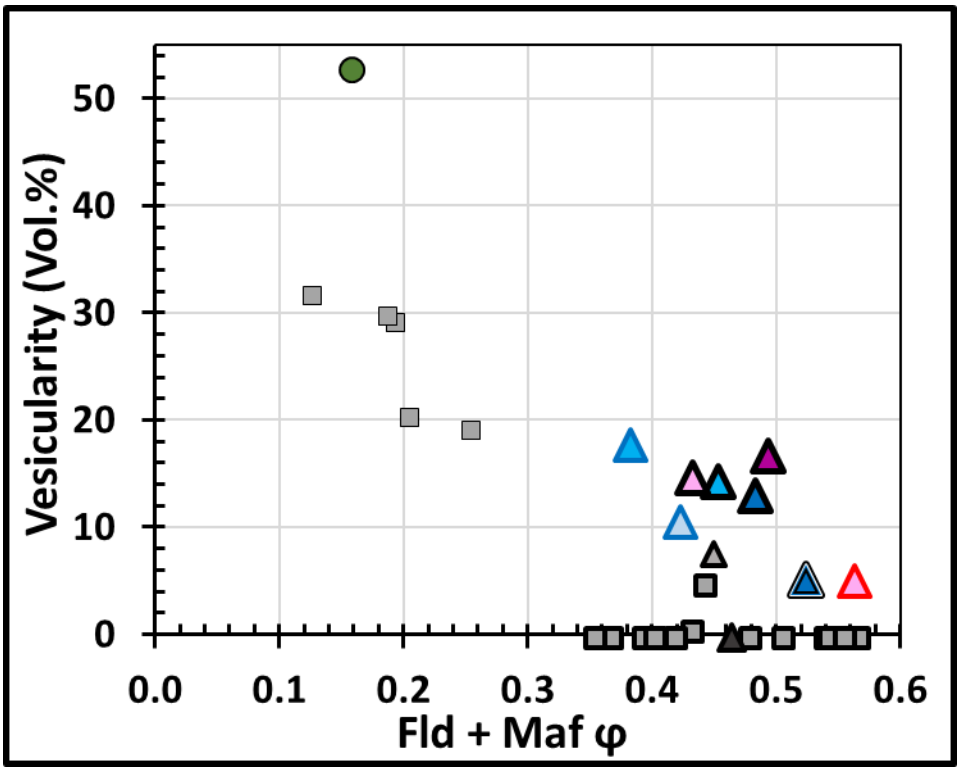

Supplementary material 3.1. *Sample vesicularity versus total (feldspar + mafics) groundmass crystal fraction for samples derived from the 2005 and 2013 Vulcanian eruptive sequences at Volcán de Colima. See* ***Fig. 3.7*** *for symbols.*

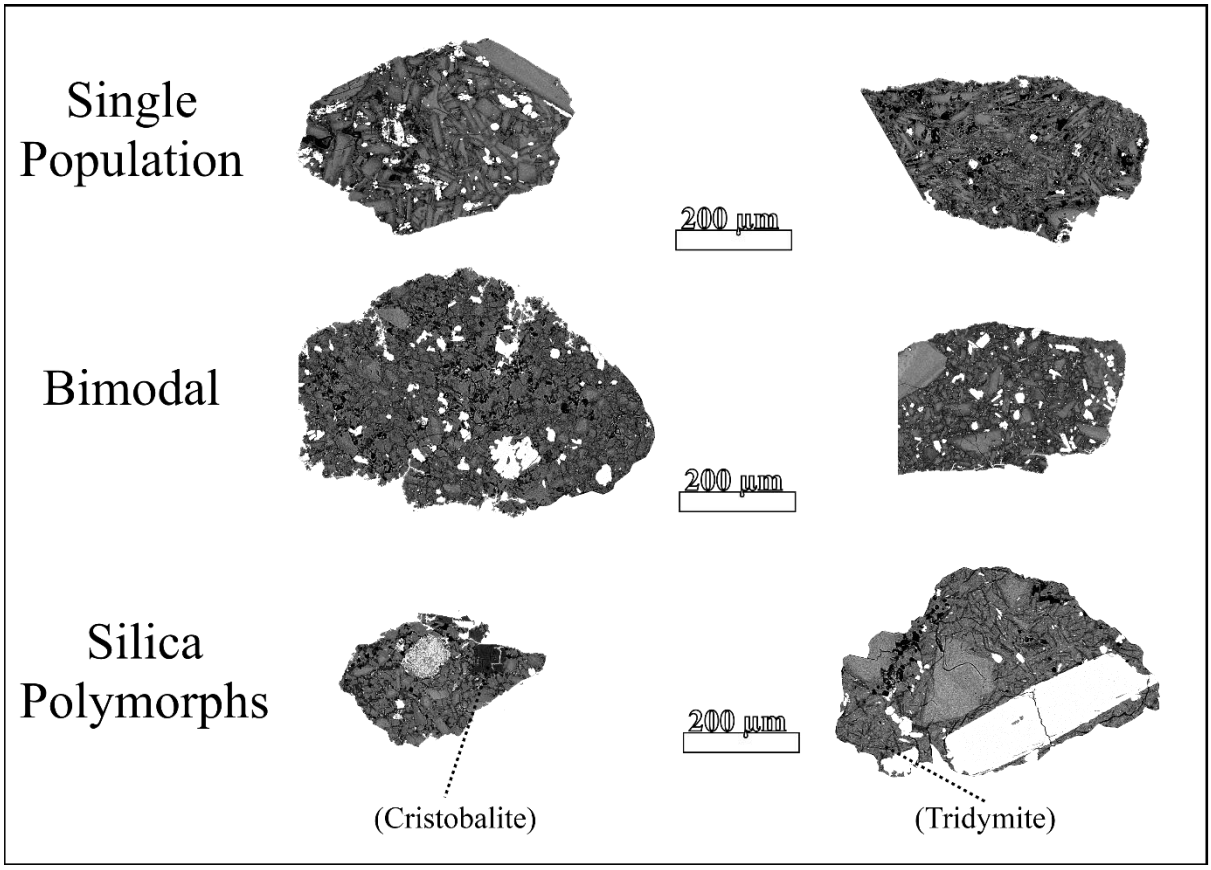

Supplementary material 3.2. *Types of holocrystalline textures found in BAF samples. Single Population textures consist of groundmass composed fully of crystals with similar textural characteristics. Bimodal holocrystalline textures have commonly a population of large crystals and very small contrasting crystals filling the rest of the groundmass. Some holocrystalline particles devitrified silica polymorph minerals as Cristobalite and Tridymite.*

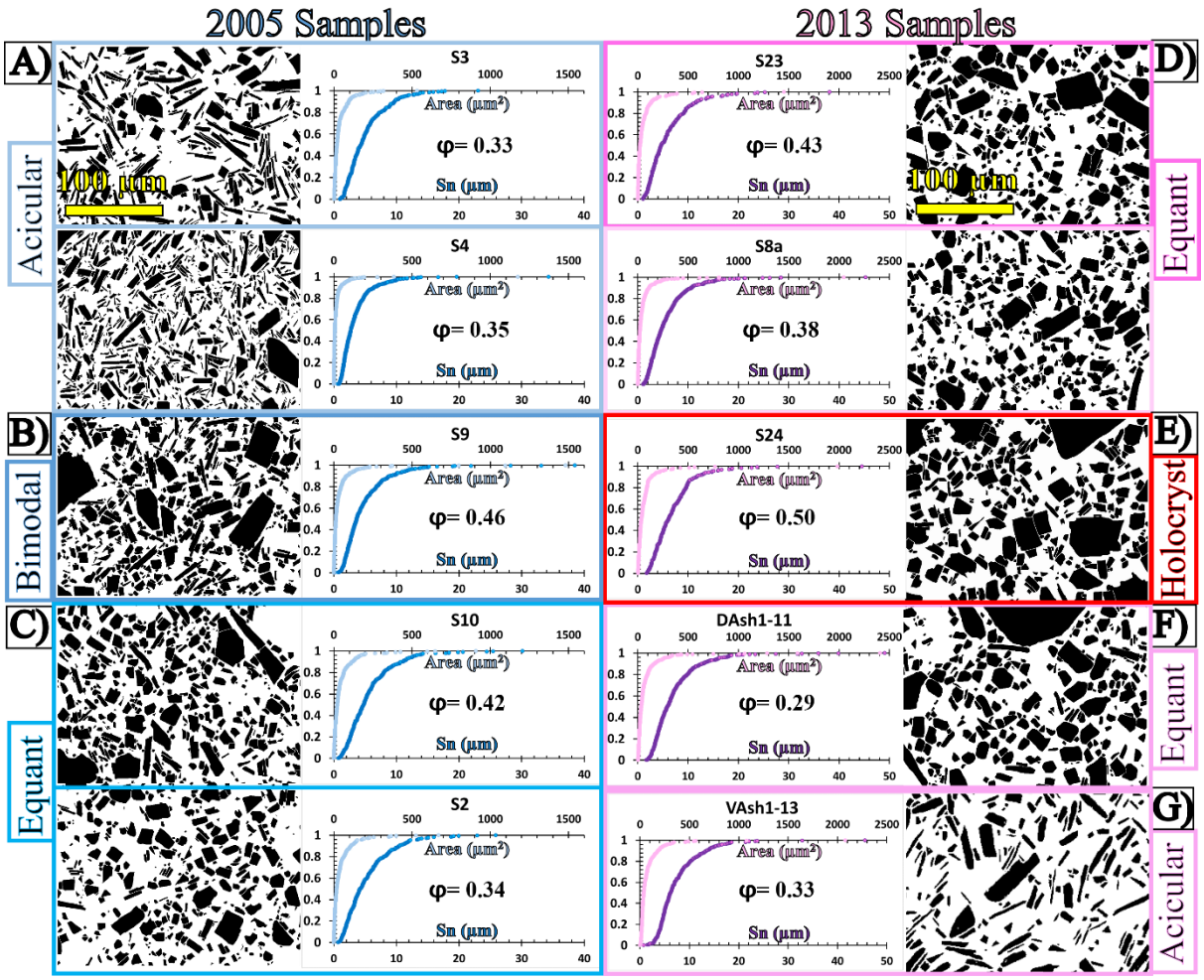

Supplementary material 3.3. *Cumulative size (dark-shaded) and area (light-shaded) distributions of microlites (Sn < 50µm) in BAF samples from the 2005 and 2013 Vulcanian eruptions. Next to each plot is the binary image of the feldspar crystals from which the distributions were made.*

Chapter 4

The extent of syn-eruptive growth on pre-existing crystals and its effects on groundmass textures

Author contribution and declaration: I processed and analysed the textural and chemical data. A. C. Rust and K. V. Cashman provided supervision, advice, and edits during the writing. B. Buse and S. Kearns delivered the guidance and advice pertinent to BSE-imaging and microprobe analysis and processing of chemical data. L. Roberts assisted with BSE image processing.

Abstract

Syn-eruptive crystallisation generates groundmass crystals and overgrowth rims on pre-existing crystals. Despite this, most textural studies on late-stage crystallisation are mainly directed towards the study of the smaller range of crystals (microlites), ignoring the phenocrysts. I expand crystal textural analysis from groundmass crystals to microphenocrysts and phenocrysts in products of Volcán de Colima covering different eruptive intensities and styles. The integrated crystal-size (groundmass + phenocryst) cumulative number density and area distributions for the 1913 sub-Plinian, 2004 lava flow and 2005 block-and-ash events suggest that, as a whole, more extensive crystallisation takes place in low-intensity eruptions. Also, larger maximum crystal sizes in both groundmass and phenocrysts populations develop in lower intensities and therefore, the microlite-phenocryst boundary depends on intensity. Identification of compositional features in crystals that most likely relate to syn-ascent crystallisation suggests that uninterrupted oscillatory zoning and, certainly, albitic rims crystallise during the eruption. This case study demonstrates that integrated textural analyses of all crystal sizes are necessary to produce accurate estimates of the total syn-eruptive crystallisation, which has significant implications for both modelling the late-stage rheological properties of magma that ultimately control eruptive behaviour.

Keywords: Phenocryst overgrowth, microlites, crystal size distribution, albitic rims, zoning, Volcán de Colima

4.1. Introduction

Magma ascent rate and eruption dynamics can be constrained using crystal textures in eruption products. Textural investigations have generally focussed on groundmass (i.e. microlite) crystallisation, without considering how syn-eruptive crystallisation of overgrowth rims on pre-existing crystals affects groundmass textures, despite recognised growth on microphenocrysts and phenocrysts (*Cashman, 1998; Martel and Schmidt, 2003; Riker et al., 2015*). Indeed, experiments by *Riker et al. (2015)* showed that decompression of volatile-saturated rhyodacite caused crystallisation on pre-existing crystals that accounted for ~25 - 50 vol.% of the total decompression-induced crystal volume increase.

In Chapter II, I showed that $AR_{AV.}$ of plagioclase in samples derived from a set of recent steady effusive eruptions of Volcán de Colima has a linear correlation with the log VER of the respective events (**Table 2.5**, **Fig.2.9**, Chapter II). However, I also showed in Chapter II that the same plagioclase $AR_{AV.}$ – VER correlation of products derived from high-intensity eruptions such as sub-Plinian events does not show a clear relationship (**Table 2.5**, **Fig.2.9**, Chapter II). Conversely, φ was the textural attribute that demonstrated the best association to log VER for the whole sample set, including the one well-constrained sub-Plinian event (**Table 2.5**, **Fig. 2.10**, Chapter II). φ is also more often used to quantify and infer decompression and ascent rates in natural samples. In spite of this, in Chapter II I show that φ is more susceptible than $AR_{AV.}$ with changes in effusion rate during the development of an effusive event (e.g. **Fig.2.6** in Chapter II) and therefore, it could be less accurate to calculate the average conditions of ascent from φ.

Unsteady eruptions, such as Vulcanian eruptions, have a higher natural variability of ascent kinetics and therefore crystal textures than steady eruptions (e.g. effusive and sub-Plinian eruptions) since, besides crystallisation during magma ascent, there is an intra-conduit

dynamic component of downward fragmentation that quenches magma at different depths. Thus, the textural interpretation of samples from unsteady eruptions requires a different approach. In Chapter III, crystal textures in representative samples for different stages of unsteady-style eruptions of Volcán de Colima show that crystal textures can capture efficiently (1) the conditions of ascent during conduit refill, or (2) pre-extrusive, intra-conduit conditions that are quenched during fragmentation in explosive stages. The previous chapters thus highlight the importance of integrating different groundmass textural attributes by considering additional crystal features such as zoning or composition and expanding to other crystal populations (e.g. phenocrysts) for a better assessment of eruption kinetics.

In this chapter, I assess the efficiency of decompression-induced crystal rim growth in samples from Volcán de Colima derived from events of known eruptive histories. I expand on previous work (Chapters II and III) by quantifying rim growth on phenocrysts and the effects of different ascent rates (paths) on crystal shapes, and therefore on the kinetic processes of crystal nucleation and growth. I show that crystallisation on phenocrysts is more significant for eruptions with lower volumetric eruption rates (VER), and thus that events with lower VER have higher phenocryst φ (PhC φ) relative to eruptions with higher VER. Texturally, the phenocrysts of low-VER eruptions have thicker rims and are larger but have similar phenocryst number densities to those of high-VER eruptions.

Table 4.1. *Table of symbols and abbreviations used in Chapter IV.*

Chapter IV - Table of symbols and abbreviations	
Symbol/Acronym	**Definition**
Ab	Albite
AbRim	Albitic rim on plagioclases
An	Anorthite
AR	Crystal aspect ratio
$AR_{AV.}$	Average crystal aspect ratio
BAF	Block-and-ash flow
BSE	Back-scatter electron analysis
c	Intersection on axis Y
Comp.	Complete
CSD	Crystal size distribution
Fld	Feldspar mineral phases
GS	Grey scale
GSV	Grey scale value
I.	Image
Kv	Kilovolts
L	Long axis
LF	Lava flow
Log.	Logarithmic value
m	slope
Maf	Mafic mineral phases (pyroxenes, Fe-Ti oxides, amphiboles and olivine)
Max.	Maximum value
Min.	Minimum value
ml	Microlite-size crystals
mol %	Mole percentage of a given element
MPa	Megapascals
N	North
N_A	Crystal number density
nA	Nanoamperes or Number of crystals in a bin of crystal areas
Osc.	Oscillatory zoning
P	Pressure
P_f	Pressure at final conditions
PhC	Phenocryst-size crystals
Pn	Sub-Plinian eruptions
px.	Pixel

R^2	Coefficient of determination
S	South or Short axis
Sn	Crystal size
Sn_{MAX}	Maximum crystal size in a sample
VER	Average volumetric eruption rates
vol. %	Percentage of a given element per sample volume
Vulc.	Vulcanian eruption
ΔT	Degree of undercooling
σ	Standard deviation
φ	Crystal fraction

4.2. Background

Groundmass crystal textures are commonly formed by degassing-driven crystallisation during magma ascent through the volcanic conduit. The anhydrous nature of plagioclase makes it particularly sensitive to changes in water content in the melt, therefore, it is an adequate mineral phase to associate with syn-eruptive dehydration of magma in time through effective degassing. Based in my previous chapters, total groundmass crystal fraction (GM φ) and average plagioclase aspect ratios ($AR_{AV.}$) are two textural attributes that demonstrably correlate with eruptive intensities in natural products of Volcán de Colima. In this chapter we extrapolate and quantify the effects of crystallisation in populations of larger crystals (phenocrysts) in relation to eruptive intensities.

4.2.1. Plagioclase textures and compositions in Volcán de Colima

Plagioclase is the most abundant phenocryst and groundmass mineral in Volcán de Colima lavas (13-34 vol.%, *Luhr, 2002*; *Mora et al., 2002*; *Reubi and Blundy, 2008*; *Lavallée et al., 2012*). Plagioclase crystals in Volcán de Colima are predominantly Labradorite-Andesine in composition (An_{30-70}), with more than 70 vol.% An_{50-60}; more An-rich compositions (>An_{70}) usually occur as An-rich cores (**Fig.4.1**., *Allan, 1984; Luhr, 1992,2002*; *Mora et al., 2002*; *Atlas et al., 2006*; *Reubi and Blundy, 2008*; *Crummy et al., 2014*).

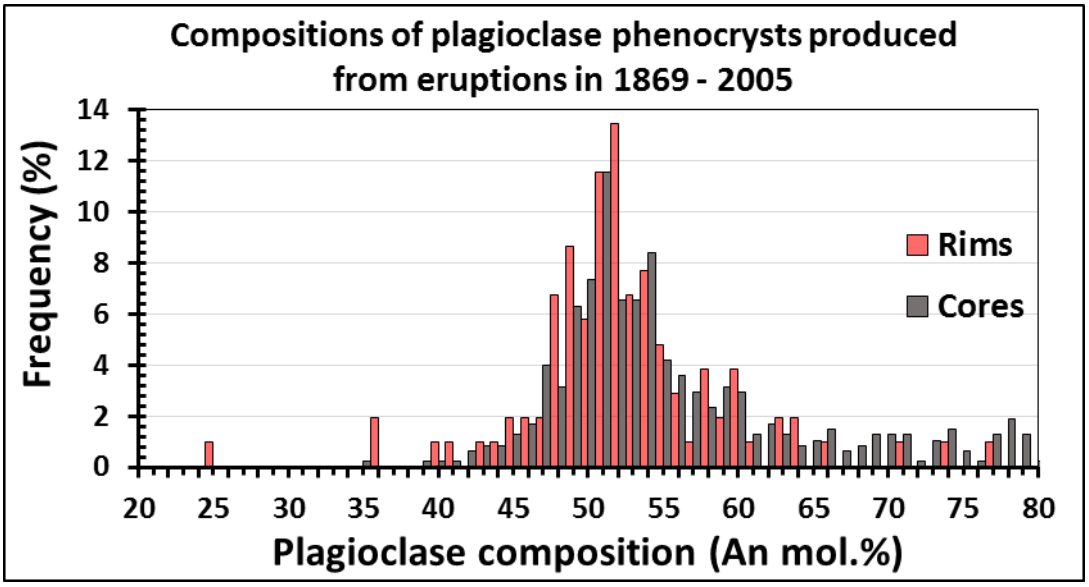

Figure 4.1. *Frequency distribution for rim and core compositions of plagioclase phenocrysts in products erupted between 1869 and 2005 at Volcán de Colima (n = 575). The compositional data were retrieved after Allan (1984); Luhr (1992, 2002); Mora et al. (2002); Reubi and Blundy (2008).*

Equilibrium and disequilibrium textures are observed in Volcán de Colima plagioclases (*Luhr and Carmichael, 1980*; *Mora et al., 2002*; *Reubi and Blundy, 2008*). Clear oscillatory zoning is the most characteristic texture in phenocrysts of An_{40-60}, with weak changes in composition between oscillations (< 10 mol.% An) (*Reubi et al., 2013*). The same compositional ranges in oscillatory textures are found irrespective of whether or not a crystal has a resorbed rim (*Reubi et al., 2013*). The plagioclase crystals tend to have decreased An-contents towards the rims (normal zoning) and have a more calcic core. The crystal rim compositions of plagioclase crystals from eruptive events between 1869 and 2005 are predominantly An_{35-60}; cores are generally more An-rich but cover a broader compositional range than the rims (up to An_{80}) (based in a population of n = 575, **Fig. 4.1**; *Allan, 1984*; *Luhr, 1992, 2002*; *Mora et al., 2002*; *Reubi and Blundy, 2008*). The cores can be inclusion-free, resorbed with abundant inclusions, or have an inclusion-free centre with an inclusion-rich boundary between the core and the next textural zone (*Luhr and Carmichael, 1980*; *Mora et al., 2002*). Rims on plagioclases of the 1913 eruption are more An-rich than the ones in the lavas (*Savov et al., 2008*). Most of the resorbed textures in phenocrysts consist of patchy cores

with melt inclusions and mixed An-rich (An_{65-82}) and An-poor (An_{45-55}) patches (*Reubi and Blundy, 2008*).

4.3. Methodology

I quantified abundance of microlites (GM φ, Sn < 50 µm) and phenocrysts (PhC φ, Sn > 50 µm), and constructed cumulative distributions of whole crystal populations (i.e. microlites and phenocrysts) in samples from historic eruptions at Volcán de Colima of different eruptive intensities and styles. In combination with this batch analysis, I qualitatively assessed plagioclase zoning patterns as indicators for stages of syn-ascent crystallisation. The style and intensity of eruptions, the samples analysed, and the applied methods relevant to this chapter are presented in **Table 4.2**. For more detailed descriptions of the events, sampling location and methodology I refer the reader to Chapter II.

Table 4.2. *Textural and chemical analyses performed on crystal components of samples from a range of eruptive events at Volcán de Colima. The "X" in the table cells indicates that the analysis listed on top of each column was performed for the sample indicated in that row. The asterisk by the year of eruption indicates that the average VER value for that sample was estimated using the best-fit textural parameter (see Chapters II and III).*

Events				Methods					
Year of event	**Sampled products**	**VER (m^3/s)**	**Sample**	**GS-An calibration**	**CSD of Fld zones**	**CSD of whole Fld population**	**Crystal modes of whole population**	**Modes of Fld textures**	**Fld PhC shape analysis**
1818*	Plinian fall-out	39000	S1818				X	X	
1869	Lava flow	30.3	S26				X	X	
1913	Plinian fall-out	13900	S1913			X	X	X	X
1961	Lava flow	1.16	S22				X	X	
1975 S	Lava flow	11.9	S30				X	X	
1975 N	Lava flow	0.62	S28				X	X	
1998	Lava flow	5.71	S1a				X	X	
2004	Lava flow	2.89	S1			X	X	X	X
2005*	Blocks from BAF	0.053	S2	X	X	X	X	X	X
			S9	X					
2013	Blocks from BAF	0.078	S23				X	X	

Table 4.3. *Imaging settings for integrated Population Density Distributions*

Event	Sample	Magnification	No. of images	Composite Image Resolution px. (µm)	Comp. I. Area Px^2	Comp. I. Area mm^2	Comp. I. Void-free Area mm^2	Pixel size (µm)	Sn Min (µm)	Sn Max (µm)	Min. Significant Particle size (µm)
1913	S1913	500 x	1	2560 x 1920 (254 x 190.5)	4915200	0.05	0.04	0.1	2	18.8	1
		300 x	12	7780 x 7824 (804.58 x 809.13)	60870720	0.65	0.31	0.1	2	277.2	1
		60 x	279	8315 x 3525 (17268.96 x 7473.49)	29310375	131.75	52.12	2.1	40	751.8	19
2004	S1	500 x	1	1280 x 960 (254 x 190.5)	1228800	0.05	0.05	0.2	2	19.1	2
		300 x	1	4096 x 3072 (438.27 x 328.7)	12582912	0.14	0.14	0.1	2	103.9	1
		60 x	368	10440 x 5106 (38210.41 x 18687.96)	53306640	714.07	610.17	3.7	40	2039.7	33
2005	S2	500 x	1	1280 x 960 (254 x 190.5)	1228800	0.05	0.05	0.2	2	25.9	2
		300 x	9	9187 x 6917 (1191.73 x 897.27)	63546479	1.07	0.92	0.1	2	110.8	1
		60 x	156	10417 x 4167 (36153.69 x 14462.17)	43407639	522.86	384.63	3.5	40	2155.5	32

4.3.1. BSE-imaging

I collected individual BSE-images of thin-sections and polished cut- sections at magnifications of 500, 300 and 60 -fold to cover the widest possible range of feldspar crystal sizes. The BSE-images were taken using a Hitachi S-3500N scanning electron microscope at a beam current of 20kV, 5nA intensity and a working distance of 25 mm. To build composite images (i.e. large thin-section areas composed of several stitched images), I individually adjusted magnification and capture scanning times, depending on the total area of coverage. A balance between image resolution and scanning time for each individual composite was necessary for efficiency: larger composite images required shorter scanning times for each individual image than smaller composites and ranged between 100 – 400 s for smaller matrices and 80 – 200 s for larger. Maximum total scanning times of 9 hours were used to minimise darkening or brightening effects in the images caused by fluctuations in the beam current during prolonged captures. Brightness and contrast levels were manually adjusted for consistent greyscale values. Each BSE image generated was automatically stitched and their brightness and contrast readjusted in ImageJ® to constrain greyscale ranges representative of the feldspar compositions in the samples.

4.3.2. Cumulative distributions of crystal sizes captured at different magnifications

I constructed cumulative distributions of crystal sizes from feldspar microlites (Sn < 50 µm) up to the largest phenocrysts (Sn > 50 µm) by analysing images at different magnifications (500x, 300x and 60x, **Fig. 4.2**). I analysed three samples spanning the eruptive intensity and style spectrum within my suite of Volcán de Colima sampled historic eruptions: 1913 Pn, 2004 LF and 2005 BAF. From highest to lowest intensity the samples correspond to the 1913 sub-Plinian eruption (1.4 x 10^4 m^3/s); the 2004 lava flow (3 m^3/s), and the 2005 BAF (0.05 m^3/s) (**Table 4.2**). From the latter, I selected sample S2 as representative of a stage of ascent during

the 2005 Vulcanian eruption (as opposed to conduit fragmentation) based on textural associations detailed in **Section 3.5.3** of Chapter III. The resolution of the individual BSE-images, the total number of images used to build the composite images and the total areas (in pixels and in µm) are presented in **Table 4.3**.

I created binary masks of feldspar crystals and voids (bubbles and cracks) for all composite-images (**Fig. 4.2**). The area of voids was subtracted from the total area of each respective image to perform textural measurements on a vesicle-free basis. I measured the feldspar areas and their maximum and minimum axis lengths based on a best-fit ellipse in Image J®. A minimum crystal size was determined considering 1) the pixel size at each magnification, 2) a crystal-size overlap between the different magnifications, and 3) consistency at each magnification amongst all the studied samples. Based on these criteria, the minimum crystal sizes were 2 µm for images at 500x and 300x, and 40 µm for images at 60x (**Table 4.3**). Crystal sizes were determined using the square root of the area of each crystal (Sn= √Area) to minimize 2-D shape effects on size.

The crystal size (Sn) distributions of samples are compared using cumulative crystal number densities (N_A). Cumulative N_A was calculated by listing all crystals in an image in order of increasing size and counting the number of crystals in the image smaller than each size. These cumulative number of crystals data were normalised by the vesicle-free area of the image, generating cumulative crystal number density distributions. Therefore, cumulative N_A(Sn) = number of crystals smaller than Sn per vesicle-free area.

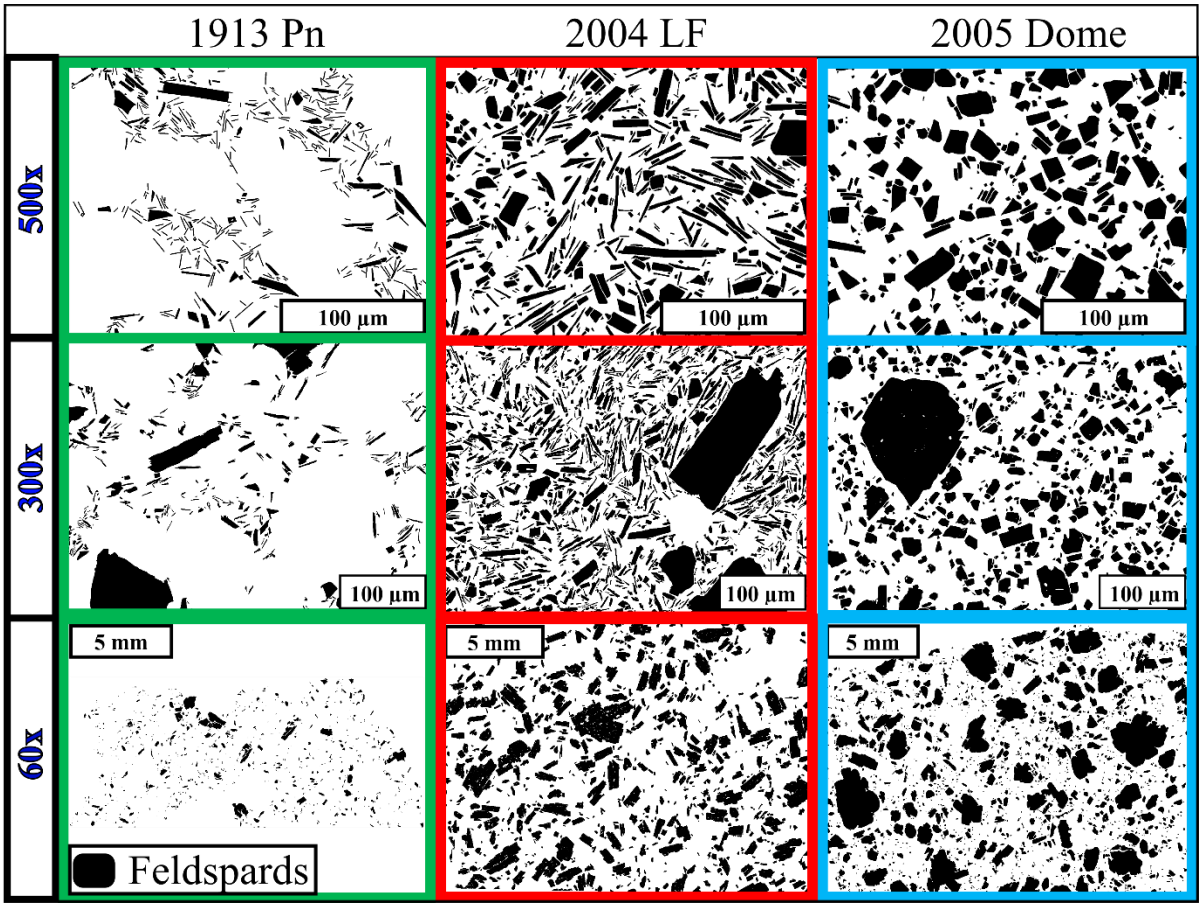

Figure 4.2. *Feldspar binary masks of thin-sections at 500, 300 and 50 -fold magnification from different eruptive-style products: 1913 sub-Plinian, 2004 lava flow and 2005 Vulcanian eruptions.*

4.3.3. Modes of phenocryst crystals

I performed point-counting on the BSE-composite maps of whole thin-sections of 1869, 1961 1975 N, 1975 S, 1998 and 2004 LFs, and 2005 and 2013 BAF eruptions, and 60 -fold images of a cut, polished pumice clast from both 1818 and 1913 sub-Plinian eruptions of Volcán de Colima. I assigned six classes for the point-counting: voids, groundmass (microlites and glass) mafic phases, and three specific textural classes for feldspar phenocrysts. A minimum of 2000 counts was performed on each sample, with up to 500 additional counts for highly vesicular samples. Modes were calculated for each class and estimated at void-free, groundmass-free and mafic-free bases to constrain the proportions of feldspar textures alone. The sum of the modes of the different feldspar textures was used to calculate the proportion of feldspar phenocrysts in the sample. The modes of the groundmass components quantified in

Chapter II were calibrated and combined with the phenocryst proportions estimated in this chapter to yield components for the entire sample.

The three classes assigned for the plagioclase textures are: resorbed, oscillatory zoning and albitic rims (**Fig. 4.3**). Resorption textures are features that are neither homogenous nor display a clear pattern (i.e. anhedral, **Fig. 4.3**). Oscillatory zoning consists of concentric zones of contrasting An-content (**Fig. 4.3**). Albitic rims (AbRims) are homogenous growth mantles of low An-content (**Fig. 4.4**). AbRims can be found surrounding crystals (**Fig. 4.4A**), within embayments on phenocrysts (**Fig. 4.4B**), and between confined walls between different crystals (**Fig. 4.4C-D**).

I performed an additional visual evaluation to distinguish between uninterrupted oscillations (green-shaded frames in **Fig. 4.3**) and those disrupted to some extent by resorption features (red-shaded frames in **Fig. 4.3**). Using this additional sub-classification, I attempted to distinguish the proportions of inherited oscillatory textures (i.e. those that did not crystallised syn-eruptively but were recycled) from oscillations that crystallised during eruptive activity.

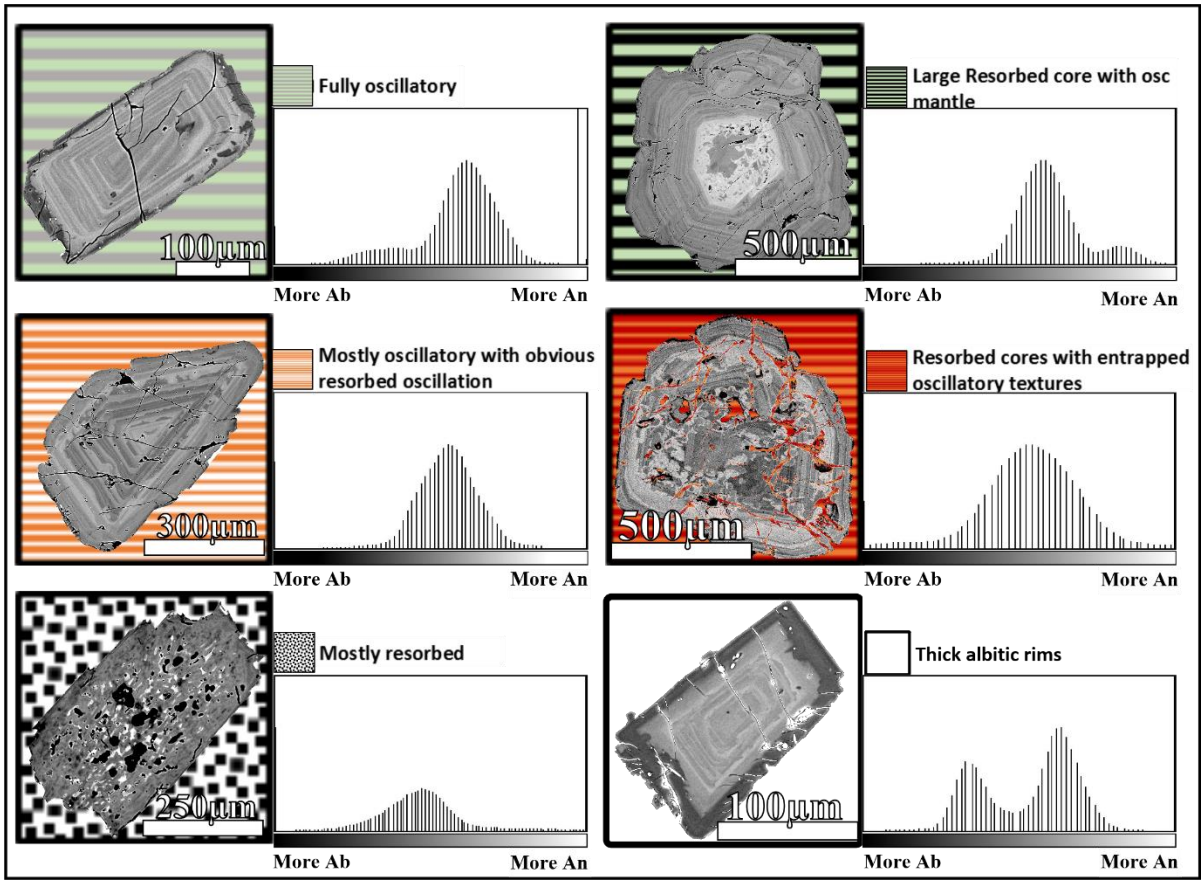

Figure 4.3. *Dominant textures in phenocryst feldspars found in the sample set used in this study. The frames with green backgrounds represent crystals with continuous oscillatory zones; red shades are crystals where an obvious resorption zone interrupts the oscillatory pattern. Grayscale frequency distributions are displayed next to each crystal to show variations in compositions within the different crystal textures.*

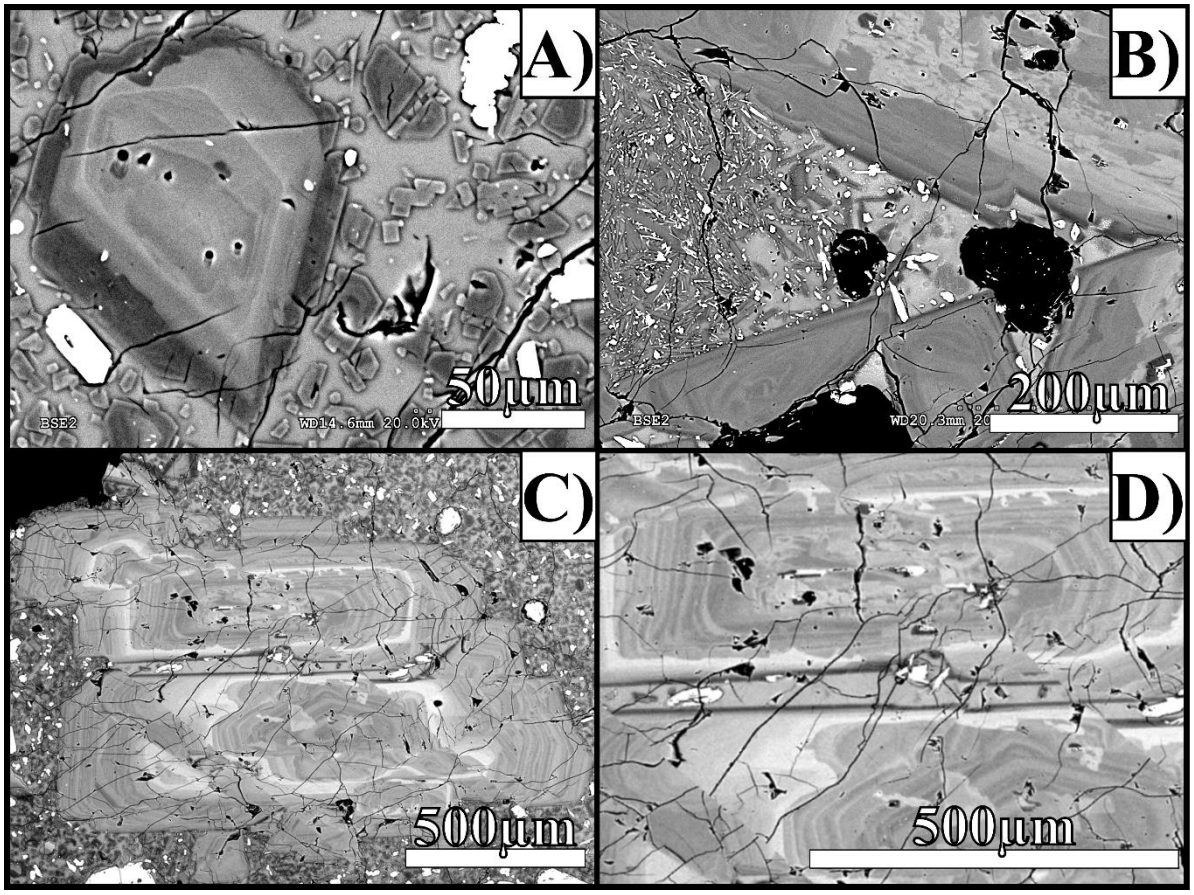

Figure 4.4. *Environments for the development of albitic margins:* ***A)*** *As margins surrounding crystals (AbRims),* ***B)*** *Within embayments in phenocrysts, adjacent to locally low-crystallinity groundmass, and* ***C)*** *on margins between close crystals.* ***D)*** *Magnified view central portion of panel* ***C****, showing albitic rims on portions of adjacent phenocrysts, also associated with low-crystallinity groundmass.*

4.3.4. Quantification of compositional zones in feldspars

Chemical compositions were measured for plagioclase crystals in the 2005 BAF sample S2 using an Electron Microbeam JEOL JXA8530F Hyperprobe. To achieve the best possible spatial resolution, I used an accelerating voltage of 20kV, an intensity of 10 nA and a beam size of 1µm diameter. Na and K were analysed first to limit element migration, followed by major and then minor elements. Areas of different compositions (proportional to different greyscales on feldspars in BSE-imaging) were analysed to cover the widest range of compositions found for the specimens of each sample (**Fig. 4.5**). BSE-images that included the crystals on which chemical measurements were previously performed were obtained at a

voltage of 20kV, an intensity of 5nA, working distance of 15mm, 500x magnification and 400 seconds scanning times. Brightness was manually set to the minimum level to maximise the contrast of the images, and to constrain a specific range of greyscale for the feldspar compositions in the sample.

Using Image J, I measured the greyscale value (GSV) in spots of areas of 1 μm diameter in the BSE-images, matching the beam size area used for the chemical analysis (**Fig. 4.5A**). The GSV was calibrated with the corresponding An mol.% measured in the crystal based on the linear correlation: An mol% = (GSV * m) + c (**Fig. 4.5B**). The GSV proxy was re-calibrated for each analysed BSE-image due to differences in BSE-acquisition conditions.

Using the GSV-An mol.% regression, I built a compositional proxy for GSV in Image J that was used to quantify areas of specific compositional ranges within individual crystals using the Region of Interest tool (**Fig. 4.6A**). The values estimated using the GSV-An mol% calibration were compared with reported compositions for Volcán de Colima feldspars (e.g. **Fig. 4.1**) to validate that they were within realistic ranges. Total area of individual crystals (whole crystals) and the areas within each crystal corresponding to the compositional range of the sharp albitic rims (AbRims, An_{10-35}, **Fig. 4.6B**) could then be compared directly. The proportions crystal rim and core obtained automatically using the Region of Interest tool were compared to manual measurements of 150 crystals of random sizes for validation.

I measured areas of whole crystals, albitic rims and cores (whole crystal area – albitic rim area) of plagioclase crystals in a 300x magnification BSE composite image of Sample 2 (erupted in 2005, **Table 4.3**), providing data on crystals of a range of sizes including both microlites and phenocrysts. Finally, I obtained individual high-resolution BSE-images of larger crystals cut along a main crystallographic axis with albitic rims around the entire perimeter (**Fig. 4.7.**).

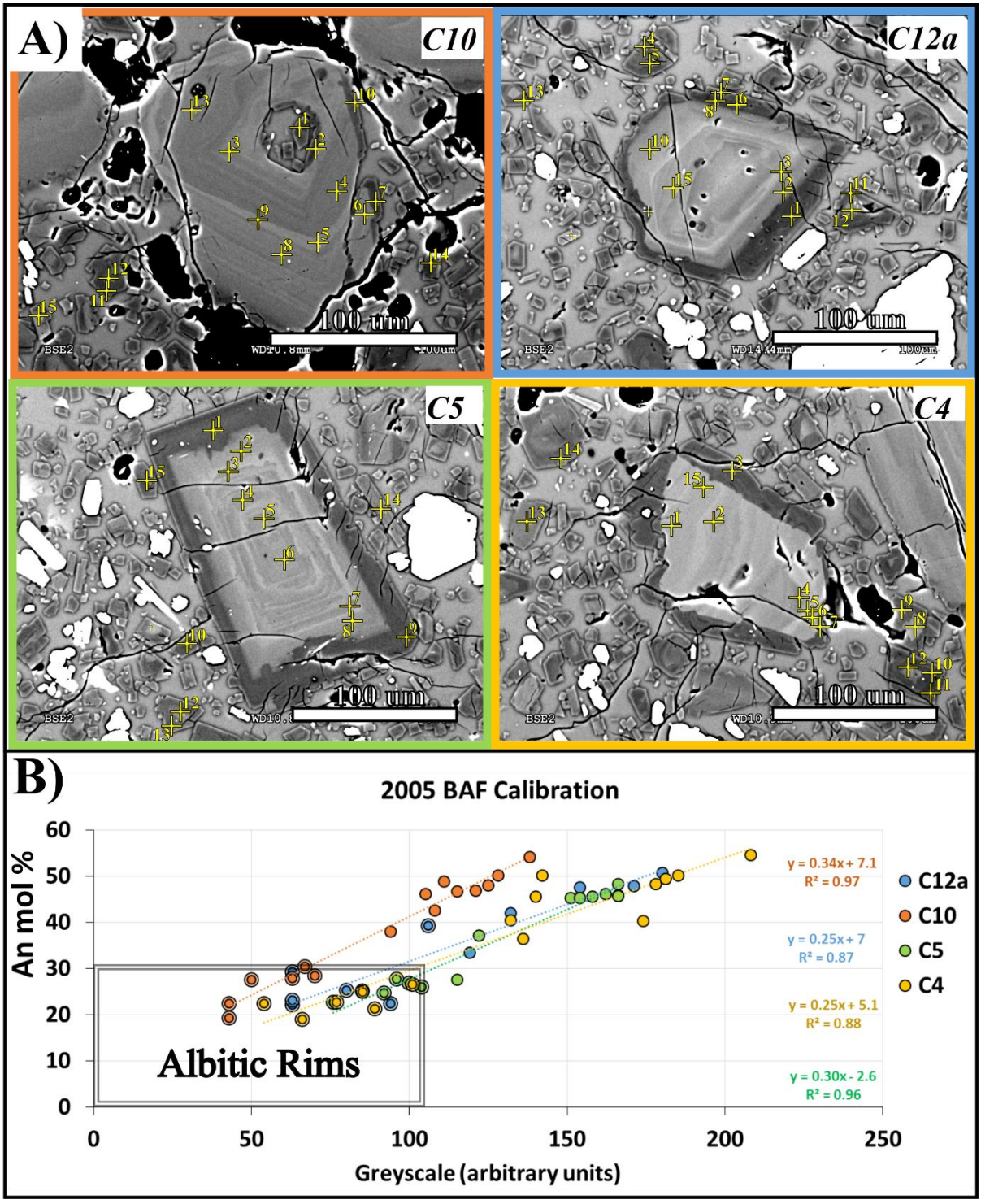

Figure 4.5. *Calibration of BSE images for plagioclase An contents.* ***A)*** *Points analysed in feldspars. Each analysed spot is indicated with a yellow "+".* ***B)*** *Calibration of greyscale values (in arbitrary units) from BSE-images to an associated An mol. % value directly measured for different zones of feldspars found in a sample from the 2005 BAF event. Each dot in the plot represents an individual chemical analysis. The thicker border on some of the dots indicates that the analyses were located within the distinctive dark-rim of the feldspars.*

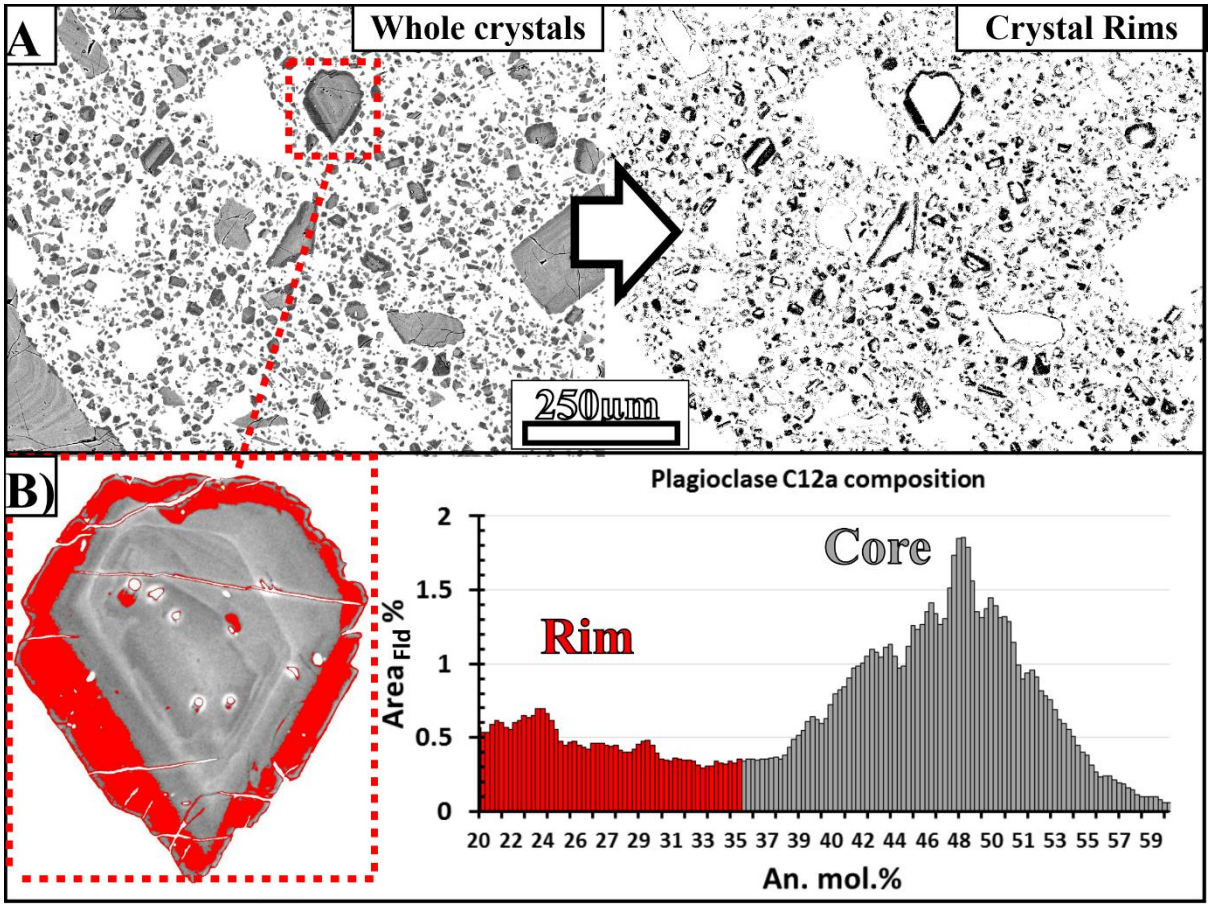

Figure 4.6. *Textural discrimination of plagioclase zones.* ***A)*** *Textural discrimination of individual crystal areas from BSE-images of a 2005 BAF block of Volcán de Colima.* ***B)*** *Compositional proportions of an individual plagioclase (C12a, red, dashed-box) using a BSE-greyscale vs An mol% calibration. The An mol% corresponding to the rims (AbRim) is highlighted in red on the crystal and the histogram.*

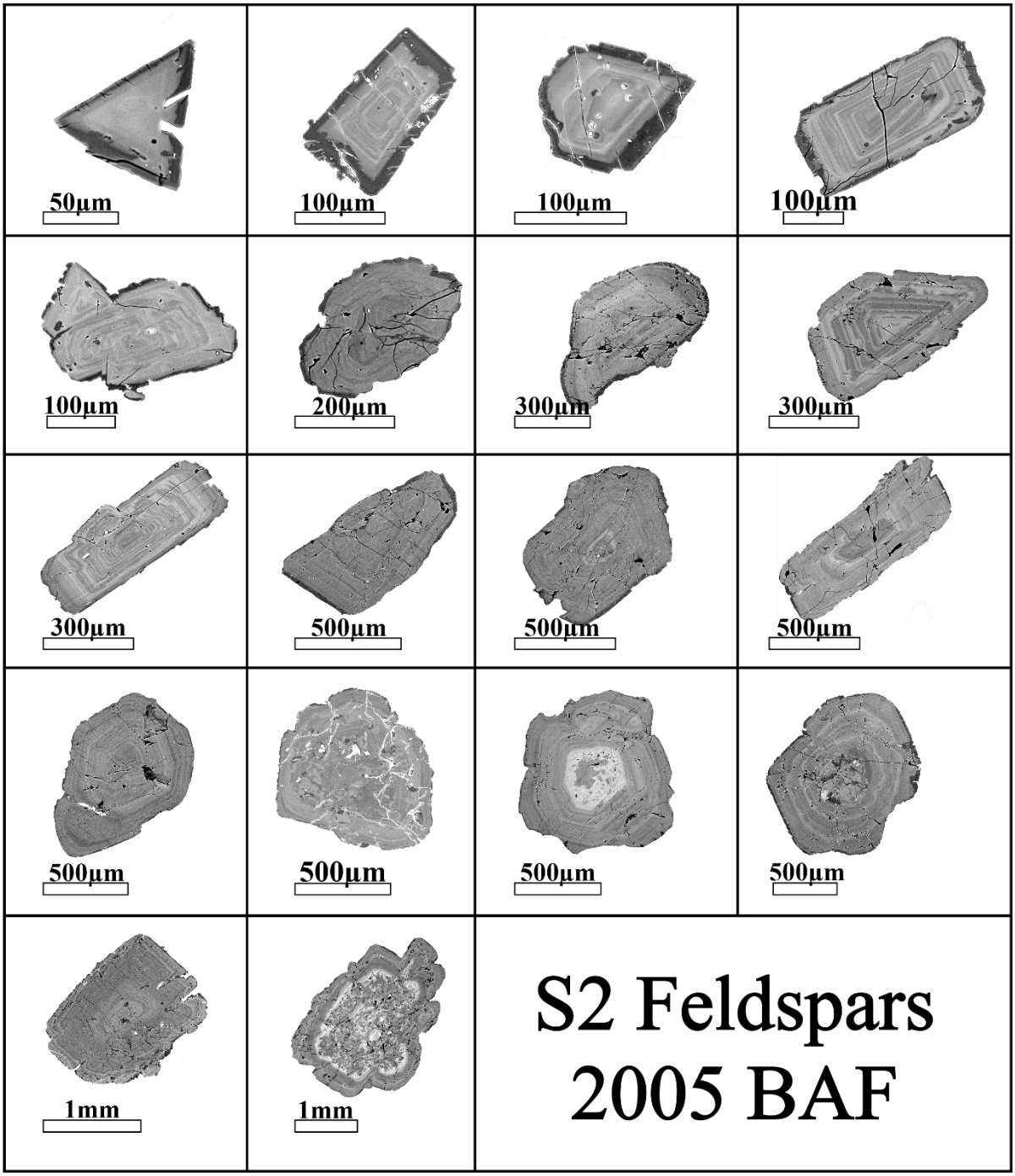

Figure 4.7. *Feldspar crystals with an AbRim in S2 from the 2005 BAF. Crystals are from different sizes and are cut along one of their main axes (a, b and c).*

4.4. Results

4.4.1. Correlation of crystal abundance with average intensities

Both total (plagioclase and mafic) and plagioclase groundmass crystallinities increase for lower eruptive intensity for Volcán de Colima recent eruptions (**Fig.2.10** in Chapter II). Combined, GM φ and PhC φ provide an integrated view of how average VER controls the extent of degassing-induced crystallisation during eruptions and how φ physically distributes in the crystallising magmas. In **Table 4.4.** and **Figure 4.8** φ-VER correlations for plagioclase and all mineral phases in groundmass and at phenocryst-sizes are presented to show the degree of φ in samples of individual eruptions and the effects that eruptive intensity exerts in the extent and distribution of φ for large crystals.

The six trends of crystal fractions presented in **Figure 4.8** (for plagioclase alone or plagioclase + mafic, and microlites alone or phenocrysts or total crystallinity) display a negative correlation with the Log VER within a 95% confidence (**Table 4.4.**). The φ-VER correlations for the microlite populations and the microlite + phenocryst group have fits with $R^2 \geq 0.8$ (**Table 4.4.**); the fits of the phenocryst-size group on the other hand are significantly more scattered, with $R^2 \leq 55$ (**Table 4.4.**). The φ-VER trends for microlites have a steeper (more negative) slope than the trends for phenocrysts, suggesting more microlite crystallisation than rim growth on phenocrysts during ascent.

Table 4.4. *Straight-line fits for different mineral phases and size populations. The straight-line fits (following y= mx + c) are between log. VER (as the variable "x") and the value of φ (variable" y") for each combination of mineral phases and sizes represented as different rows in the table P-values estimated from regression analysis for each of the correlations and the significance of the respective fits (to a 95% probability) are shown in the table.*

Equations for straight line fits of log. VER versus φ for different mineral phases and size populations						
Combinations of parameters for φ (variable "y")		**Equation values for the fits**			**Regression analysis**	
Mineral phase	Crystal size population	Slope	Intercept	R^2	P-Value	Statistically significant when α=0.05
Feldspars	Microlites	-0.025	0.2	0.88	0.002	YES
Feldspars + Mafics	Microlites	-0.03	0.24	0.85	0.003	YES
Feldspars	Phenocrysts	-0.016	0.29	0.42	0.042	YES
Feldspars + Mafics	Phenocrysts	-0.014	0.41	0.55	0.021	YES
Feldspars	Microlites + Phenocrysts	-0.041	0.49	0.8	0.003	YES
Feldspars + Mafics	Microlites + Phenocrysts	-0.043	0.65	0.82	0.004	YES

The 1818 Pn and the 2005 eruptions were not included in the fits to the φ-VER trends (**Fig. 4.8**) because of relatively large uncertainties in VER for these eruptions (**Section 2.5.3** in Chapter II and **Table 3.4** in Chapter III). However, using VER estimates based on groundmass textures data from these two eruptions (**Table 2.5** in Chapter II for the 1818 Pn sample, and **Table 3.4** in Chapter III for the 2005 values) are consistent with the rest of the suite; notably, the 1818 and 1913 Pn magmas crystallised a similar amount of both microlites and phenocrysts. The VER values for the 2005 BAF were determined based on samples that crystallised during ascent (as opposed to downward fragmentation process) during the 2005 eruption (see Chapter III for details).

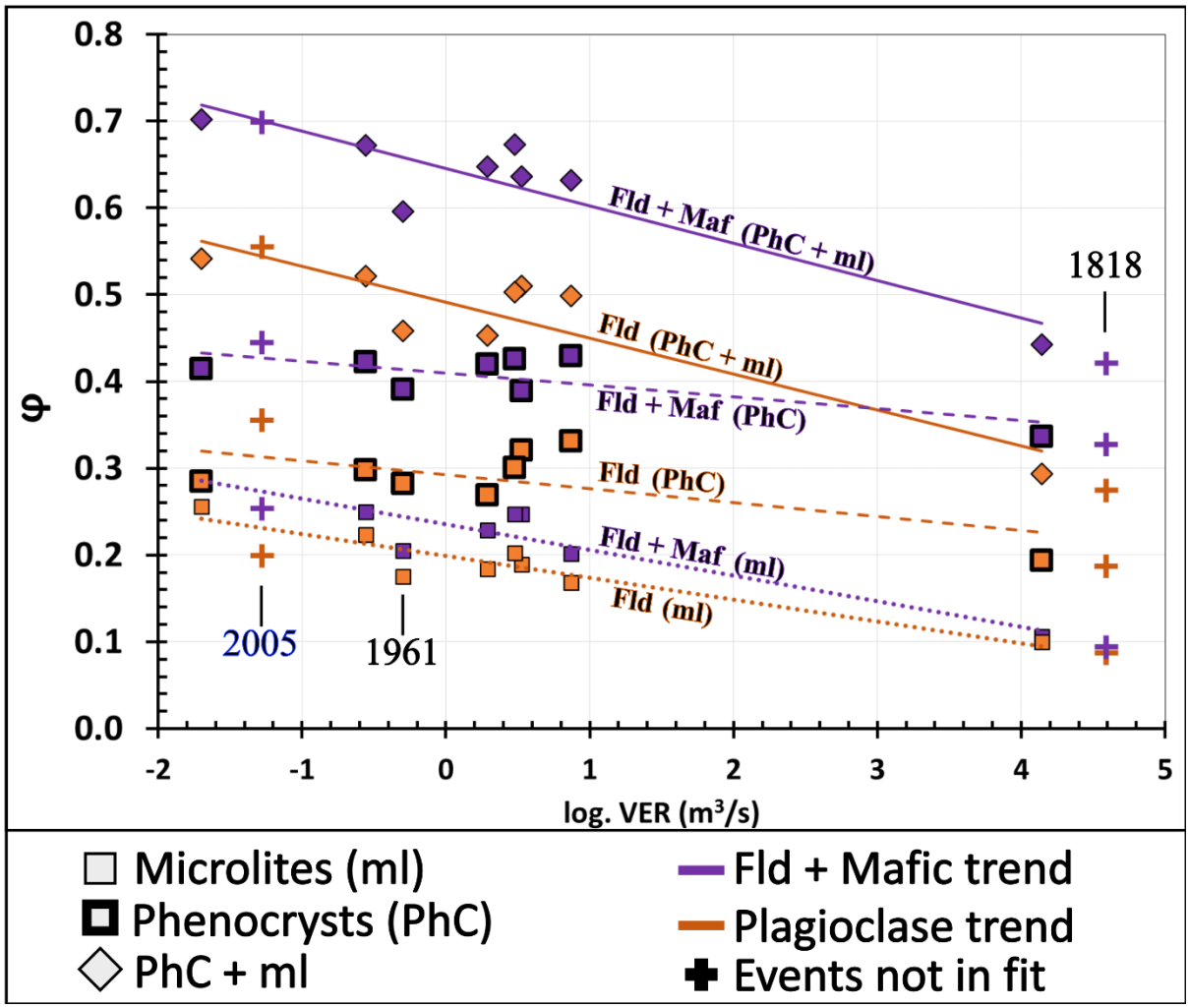

Figure 4.8. *Crystal fraction correlated with intensity for different crystal phases and sizes in a set of eruptive events at Volcán de Colima. The orange trend-lines correspond to fractions of feldspar crystals only; purple, indicates fractions of feldspars and mafic components combined. The values of the log VER - φ linear fit equations are presented in* ***Table 4.4****. The textural values and the best-fit VER estimates for the 1818 and 2005 events are presented for reference but these are not included in the calculation of the trend lines displayed in this figure (refer to the main text for more details).*

4.4.2. Plagioclase phenocryst textures

The proportions of different textural zones of plagioclase phenocrysts for the whole sample suite of Volcán de Colima were determined by point counting and visual estimation (**Table 4.2**). **Figure 4.9A** shows the modes from point counting of resorbed textures, oscillatory zoning and albitic rims of the sampled products in decreasing order of eruptive intensity (from left to right). The oscillatory texture category included a variety of textures in both cores (e.g.

with discrete patches of oscillatory zoning disrupted by resorption features) and mantles of oscillatory compositions fully surrounding crystals. **Figure 4.9B** provides further subdivision of the oscillatory category based on visual estimates of the proportions of inherited (recycled) and syn-eruptive textures on feldspar phenocrysts (that were combined as "oscillatory" in **Fig. 9A**).

The resorbed textures show a positive correlation with average VER, with the lowest modes corresponding to the BAF samples and the largest values to the sub-Plinian samples (**Fig. 4.9**). However, the abundance of resorbed textures – VER relationship is not systematic amongst the intermediate-intensity events (**Fig. 4.9A**). The 1869 and 1998 LFs are the two lava flows with the highest vol.% of resorbed textures, which also matches with the highest phenocryst φ in the whole sample suite studied (**Fig. 4.9**).

The abundance of oscillatory textures shows a general negative correlation with VER (**Fig. 4.9**). Amongst the LF group, the proportion of oscillatory textures is lower in samples with higher proportions of Resorbed textures (1869 and 2004). I additionally observe that the largest proportion of inherited oscillatory textures (i.e. red-shaded modes in **Fig. 4.9B**) correspond to the 1975 S and 2004 LFs and the 2013 BAF (> 40 vol.%, **Fig. 4.9A**).

Like the oscillatory zones, AbRims show a negative correlation with average VER, and are absent in crystals of the sub-Plinian (highest VER) events (**Fig. 4.9A**). In long-LFs (final length > 2 km, the length of the 2004 LF), which are the products of moderate VERs, the albitic rims do not completely surround crystals and are mainly found within embayments or only on the sides of phenocrysts which are close to each other (**Fig. 4.4B-D**). In samples of eruptions with VER < 0.5 m^3/s, such as short-LFs (final length ≤ 1961 LF) and lava domes, there are clear AbRims around feldspar microlites and phenocryst (**Fig. 4.4A**). Although complete AbRims around crystals represents the main distinction between low-VER events and the rest

of my suite, isolated pockets of crystals (microlites and phenocrysts) with complete AbRims were found within the 1998 LF sample. This sample has a higher proportion of AbRims than other LFs within the intermediate VER group (**Fig. 4.9A**).

4.4.3. Proportions of albitic rims

Sharp AbRims around feldspars are a distinctive texture in samples derived from events with average intensities below 0.5 m^3/s ($10^{-0.3}$) (**Fig. 4.5A**, **Fig. 3.1** in Chapter III). **Figure 4.11** shows the proportion of AbRims (measured as √Area) for individual crystals of different sizes (Sn) within a BAF sample (S2, 2005 BAF). Below the 100 – 200 µm range, the proportion of crystallisation (based on Sn) represented by the AbRims is predominantly > 0.4 (**Fig. 3.10** of Chapter III; **Fig. 4.11**), whereas for larger crystals the AbRim proportions are within 0.1 - 0.4 and mostly < 0.3, with almost all within 0.1-0.2 for Sn > 500 µm (**Fig. 4.11**).

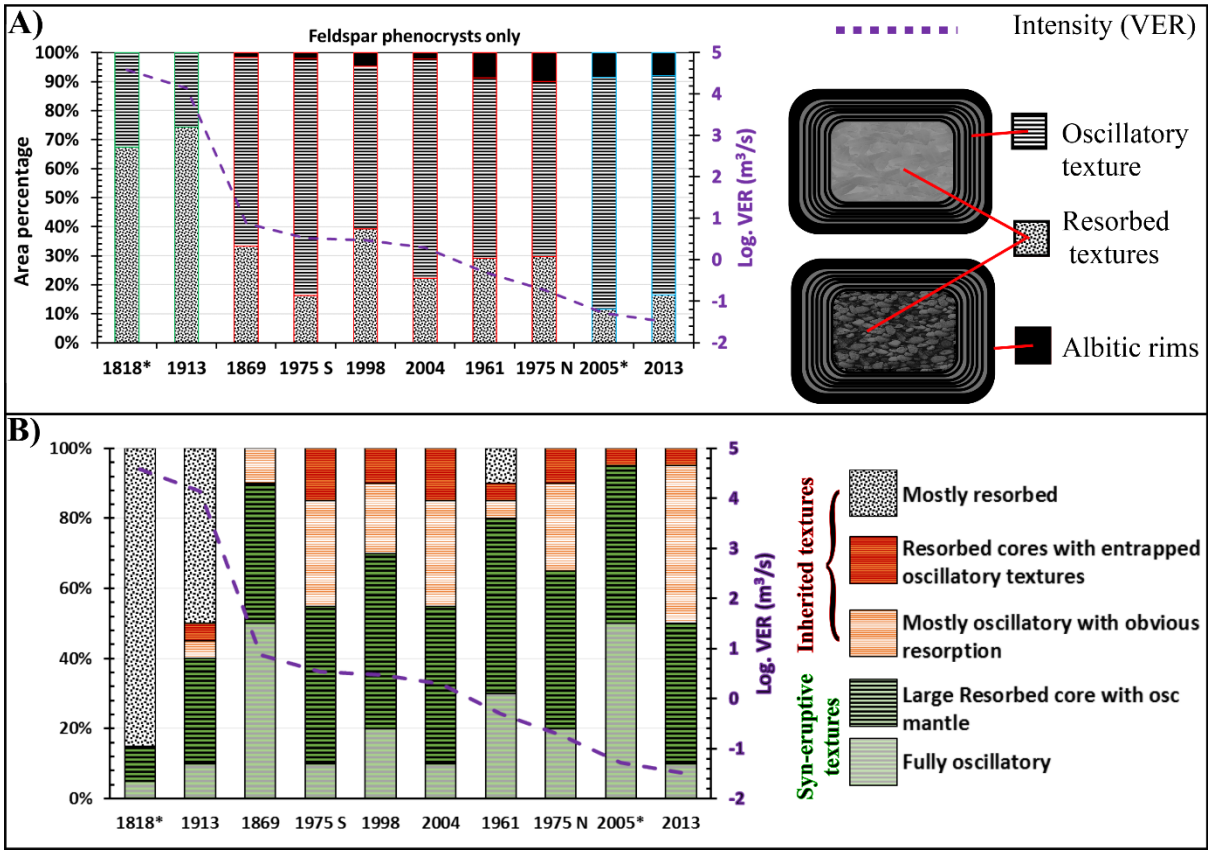

Figure 4.9. *Modal analysis of components and textures (in feldspar phenocrysts) after point-counting on BSE-images for samples placed in order of decreasing eruption intensity (VER).* ***A)*** *Feldspar phenocryst textures on a mafics- and void – free basis. The outline colour of each column indicates the eruptive style to which each of the samples is associated: green, Plinian; red, lava flow, and blue, Block-and-ash flow. To the right are sketches of feldspar phenocrysts with each of the textures indicated with a line. Two examples are given for what was counted as "resorbed" textures (clear patches or faded zones). Albitic rims develop around the crystals for eruptions with intensities of the 1961 LF and lower, whereas they grow within crystal embayments only for intensity values between the 2004 and 1869 LFs.* ***B)*** *Qualitative estimations of modes of dominant feldspar crystal textures within the broad category of "oscillatory" in panel A. Red shades indicate that an obvious resorption interrupts an oscillatory pattern (cores; interpreted as inherited textures); green background represents continuous oscillatory zones (interpreted as syn-eruptive textures). The events are displayed in order of descending eruptive intensity (horizontal axis). An asterisk next to the year of some events indicate that the average VER (dashed purple line) was estimated from the best-fits of textural parameters (see Chapters II and III for details). Examples of the proportion of combined classes are displayed in* ***Figure 4.3****.*

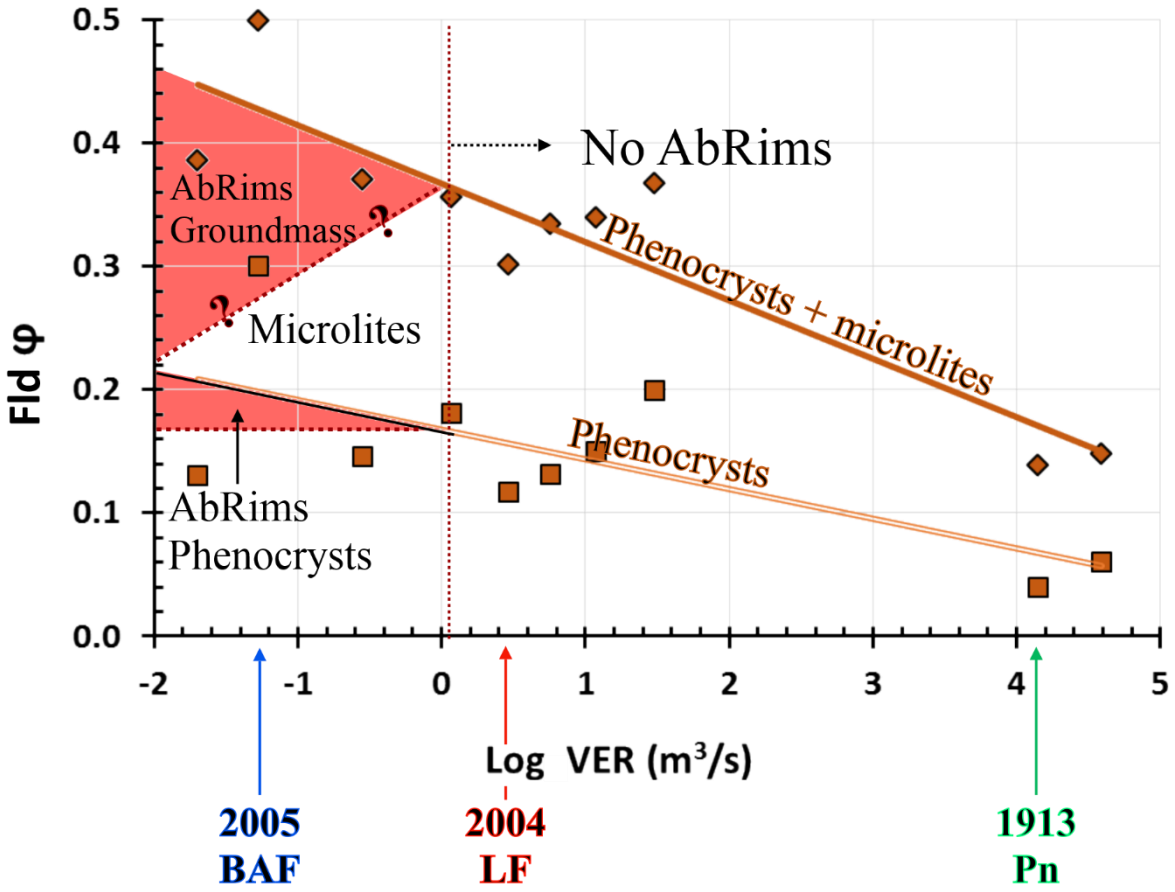

Figure 4.10. *Schematic representation of proportions of plagioclase crystal size populations and AbRims correlated with average VER for Volcán de Colima events analysed in this study. The phenocryst φ are normalised to modes of only syn-eruptive textures (i.e. undisturbed oscillatory zones and AbRims). Red-shaded zones illustrate the potential φ-VER ranges within which AbRims can be found. Intensities for the 1913 Pn, 2004 LF and 2005 BAF eruptions are indicated in the sketch for reference.*

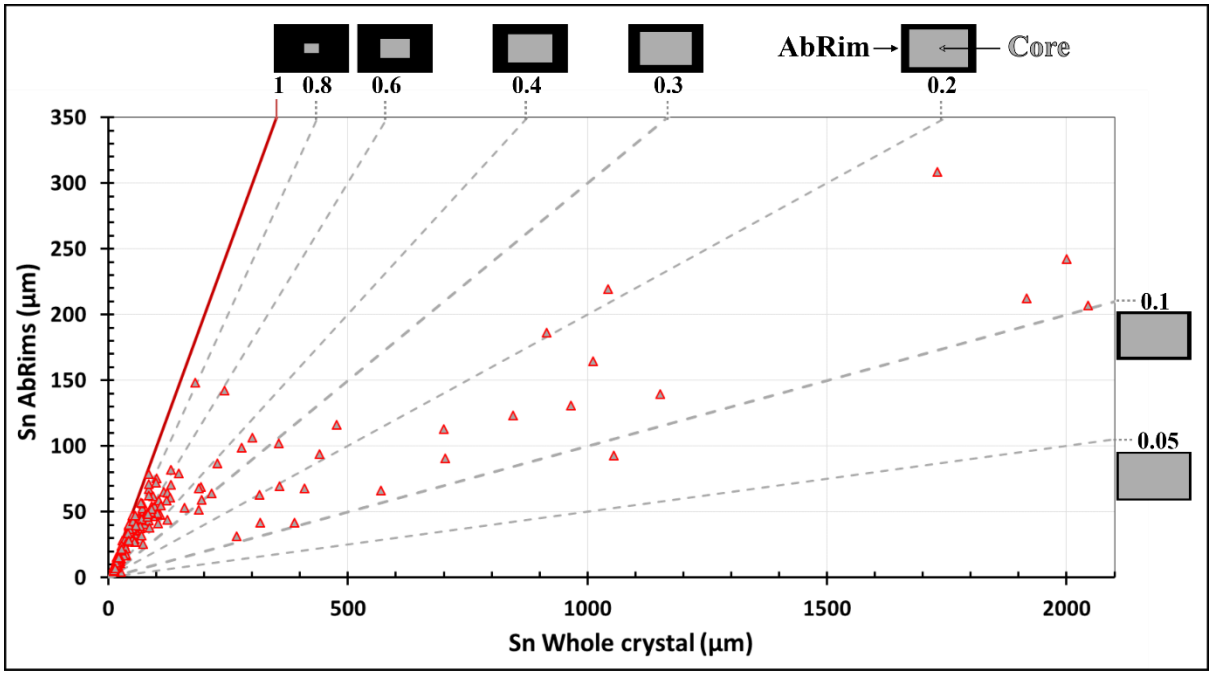

Figure 4.11. *Sn (square root of area) of albitic rims versus Sn of whole (core + rim) for both microlites and phenocryst crystals in sample S2 from the 2005 Vulcanian sequence. The red line corresponds to no core (i.e. the whole crystal is albitic). Sketches of the different proportions of AbRim/Whole crystal are based on the $AR_{AV.}$ (S/L= 0.64) of the crystals in the sample analysed and are displayed for reference. A close-up for the AbRims-Whole crystal proportions for Whole crystal Sn < 50 µm is found in* ***Fig. 3.10*** *of Chapter III. The 18 largest crystals analysed in this figure are displayed in* ***Figure 4.7****.*

4.4.4. Cumulative number density distributions at different eruptive intensities

Figure 4.12 shows the size-integrated cumulative distributions of feldspars (microlites and phenocrysts) covering ranges of crystal sizes from Sn = 2µm up to the maximum crystal size measured in each sample (Sn_{MAX}). The distributions for the three samples are bimodal, showing an abrupt increase in number density at the smallest crystal sizes (Sn 2 to ~ 10 µm) followed by a decrease in slope that remains relatively constant toward the larger sizes (**Fig. 4.12**). Amongst the three samples, the abruptness of the change of slope and the highest feldspar number density reached, both increase with average VER values of the eruptions. Conversely, the largest phenocrysts of each sample (phenocryst Sn_{MAX}) decreases with increasing VER, with the 1913 Pn having a phenocryst Sn_{MAX} of 752 µm, followed by the 2004 LF with Sn_{MAX} of 2040 µm, and the 2005 showing the largest at Sn_{MAX} of 2155 µm (**Fig. 4.12**).

The three distributions show a gap (lack of counted crystals) after the change in slopes (**Fig. 4.12**). In general, such gaps could be associated with resolution limitations at the magnifications where the BSE-images were taken, but here the scarcity of crystals appears to be real as there was sufficient overlap between the crystal sizes analysed at each magnification (**Table 4.3**). These gaps get narrower with decreasing VER (**Fig. 4.12**). The Sn value at the left side of the gap in the distributions (the "groundmass Sn_{MAX}") decreases with greater VER in a similar manner to the phenocryst Sn_{MAX} (**Fig. 4.12**). In this regard, the 1913 Pn sample has the lowest groundmass Sn_{MAX} at 19 µm, progressively (with decreasing average VER), this is followed by Sn_{MAX} values of 23 µm and 32 µm for the 2004 LF and the 2005 samples respectively.

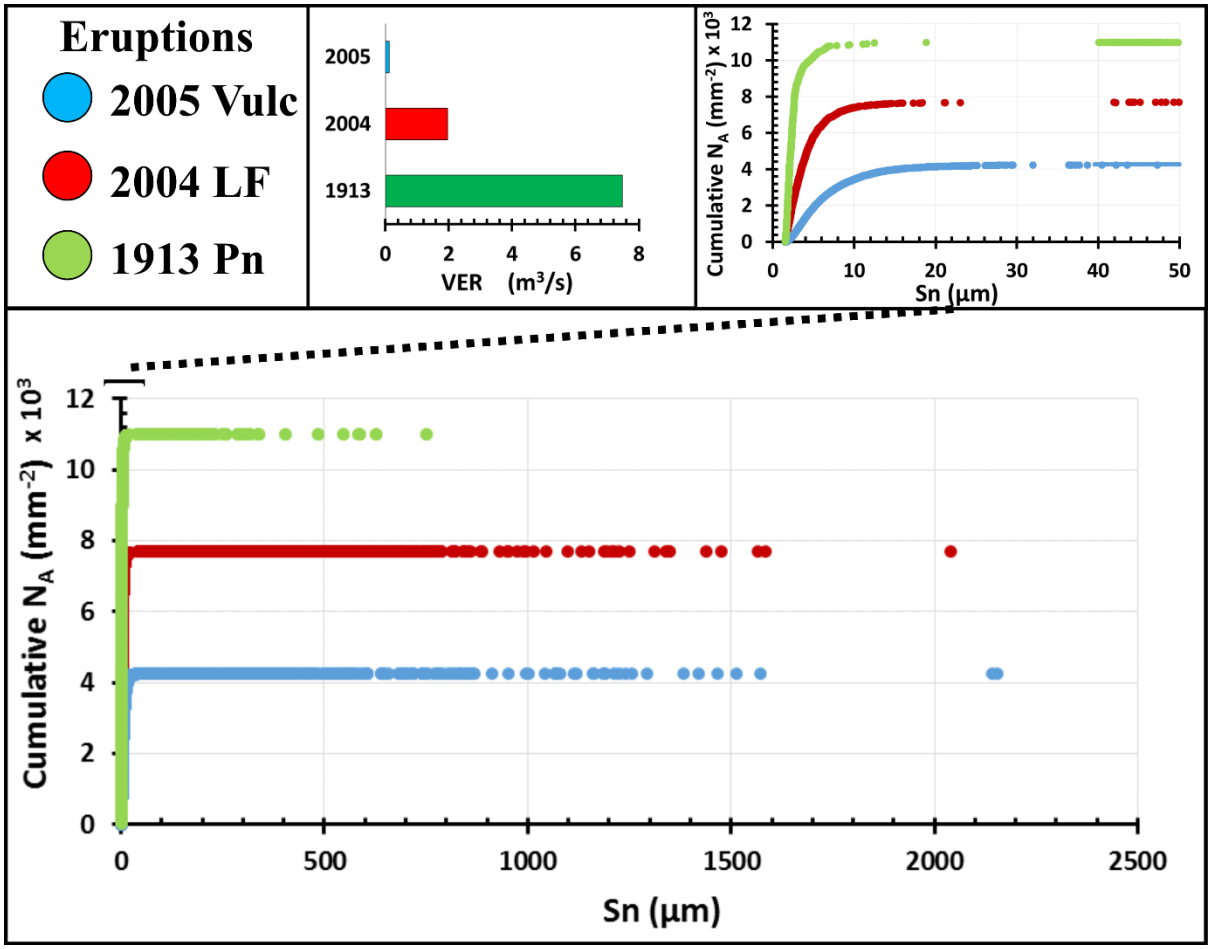

Figure 4.12. *Cumulative number density distribution of whole feldspar populations for erupted products of Volcán de Colima with different eruptive intensities: Plinian tephra, lava flow and BAF. Cumulative N_A distributions for microlites (Sn < 50 µm) and VERs for the three eruptions are presented as top insets for reference. Sn = √Area.*

4.4.5. Shape of plagioclase phenocrysts

I performed shape analysis for all phenocrysts (Sn > 50 µm) exposed in the polished mount or thin section of samples of three Volcán de Colima eruptions of a range of intensities: 1913 Pn, 2004 LF and 2005 BAF (**Fig. 4.13**). The 20 largest phenocrysts of each sample are presented in **Fig. 4.14**. Phenocrysts corresponding to the eruption with the lowest ascent rate (2005 BAF) are more equant than those from the intermediate intensity event (2004 LF). Phenocrysts from the 2005 BAF show $AR_{AV.}$ of 0.62 (σ = 0.17), whereas in the 2004, phenocrysts $AR_{AV.}$ is 0.52 (σ = 0.18). This contrast is in good agreement with the equivalent $AR_{AV.}$ in groundmass crystals for the respective samples (**Fig. 4.13**; S2, 2005 $AR_{AV.}$ = 0.64;

S1, 2004 LF $AR_{AV.}$ = 0.37; **Table 3.2** in Chapter III). In the 1913 Pn sample, the $AR_{AV.}$ of phenocrysts is 0.48 (σ = 0.19) whereas the microlite $AR_{AV.}$ = 0.22. The difference in $AR_{AV.}$ between the microlite and the phenocryst populations in the three events (**Fig. 4.13**) are 0.26 (1913 Pn); 0.15 (2004 LF), and 0.02 (2005 BAF), indicating that crystal shape is more consistent in low-intensity eruptive events.

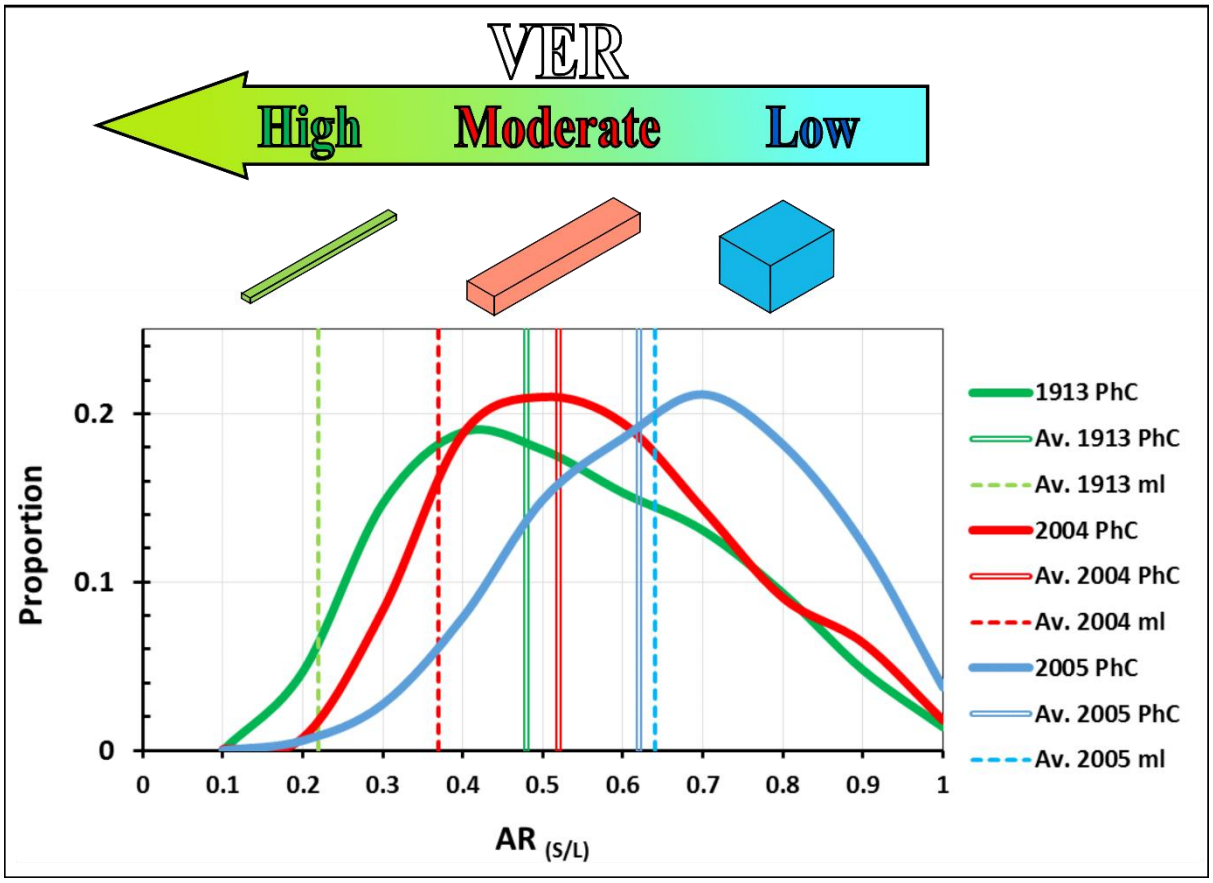

Figure 4.13. *Shape analysis of all feldspar sizes from individual samples representing 3 different eruptive styles: 1913 Pn, 2004 LF and 2005 BAF. Thick solid-lines indicate the distribution of phenocryst crystal shapes (AR) in the samples. Vertical double-lines show the phenocrysts* $AR_{AV.}$ *and vertical dashed-lines the average microlite* $AR_{AV.}$ *in each sample.*

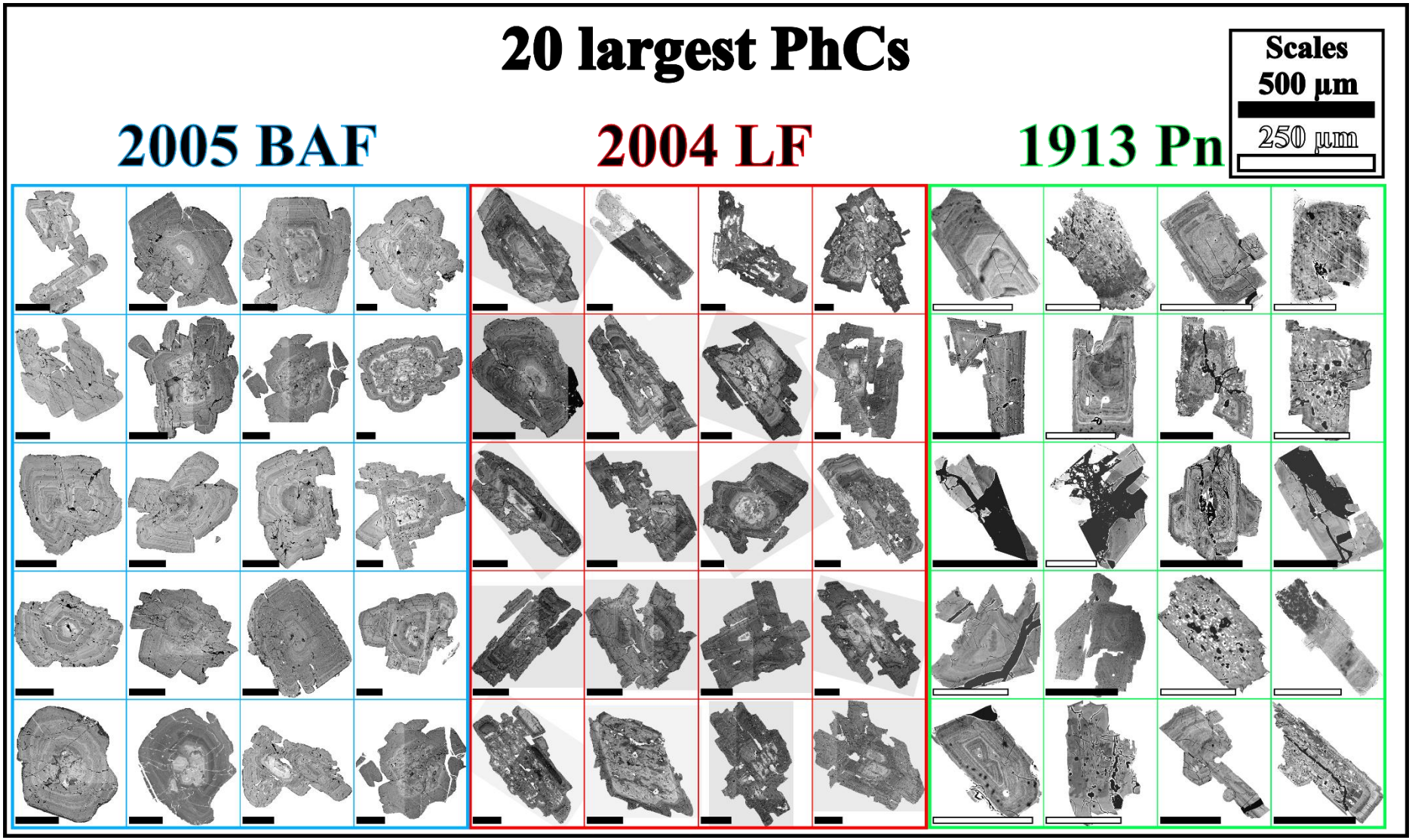

Figure 4.14. *20 Largest feldspar crystals in samples S1913 (1913Pn); S1 (2004LF), and S2 (2005BAF).*

4.4.6. Number density distributions of albitic rims

The relative sizes of cores and rims of crystals as a function of crystal size provides constraints on the compositional variability with time and kinetic regimes of crystallisation during ascent. For this reason, I correlate the cumulative number density distributions of the whole crystals, AbRims and crystal cores (whole crystal – AbRim) for a 300x BSE image of sample S2 from the 2005 BAF (**Fig. 4.15**). The total plagioclase φ in this image is 0.33, out of which 0.20 corresponds to crystal cores, and 0.13 to the AbRims. As for whole crystals, the AbRims and crystal cores display an abrupt increase in number density between the 2 – 10 μm size range, after which the slope in the distribution remains relatively constant. The lowest number densities are reached by the AbRims distribution (2674 crystals/mm^2), whereas cores and whole crystals have very similar number densities (4240 versus 4253 crystals/mm^2), indicating that there are very few crystals in the image that are entirely of AbRim composition and almost all crystals have a portion that is more An-rich than the AbRims. The Sn_{MAX} is the largest for the whole-crystal group (Sn_{MAX} =111 μm), then for the crystal cores (Sn_{MAX} =93 μm), and finally and the lowest value corresponds to the AbRims (Sn_{MAX} =60 μm).

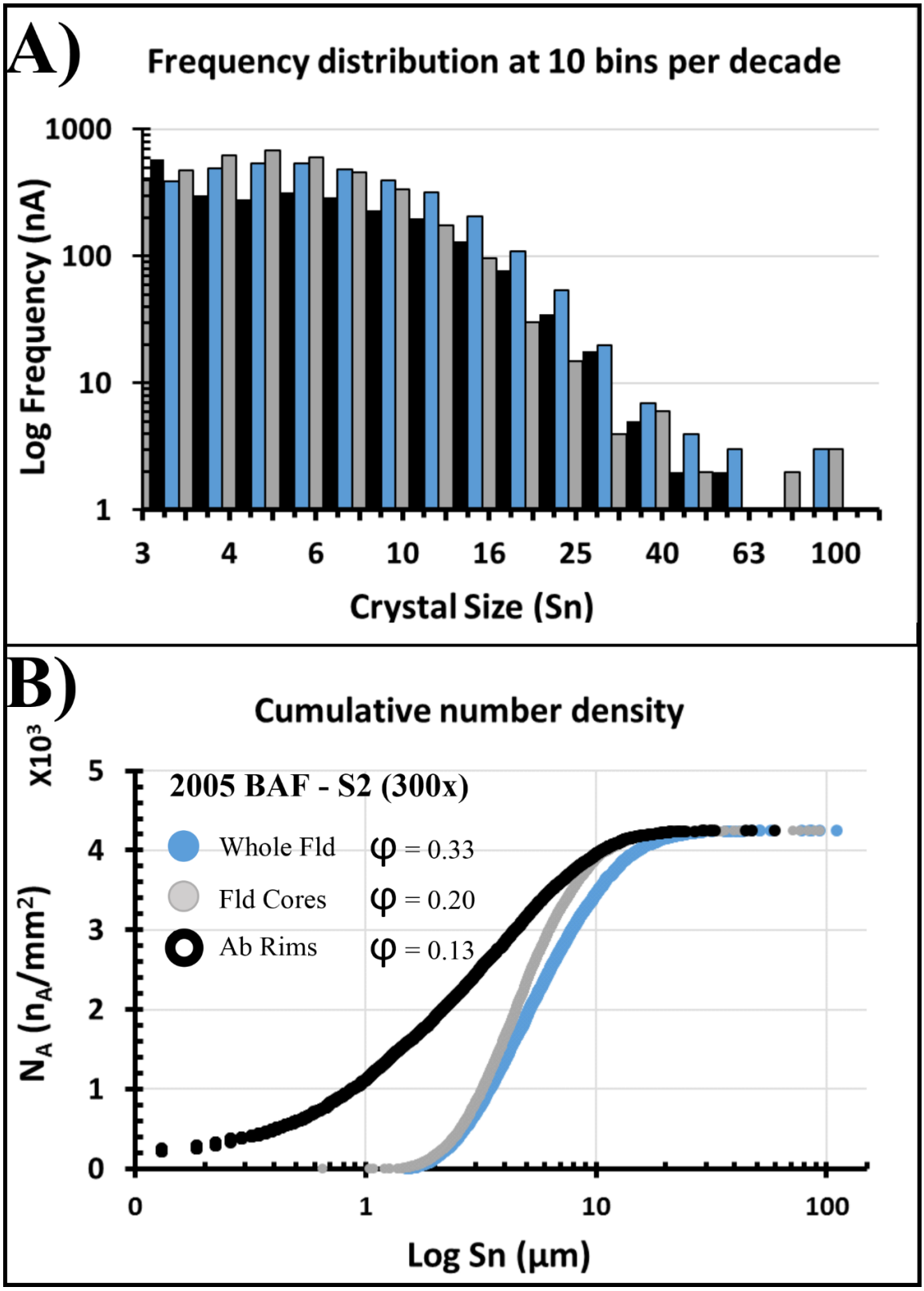

Figure 4.15. *Distributions of compositional zones in plagioclase.* ***A)*** *Frequency size distribution, and* ***B)*** *Cumulative number density distributions with crystal size as a function of area (Sn= √Area) for complete feldspars (whole feldspars) and differentiated zones (AbRims and crystal cores) within sample S2 from the 2005 BAF at 300x (crystal population presented in* ***Fig. 4.6A****).*

4.5. Discussion

In Chapter II, I showed that some batch attributes of groundmass crystals (Sn < 50 μm) display log linear correlations with VER for a suite of historic events of various intensities and eruptive styles at Volcán de Colima, Mexico (**Fig.2.10A**, Chapter II). Besides the syn-ascent crystallisation of groundmass, evidence for degassing-induced phenocryst overgrowth during magma ascent has been recognised in natural volcanic systems (e.g. *Blundy and Cashman, 2001*; *Reubi et al., 2013*) and observed in controlled decompression experiments (e.g. *Martel et al., 2012*; *Riker et al. 2015*). In this chapter, I examine the extent of syn-eruptive crystallisation that occurred as overgrowths on phenocrysts in natural samples; I contrast crystal textures in eruptive products with available experimental studies to deduce the crystallisations kinetics involved and extend the textural-VER correlation to the larger crystals. This is important because syn-eruptive phenocryst crystallisation may affect both qualitative and quantitative assessments of late-stage crystal textures, rheology and magma ascent dynamics that ultimately control eruptive behaviour.

4.5.1. Effects of eruption rates on phenocryst crystallisation

Most quantitative studies of ascent-induced crystallisation focus on the groundmass fraction, since 1) microlites often correspond to the later stages of crystallisation (form syn-eruptively), and 2) smaller crystals coarsen faster than phenocrysts because they have more surface area per unit volume (*Higgins, 2011*). The effects of late-stage crystallisation are illustrated in the φ-VER correlations for plagioclase alone and plagioclase + mafic components in **Figure 4.8**. Here, there is an overall trend of the phenocryst crystallinity (PhC φ) decreasing with increasing VER. The PhC φ-VER trendlines (both total phenocrysts and plagioclase phenocrysts alone) are strongly affected by the 1913 Plinian eruption datum, which has the lowest PhC φ (~ 0.37). If the Plinian data are excluded, PhC φ could be considered constant for intermediate and low-VER eruptions. However, examination of BSE images of plagioclase

crystals shows that they have complex growth histories that include variable amounts of resorption (loss of crystallinity) and both late-stage pre-eruptive (oscillatory-zoned mantles), and in some cases, syn-eruptive overgrowths (oscillatory-zoned mantles and AbRims) (**Fig. 4.9**).

Modal analysis of plagioclase phenocrysts shows abundant resorption features in the plagioclase cores transported by high-VER events (1818 and 1913 Pn eruptions), as well as in crystals from some large effusive eruptions (e.g., 1869 and 1998 LFs; **Fig. 4.9**). The suggested trigger for these eruptions involves mixing between a hotter, water-rich magma batch ascending from the mantle wedge and a more differentiated magma that was stored in a deep reservoir beneath the volcano (*Luhr and Carmichael, 1980*, *1990*, *Luhr, 2002*). Pyroclasts from the 1818 and 1913 eruptions also have lower PhC φ, which is not only consistent with extensive resorption but also suggests that most of the erupted phenocrysts did not undergo significant (if any) crystallisation during ascent. The high proportion of resorption textures in the 1869 and 1998 LFs (**Fig. 4.8** and **4.9A**), suggests that these eruptions may also have decreased in crystallinity during mixing and ascent.

Oscillatory zoning records changes in either the intensive parameters of magma storage or episodes of magma recharge and/or convection in a magma reservoir (*Ginibre et al., 2002*; *Streck, 2008*). The multiple potential origins of oscillatory zoned mantles make it difficult to estimate the amount of feldspar crystallization associated with syn-eruptive magma ascent. **Figure 4.9a** shows, however, that the extent of oscillatory zoning generally increases as VER decreases and is particularly extensive in the 1975 S and 2004 LFs. The feldspar phenocrysts in these lava flows also show high proportions of core resorption (**Figs. 4.3** and **4.9B**), which suggests that oscillatory zoning in these crystals occurred long before eruption, which would suggest that perhaps they do not belong in the oscillatory zoning category in **Figure 4.9A**.

Homogenous albitic rims (AbRims) are the clearest textural example of syn-eruptive crystallisation, as they form crystals margins (**Fig. 4.4**). The component of PhC φ comprising AbRims shows a negative correlation with VER (**Fig. 4.9A**). Albitic plagioclase margins are almost ubiquitous in products from eruptions with VER ≤ 0.5 m^3/s, such as lava domes/plugs and LFs < 1170 m long. Intermediate-VER eruptions (LFs of final length > 2 km; **Fig. 3.1** in Chapter III) contain AbRims only within embayments and clusters of mafic crystals (**Fig. 4.4B-D**); AbRims are absent at higher VER.

Assuming that dissolution and resorption textures are not associated with late-stage magma ascent and eruption, I estimated PhC φ of syn-ascent crystallisation. As noted above, crystal zoning patterns associated with magma ascent and eruption (oscillatory zoning and AbRims) are more extensive in low intensity than in high intensity eruptive products (**Fig. 4.9**). For example, the 2005 BAF sample (VER estimated at 0.05 m^3/s) has a net feldspar PhC φ = 0.36 (**Fig. 4.8**), of which ~ 89% corresponds to oscillatory zoning + AbRims (**Fig. 4.9A**). As most of the oscillatory zoning (~ 95%) is continuous (**Fig. 4.9B**), crystallization associated with eruption accounts for PhC φ ~ 0.30 (**Fig. 4.10**). This value constitutes a maximum bound on syn-ascent crystallisation because of the assumption that all oscillatory zoning is related to the eruptive event (that is, occurs in shallow pre-eruptive storage regions).

The relatively homogenous composition of AbRims (**Fig. 4.4** and **4.6**), as well as their clear correlation with late-stage crystallization, make this texture very suitable for quantitative analysis. An example is provided in **Figure 4.11**, which displays the proportions of AbRims on crystals of 2 ~ 2000 μm for 2005 BAF sample S2 (**Fig. 4.6**). AbRims grow on crystals of any size, from microlites to phenocrysts, but the rim/whole crystal proportion is higher for the smaller crystals (~30 – 100 area % in most crystals of Sn < 150 μm and ~10 – 40 area % in crystals of Sn > 150 μm).

4.5.2. Kinetic regimes of syn-eruptive crystallisation

Crystal attributes help to assess the crystallisation kinetics that can be used to constrain the paths of magma ascent that ultimately control eruptive behaviour in volcanic systems. As demonstrated in Chapters II and III, overall rates of magma ascent control textural features such as N_A, Sn, φ and AR. In this Chapter, I assess the kinetics of phenocryst crystallisation by comparing the cumulative number density and area distributions of plagioclase crystals (microlites and phenocrysts) from three representative Volcán de Colima eruptions (high, moderate and low VER): 1913 Pn, 2004 LF and 2005 BAF (**Fig. 4.12**).

In the whole-population cumulative distributions, N_A is positively correlated with average VER. The largest phenocryst measured in each sample (Sn_{MAX}), in contrast, is negatively correlated with VER, and is thus much smaller in the 1913 Pn sample than in the 2004 LF and 2005 BAF samples (**Fig. 4.12B**). Although subtler than for groundmass crystals, phenocryst AR also varies as a function of average VER (**Fig. 4.13**). Phenocryst $AR_{AV.}$ is higher and more constant in low-VER eruptions (e.g. 2005 BAF) and more variable and with a lower mode in high-intensity eruptions (e.g. 1913 Pn). These textural trends mirror those seen in the groundmass textures (Chapters II and III), and I suggest that they reflect similar kinetic regimes that span from nucleation- to growth-dominated crystallisation, and diffusion- to interface-controlled growth.

Patterns of syn-eruptive growth are revealed by cumulative number density distributions of whole crystals, crystal cores and AbRims in sample 2005 BAF S2 (**Fig. 4.15B**). All crystal components show a steep increase of N_A with size over the size range of 0-10µm; cumulative N_A then remains relatively constant as crystal size increases. The maximum phenocryst N_A is similar for the whole-crystals and the crystal-cores, consistent with the ubiquitous presence of (pre-eruptive) crystal cores. but it is higher than the maximum N_A of AbRims (**Fig. 4.15B**). Therefore, the whole-crystal N_A records the overall effective ΔT during

the ascent without being significantly affected by the addition of AbRims. This means that the AbRim textures crystallise during slow but continuous ascent (as opposed to a shallow dwell followed by a secondary ascent) and that the φ of the whole-crystals adequately integrates the average conditions of ascent so it can be related to an average VER.

The importance of understanding the crystallisation kinetics of AbRims relates to their relevance as a record of late-stage crystallisation processes. Although sharp, compositionally contrasting rims like the AbRims are not rare in nature (e.g. lava domes and short lava flows in my sample suite, **Fig.2.1** in Chapter II, and lava domes from Mount St. Helens, *Cashman and McConnell, 2005*; *Cashman et al., 2008*, and Merapi, *Hammer et al., 2000*; *Preece et al., 2003*), they are not commonly observed experimentally. *Riker et al. (2015)*, however, report thin, sharp rims of more evolved composition in decompression experiments where rapid and large ΔP was followed by substantial dwell times (168 hr) at low pressures (26 MPa). Short (< 43 hr) dwell times, in contrast, produced plagioclase either no (high pressure) or diffuse (low pressure) rims. Cooling experiments on similar samples (rhyodacites of Mount St. Helens, *Rutherford et al., 1985*) further suggest that the way in which undercooling was induced (cooling versus decompression) or the path (continuous versus instantaneous), is not as important for the development of sharp, albitic rims as the dwell time at low P.

During decompression, AbRims form in response to changes in water activity caused by decompression and degassing (*Hammer et al., 2000*). The albitic composition is produced by a shift of the An-Ab + liquid cotectic line of crystallisation towards the alkali + liquid curve as a result of water loss (*Hammer et al., 2000*; *Noguchi et al., 2006*). Continued crystallisation and degassing cause the melt to become more enriched in alkalis, which further changes the equilibrium composition. The cumulative number density distribution of AbRims (**Fig. 4.15B**) and a drop in the K_2O-SiO_2 fractionation path in the matrix glass compositions

(**Supplementary Material 2.6** in Chapter II) reflect the protracted and extensive decompression-induced crystallisation in low VER eruptions.

4.5.3. Implications for estimates of eruptive behaviour

Traditional studies that consider only the groundmass crystals overlook the information that can be derived from contemporaneous phenocryst overgrowth. This study shows that this omission can be problematic, especially when analysing the crystal textures of eruptive products derived from low-intensity eruptions. The outcome of my textural analysis demonstrated that there is a ubiquitous crystal overgrowth, particularly at the lower spectrum of eruptive intensity (**Fig. 4.11**) and that this overgrowth both increases the Sn (**Fig. 4.11** and **4.12**) and affects the shape (**Fig.4.13** and **4.14**) of all crystals (microlites and phenocrysts), ultimately, causing an overall increase in the net φ of a sample (**Fig. 4.8**, **4.10**). Crystal overgrowths also help to define a boundary between what is defined as "microlites" and "phenocrysts" (**Fig. 4.12B**) based on the crystal sizes, which also appears to correlate with eruption conditions (**Fig. 4.12**). This is important, as definitions of "microlites" often relies on arbitrary size boundaries that range < 100 µm (*Couch et al., 2003*; *Martel and Poussineau, 2007*; *Clarke et al., 2007*) to < 15 µm (*Hammer et al., 1999*), with any number of values between that range (e.g. < 35 µm, *Wright et al., 2012*; < 50 µm, *Noguchi et al., 2008*; *Preece et al., 2013*; < 60 µm, *Szramek et al., 2006*; *Scott et al., 2012*).

Quantitative assessments of groundmass crystal textures in the previous chapters were performed using an arbitrary definition of microlite crystals as Sn < 50 µm. However, decreasing the microlite size limit from 50 to 35 µm (for comparison to another dataset), did not significantly affect φ or the φ – Log VER correlation (**Fig. 2.10** in Chapter II). There are few crystals between the groundmass Sn_{MAX} of each sample and the arbitrary microlite-phenocryst size-boundary of 50 µm applied in all chapters of this thesis. Furthermore, the groundmass Sn_{MAX} in the cumulative distribution for the lowest intensity eruption plotted in

Figure 4.12 (2005 BAF, with the highest Sn_{MAX} value) is 32 µm, below the second limit set at 35 µm. The gaps in cumulative N_A data, however, suggest that the set limit at Sn < 50 µm used to quantify groundmass textures is too high for eruption products from Volcán de Colima, and that the difference between the arbitrarily defined boundary and the real boundary increases for eruptions of higher intensity. Hence, I propose that in order to quantify "groundmass crystallinity", the size-range that defines microlites from phenocrysts needs to be adequately adapted to the eruptive conditions (intensity and style) and to specific volcanic systems (indeed, the variation of φ for the same VER is different at Volcán de Colima and Tungurahua, **Fig.2.10B** in Chapter II).

Our previous assessments of ubiquitous crystal overgrowth at slow to intermediate eruptions further suggest that we should re-visit the syn-ascent crystallisation kinetics extracted from conventional quantitative methods of textural analyses (e.g. CSDs or batch textural parameters) and that phenocryst growth can play a significant role toward understanding eruptive behaviour in nature. Furthermore, omitting textural information of crystals formed at low magmatic ascent rates could have great repercussions in hazard assessments. For instance, high frequency events such as Vulcanian eruptions often shift between violent explosive stages and effusive dome growth (e.g. Chapter III). Whether the eruption is explosive or effusive greatly depends on the rheological evolution of the ascending magma that ultimately controls the efficiency of degassing (i.e. inefficient degassing can build overpressure that leads to violent rupture of the confining magma). The efficiency of degassing, in turn, may be largely modulated by interactions, which depend on crystal content, sizes, shapes and distributions (*Cimarelli et al., 2011*; *Mader et al., 2013*, *Oppenheimer et al., 2015*). Therefore, I advocate a holistic size-population approach when quantifying and interpreting textural parameters to allow for more accurate forecasts of eruptive behaviour of natural systems.

4.6. Conclusion

Phenocryst overgrowth occurs as an effect of degassing-induced crystallisation during magma ascent in volcanoes (*Cashman, 1988*; *Blundy and Cashman, 2001*; *Martel and Schmidt, 2003*). *Riker et al. (2015)* decompression experiments showed that two main kinetic conditions favour larger volume fractions of phenocryst overgrowth (with up to ~ 50 vol.%): (1) low decompression rates and (2) prolonged time at low pressures (e.g. 1MPa/hr at P_f = 25 MPa). In natural volcanic systems, slow ascent rates and shallow residence of magma are common during dome-forming eruptions.

In this chapter, I not only show evidence that significant phenocryst overgrowth occurs in natural volcanic systems, but also demonstrate its dependence on the average VER (**Fig. 4.8**). Similar to their microlite counterpart, phenocrysts attain larger Sn and AR with decreasing eruptive intensity (**Fig. 4.12** and **4.13**), highlighting an interface-controlled regime of crystallisation. The very low overgrowth PhC φ estimated from phenocrysts texture proportions (**Fig. 4.8**, **4.9**) and the broader AR distributions and large discrepancy between average $AR_{AV.}$ of GM and $AR_{AV.}$ of PhC in the high intensity eruptions (**Fig. 4.13**), as well as the relatively constant N_A of larger crystals in samples of contrasting intensities (**Fig. 4.12** and **4.15**), suggest that overgrowth exclusively corresponds to a growth-dominated regime.

Finally, this work highlights the importance of integrating phenocryst rim overgrowth in textural analysis for the interpretation of syn-eruptive processes, especially for events of lower intensities where overgrowth becomes more significant. Low intensity eruptions, such as dome-forming events, often experience the largest rheological changes due to extensive degassing during slow magma ascents. The larger increase in crystallinity and the decrease in viscosity from extensive degassing ultimately drive the unsteady nature of slow-ascent sequences. This, combined with the relatively high frequency of these events, entails the holistic approach of textural analysis for adequate risk assessments of volcanic eruptions.

Chapter 5

Conclusions, implications and further applicability

Groundmass crystals can be used to determine ascent conditions of volcanic eruptions. In particular, two approaches are generally used to investigate syn-eruptive crystallisation of magmas from crystal textures: (1) crystallisation experiments on magma analogues, and (2) textural and chemical analyses of natural samples. The experimental approach investigates the kinetics of magma crystallisation under controlled settings and with different ranges of physicochemical variables (P, T, x). These experiments seek to analogically recreate both intra-conduit degassing and crystallisation during magma ascent at different rates and decompression paths (e.g. *Geschwind and Rutherford, 1995*; *Hammer and Rutherford, 2002*; *Couch et al., 2003*; *Martel and Poussineau, 2007*; *Hammer, 2008*; *Shea and Hammer, 2013*). The second approach, which combines analyses of natural samples with observations of eruptive processes, makes use of some of the findings from experimental work. Specifically, these studies link the intra-conduit kinetics with external characteristics of volcanic eruptions such as eruptive magnitude and intensity (e.g. *Hammer et al 1999*; *Wright et al., 2012* and *Preece et al., 2013*), and eruptive style and transitions in eruptive styles (e.g. *Cashman and McConnell, 2005*; *Hammer et al 1999, 2000* and *Preece et al., 2013, 2016*). This thesis offers a variation on the second approach. The implications, outlook and recommendations for future work laid out in this chapter are focused on the analyses of crystal textures of natural erupted products and their links to physical and behavioural features of volcanic eruptions.

Table 5.1. *Table of symbols and abbreviations used in Chapter V.*

Chapter V - Table of symbols and abbreviations	
Symbol/Acronym	**Definition**
Ab	Albite
An	Anorthite
$AR_{AV.}$	Average crystal aspect ratio
BAF	Block-and-ash flow
BSE	Back-scatter electron analysis
GM	Groundmass
LF	Lava flow
MPa	Megapascals
N_A	Crystal number density
P	Pressure
Pn	Sub-Plinian eruptions
R^2	Coefficient of determination
T	Temperature
vol. %	Percentage of a given element per sample volume
wt.%	Percentage of a given element per sample weight
x	Chemical composition of a system
φ	Crystal fraction

5.1. Assessing physical proxies for volcanic eruption rates.

Post-eruptive crystallisation during the emplacement of silicic lavas is limited by the highly viscous nature of the melt (*Preece et al., 2013*). For the same lava compositions, flows of different lengths can have variable crystallinities, yet along an individual flow, crystallinity varies less (*Muir et al., 2014*). Furthermore, for cooling-limited lava flows, the advance during emplacement strongly depends on the rheology at the front (*Castruccio et al., 2014*) and the distance from the vent to the front is strongly dependent on the average effusion rate of the eruption (*Walker, 1973*). Therefore, I tested how crystal textures at the lava flow fronts associate with the final flow lengths and with the average eruptive conditions of the respective events. First, I performed image analysis of crystal textures for various samples collected along a well-monitored, historic lava flow at Volcán de Colima (2004 lava flow). I found that,

although there is textural variability along the flow, the average values of the textural parameters analysed are similar to the textural values of the sample collected at the front (**Fig. 2.6** in Chapter II). Second, I compiled the final lengths of 7 different lava flows as well as the textural values of groundmass crystals from samples collected at the flow fronts. This led to the discovery that both parameters display linear correlations with the average eruption rate (**Fig. 2.7**, **2.9** and **2.10**).

My findings confirm from a textural perspective that the final length of lava flows can work as a physical proxy for average eruption rates as suggested by *Walker (1973).* Furthermore, they show that lava flow fronts are adequate sampling sites, since the textures in samples from the fronts texturally correlate with the average eruptive intensity. Therefore, this type of study can be applied to a wide variety of field sites: flow fronts are often more easily accessible. A further observation is that samples remobilised from inaccessible lava fronts as rockfalls or block-and-ash flows could also be suitable to estimate average eruption rates. The correlation between the crystal textures, the final flow lengths, and the average eruption rates suggest feedback between ascent rate and the rheological changes caused by degassing and crystallisation that create the resistance to magma ascent in the conduit.

Some limitations in my work are: (1) textural variability along an individual lava flow was tested for only one event; (2) the physical measurements of the lava flows have large uncertainties associated with the resolution of the imagery used and to the lack of pre-eruptive ground data; (3) for most flows, only samples collected at the fronts were analysed, and (4) eruption rates reported in literature for most eruptions are based on limited observations, can be vague (e.g. dimensions estimated from comparison to sizes of trees; *Luhr and Carmichael, 1990*) and do not indicate uncertainties. To address these limitations, I suggest that a first priority should be to run more analyses on a series of samples from several lava flows of Volcán de Colima to test textural variability in silicic lava flows. Second, in recent years the coverage

and quality of aerial imagery of the edifice of Volcán de Colima has improved (e.g. *James and Varley, 2012*), and is complemented by precise, land-based topographical measurements (e.g. *García-Nava, 2016*). These tools should be used for more robust estimations of lava flow and dome dimensions and thus eruption rates. I also suggest that comparative textural studies should be extended to different volcanoes (of both similar and different compositions to Volcán de Colima).

5.2. Considerations on the style of eruptions when studying degassing-induced textures.

When quantifying volumes of erupted material from deposits, natural processes such as reworking, erosion or overlapping of eruptive sequences, often affect the results. Poor measurements of erupted material lead to large uncertainties when estimating the magnitude and intensity of volcanic eruptions. Recent studies on syn-eruptive, degassing-induced magmatic textures suggest that some textural attributes of bubbles and crystals preserve evidence of the rate of magma ascent in the conduit that correlates with volumetric eruption rates (*Hammer et al., 2000*; *Poland et al., 2014*; *Cashman and Scheu, 2015*). Most works comparing crystalline textures of natural samples with volcanic processes in nature aim to recreate pre- and syn-eruptive stratigraphy, decompression rates, and ascent rates in the conduit that affect eruptive behaviour (e.g. *Hammer et al., 1999, 2000*; *Cashman and McConnell, 2005*; *Preece et al., 2013, 2016*). Only a few of these studies directly compare textural parameters with eruption rates (e.g. *Hammer et al., 2000*; *Wright et al., 2012*).

Hammer et al. (2000) performed a correlation between eruption rates and textural parameters for four different eruptive periods (1986-88, 1992-93, 1994 and 1995) at Merapi, Indonesia. They found that the groundmass crystal number density (N_A) versus average eruption rates showed the best fit ($R^2 = 0.98$), and that the straight-line regression could be used to reconstruct unknown intensities at Merapi. Contrary to the case for Merapi *(Hammer et al., 2000*), I found

that the relationship between N_A and eruption rate was poor (R^2= 0.22) and not statistically significant (**Table 2.5** in Chapter II).

In another study, *Wright et al. (2012)* analysed crystal textures in andesitic ash samples erupted between 1999 and 2006 at Tungurahua, Ecuador, during Strombolian, Vulcanian and sub-Plinian eruptions. They observed that volumetric eruption rate (estimated from the cumulate volume emission over a 2-month period) correlated with the groundmass crystallinity. Moreover, they proposed a relationship between the eruption rate and eruption style, explained by the extent of degassing and crystallisation in time and thus on the rheological properties of magma.

Compared with the Merapi (*Hammer et al., 2000*) and Tungurahua (*Wright et al., 2012*) datasets, my work at Volcán de Colima covered a longer period of eruptive activity and a broader range of eruptive styles (Chapter II), yet I still found similar relationships between crystallinity and eruption rates. All three field sites have similar bulk compositions, although Merapi (~ 56 wt. % SiO_2) and Tungurahua (~ 58 wt. % SiO_2) have slightly less silicic lavas than Volcán de Colima (~ 61 wt. % SiO_2). Despite this slight variation in SiO_2 content, overlaying the three different datasets reveals remarkably good agreement between the slopes of the linear relationships for crystallinity and eruption rate (**Fig. 2.10** in Chapter II). The main discernible difference is that the Tungurahua samples have slightly lower crystallinity values.

The observation that crystallinities at Tungurahua were lower (despite the fact that lavas of less silicic compositions should lead to more crystallisation), suggests that eruptive style may also play a role in the extend of degassing-induced crystallisation. Indeed, whereas the samples used for the textural fits at Volcán de Colima were produced during steady-style (sustained) eruptions (e.g. effusive eruptions), most of the samples at Tungurahua were derived from unsteady (pulsatory) eruptions (Strombolian and Vulcanian). On the other hand, the

crystallinity versus eruption rate fit for the Merapi samples, which derived from lava domes (effusive eruptions), is almost identical to the fit of Volcán de Colima samples (**Fig. 2.10** in Chapter II). Nevertheless, Merapi crystallinity data has significant more scatter (R^2= 0.46) and is below a 95% confidence value (**Table 2.5** in Chapter II).

To test the effects of eruptive style on the final degree of degassing-induced crystallisation, I expanded my textural analysis on products derived from two different Vulcanian eruptions at Volcán de Colima (2005 and 2013). The samples include products associated with both effusive (lava dome and flow) and explosive (ash-fall) stages of the Vulcanian eruptions. Therefore, I could distinguish between two dynamic processes that occur in the conduit: (1) Conduit (re)fill, controlled by bubble-driven magma ascent, and (2) Downward fragmentation and evacuation of magma in the conduit that rather reflects supersaturation conditions at different depths of residence (*Clarke et al., 2007*). My study included textural data from ash and blocks that were produced during block-and-flows. Additionally, I incorporated to my analysis available textural data from air-fall ash and clasts derived from 2013 activity including rockfalls from the growing dome and ballistics after *Cassidy et al. (2015)*. Therefore, I covered a range of materials representing different stages of the 2005 and 2013 Vulcanian eruptions at Volcán de Colima. Samples associated with slow, effusive stages of conduit (re)fill could be distinguished by the presence of sharp, albitic rims on feldspars, and by low matrix vesicularity. Conversely, ash produced during explosive stages where the conduit experienced fragmentation and evacuation would lack albitic rims and tend to have higher vesicularities.

For the samples that I texturally associated with crystallisation during conduit (re)fill, I estimated eruption rate values using best-fit linear correlations that I previously determined from known data for effusive and sub-Plinian eruptions at Volcán de Colima (Chapter II). The resultant eruption rates for some of the samples were comparable with reported effusion rates

using visual estimations of intra-eruptive lava domes for the 2005 Vulcanian sequence (my data: 2.1 ± 1.4 m^3/s, versus 1.2 to 4.6 m^3/s after *Varley et al., 2010a*). My investigation was complicated by the scarcity of detailed records on eruption rates. Therefore, I could not adequately calibrate my textural results for the two different stages of the Vulcanian eruptions. Whereas eruption rate values estimated for samples associated with magma ascent during conduit (re)fill were within the usual ranges reported for Volcán de Colima lava domes, the eruption rate estimates from ash-fall textures resulted in values as high as the sub-Plinian eruptions of Volcán de Colima (**Fig. 3.12** in Chapter III). Therefore, my method overestimates eruption rates for the explosive phase of Vulcanian eruptions. These observations are important because some textural studies combine textural analysis of products from steady and unsteady eruption styles irrespectively (e.g. *Hammer et al., 2000*; *Preece, 2013, 2016*). My analysis suggests that different approaches should be applied to products from the two different magma rise dynamics during Vulcanian eruptions.

Textures in samples associated with fragmentation in the conduit can be adequate to constrain stratigraphic intra-conduit conditions of supersaturation (e.g. *Cashman and McConnell, 2005*; *Preece et al., 2016*) or indicate the supersaturation at the fragmentation depth (*Clarke et al., 2007*). Previous studies have shown that conduit fragmentation depth correlates with the intensity of Vulcanian explosions (*Druitt et al., 2002*; *Clarke et al., 2007*). On this basis, it seems entirely likely that future advances in estimates of eruption rates from textural and chemical analyses on samples erupted by fragmentation could allow the estimation of eruption rates of the explosive stages of Vulcanian eruptions.

I suggest that that eruptive intensity indeed correlates to a degree of supersaturation in the magma, and in turn is imprinted in the degassing-induced textures, irrespectively of the kinetic process leading to the eruptive output. However, independent measurements on eruption rates of the explosive stages of Vulcanian eruptions (associated with the samples that

are to be texturally analysed) are necessary to perform adequate calibrations. This party explains the difference in groundmass crystallinity observed in the linear fits for crystallinity versus eruption rate in samples from Volcán de Colima and Tungurahua (**Fig. 2.10** in Chapter II). I propose that future investigations seeking to calibrate textures with intensity should distinguish between processes related to slow ascent versus fragmentation and should analyse the resulting textures separately for each of the processes. A more solid way to being able to identify conduit (re)fill and conduit fragmentation could be obtained by complementing the textural data and observations of the eruptions with geophysical evidence (e.g. seismicity, *Varley et al., 2010b*; ground deformation, *Preece et al., 2013*; gas flux measurements, *Cassidy et al., 2015*).

5.3. How to improve the development of petrological proxies for assessment of volcanic activity in the future.

Phenocryst crystallisation is not exclusively limited to cooling of magma within a deep reservoir. Most phenocryst overgrowth occurs primarily during ascent after degassing of water-saturated magma caused by decompression (*Blundy and Cashman, 2001*). In fact, besides crystallisation of groundmass, evidence for degassing-induced phenocryst overgrowth has also been observed in controlled decompression experiments (e.g. *Martel et al., 2012*; *Riker et al. 2015*). Estimates of crystal overgrowth related to degassing-induced crystallisation can be made under controlled experimental settings by measuring crystallinity before and after decompression (e.g. *Riker et al., 2015*). Quantifying overgrowth in crystals of natural samples is more complicated than in experiments, since it is necessary to define what portions of the crystal correspond to pre-ascent stages and what portions grew during syn-eruptive ascent. Some authors suggest that phenocrysts with euhedral margins and rims of oscillatory zoning reflect polybaric, near-isothermal processes of decompression-induced fractional crystallisation (*Blundy and Cashman, 2001*). *Reubi et al. (2013)* suggested, based on feldspar-

hosted melt inclusion volatile contents from Volcán de Colima, that oscillatory borders developed syn-eruptively and that the melt was sealed and entrapped during magma ascent due to crystal overgrowth. Another late-stage textural feature commonly observed in natural samples are feldspars with sharp, albitic rims (e.g. lava domes and short lava flows in my sample suite, **Fig.2.1** in Chapter II, and lava domes from Mount St. Helens, *Cashman and McConnell, 2005*; *Cashman et al., 2008*, and Merapi, *Hammer et al., 2000*; *Preece et al., 2013*). However, they are rarely attained experimentally. Only a couple of decompression experiments on Mount St Helens melts produced thin, albitic rims on feldspars (*Rutherford et al., 1985*; *Riker et al., 2015*). *Rutherford et al. (1985)* reported that long dwell times at low pressures produced sharp, albitic rims during cooling experiments and *Riker et al. (2015)* also produced thin and sharp albitic rims around feldspars during rapid decompression experiments that were followed by long dwell times (168 hours) at low pressures (26 MPa). Previous experimental data suggest that long dwell times at low pressures produces crystallisation of albitic rims as progressive degassing causes the melt to become more enriched in alkalis and shifts the An-Ab + liquid cotectic line of crystallisation towards the alkali + liquid curve (*Hammer et al., 2000*; *Noguchi et al., 2006*).

Despite evidence for degassing-induced crystal overgrowth, there are no detailed quantitative studies of the proportion of phenocryst syn-eruptive crystallisation in natural products. Based on the suggestion of *Blundy and Cashman (2001)* that oscillatory zoning mostly occurs as overgrowth from ascent, and that albitic rims correspond to late-stage crystallisation, I analysed BSE-scans of plagioclase phenocrysts to estimate the proportion and distribution of these textural features from products associated with different eruptive intensities and styles from Volcán de Colima. My results show that the proportion of both oscillatory zoning and albitic rims negatively correlate with eruptive intensity (**Fig.4.9** in Chapter IV), suggesting that more extensive degassing-induced crystallisation occurs as

overgrowth around phenocrysts at lower-intensity eruptions. Moreover, a detailed analysis of the distribution of albitic rims showed that these overgrowths are ubiquitous on microlites and phenocrysts from a sample derived from a low-intensity eruption (**Fig.4.11** in Chapter IV). This supports the hypothesis that degassing-induced crystallisation may affect all crystals in ascending magma. Further textural analysis of complete size-populations of crystals from samples representing high, intermediate, and low eruptive intensities (1913 Pn, 2004 LF and 2005 BAF) highlights the dominant role of kinetic processes of crystallisation relative to intensity and its separate effects on the microlites and phenocrysts groups. Shape analysis and the integration of cumulative number density and area distributions of the three samples showed that crystal-growth kinetics are dominant at low-intensity eruptions, whereas nucleation dominates at higher-intensities, albeit with a reduced effect on phenocryst crystal growth (**Fig.4.12** and **4.13** in Chapter IV).

Additionally, I was able to determine microlite and phenocryst maximum crystal sizes at each of the samples based on gaps in the distribution of their whole crystal populations (**Fig.4.12** in Chapter IV). I observed that larger maximum crystal sizes, in both groundmass and phenocrysts populations, develop at lower intensities and shift towards smaller microlite sizes, (with a larger gap between small and large crystals) with increasing intensity, indicating that the microlite-phenocryst size-boundary also depends on intensity. These results suggest two fundamental considerations for robust textural analysis in the future: (1) phenocryst degassing-induced overgrowth should be quantified in addition to groundmass crystallisation in order to characterize syn-eruptive processes from crystal textures, and (2) based on a complete size-analysis, the size-definition of “microlites” and “phenocrysts” should be carefully defined. These two considerations are imperative for future studies, as (1) most current studies on ascent-related crystallisation only consider groundmass crystals (e.g. *Hammer et al 1999, 2000*; *Hammer and Rutherford, 2002*; *Couch et al., 2003*; *Cashman and*

McConnell, 2005; *Martel and Poussineau, 2007*; *Hammer, 2008*; *Wright et al., 2012*; *Shea and Hammer, 2013*; *Preece et al., 2013, 2016*), and (2) the definition of "microlites" often relies on arbitrary size boundaries that range from < 100 μm (*Couch et al., 2003*; *Martel and Poussineau, 2007*; *Clarke et al., 2007*) to < 15 μm (*Hammer et al., 1999*), with any number of values in between (e.g. < 35 μm, *Wright et al., 2012*; < 50 μm, *Noguchi et al., 2008*; *Preece et al., 2013*; < 60 μm, *Szramek et al., 2006*; *Scott et al., 2012*).

Finally, correlating the crystallinity of all mineral phases (both microlites and phenocryst) from each sample with the respective average eruption rates of the eruptions from which they were derived, showed similar straight-line slopes to that of the groundmass feldspar correlations analysed in Chapters II and III (**Fig. 4.8** in Chapter IV). Although there is currently no work that has applied this approach, I advocate for future textural analyses to integrate the whole spectrum of crystal sizes and mineral phases at particular volcanoes to develop tight petrological correlations with physical and intensive eruptive parameters. This would have the potential to serve as reconstruction tools to support hazards assessment and risk management.

5.4. Proposed model for eruptive styles at Volcán de Colima in the context of syn-eruptive textures

There are two main phases of crystallisation that can be related to different processes in arc stratovolcanoes like Volcán de Colima. The first phase corresponds to crystallisation in reservoir regions at depth, where chemical differentiation and magma heat loss to the surrounding medium, over extended periods of time, cause the development of crystals. Large, equant crystals of less evolved compositions typically result from this phase. The second phase occurs when magma is in disequilibrium during near-isothermal ascent. The rate and path of this ascent significantly controls the physicochemical features in the produced crystals, particularly in anhydrous minerals, such as plagioclase, since these are more sensitive to changes in dissolved water in the melt as it experiences exsolution and degassing. Since the

latter process was the focus of this thesis, I summarise in this section my interpretation of syn-ascent crystallisation kinetics inferred from textural analysis performed on a suite of Volcán de Colima lavas that encompass a wide range of eruptive intensities and styles.

Previous studies suggest the magmatic system at Volcán de Colima can be divided into three main sections: a deep magma reservoir (~ 8 -10 km depth, *Luhr and Carmichael, 1980, 1990*; *Luhr, 2002; Luhr, 2006*), a shallower reservoir or a region of interconnected dykes (~ 3 -7 km depth, *Zobin et al., 2012*; *Reubi et al., 2013*), and a shallow, network of dykes (*Lavallée et al., 2012*) (**Fig. 5.1**). The textural attributes of the erupted lavas reflect the integrated effects of the distance travelled from source to vent (proportional to a net degree of undercooling derived from the extent of decompression), the ascent rate and the thermal and chemical state of the ascending magma batch.

Two main eruptive triggers are proposed at Volcán de Colima:

(1) The Plinian scenario, where an input of fresh magma of more mafic composition intrudes a deep reservoir and mixes with more differentiated magma. This process is generally recognised as the main cause of sub-Plinian eruptions at Colima (*Luhr and Carmichael, 1980, 1990*; *Luhr, 2002*).

(2) The second scenario involves lavas originating from a shallower source. Magma ascent from this region would therefore be shorter in distance and possibly in time, which can result in large rheological changes in the ascending magma that would ultimately control whether magma extrusion is effusive or explosive (**Fig. 5.1**).

I provide a general overview on crystal textures that can be expected as a result of syn-eruptive crystallisation at three different scenarios of magma ascent rates that prevail at Volcán de Colima.

In sub-Plinian eruptions, the input of fresh magma at depth creates a large disequilibrium between the pre-existing crystals and the hybrid melt, resulting in extensive resorption of crystals (**Fig. 5.1**). The highly buoyant, hybrid magma quickly ascends and the high degree of undercooling results in magma with a low crystal fraction, high crystal number densities, and crystals of small size and either more acicular or complex shapes (e.g. hoppered or dentritic) in a vesicular matrix (**Fig. 5.1**). This scenario is dominated by a nucleation regime of crystallisation, and thus, most of the crystallisation occurs in the groundmass rather than as phenocryst overgrowth. The products erupted consist of relatively small (compared with those in lava flows and domes), mostly resorbed phenocrysts in a vesicular groundmass with a large number of small, elongated microlites (**Fig. 5.1.**)

Eruptive deposits generated during moderate eruption rates, such as effusive lava flow-forming events (~ 2 to 4 m^3/s; **Table 2.2** and **Fig. 2.10**), have more time to crystallise than those from (sub-)Plinian eruptions. Additionally, if they derive from a shallower source region, the net decompression experienced is less. Contrasted with the sub-Plinian case, pre-ascent crystals in magma batches associated with moderate ascent rates experience rim overgrowth simultaneously with groundmass crystallisation. Therefore, although different kinetic processes act according to crystal size (growth on pre-existing particles is generally favourable), overall groundmass and phenocryst rims share the same ascent history but differ in some of their batch attributes. Also, phenocrysts in this scenario are likely to attain slightly elongate shapes as a consequence of diffusion-controlled growth. The erupted products from moderate ascent rate scenarios therefore have large isolated phenocrysts and/or crystal glomerates that have thick oscillatory zoned rims. These are within a groundmass of numerous crystals of acicular shapes and larger sizes than the sub-Plinian products, which consequently leads to a higher GM φ.

At the slowest ascent rates (e.g. associated with dome growth), crystallization occurs almost completely within a growth regime influenced by low effective degrees of supersaturation. Overgrowth of phenocrysts in this case can be comparable to groundmass crystallization (reaching up to 40 or 50 vol.%; Chapter IV and *Riker et al., 2015*). The slow and protracted crystallisation associated with very slow magma ascent includes crystallisation under more water-depleted conditions, resulting in sharp rims (highly contrasting with the crystal interiors) of more homogenous and albitic composition. Such extensive crystallisation within the growth-dominated regime leads to large phenocrysts with thick oscillatory internal patterns surrounded by sharp, albitic rims. The groundmass in this scenario has the lowest N_A of the three ascent scenarios and the crystals are relatively large and close to equant in shape (high $AR_{AV.}$). The larger microlites have more anorthite-rich cores with a contrasting albitic rim, whereas the smallest crystals are mostly of albitic composition. The GM φ can be similar to the moderate ascent scenario because a substantial proportion of crystallisation occurs on phenocrysts.

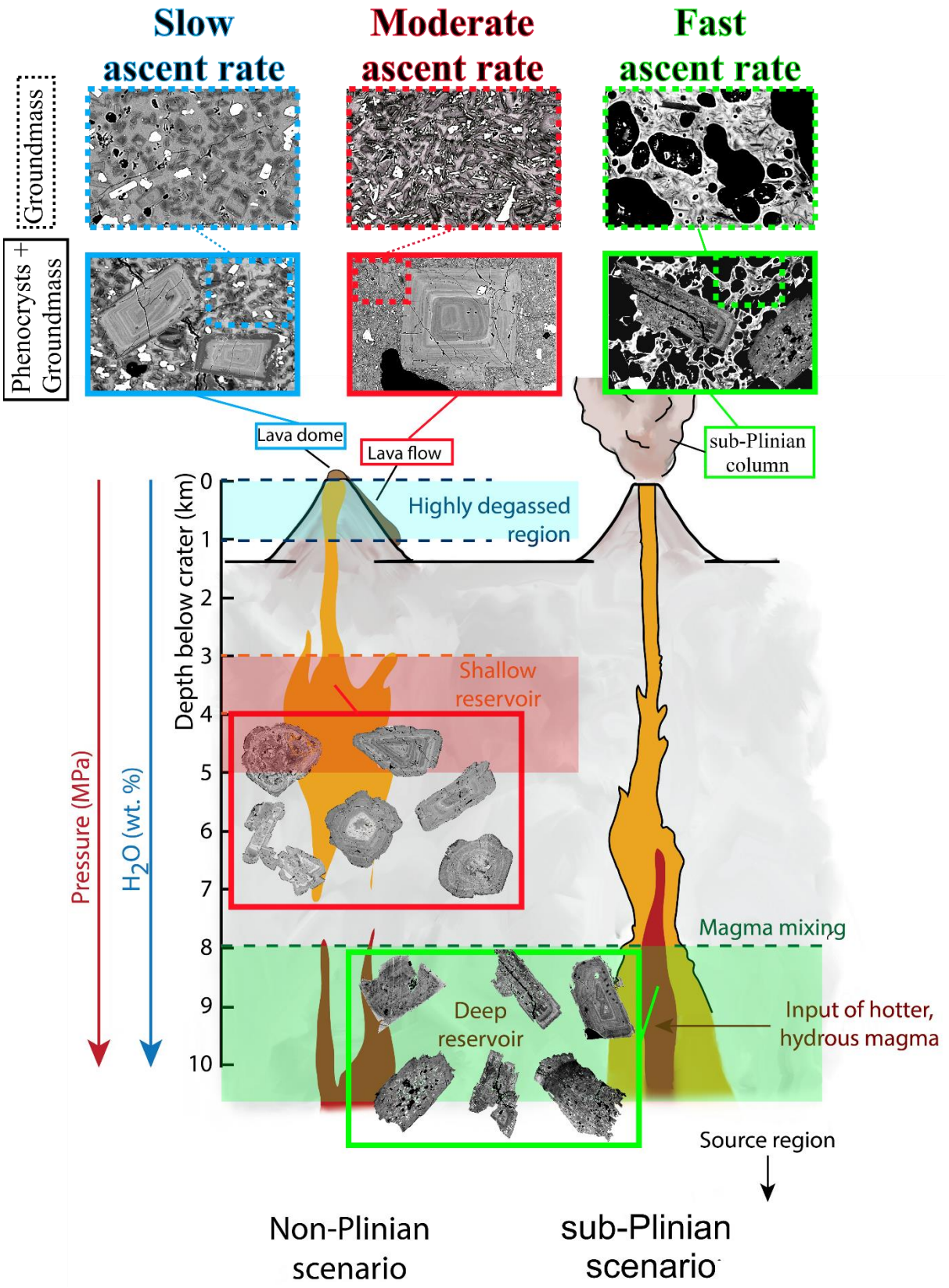

Figure 5.1. *Schematic of the two main eruptive scenarios recognised at Volcán de Colima. Example BSE-images of phenocryst and microlite crystals at depth and in erupted products are linked to regimes of ascent rates.*

5.5. Closing remarks

I conclude this work answering my initial question: "Is it possible to develop a robust geological tool for the interpretation and reconstruction of syn-eruptive volcanic processes at Volcán de Colima?". The answer is affirmative. It could even be developed for other volcanoes, however, to achieve this, some important points must be considered.

First, post-eruptive crystallisation of lavas may affect the final crystal textures and therefore would no longer exclusively reflect the integrated kinetics of ascent crystallisation. Thus, it is important to assess the extent of emplacement crystallisation. Also, it is important to consider that the different batch textural attributes (crystal fraction, number density of crystals, average size and morphology) may be susceptible to fluctuations in and the magnitude of eruption rates. One should contrast their variability within individual eruptive sequences and amongst products that represent a range of eruptive intensities and styles. A third consideration is that crystalline attributes in eruptive products originated from Vulcanian eruptions may reflect a degree of undercooling associated with the supersaturation at different depths within the magmatic conduit rather than reflecting the integrated degassing of a magma batch caused by its buoyant ascent to the surface. It is necessary to identify the intra-conduit process behind the origin of Vulcanian products by complementing the analysis of batch textures with the identification of additional compositional features (e.g. albitic rims) or vesicularity. Additionally, some studies provide detailed geophysical evidence for magma ascent (e.g. seismicity, *Varley et al., 2010b*; ground deformation, *Preece et al., 2013*, and flux of gases, *Cassidy et al., 2015*) and, these could be combined with textural analysis and visual monitoring to develop detailed studies of syn-eruptive processes of degassing and crystallisation. Finally, by utilizing a holistic approach that integrates batch textural parameters and compositional features (zoning patterns) of crystals of all sizes (microlites and phenocrysts) and mineral

phases rather than only considering groundmass feldspars, this research expanded the classical textural analyses of degassing-induced crystallisation.

In conclusion, an integrated textural approach, taking into account the listed considerations, enables the use of syn-eruptive textures as proxies for intensive parameters of volcanoes. The ultimate applicability of this approach in volcanology is as a petrological tool for the identification and reconstruction of eruptive behaviour necessary for robust risk assessments by correlating textures that preserve records of eruptive conditions in accessible samples with dynamics of magma ascent, degassing and crystallisation that determine eruptive behaviour.

References

Alidibirov, M. A. (1994). A model for viscous magma fragmentation during volcanic blasts. Bulletin of Volcanology, 56(6-7), 459-465.

Alidibirov, M. A., & Dingwell, D. B. (1996). Magma fragmentation by rapid decompression. Nature, 380(6570), 146-148.

Arreola, J. M. (1915). Catálogo de las erupciones antiguas del volcán de Colima. Memorias de la Sociedad Científica Antonio Alzate (32), 443-481.

Arzilli, F., & Carroll, M. R. (2013). Crystallization kinetics of alkali feldspars in cooling and decompression-induced crystallization experiments in trachytic melt. Contributions to Mineralogy and Petrology, 166(4), 1011-1027.

Atlas, Z. D., Dixon, J. E., Sen, G., Finny, M., & Martin-Del Pozzo, A. L. (2006). Melt inclusions from Volcán Popocatépetl and Volcán de Colima, Mexico: melt evolution due to vapor-saturated crystallization during ascent. Journal of Volcanology and Geothermal Research, 153(3), 221-240.

Blundy, J., & Cashman, K. (2001). Ascent-driven crystallisation of dacite magmas at Mount St Helens, 1980-1986. Contributions to Mineralogy and Petrology, 140(6), 631-650.

Borgia, A., & Linneman, S. R. (1990). On the Mechanisms of Lava Flow Emplacement and Volcano Growth - Arenal, Costa-Rica. Lava Flows and Domes, 2, 208-243.

Borgia, A., Linneman, S., Spencer, D., Morales, L. D., & Andre, J. B. (1983). Dynamics of Lava Flow Fronts, Arenal-Volcano, Costa-Rica. Journal of Volcanology and Geothermal Research, 19(3-4), 303-329.

Bretón-González, M. B., Ramírez, J. J., & Navarro, C. (2002). Summary of the historical eruptive activity of Volcán de Colima, Mexico 1519-2000. Journal of Volcanology and Geothermal Research, 117(1-2), 21-46.

Cabrera-Gutiérrez, R. (2010). Modelo de emisión de masa para la erupción de 1998 del Volcán de Colima, México (Unpublished Ph.D. Thesis). Universidad Nacional Autónoma de México, Mexico.

Capra, L., Macías, J. L., Cortés, A., Dávila, N., Saucedo, R., Osorio-Ocampo, S., Arce, J.L., Gavilanes-Ruiz, J.C., Corona-Chávez, P., García-Sánchez, L. & Sosa-Ceballos, G.

(2016). Preliminary report on the July 10–11, 2015 eruption at Volcán de Colima: Pyroclastic density currents with exceptional runouts and volume. *Journal of Volcanology and Geothermal Research*, 310, 39-49.

Cashman, K. V. (1988). Crystallization of Mount St. Helens 1980–1986 dacite: a quantitative textural approach. Bulletin of Volcanology, 50(3), 194-209.

Cashman, K. V. (1992). Groundmass Crystallization of Mount St Helens Dacite, 1980-1986 - a Tool for Interpreting Shallow Magmatic Processes. Contributions to Mineralogy and Petrology, 109(4), 431-449.

Cashman, K. V. (2004). Volatile controls on magma ascent and eruption. The State of the Planet: Frontiers and Challenges in Geophysics, 109-124.

Cashman, K. V., & Blundy, J. (2000). Degassing and crystallization of ascending andesite and dacite. Philosophical Transactions of the Royal Society of London A: Mathematical, Physical and Engineering Sciences, 358(1770), 1487-1513.

Cashman, K. V., & McConnell, S. M. (2005). Multiple levels of magma storage during the 1980 summer eruptions of Mount St. Helens, WA. Bulletin of Volcanology, 68(1), 57-75.

Cashman, K. V., & Scheu, B. (2015). Magmatic fragmentation. In The Encyclopedia of Volcanoes. – 2nd Ed. Academic Press. U.S.A., 459-471.

Cashman, K. V., Thornber, C. R., & Kauahikaua, J. P. (1999). Cooling and crystallization of lava in open channels, and the transition of Pāhoehoe Lava to'A'ā. Bulletin of Volcanology, 61(5), 306-323.

Cashman, K. V., Thornber, C. R., & Pallister, J. S. (2008). From dome to dust: Shallow crystallization and fragmentation of conduit magma during the 2004-2006 dome extrusion of Mount St. Helens, Washington. US Geological Survey professional paper, (1750), 387-413.

Cassidy, M., Cole, P. D., Hicks, K. E., Varley, N. R., Peters, N., & Lerner, A. H. (2015). Rapid and slow: Varying magma ascent rates as a mechanism for Vulcanian explosions. Earth and Planetary Science Letters, 420, 73-84.

Castruccio, A., Rust, A. C., & Sparks, R. S. J. (2014). Assessing lava flow evolution from post-eruption field data using Herschel–Bulkley rheology. Journal of Volcanology and Geothermal Research, 275, 71-84.

Cimarelli, C., Costa, A., Mueller, S., & Mader, H. M. (2011). Rheology of magmas with bimodal crystal size and shape distributions: Insights from analogue experiments. Geochemistry, Geophysics, Geosystems, 12(7).

Cioni, R., Pistolesi, M. & Rosi, M. (2015). Plinian and SubplinianSub-Plinian Eruptions. In The Encyclopedia of Volcanes. – 2nd Ed. Academic Press. U.S.A., 519-534

Clarke, A. B., Ongaro, T. & Belousov, A. (2015). Vulcanian Eruptions. In The Encyclopedia of Volcanes. – 2nd Ed. Academic Press. U.S.A., 505-518.

Clarke, A. B., Phillips, J. C., & Chojnicki, K. N. (2009). An investigation of Vulcanian eruption dynamics using laboratory analogue experiments and scaling analysis. Studies in Volcanology, 2, 155-166.

Clarke, A. B., Stephens, S., Teasdale, R., Sparks, R. S. J., & Diller, K. (2007). Petrologic constraints on the decompression history of magma prior to Vulcanian explosions at the Soufrière Hills volcano, Montserrat. Journal of Volcanology and Geothermal Research, 161(4), 261-274.

Cortés, A., Macías, J. L., Capra, L., & Garduño-Monroy, V. H. (2010). Sector collapse of the SW flank of Volcán de Colima, México: The 3600yr BP La Lumbre–Los Ganchos debris avalanche and associated debris flows. Journal of Volcanology and Geothermal Research, 197(1), 52-66.

Couch, S., Sparks, R. S. J., & Carroll, M. R. (2003). The kinetics of degassing-induced crystallization at Soufriere Hills Volcano, Montserrat. Journal of Petrology, 44(8), 1477-1502.

Crummy, J. M., Savov, I. P., Navarro-Ochoa, C., Morgan, D. J., & Wilson, M. (2014). High-K Mafic Plinian Eruptions of Volcan de Colima, Mexico. Journal of Petrology, 55(11), 2155-2191.

De la Cruz-Reyna, S. (1993). Random patterns of occurrence of explosive eruptions at Colima Volcano, Mexico. Journal of Volcanology and Geothermal research, 55(1), 51-68.

Deardorff, N. D., & Cashman, K. V. (2012). Emplacement conditions of the c. 1,600-year bp Collier Cone lava flow, Oregon: a LiDAR investigation. Bulletin of volcanology, 74(9), 2051-2066.

Dietterich, H. R., Cashman, K. V., Rust, A. C., & Lev, E. (2015). Diverting lava flows in the lab. Nature Geoscience, 8(7), 494-496.

Druitt, T.H., Young, S.R., Baptie, B., Bonadonna, C., Calder, E.S., Clarke, A.B., Cole, P.D., Harford, C.L., Herd, R.A., Luckett, R. and Ryan, G. (2002). Episodes of cyclic Vulcanian explosive activity with fountain collapse at Soufrière Hills Volcano, Montserrat. Memoirs-Geological Society of London, 21, 281-306.

Eichelberger, J. C. (1995). Silicic volcanism: ascent of viscous magmas from crustal reservoirs. Annual Review of Earth and Planetary Sciences, 23(1), 41-63.

García-Nava, A. (2016). Caracterización Reológico-Morfológica de los Flujos de Lava 1961-1962 y 2004 del Volcán de Colima (Unpublished Bachelor of Science thesis). Universidad de Colima, Mexico.

Gertisser, R., Charbonnier, S. J., Keller, J., & Quidelleur, X. (2012). The geological evolution of Merapi volcano, Central Java, Indonesia. Bulletin of volcanology, 74(5), 1213-1233.

Geschwind, C. H., & Rutherford, M. J. (1995). Crystallization of microlites during magma ascent: the fluid mechanics of 1980–1986 eruptions at Mount St Helens. Bulletin of Volcanology, 57(5), 356-370.

Gibb, F. G. (1974). Supercooling and the crystallization of plagioclase from a basaltic magma. Mineralogical Magazine, 39(306), 641-653.

Ginibre, C., Kronz, A., & WoÈrner, G. (2002). High-resolution quantitative imaging of plagioclase composition using accumulated backscattered electron images: new constraints on oscillatory zoning. Contributions to Mineralogy and Petrology, 142(4), 436-448.

Gonnermann, H. M., & Manga, M. (2003). Explosive volcanism may not be an inevitable consequence of magma fragmentation. Nature, 426(6965), 432.

Gonnermann, H. M., & Manga, M. (2007). The fluid mechanics inside a volcano. Annual Reviews in Fluid Mechanics., 39, 321-356.

Gottsmann, J., De Angelis, S., Fournier, N., Van Camp, M., Sacks, S., Linde, A., & Ripepe, M. (2011). On the geophysical fingerprint of Vulcanian explosions. Earth and Planetary Science Letters, 306(1-2), 98-104.

Griffiths, R. W. (2000). The dynamics of lava flows. Annual Review of Fluid Mechanics, 32(1), 477-518.

Guest, J. E., Kilburn, C. R. J., Pinkerton, H., & Duncan, A. M. (1987). The evolution of lava flow-fields: observations of the 1981 and 1983 eruptions of Mount Etna, Sicily. Bulletin of Volcanology, 49(3), 527-540.

Hall, M. L., Robin, C., Beate, B., Mothes, P., & Monzier, M. (1999). Tungurahua Volcano, Ecuador: structure, eruptive history and hazards. Journal of Volcanology and Geothermal Research, 91(1), 1-21.

Hammer, J. E. (2008). Experimental studies of the kinetics and energetics of magma crystallization. Reviews in mineralogy and geochemistry, 69(1), 9-59.

Hammer, J. E., & Rutherford, M. J. (2002). An experimental study of the kinetics of decompression-induced crystallization in silicic melt. Journal of Geophysical Research-Solid Earth, 107(B1).

Hammer, J. E., Cashman, K. V., & Voight, B. (2000). Magmatic processes revealed by textural and compositional trends in Merapi dome lavas. Journal of Volcanology and Geothermal Research, 100(1-4), 165-192.

Hammer, J. E., Cashman, K. V., Hoblitt, R. P., & Newman, S. (1999). Degassing and microlite crystallization during pre-climactic events of the 1991 eruption of Mt. Pinatubo, Philippines. Bulletin of Volcanology, 60(5), 355-380.

Higgins, M. D. (2011). Quantitative petrological evidence for the origin of K-feldspar megacrysts in dacites from Taapaca volcano, Chile. Contributions to Mineralogy and Petrology, 162(4), 709-723.

Instituto Nacional de Estadísitica y Geografía (2012). E13B35A2 [GRID]. Aguascalientes, Mexico. Available: INEGI Products, Modelos Digitales de Elevación de Alta Resolución LiDAR Data http://www3.inegi.org.mx/sistemas/productos/ (Accessed 2013).

James, M. R., & Varley, N. (2012). Identification of structural controls in an active lava dome with high resolution DEMs: Volcán de Colima, Mexico. Geophysical Research Letters, 39 (22).

Kauahikaua, J., Cashman, K. V., Mattox, T. N., Heliker, C. C., Hon, K. A., Mangan, M. T., & Thornber, C. R. (1998). Observations on basaltic lava streams in tubes from Kilauea Volcano, island of Hawai'i. Journal of Geophysical Research: Solid Earth, 103(B11), 27303-27323.

Klug, C., & Cashman, K. V. (1996). Permeability development in vesiculating magmas: implications for fragmentation. Bulletin of Volcanology, 58(2), 87-100.

Lavallée, Y., Varley, N. R., Alatorre-Ibargüengoitia, M. A., Hess, K. U., Kueppers, U., Mueller, S., Richard, D., Scheu, B., Spieler, O. & Dingwell, D. B. (2012). Magmatic architecture of dome-building eruptions at Volcán de Colima, Mexico. Bulletin of Volcanology, 74(1), 249-260.

Lipman, P. W., & Banks, N. G. (1987). AA flow dynamics, Mauna Loa 1984. US Geological Survey Prof. Pap, 1350, 1

Liu, Y., & Zhang, Y. (2000). Bubble growth in rhyolitic melt. Earth and Planetary Science Letters, 181(1), 251-264.

Luhr, J. F. (1992). Slab-derived fluids and partial melting in subduction zones: insights from two contrasting Mexican volcanoes (Colima and Ceboruco). Journal of Volcanology and Geothermal Research, 54(1-2), 1-18.

Luhr, J. F. (2002). Petrology and geochemistry of the 1991 and 1998–1999 lava flows from Volcán de Colima, México: implications for the end of the current eruptive cycle. Journal of Volcanology and Geothermal Research, 117(1), 169-194.

Luhr, J. F., & Carmichael, I. S. E. (1980). Colima Volcanic Complex, Mexico .1. Post-Caldera Andesites from Volcan Colima. Contributions to Mineralogy and Petrology, 71(4), 343-372.

Luhr, J. F., & Carmichael, I. S. E. (1981). The Colima Volcanic Complex, Mexico .2. Late-Quaternary Cinder Cones. Contributions to Mineralogy and Petrology, 76(2), 127-147.

Luhr, J. F., & Carmichael, I. S. E. (1990). Petrological monitoring of cyclical eruptive activity at Volcán Colima, México. Journal of Volcanology and Geothermal Research, 42(3), 235-260.

Luhr, J. F., & Prestegaard, K. L. (1988). Caldera Formation at Volcano Colima, Mexico, by a Large Holocene Volcanic Debris Avalanche. Journal of Volcanology and Geothermal Research, 35(4), 335-348.

Luhr, J. F., Navarro-Ochoa, C., & Savov, I. P. (2010). Tephrochronology, petrology and geochemistry of Late-Holocene pyroclastic deposits from Volcan de Colima, Mexico. Journal of Volcanology and Geothermal Research, 197(1-4), 1-32.

Macías, J. L., Saucedo, R., Gavilanes, J. C., Varley, N., Velasco Garcia, S., Bursik, M. I., Vargas-Gutierrez, V. & Cortes, A. (2006). Flujos piroclásticos asociados a la actividad explosiva del Volcán de Colima y perspectivas futuras. GEOS, 25 (3), 340-351.

Macías, J. L., Sosa-Ceballos, G., Arce, J. L., Gardner, J. E., Saucedo, R., & Valdéz, G. (2017). Storage conditions and magma processes triggering the 1818CE Plinian eruption of Volcán de Colima. Journal of Volcanology and Geothermal Research.

Mader, H. M., Llewellin, E. W., & Mueller, S. P. (2013). The rheology of two-phase magmas: a review and analysis. Journal of Volcanology and Geothermal Research, 257, 135-158.

Malin, M. C. (1980). Lengths of Hawaiian lava flows. Geology, 8(7), 306-308.

Mangan, M., & Sisson, T. (2000). Delayed, disequilibrium degassing in rhyolite magma: decompression experiments and implications for explosive volcanism. Earth and Planetary Science Letters, 183(3), 441-455.

Martel, C. (2012). Eruption dynamics inferred from microlite crystallization experiments: application to Plinian and dome-forming eruptions of Mt. Pelée (Martinique, Lesser Antilles). Journal of Petrology, 53(4), 699-725.

Martel, C., & Poussineau, S. (2007). Diversity of eruptive styles inferred from the microlites of Mt Pelée andesite (Martinique, Lesser Antilles). Journal of Volcanology and Geothermal Research, 166(3), 233-254.

Martel, C., & Schmidt, B. C. (2003). Decompression experiments as an insight into ascent rates of silicic magmas. Contributions to Mineralogy and Petrology, 144(4), 397-415.

Martel, C., Bourdier, J. L., Pichavant, M., & Traineau, H. (2000). Textures, water content and degassing of silicic andesites from recent plinian and dome-forming eruptions at Mount Pelée volcano (Martinique, Lesser Antilles arc). Journal of Volcanology and Geothermal Research, 96(3), 191-206.

Martel, C., Dingwell, D. B., Spieler, O., Pichavant, M., & Wilke, M. (2001). Experimental fragmentation of crystal-and vesicle-bearing silicic melts. Bulletin of Volcanology, 63(6), 398-405.

Martin del Pozzo, A. L., Romero V. H., Ruiz-Kitcher R. E. (1987). Los flujos piroclásticos del Volcán de Colima, Mexico. Geofísica Internacional, 26(2), 291-307.

Medina, F., Espíndola, J. M., De la Fuente, M., & Mena, M. (1996). A gravity model of the Colima, Mexico region. Geofísica Internacional, 35(4).

Melnik, O., & Sparks, R. S. J. (1999). Nonlinear dynamics of lava dome extrusion. Nature, 402(6757), 37-41.

Melnik, O., & Sparks, R. S. J. (2002). Dynamics of magma ascent and lava extrusion at Soufrière Hills Volcano, Montserrat. Geological Society, London, Memoirs, 21(1), 153-171.

Mooser, F., & Maldonado-Koerdell, M. M. (1963). Mexico: national report on volcanology: presented to the XIII general assembly of the International Union of Geodesy and Geophysics, Berkeley, 1963. sl.

Mora, J. C., Macias, J. L., Saucedo, R., Orlando, A., Manetti, P., & Vaselli, O. (2002). Petrology of the 1998-2000 products of Volcan de Colima, Mexico. Journal of Volcanology and Geothermal Research, 117(1-2), 195-212.

Mueller, S. B., Varley, N. R., Kueppers, U., Lesage, P., Davila, G. Á. R., & Dingwell, D. B. (2013). Quantification of magma ascent rate through rockfall monitoring at the growing/collapsing lava dome of Volcán de Colima, Mexico. Solid Earth, 4(2), 201.

Muir, D. D., Blundy, J. D., Hutchinson, M. C., & Rust, A. C. (2014). Petrological imaging of an active pluton beneath Cerro Uturuncu, Bolivia. Contributions to Mineralogy and Petrology, 167(3).

Naranjo, J. A., Sparks, R. S. J., Stasiuk, M. V., Moreno, H., & Ablay, G. J. (1992). Morphological, structural and textural variations in the 1988–1990 andesite lava of Lonquimay Volcano, Chile. Geological Magazine, 129(06), 657-678.

Navarro-Ochoa, C., Gavilanes-Ruiz, J. C., & Cortes-Cortes, A. (2002). Movement and emplacement of lava flows at Volcan de Colima, Mexico: November 1998-February 1999. Journal of Volcanology and Geothermal Research, 117(1-2), 155-167.

Newhall, C. G., & Self, S. (1982). The volcanic explosivity index (VEI) an estimate of explosive magnitude for historical volcanism. Journal of Geophysical Research: Oceans, 87(C2), 1231-1238.

Noguchi, S., Toramaru, A., & Nakada, S. (2008). Relation between microlite textures and discharge rate during the 1991–1995 eruptions at Unzen, Japan. Journal of Volcanology and Geothermal Research, 175(1), 141-155.

Noguchi, S., Toramaru, A., & Shimano, T. (2006). Crystallization of microlites and degassing during magma ascent: constraints on the fluid mechanical behavior of magma during the Tenjo Eruption on Kozu Island, Japan. Bulletin of Volcanology, 68(5), 432-449.

Núñez-Cornú, F., Nava, F. A., De la Cruz-Reyna, S., Jiménez, Z., Valencia, C., & García-Arthur, R. (1994). Seismic activity related to the 1991 eruption of Colima volcano, Mexico. Bulletin of Volcanology, 56(3), 228-237.

Oppenheimer J., Rust A.C., Cashman K.V. and Sandnes B. (2015) Gas migration regimes and outgassing in particle-rich suspensions. Frontiers in Physics, 3(60), 1-13.

Pinkerton, H., & Wilson, L. (1994). Factors controlling the lengths of channel-fed lava flows. Bulletin of Volcanology, 56(2), 108-120.

Poland, M. P. (2014). Time-averaged discharge rate of subaerial lava at Kīlauea Volcano, Hawai ‘i, measured from TanDEM-X interferometry: Implications for magma supply and storage during 2011–2013. Journal of Geophysical Research: Solid Earth, 119 (7), 5464-5481.

Preece, K., Barclay, J., Gertisser, R., & Herd, R. A. (2013). Textural and micro-petrological variations in the eruptive products of the 2006 dome-forming eruption of Merapi volcano, Indonesia: implications for sub-surface processes. Journal of Volcanology and Geothermal Research, 261, 98-120.

Preece, K., Gertisser, R., Barclay, J., Berlo, K., & Herd, R. A. (2014). Pre-and syn-eruptive degassing and crystallisation processes of the 2010 and 2006 eruptions of Merapi volcano, Indonesia. Contributions to Mineralogy and Petrology, 168(4), 1-25.

Preece, K., Gertisser, R., Barclay, J., Charbonnier, S. J., Komorowski, J. C., & Herd, R. A. (2016). Transitions between explosive and effusive phases during the cataclysmic 2010 eruption of Merapi volcano, Java, Indonesia. Bulletin of Volcanology, 78(8), 1-16.

Reubi, O., & Blundy, J. (2008). Assimilation of plutonic roots, formation of high-K 'exotic'melt inclusions and genesis of andesitic magmas at Volcán de Colima, Mexico. Journal of Petrology, 49(12), 2221-2243.

Reubi, O., Blundy, J., & Varley, N. R. (2013). Volatiles contents, degassing and crystallisation of intermediate magmas at Volcan de Colima, Mexico, inferred from melt inclusions. Contributions to Mineralogy and Petrology, 165(6), 1087-1106.

Reubi, O., Sims, K. W., Varley, N., Reagan, M., & Eikenberg, J. (2015). Timescales of degassing and conduit dynamics inferred from 210Pb–226Ra disequilibria in Volcan de Colima 1998–2010 andesitic magmas. Geological Society, London, Special Publications, 422(1), 189-206.

Reyes-Dávila, G. A., Arámbula-Mendoza, R., Espinasa-Pereña, R., Pankhurst, M. J., Navarro-Ochoa, C., Savov, I., Vargas-Bracamontes, D.M., Cortés-Cortés, A., Gutiérrez-Martínez, C., Valdés-González, C. & Domínguez-Reyes, T. (2016). Volcán de Colima dome collapse of July, 2015 and associated pyroclastic density currents. Journal of Volcanology and Geothermal Research, 320, 100-106.

Riker, J. M., Cashman, K. V., Rust, A. C., & Blundy, J. D. (2015). Experimental constraints on plagioclase crystallization during H 2 O-and H 2 O–CO 2-saturated magma decompression. Journal of Petrology, 56(10), 1967-1998.

Robin, C., Camus, G., & Gourgaud, A. (1991). Eruptive and Magmatic Cycles at Fuego-De-Colima Volcano (Mexico). Journal of Volcanology and Geothermal Research, 45(3-4), 209-225.

Roverato, M., Capra, L., Sulpizio, R., & Norini, G. (2011). Stratigraphic reconstruction of two debris avalanche deposits at Colima Volcano (Mexico): insights into pre-failure

conditions and climate influence. Journal of Volcanology and Geothermal Research, 207(1), 33-46.

Rust, A. C., & Cashman, K. V. (2004). Permeability of vesicular silicic magma: inertial and hysteresis effects. Earth and Planetary Science Letters, 228(1), 93-107.

Rust, A. C., Cashman, K. V., & Wallace, P. J. (2004). Magma degassing buffered by vapor flow through brecciated conduit margins. Geology, 32(4), 349-352.

Rutherford, M. J., Sigurdsson, H., Carey, S., & Davis, A. (1985). The May 18, 1980, eruption of Mount St. Helens: 1. Melt composition and experimental phase equilibria. Journal of Geophysical Research: Solid Earth, 90(B4), 2929-2947.

Ryan, A. (2010). Lava Flow Morphology and Rheology at Volcán de Colima, México (Unpublished Bachelor of Arts thesis). Colorado College, U.S.A.

Salzer, J. T., Nikkhoo, M., Walter, T. R., Sudhaus, H., Reyes-Dávila, G., Bretón, M., & Arámbula, R. (2014). Satellite radar data reveal short-term pre-explosive displacements and a complex conduit system at Volcán de Colima, Mexico. Frontiers in Earth Science, 2, 12.

Samaniego, P., Le Pennec, J. L., Robin, C., & Hidalgo, S. (2011). Petrological analysis of the pre-eruptive magmatic process prior to the 2006 explosive eruptions at Tungurahua volcano (Ecuador). Journal of Volcanology and Geothermal Research, 199(1-2), 69-84.

Saucedo, R., Macias, J. L., Bursik, M. I., Mora, J. C., Gavilanes, J. C., & Cortes, A. (2002). Emplacement of pyroclastic flows during the 1998-1999 eruption of Volcan de Colima, Mexico. Journal of Volcanology and Geothermal Research, 117(1-2), 129-153.

Saucedo, R., Macías, J. L., Gavilanes, J. C., Arce, J. L., Komorowski, J. C., Gardner, J. E., & Valdez-Moreno, G. (2010). Eyewitness, stratigraphy, chemistry, and eruptive dynamics of the 1913 Plinian eruption of Volcán de Colima, México. Journal of Volcanology and Geothermal Research, 191(3), 149-166.

Saucedo, R., Macías, J. L., Gavilanes, J. C., Arce, J. L., Komorowski, J. C., Gardner, J. E., & Valdez-Moreno, G. (2011). "Corrigendum to Eyewitness, stratigraphy, chemistry, and eruptive dynamics of the 1913 Plinian eruption of Volcan de Colima, Mexico" [Journal of Volcanology and Geothermal Research 191 (2010) 149–166]. Journal of Volcanology and Geothermal Research, 207(1), 67.

Savov, I. P., Luhr, J. F., & Navarro-Ochoa, C. (2008). Petrology and geochemistry of lava and ash erupted from Volcán Colima, Mexico, during 1998–2005. Journal of Volcanology and Geothermal Research, 174(4), 241-256.

Scandone, R., Cashman, K. V., & Malone, S. D. (2007). Magma supply, magma ascent and the style of volcanic eruptions. Earth and Planetary Science Letters, 253(3), 513-529.

Schipper, C. Ian, et al. "Cristobalite in the 2011–2012 Cordón Caulle eruption (Chile)." Bulletin of Volcanology 77.5 (2015): 34.

Scott, J. A., Mather, T. A., Pyle, D. M., Rose, W. I., & Chigna, G. (2012). The magmatic plumbing system beneath Santiaguito Volcano, Guatemala. Journal of Volcanology and Geothermal Research, 237, 54-68.

Self, S., Wilson, L., & Nairn, I. A. (1978). Vulcanian eruption mechanisms.

Shea, T., & Hammer, J. E. (2013). Kinetics of cooling-and decompression-induced crystallization in hydrous mafic-intermediate magmas. Journal of Volcanology and Geothermal research, 260, 127-145.

Sheldrake, T. E., Sparks, R. S. J., Cashman, K. V., Wadge, G., & Aspinall, W. P. (2016). Similarities and differences in the historical records of lava dome-building volcanoes: Implications for understanding magmatic processes and eruption forecasting. Earth-Science Reviews, 160, 240-263.

Sparks, R. S. J. (2003). Forecasting volcanic eruptions. Earth and Planetary Science Letters, 210(1), 1-15.

Sparks, R. S. J., & Wilson, L. (1976). A model for the formation of ignimbrite by gravitational column collapse. Journal of the Geological Society, 132(4), 441-451.

Streck, M. J. (2008). Mineral textures and zoning as evidence for open system processes. Reviews in Mineralogy and Geochemistry, 69(1), 595-622.

Swanson, S. E. (1977). Relation of nucleation and crystal-growth rate to the development of granitic textures. American Mineralogist, 62(9-10), 966-978.

Szramek, L., Gardner, J. E., & Larsen, J. (2006). Degassing and microlite crystallization of basaltic andesite magma erupting at Arenal Volcano, Costa Rica. Journal of Volcanology and Geothermal Research, 157(1), 182-201.

Taddeucci, J., Edmonds, M., Houghton, B., James, M. R. & Vergniolle, S. (2015) Hawaiian and Strombolian Eruptions. In The Encyclopedia of Volcanoes. – 2nd Ed. Academic Press. U.S.A., 485 – 499.

Teng, H. H. (2013). How ions and molecules organize to form crystals. Elements, 9(3), 189-194.

Thorpe, R. S., Gibson, I. L., & Vizcaino, J. S. (1977). Andesitic Pyroclastic Flows from Colima Volcano. Nature, 265(5596), 724-725.

Toramaru, A. (2006). BND (bubble number density) decompression rate meter for explosive volcanic eruptions. Journal of Volcanology and Geothermal Research, 154(3), 303-316.

Toramaru, A., Noguchi, S., Oyoshihara, S., & Tsune, A. (2008). MND (microlite number density) water exsolution rate meter. Journal of Volcanology and Geothermal Research, 175(1-2), 156-167.

Tuffen, H., Dingwell, D. B., & Pinkerton, H. (2003). Repeated fracture and healing of silicic magma generate flow banding and earthquakes? Geology, 31(12), 1089-1092.

Vargas-Gutierrez, V. R. (2009). Estratigrafía de los Flujos de Bloques y Ceniza Asociados a la Actividad 2005 en el Volcán de Colima, México (Unpublished Master of Science thesis). Universidad Nacional Autónoma de México, Mexico.

Varley, N. R., Arámbula-Mendoza, R., Reyes-Dávila, G., Sanderson, R., & Stevenson, J. (2010). Generation of Vulcanian activity and long-period seismicity at Volcán de Colima, Mexico. Journal of Volcanology and Geothermal Research, 198(1), 45-56.

Varley, N. R., Arámbula-Mendoza, R., Reyes-Dávila, G., Stevenson, J., & Harwood, R. (2010). Long-period seismicity during magma movement at Volcán de Colima. Bulletin of volcanology, 72(9), 1093-1107.

Vergniolle, S., & Brandeis, G. (1996). Strombolian explosions: 1. A large bubble breaking at the surface of a lava column as a source of sound. Journal of Geophysical Research: Solid Earth, 101(B9), 20433-20447.

Vergniolle, S., Brandeis, G., & Mareschal, J. C. (1996). Strombolian explosions: 2. Eruption dynamics determined from acoustic measurements. Journal of Geophysical Research: Solid Earth, 101(B9), 20449-20466.

Verma, S. P., & Luhr, J. F. (1993). Sr-Nd-Pb isotope and trace element geochemistry of calc–alkaline andesites from Volcán Colima, Mexico.Geofisica Internacional, 32(4).

Voight, B., Sparks, R. S. J., Miller, A. D., Stewart, R. C., Hoblitt, R. P., Clarke, A., Ewart, J., Aspinall, W.P., Baptie, B., Calder, E.S. & Cole, P. (1999). Magma flow instability and cyclic activity at soufriere hills volcano, montserrat, british west indies. Science, 283(5405), 1138-1142.

Wadge, G. (1978). Effusion rate and the shape of aa lava flow-fields on Mount Etna. Geology, 6(8), 503-506.

Walker, G. P. L. (1973). Lengths of Lava Flows. Philosophical Transactions of the Royal Society A: Mathematical Physical and Engineering Sciences, 274(1238), 107-118.

Woods, A. W., & Koyaguchi, T. (1994). Transitions between explosive and effusive eruptions of silicic magmas. Nature, 370(6491), 641-644.

Wright, H. M., Cashman, K. V., Mothes, P. A., Hall, M. L., Ruiz, A. G., & Le Pennec, J. L. (2012). Estimating rates of decompression from textures of erupted ash particles produced by 1999–2006 eruptions of Tungurahua volcano, Ecuador. Geology, 40(7), 619-622.

Wright, H. M., Cashman, K. V., Rosi, M., & Cioni, R. (2007). Breadcrust bombs as indicators of Vulcanian eruption dynamics at Guagua Pichincha volcano, Ecuador. Bulletin of Volcanology, 69(3), 281-300.

Zobin, V. M., Arámbula, R., Bretón, M., Reyes, G., Plascencia, I., Navarro, C., Téllez, A., Campos, A., González, M., León, Z. & Martínez, A. (2015). Dynamics of the January 2013–June 2014 explosive-effusive episode in the eruption of Volcán de Colima, México: insights from seismic and video monitoring. Bulletin of Volcanology, 77(4), 31.

Zobin, V. M., González-Amezcua, M., & Reyes-Dávila, G. (2002). Seismotectonic deformation of the volcanic edifice prior to the 1998 lava eruption of Volcán de Colima, México. Bulletin of volcanology, 64(5), 349-355.

Zobin, V. M., Navarro, C., Reyes-Davila, G., Orozco, J., Breton, M., Tellez, A., Reyes-Alfaro, G. & Vazquez, H. (2006). The methodology of quantification of volcanic explosions

from broad-band seismic signals and its application to the 2004-2005 explosions at Volcan de Colima, Mexico. Geophysical Journal International, 167(1), 467-478.

Zobin, V. M., Navarro-Ochoa, C. J., & Reyes-Dávila, G. A. (2006). Seismic quantification of the explosions that destroyed the dome of Volcán de Colima, Mexico, in July–August 2003. Bulletin of volcanology, 69(2), 141-147.

Zobin, V. M., Varley, N. R., Gonzalez, M., Orozco, J., Reyes, G. A., Navarro, C., & Breton, M. (2008). Monitoring the 2004 andesitic block-lava extrusion at Volcán de Colima, Mexico from seismic activity and SO2 emission. Journal of Volcanology and Geothermal Research, 177(2), 367-377.